

# IRE Transactions



## Microwave Theory and Techniques

UNIVERSITY OF HAWAII  
LIBRARY

Volume MTT-9

**JANUARY, 1961**

Number 1

*Published Bimonthly*

PERIODICAL

### In This Issue

UHF Strip Transmission Line Hybrid Junction

Gallium-Arsenide Point-Contact Diodes

Characterization of Microwave Variable Capacitance Diodes

Optimum Design of Wide-Band Parametric Amplifiers

A Low-Noise X-Band Parametric Amplifier Using a Silicon Mesa Diode

Four Frequency Parametric Up-Converters

Ferrites with Planar Anisotropy at Microwave Frequencies

Wide-Band Resonance Isolator

Maser Operation at Signal Frequencies Higher than Pump Frequency

A Solid-State Microwave Source

Propagation of Waves in a Plasma in a Magnetic Field

Magnetoplasma Effects in Solids

Coherent Excitation of Plasma Oscillations in Solids

Pulsed Millimeter-Wave Generation Using Ferrites

TK 7800  
523

PUBLISHED BY THE

Professional Group on Microwave Theory and Techniques



## IRE PROFESSIONAL GROUP ON MICROWAVE THEORY AND TECHNIQUES

The Professional Group on Microwave Theory and Techniques is an association of IRE members with professional interest in the field of Microwave Theory and Techniques. All IRE members are eligible for membership and will receive all Group publications upon payment of the prescribed annual fee of \$3.00. Members of the American Physical Society and the Institution of Electrical Engineers of Great Britain may become affiliated with PGM TT and receive all Group publications upon payment of the Affiliate fee of \$7.50 per year.

### Administrative Committee

#### Chairman

K. TOMIYASU

#### Vice Chairman

T. N. ANDERSON

#### Secretary-Treasurer

H. M. ALTSCHULER

R. E. BEAM

A. C. BECK

S. B. COHN

R. C. HANSEN

W. W. MUMFORD

A. A. OLINER

R. A. RIVERS

S. W. ROSENTHAL

T. S. SAAD

R. F. SCHWARTZ

G. SHAPIRO

G. SINCLAIR

P. D. STRUM

M. C. THOMPSON

R. D. WENGENROTH

#### *Ex-Officio*

W. L. PRITCHARD

#### *Honorary Life Members*

G. C. SOUTHWORTH

A. G. CLAVIER

#### Editor

DONALD D. KING

### PGMTT Chapters

Albuquerque-Los Alamos  
Baltimore  
Boston  
Buffalo-Niagara  
Chicago  
Columbus  
Denver-Boulder  
Long Island  
Los Angeles  
New York

R. L. O'Nan  
J. C. Wiltse  
C. E. Faffick  
E. S. Schlichter  
Robert Janowiak  
B. Querido  
G. E. Schafer  
B. Aaron  
R. C. Hansen  
Eugene Torgow

Northern N.J.  
Omaha-Lincoln  
Orange Belt  
Philadelphia  
San Diego  
San Francisco  
Schenectady  
Syracuse  
Tokyo, Japan  
Washington, D.C.

R. M. Foley  
C. O. Jett  
D. Sabih  
T. J. Vaughan  
H. O. Dickstein  
E. M. T. Jones  
C. C. Allen  
J. C. Williamson  
Kiyoshi Morita  
Benjamin Bernstein

### IRE TRANSACTIONS®

#### on Microwave Theory and Techniques

Published by The Institute of Radio Engineers, Inc., for the Professional Group on Microwave Theory and Techniques, at 1 East 79th Street, New York 21, N.Y. Responsibility for the contents rests upon the authors, and not upon the IRE, the Group, or its members. Annual subscription price: non-members, \$17.00; colleges and public libraries, \$12.75. Individual copies of this issue and all available back issues may be purchased at the following prices: IRE members (one copy) \$2.25, libraries and colleges \$3.25, all others \$4.50.

Address all manuscripts to Donald D. King, PGM TT Editor, Electronic Communications, Inc., 1830 York Road, Timonium, Md. Submission of three copies of manuscripts, including figures, will expedite the review.

COPYRIGHT ©1961—THE INSTITUTE OF RADIO ENGINEERS, INC.

Printed in U.S.A.

All rights, including translations, are reserved by the IRE. Requests for republication privileges should be addressed to the Institute of Radio Engineers, 1 E. 79th St., New York 21, N.Y.



# IRE Transactions

## on

# Microwave Theory and Techniques

5856-130

## EDITORIAL BOARD

*Editor*

Donald D. King

*Advertising Editor*

Robert A. Rivers

B. A. Auld  
D. J. Angelakos  
F. R. Arams  
W. P. Ayres  
R. W. Beatty  
A. D. Berk  
A. D. Bresler  
J. C. Cachieris  
S. B. Cohn  
P. D. Coleman  
R. E. Collin  
W. B. Day  
M. P. Forrer  
I. Goldstein  
R. C. Hansen  
H. Heffner  
E. M. T. Jones  
R. W. Klopfenstein  
P. A. Loth  
R. V. Lowman  
T. Moreno  
S. P. Morgan  
K. S. Packard, Jr.  
J. Reed  
J. M. Richardson  
P. A. Rizzi  
S. D. Robertson  
R. F. Schwartz  
W. Sichak  
D. C. Stinson  
E. Strumwasser  
L. Swern  
P. H. Vartanian, Jr.  
H. T. Villeneuve  
M. T. Weiss  
G. J. Wheeler  
R. F. Whitmer  
J. C. Wiltse  
L. Young  
F. J. Zucker

Volume MTT-9

JANUARY, 1961

Number 1

## TABLE OF CONTENTS

Frontispiece, 1959 Microwave Prize. . . . . Bert A. Auld 2

CONTRIBUTIONS FROM THE 1960 NATIONAL  
MICROWAVE SYMPOSIUM

UHF Strip Transmission Line Hybrid Junction. . . . .	I. Tatsuguchi	3
Gallium-Arsenide Point-Contact Diodes. . . . .	W. M. Sharpless	6
Characterization of Microwave Variable Capacitance Diodes. . . . .	Sverre T. Eng	11
Correction to "Scattering of a Plane Wave on a Ferrite Cylinder and Normal Incidence". . . . .	Wilhelm H. Eggimann	22
A Study of the Optimum Design of Wide-Band Parametric Amplifiers and Up-Converters. . . . .	George L. Matthaei	23
Correction to "Impedances of an Elliptic Waveguide (for the $H_1$ Mode)". . . . .	G. R. Valenzuela	38
A Low-Noise X-Band Parametric Amplifier Using a Silicon Mesa Diode. . . . .	R. D. Weglein and F. Keywell	39
Design and Operation of Four-Frequency Parametric Up-Converters. . . . .	J. A. Luksch, E. W. Matthews and G. A. VerWys	44
Ferrites with Planar Anisotropy at Microwave Frequencies. . . . .	Isidore Bady	52
Wide-Band Resonance Isolator. . . . .	W. W. Anderson and M. E. Hines	63
Maser Operation at Signal Frequencies Higher than Pump Frequency. . . . .	Frank R. Arams	68
A Solid-State Microwave Source from Reactance-Diode Harmonic Generators. . . . .	T. M. Hytlin and K. L. Kotzebue	73
Propagation of Waves in a Plasma in a Magnetic Field. . . . .	William P. Allis	79
Magnetoplasma Effects in Solids. . . . .	Benjamin Lax	83
Coherent Excitation of Plasma Oscillations in Solids. . . . .	David Pines	89
Pulsed Millimeter-Wave Generation Using Ferrites. . . . .	B. J. Elliott, T. Schaug-Petterson and H. J. Shaw	92

## CORRESPONDENCE

Tuning Range of the Backward Traveling-Wave Parametric Amplifier. . . . .	Thomas M. Straus	95
Size Effect in the Measurement of Microwave Permeability of Ferrites. . . . .	B. Maher and L. Silber	96
Cutoff Variable Reactor. . . . .	Koryu Ishii	96
Single-Mode Cavity Maser at 2200 MC. . . . .	D. W. Hanson and J. J. Rowley	97
Higher-Order Evaluation of Dipole Moments of a Small Circular Disk for Arbitrary Incident Fields. . . . .	Wilhelm H. Eggimann	98
Capacitance Definitions for Parametric Operation. . . . .	Hubert Heffner	98
A Tunnel-Diode Amplifying Converter. . . . .	L. E. Dickens and C. R. Gneiting	99
Impedance Matching by Charts. . . . .	Michael R. Leibowitz	101
Theoretical Evaluation of Resonance Frequencies in a Cylindrical Cavity with Radial Vanes. . . . .	A. Singh and R. A. Rao	101
PGMTT News, 1960 National Microwave Symposium. . . . .		103
Contributors. . . . .		105





Bert A. Auld

Recipient of the 1959 Microwave Prize



**The Institute of Radio Engineers**  
**Professional Group on Microwave Theory and Techniques**  
**1959 Microwave Prize**

to

**Bert A. Auld**

for a very significant contribution to the field of endeavor of the IRE-PGMS in his paper entitled "The Synthesis of Symmetrical Waveguide Circulators" published in the IRE TRANSACTIONS-MOS-7, No. 2, pp. 238-246, April 1959. The paper treated for the first time the general cases of symmetrical ferrite circulators.

May 10, 1960



*A. A. Oliner*  
Chairman, PGMS

*H. W. Mumford*  
Chairman, PGMS  
Awards Committee



# UHF Strip Transmission Line Hybrid Junction\*

I. TATSUGUCHI†

**Summary**—A hybrid junction has been developed using a symmetrical strip transmission line for application in the UHF range. It has a frequency band of  $\pm 20$  per cent where the input voltage standing-wave ratios at all ports are less than 1.26 (2 db), the power divisions are within 0.1 db, and the difference in power between the series input and parallel input ports is less than 0.3 db. The isolation is greater than 40 db and 24 db, respectively, for the two pairs of conjugate ports. These circuits are relatively small, light-weight, simple to build and reproduce, and are inexpensive.

The approximate equivalent circuit of the configuration assuming transmission in the TEM mode is presented. The results of the analysis and the important features in the design and fabrication and a few modifications of the configuration are discussed.

## INTRODUCTION

A HYBRID junction is a four-port network which, when properly terminated, has the characteristic of transferring energy from any one port equally to two of the other ports with no energy appearing directly at the fourth or conjugate port. Some typical forms of hybrid junctions are the magic tee, hybrid ring and the 3-db directional coupler. These hybrid junctions are useful in balanced mixers, impedance measuring devices, modulators, phase adjusters, tuners, comparators, etc.

The hybrid junctions discussed here appear in printed symmetrical strip transmission line forms. They are designed for the UHF region. They have a broad bandwidth, good power division, isolation, and impedance match. They are relatively small, lightweight, simple to build and reproduce, and are inexpensive.

## PRINTED-CIRCUIT HYBRID JUNCTION

A sketch of the printed-circuit hybrid junction constructed in strip transmission line is shown in Fig. 1. The side view of the circuit shows the transmission line with conductors I and II embedded in a dielectric layer sandwiched between two ground planes. Conductors I and II are mirror images except in the region of  $A-B-B'-A'$ . The circuit is assembled by laying conductor I over on II so that the corresponding parts align. At the center of conductor II, a thin dielectric sheet is located such that when assembled, the horizontal line 2 will not make contact to the pieces of conductors beneath the dielectric sheet. The purpose of the pieces of conductors is to connect points  $A$  to  $A'$  and  $B$  and  $B'$ . The lines are connected to the ground planes at four points marked with  $X$ . These form short-circuited quarter-wavelength elements. The boards are assembled and the ground planes tied together with screws spaced about one inch apart.

\* Received by the PGMTT, February 26, 1960; revised manuscript received, July 25, 1960. The work reported in this paper was supported by Army Ordnance under Military Contract No. DA-30-069-ORD-1955.

† Bell Telephone Labs., Inc., Whippany, N. J.

The number of grounding screws is increased in the vicinities of corners and transitions, in order to prevent undesirable higher-order modes of propagation. All screws are located beyond the major portion of the TEM field. A photograph of the circuit is shown in Fig. 2.

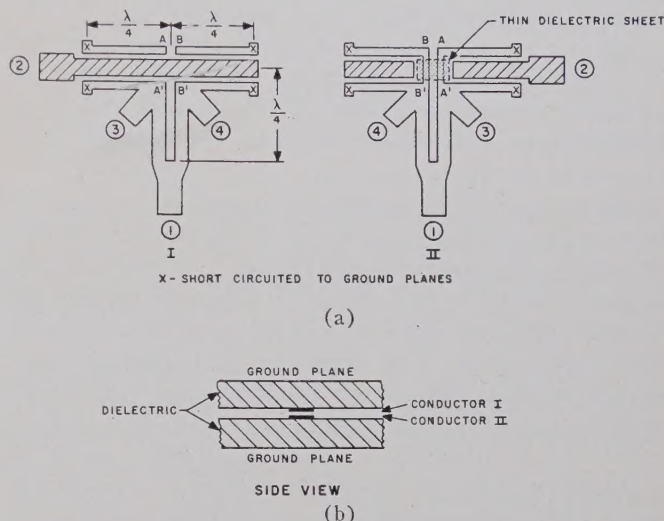


Fig. 1—Strip transmission line hybrid junction; (a) top view, (b) side view.

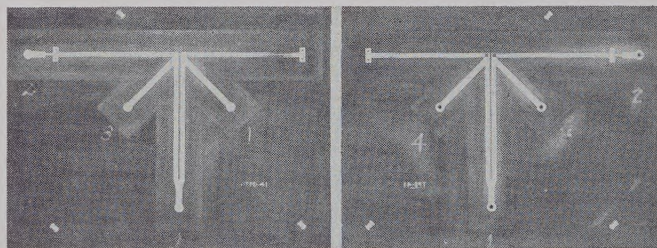


Fig. 2—Photograph of hybrid junction.

Referring to Fig. 1, we see that ports 1 and 2 are one pair of conjugate arms and ports 3 and 4 are the other pair. Port 1 feeds 3 and 4 in parallel through a directly-coupled quarter-wavelength transformer. Its characteristic impedance should be equal to

$$Z_0' = \sqrt{\left(\frac{Z_3}{Z_3 + Z_4}\right)Z_1},$$

where  $Z_n$  is the impedance terminating port  $n$ .

Port 2 feeds 3 and 4 in series through a quarter-wavelength coupled section. Its characteristic impedance was determined empirically. As a first approximation, it was set equal to



$$Z_0'' = \sqrt{(Z_3 + Z_4)Z_2},$$

where  $Z_0''$  was equal to the characteristic impedance of an isolated line. This value will be decreased by the proximity of the short-circuited quarter-wavelength line used as part of the coupling device. To obtain sufficient coupling to the loads with a short-circuited quarter-wavelength line placed along only one edge of line 2, we would have to use a very narrow coupling gap which would be impractical. A gap of practical width can be realized by using short-circuited quarter-wavelength sections placed along both edges of line 2. The characteristic impedance of these elements should be high in order to maintain a broad band response.

The open-circuited quarter-wavelength section of line 2 is used to compensate for the variation in load impedances as seen from port 2. It also makes the circuit symmetrical. This should improve the balance characteristics.

Assuming a TEM mode of transmission, we can derive an approximate equivalent circuit from the hybrid junction configuration shown in Fig. 1. Starting at port 2, the two loads 3 and 4 are fed by a quarter-wavelength coupled section in series with an open-circuited quarter-wavelength stub. The short-circuited quarter-wavelength sections used in the coupling from port 2 and with the open-circuited stubs appear in shunt across the two loads. In addition, the loads are fed in parallel by a quarter-wavelength transformer which is connected to port 1. This equivalent circuit configuration is shown in Fig. 3.

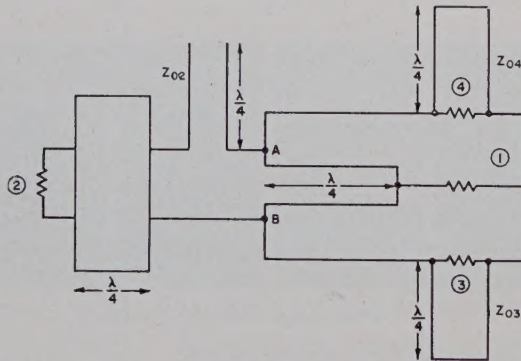
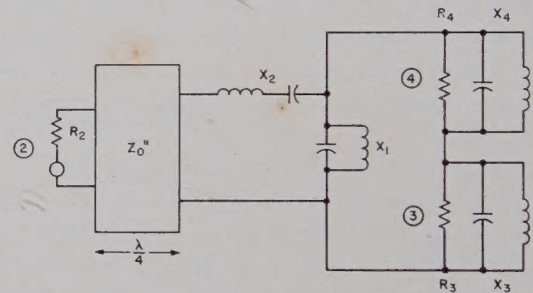


Fig. 3—Equivalent circuit of hybrid junction.

The operation of the hybrid junction can easily be analyzed from the equivalent circuit of Fig. 3. A signal applied at port 2 appears in series across the loads at 3 and 4. No energy appears at port 1 because it is tapped at the mid-point of points A-B. A signal applied at port 1 appears in parallel across the loads 3 and 4, and no energy appears at 2 because points A-B are at the same potential. This assumes matched conditions. Ports 1 and 2 are isolated from each other and are one pair of conjugate arms. Ports 3 and 4 are the other pair of conjugate arms which are also isolated from each other.

The quarter-wavelength transformer at port 1 is directly coupled to the two loads in parallel. The  $Z_0$  necessary to match the input circuit is low and port 1 is relatively broadband. The transformer at port 2 requires a relatively high  $Z_0$  in order to match the input to the two loads in series and also the coupling to the loads is across an air gap. This makes this port relatively narrow band and the input impedance quite dependent on the dimensions of the coupling gap.

Port 2 is the most critical terminal, and to determine its characteristics a simplification can be made to the equivalent circuit. A simplified circuit is shown in Fig. 4. Analysis of this circuit indicates that  $Z_{03}$  and  $Z_{04}$  of the short-circuited quarter-wavelength line should be high and the  $Z_{02}$  of the open-circuited quarter-wavelength line should be low. For an idealized case, the  $Z_0$  of the lines could be chosen to give maximum bandwidth at port 2, but this optimum condition requires the use of characteristic impedances which may be difficult to realize in practice. Although the optimum values may not be practical, the analysis does indicate the improvement that can be achieved by the proper choice of impedances.



$$\begin{aligned} R_2 = R_3 = R_4 &= 50\Omega \\ X_3 = X_4 &= Z_{03} \tan \beta l_3 \\ l_3 &= \text{Length of short-circuited stub} \\ l_1 &= \text{Length of short-circuited line connecting terminal 1 to 3 and 4} \\ l_2 &= \text{Length of open-circuited stub} \\ Z_0'' &= \sqrt{(R_2)(R_3 + R_4)} \end{aligned}$$

$$\begin{aligned} X_1 &= Z_{01} \tan \beta l_1 \\ X_2 &= -Z_{02} \cot \beta l_2 \end{aligned}$$

Fig. 4—Modified equivalent circuit.

#### EXPERIMENTAL HYBRID JUNCTION

A printed-circuit hybrid junction is shown in Fig. 5 along with typical dimensions. Reactive elements shown at ports 1 and 2 are used to obtain the proper impedance characteristics. The measured input impedance characteristics, balance and isolation curves are shown in Figs. 6 and 7. The input VSWR at port 2 is less than 1.26 (2 db) over  $\pm 20$  per cent band. The other ports show a better response. The power divisions are within 0.1 db over the same band. The difference in power between the series and parallel input ports is about 0.3 db. The isolation for the two pairs of conjugate ports is greater than 24 db and 40 db.

Similar characteristics can be achieved in other forms of printed-circuit hybrid-junction configurations but with somewhat narrower bandwidths. A typical "Ring" hybrid junction may give a bandwidth in the order of



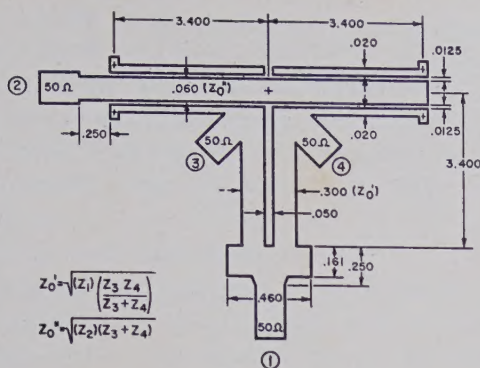


Fig. 5—Strip transmission line hybrid junction.

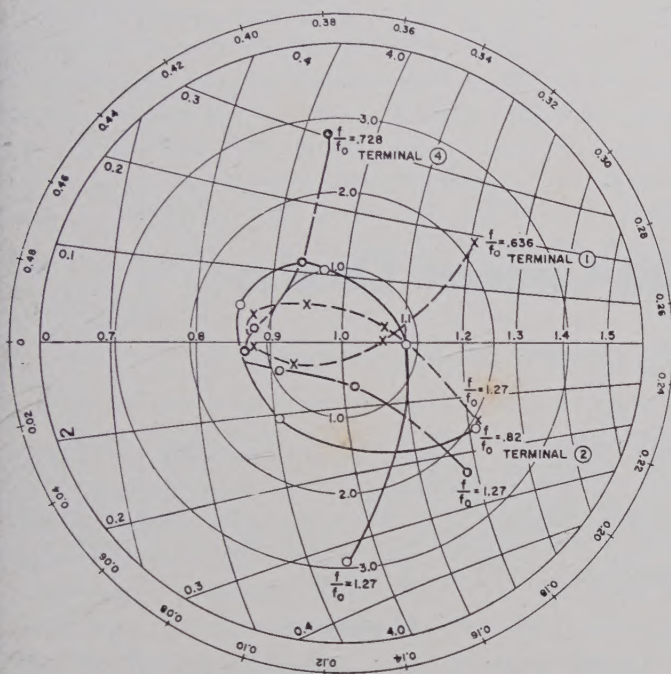
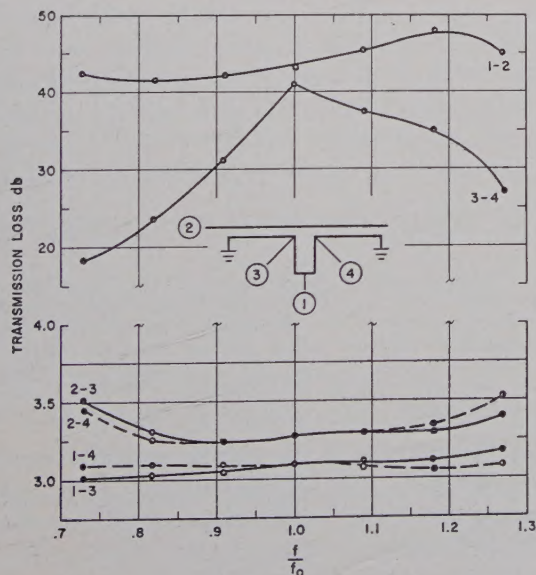


Fig. 6—Measured input impedances.

Fig. 7—Transmission loss vs  $f/f_0$ .

$\pm 5$  per cent. Good bandwidths can be realized with 3-db strip line directional couplers, but with a  $90^\circ$  phase shift.<sup>1</sup> A quarter-wavelength 3-db directional coupler gives a bandwidth of  $\pm 15$  per cent. A three-quarter-wavelength 3-db directional coupler may give a very wide bandwidth of  $\pm 50$  per cent. These directional couplers have theoretically infinite directivity but experimental models have been constructed with directivity less than 40 db.

The hybrid junction discussed here differs chiefly from other strip transmission line hybrid junctions<sup>2-4</sup> in the method of coupling from the series input port to the two loads. This is accomplished with a single-plane configuration using quarter-wavelength short-circuited lines placed along both edges of the main line. Others have done this by using a multiple-plane configuration or by the use of shorted and open-circuited quarter-wavelength elements.

#### PRECAUTIONS AND MODIFICATIONS

In the fabrication of a hybrid junction circuit, there are several precautions which should be observed. The most critical dimension is the width of the coupling gap. Any drastic deviation from the design value will affect the input impedance of port 2. This, therefore, puts a tight registration requirement in the assembly of the circuit. When the two halves of the boards are assembled, the corresponding parts of the circuit should mate, especially the coupling gap.

Symmetry is another requirement necessary in order to maintain the proper balance characteristics. This implies symmetry in the original master made by the draftsman to the symmetrical and accurate etching of the printed circuit boards. Other precautions are the frequent use of grounding screws in order to prevent the propagation of higher-order modes, the use of low-loss dielectric material and the use of well-matched transducers. A circuit made with care in observing all the precautions should give satisfactory results.

In the fabrication of the circuit there may also be a problem involved with overetching the narrow coupling gap. This problem can be eliminated by machining the critical dimension. It is possible to increase the width of the coupling gap to relieve the tolerance, but if this is done it becomes necessary to insert a low-loss, high dielectric-constant material in the gap to maintain the same effective coupling.

A modification in circuit configuration can be made to relieve some of the critical registration tolerance in

<sup>1</sup> J. K. Shimizu, "Strip-line 3-db directional couplers," 1957 IRE WESCON CONVENTION RECORD, pt. 1, pp. 4-15.

<sup>2</sup> A. Alford and C. B. Watts, Jr., "A wide band coaxial hybrid," 1956 IRE NATIONAL CONVENTION RECORD, pt. 1, pp. 171-179.

<sup>3</sup> H. G. Pascalar, "Strip-line hybrid junction," IRE TRANS. ON MICROWAVE THEORY AND TECHNIQUES, vol. MTT-5, pp. 23-30; January, 1957.

<sup>4</sup> E. M. T. Jones, "Wide-band strip-line magic-T," IRE TRANS. ON MICROWAVE THEORY AND TECHNIQUES, vol. MTT-8, pp. 160-168; March, 1960.



the assembly of the unit. The circuit can be etched only on one board and the necessary connection in the center of the configuration can be made by soldering a small strip of copper between the desired points. If such a modification is made, it may be necessary to use a thicker layer of copper or a narrower coupling gap in order to maintain the same effective coupling across the gap.

#### CONCLUSION

A printed-circuit strip transmission line hybrid junction with input voltage standing-wave ratio less than 1.26 (2 db) over  $\pm 20$  per cent band, power division within 0.1 db, and isolation of the two pairs of the con-

jugate ports greater than 24 db and 40 db has been developed for the UHF band. Circuits have been fabricated which operate satisfactorily up to 1500 mc. These hybrid junction circuits have many useful applications and can easily be reproduced if a few precautions are taken in the etching and assembly of the circuit.

#### ACKNOWLEDGMENT

The author gratefully acknowledges the many discussions and helpful suggestions by W. W. Mumford on the subject of hybrid junctions. Appreciation also goes to W. H. Conway for his help in the course of this investigation.

## Gallium-Arsenide Point-Contact Diodes\*

W. M. SHARPLESS†, FELLOW, IRE

**Summary**—This paper describes some of the work on gallium-arsenide point-contact diodes which is currently in progress at the Bell Telephone Laboratories, Holmdel, N. J. Gallium arsenide, one of the Group III-V intermetallic compounds, possesses properties which tend to make it superior to either silicon or germanium for many high-frequency diode applications. By controlling the resistivity of the gallium arsenide and the point-contact processing techniques, diodes have been fabricated specifically for use as millimeter wave first detectors, high-speed switches, and reactive elements for microwave parametric oscillators and amplifiers. The operating characteristics of several different types of gallium-arsenide reactive diodes are discussed and mention is made of simple design formulas which may be used to tentatively evaluate the performance to be expected from such diodes. Noise figure measurements are included in a résumé covering some of the experimental results that have been obtained using gallium-arsenide point-contact diodes as variable reactance elements in microwave parametric amplifiers.

#### INTRODUCTION

GALLIUM arsenide, one of the Group III-V intermetallic compounds, possesses properties which tend to make it superior to either silicon or germanium for many high-frequency diode applications. By controlling the resistivity of the gallium arsenide and using the proper processing techniques, point-contact diodes have been fabricated specifically for use as millimeter wave first detectors, high-speed switches, or reactive elements for microwave parametric oscillators

and amplifiers.<sup>1-6</sup> The important operating characteristics of different types of experimental gallium-arsenide varactor diodes will be discussed in this paper, and mention is made of the general fabrication methods employed in assembling the diodes.

#### MATERIALS

All the single-crystal gallium-arsenide (GaAs) material used in this work was prepared by J. M. Whelan, Bell Telephone Laboratories, Murray Hill, N. J. Purified material was doped to the required resistivity by regrowing the crystals in an arsenic atmosphere containing donor impurities such as sulphur, selenium, or tellurium. In order to realize the full electron mobility of the GaAs, efforts were made to avoid compensated doping. The final single crystal *N*-type material was sliced into thin disks, given a back contact of deposited

<sup>1</sup> W. M. Sharpless, "High frequency gallium arsenide point contact rectifiers," *Bell Sys. Tech. J.*, vol. 38, pp. 259-270; January, 1959.

<sup>2</sup> B. C. DeLoach and W. M. Sharpless, "An X-band parametric amplifier," *PROC. IRE*, vol. 47, pp. 1664-1665; September, 1959.

<sup>3</sup> M. Uenohara and W. M. Sharpless, "An extremely low noise 6-kMc parametric amplifier using gallium arsenide point contact diodes," *PROC. IRE*, vol. 47, pp. 2113-2114; December, 1959.

<sup>4</sup> B. C. DeLoach and W. M. Sharpless, "X-Band parametric amplifier noise figures," *PROC. IRE*, vol. 47, pp. 2114-2115; December, 1959.

<sup>5</sup> B. C. DeLoach, "17.35 and 30 kMc parametric amplifiers," *PROC. IRE*, vol. 48, p. 1323; July, 1960.

<sup>6</sup> W. M. Goodall and A. F. Dietrich, "A fractional millimicrosecond electrical stroboscope," *PROC. IRE*, vol. 48, pp. 1591-1594; September, 1960.

\* Received by the PGMTT, August 8, 1960.

† Bell Telephone Labs., Inc., Holmdel, N. J.



tin followed by a nickel plate forming a surface suitable for soldering. The material was then ultrasonically cut into 0.028-inch disks suitable for mounting in the miniature cartridge used in making the diodes. The point-contact surface was given a mirror-like finish and, immediately before setting up the diodes, the polished surface was given a light etch with a dilute solution of hydrofluoric and nitric acids.

The point-contact springs were made of phosphor-bronze wires having a diameter of from one to three mils, depending on the type of diode being assembled. In all cases, the ends of the springs were sharply pointed electrolytically to a radius of about one-tenth mil in a dilute solution of sulfuric acid.

The miniature cartridge-type case in which the GaAs diodes are mounted is shown in Fig. 1. The small GaAs disk and the phosphor-bronze point-contact spring are shown mounted on the ends of round nickel rods which are pressed into place from opposite ends of a round steel-capped quartz-insulated cartridge type holder. The use of a section of fused-quartz, thin-wall tubing provides a low-loss, low-capacity insulating section which is mechanically relatively insensitive to temperature changes.

#### FORMING TECHNIQUES

After contact is established between the point-contact wire and the polished surface of the GaAs, the point contact is electrically formed by applying a low ac voltage directly on the diode terminals. Because of the fact that the reverse impedance of these diodes is very high, most of the forming current flows in 60-cycle pulses in the forward direction. Depending upon the type of diode being formed, the peak currents are limited by the use of an appropriately sized series resistor. The static characteristic of the diode is displayed on a cathode-ray oscilloscope while the forming is in progress.

Fig. 2 shows an enlargement of the point-contact region of the diode. During the forming process, a high current density is produced at the point which heats the small point-contact area. It is believed that this allows a small amount of copper (an acceptor in GaAs) to diffuse from the phosphor-bronze point (95 per cent Cu + 5 per cent Sn) into the GaAs. The surface damage incurred during polishing probably enhances the rate of diffusion. This diffusion process forms a tiny, extremely abrupt junction which we desire for efficient operation at very high frequencies.

#### DIODE CHARACTERISTICS

The effect of varying the resistivity of the GaAs material used in the point-contact diodes is shown in Fig. 3. Typical static characteristics are shown for diodes made from *N*-type doped GaAs materials, ranging from 0.065 ohm-cm for a lightly doped sample to 0.002 ohm-

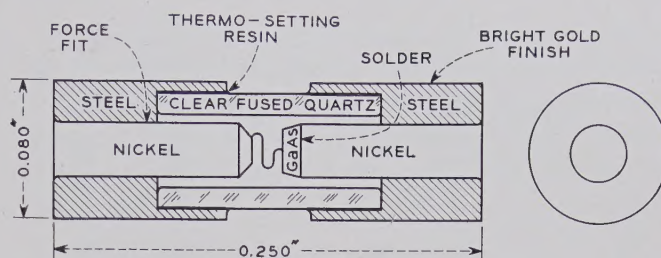


Fig. 1—Sectional view of the cartridge-type point-contact diode.

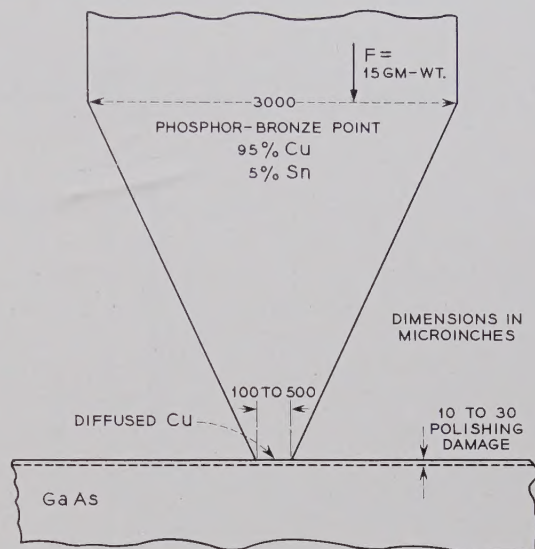


Fig. 2—Expanded view of the point-contact area (courtesy N. C. Vanderwal).

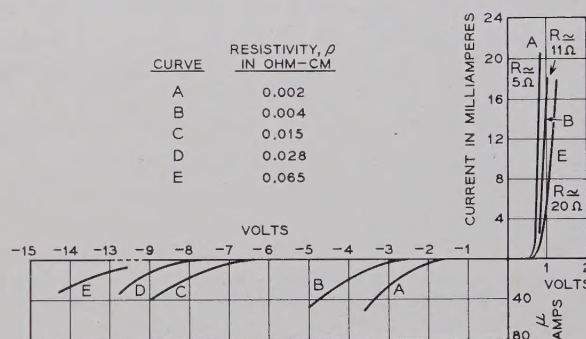


Fig. 3—Static characteristics of *N*-type gallium-arsenide point-contact diodes.

cm for heavily doped material. It should be noted that the heaviest doped material yields the lowest diode forward resistance (about 5 ohms for  $\rho = 0.002$  ohm-cm material). However, as we will see later, the capacity of the diode increases with the doping, so that a compromise must be made between lower spreading resistance and higher capacitances; for a given parametric amplifier application, the doping is usually chosen to give the highest cutoff frequency.

To illustrate this point, Figs. 4 and 5 show the measured voltage-current and voltage-capacitance charac-



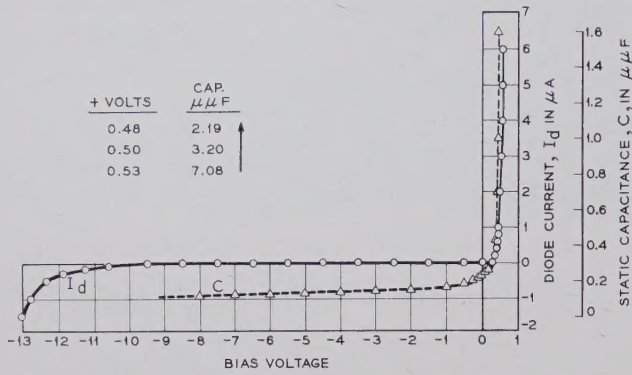


Fig. 4—Voltage-current and voltage-capacitance characteristics of a typical point contact GaAs diode ( $\rho = 0.025$  ohm-cm).

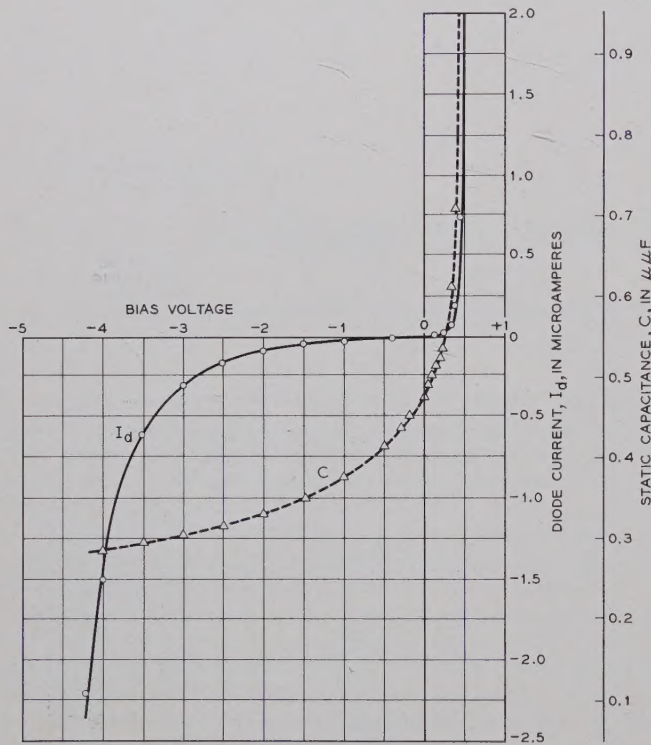


Fig. 5—Voltage-current and voltage-capacitance characteristics of a typical point-contact GaAs diode ( $\rho = 0.003$  ohm-cm).

teristics of two typical point-contact types of GaAs experimental diodes. Fig. 4 shows the curves for a diode made with 0.025-ohm-cm resistivity material which results in a spreading resistance of about 12 ohms. It is seen that the total capacitance, including the case (0.08  $\mu\mu f$ ), is about 0.1  $\mu\mu f$  for the negatively biased condition; the capacitance increases to a value nearly 15 times greater for a positive bias, which produces a forward current flow of a few microamperes. The resistive component of the impedance is still very high, however, and the capacitance may be increased to a value nearly 70 times the reverse bias value before appreciable forward current begins to flow.

Fig. 5 is a plot similar to that of Fig. 4, showing the resistive and capacitive variations with bias for a GaAs diode made with 0.003 ohm-cm material. This type of

diode has a lower spreading resistance, and the best diodes have cutoff frequencies well in excess of 100 kMc. This type of GaAs diode has, in general, given us the best noise figures in most parametric amplifier applications. It will be noticed that the capacitance may be changed over a range of about three times (0.3 to 0.9  $\mu\mu f$ ) with the resistance remaining sufficiently high so that not more than plus or minus one or two microamperes of current will flow. A typical fixed bias to use when employing this type of diode in a parametric amplifier is about minus 1.2 volts. An available pump power of less than 10 milliwatts will normally be required to drive the diode over the range mentioned.

Fig. 6 shows the measured voltage-capacitance curve for a typical experimental GaAs point-contact diode formed at low current densities. (The barrier voltage,  $\phi_0 = 0.5$ , was obtained by plotting  $1/C^2$  against the applied bias;  $\phi_0$  is the intercept on the voltage axis.) It is seen that the barrier capacitance of the diode proper (case capacitance of 0.08  $\mu\mu f$  subtracted) follows very nearly the inverse square root of the voltage rule which one would expect for the case of an abrupt junction. If

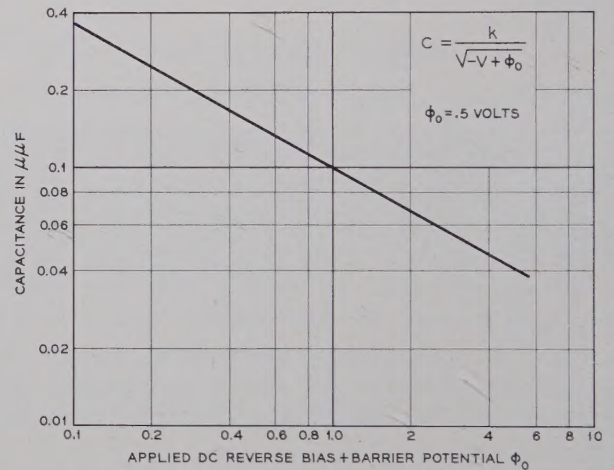


Fig. 6—Measured voltage-capacitance curve for a typical experimental GaAs point-contact diode formed at low current densities.

one forms the diodes at higher levels, a more graded junction will, in general, result and the capacity-vs-bias relation tends to approach a cube-root curve rather than the approximate square-root variation shown in Fig. 6.

There are a few rather simple formulas which may be used to tentatively evaluate the performance expected from varactor diodes used in parametric amplifier applications. These relations are shown in Fig. 7. The inductance of the diode is assumed to be small and has been neglected in the simplified analysis. The generally accepted simplified equivalent circuit of the diode is shown on the left of Fig. 7. When the diode is used as a variable reactance in a parametric amplifier, it is biased into a nonconducting region and the barrier resistance  $R$  becomes very high, of the order of megohms, and may be dropped from the active circuit. The



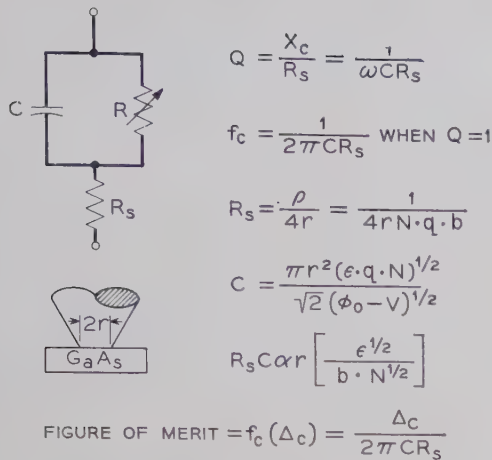


Fig. 7—Approximate formulas for tentative evaluation of the expected performance of varactor diodes in parametric amplifiers.

resulting effective high-frequency circuit thus becomes the barrier capacity  $C$  in series with the base or spreading resistance  $R_s$ . The expression for the  $Q$  of the diode at high frequency is then simply the ratio of the resistive and reactive components, and the cutoff frequency  $f_c$  is taken as the frequency at which  $Q$  becomes equal to one. In parametric diodes, we wish the  $Q$  to be as high as possible for efficient operation at the highest possible frequency.

As may be seen from the equations, the cutoff frequency  $f_c$  is inversely proportional to the product of  $C$  and  $R_s$ , and a diode design which minimizes this product is very desirable. The equations further show the important factors which contribute to the value of  $C$  and  $R_s$ . Other symbols used in these equations are as follows:

- $r$  = radius of point contact in cm
- $N$  = carrier density in  $\text{cm}^{-3}$
- $q$  = charge on electron ( $1.6 \times 10^{-19}$  coulomb)
- $\rho$  = resistivity in ohm-cm
- $b$  = mobility,  $\text{cm}^2/\text{volt-second}$
- $\epsilon$  = dielectric constant ( $\epsilon_0/36 \times 10^{-9}$ )
- $\phi_0$  = barrier height in volts
- $V$  = bias voltage.

The equation showing the factors that are proportional to the  $R_s C$  product indicates why a small-area GaAs point-contact diode should be a superior performer compared to other diodes. The small point contact means that the radius  $r$  is very small and it is seen that  $r$  enters the equation directly. The dielectric constant of the material used is also important and should be made as low as possible. Silicon has a dielectric constant  $\epsilon_0 = 12$ , germanium is 16, and GaAs is only 11.

The mobility of ordinary  $P$ -type silicon as used in the commercially available 1N-series diodes will have values of the order of only a few hundred.  $N$ -type germanium used in microwave diodes will have mobilities in a higher range, possibly between one and two thousand.  $N$ -type gallium arsenide, doped to levels desired for

microwave diodes, can be expected to have mobilities in a range as high as four or five thousand. It is seen in the equations that the value of  $R_s$ , which we wish to make small, is inversely proportional to the mobility and thus the higher we can make the mobility, the higher will be the cutoff frequency.

From the formula for  $R_s C$  product, it may also be seen that it is desirable to make the carrier density as high as possible. However, since the mobility and the resistivity of the semiconductor are also related to the carrier density, the  $R_s C$  product for a given diode will partly depend on the choice of other desired diode characteristics.

The final equation in Fig. 7 suggests a figure of merit for varactor diodes. This equation states that, in addition to the cutoff frequency, some factor related to the change in capacity with drive  $\Delta_c$  should also be included. Further, a figure of merit, to be meaningful, must be accompanied by a statement regarding the bias voltage associated with the measured values presented. The matter of a completely satisfactory definition for a varactor figure of merit is not simple and for more complete information on some of the many factors involved, the reader is referred to a few recently published notes.<sup>7,8</sup>

#### NOISE-FIGURE MEASUREMENTS

Several measurements of the input-noise figures of parametric amplifiers using our GaAs point-contact diode have been made. Parametric amplifiers are unique in that, depending upon operating conditions, the noise figures resulting can be quite different; it is therefore necessary to state the conditions under which a given series of measurements are made in order for them to be meaningful. The noise-figure measurements presented in the following paragraphs were all made under so-called degenerate conditions, where the signal frequency to be amplified is very nearly one-half the frequency of the applied pump. Fig. 8 is a schematic drawing of a parametric amplifier operating in such a mode. As shown in the upper left of the figure, the signal is introduced at a frequency slightly below half the frequency of the pump. This signal flows to the circulator input port 1 and travels to port 2 where it passes to the right through a pump-rejection filter into the parametric-diode circuitry. The diode is pictured as a lumped parallel circuit having resistance, inductance and a capacitance which will vary at the frequency of the applied pump. An amplified signal  $s$  and its image  $p-s$  will be generated and pass outward to the left toward the circulator going into port 2 and emerging from port 3, appearing frequency-wise as shown in the lower left of the figure. When a noise-figure measurement is

<sup>7</sup> R. C. Knechtli and R. D. Weglein, "Diode capacitors for parametric amplification," *J. Appl. Phys.*, vol. 31, p. 1134; June, 1960.

<sup>8</sup> K. E. Mortenson, "Comments on diode capacitors for parametric amplification," *J. Appl. Phys.*, vol. 31, p. 1135; June, 1960.



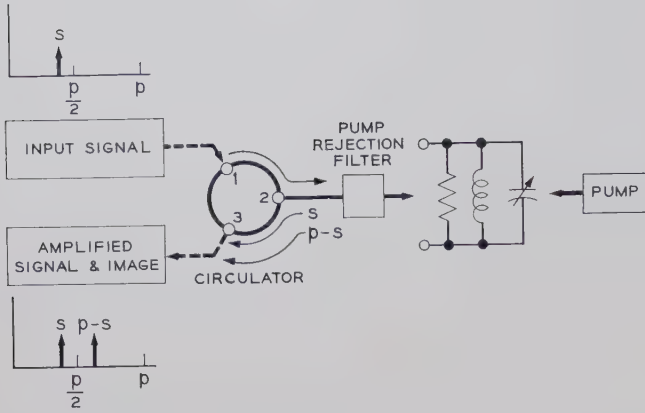


Fig. 8—Schematic drawing of a parametric amplifier operating in the degenerate mode (courtesy E. D. Reed).

made with a broad-band source, equal amounts of noise power are introduced at both the signal and image frequencies. The double-sideband noise figures thus measured for the degenerate case are 3 db better than for the single-sideband operation. When the amplifier is used for radio astronomy star-noise measurements or in connection with a receiving system employing synchronous detection in association with a synchronized transmitter, the double-sideband degenerate noise figures apply. All of the noise figures shown in Figs. 9 and 10 were measured under double-sideband degenerate conditions.

The degenerate room-temperature noise-figure measurements given in Fig. 9 were made by several different people and represent typical figures that have been obtained. The 6-kMc point was measured by Venohara; the 9-kMc point was supplied by W. L. Whirry, Hughes Aircraft Company, Culver City, Calif.; the 11-kMc point was supplied by DeLoach.<sup>4</sup> DeLoach also made the measurements represented by the point at 17.4 kMc<sup>5</sup> and he further reports that oscillations and amplification have been obtained in a parametric amplifier of his design, operating at a signal frequency of 30 kMc and pumped with a 60-kMc oscillator.<sup>5</sup> In the latter case, the GaAs diode details were removed from their cartridge holder and mounted directly across the high-frequency waveguide. In practically all cases, better noise figures than those shown in Fig. 9 have subsequently been obtained either by the use of improved circuitry or specially selected diodes. A quantity of these diodes have recently been fabricated by N. C. Vanderwal, Bell Telephone Laboratories, Allentown, Pa., for circuit evaluation.

Fig. 10 gives the results of further experiments conducted by Uenohara,<sup>3</sup> which give the measured excess noise temperature, pump power and diode current for

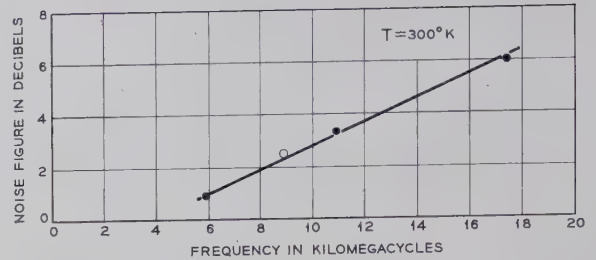


Fig. 9—Room temperature, degenerate mode, GaAs parametric amplifier noise-figure measurements.

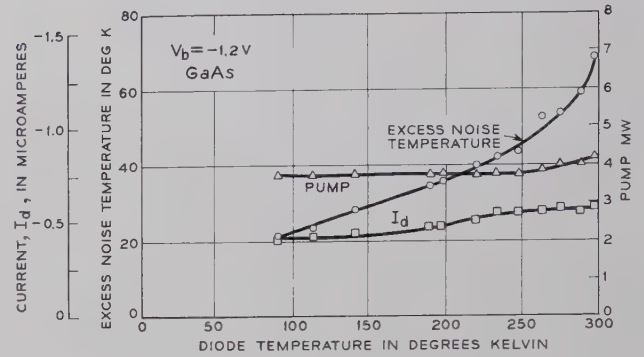


Fig. 10—Measured excess noise temperature, pump power and diode current for a typical GaAs point-contact diode cooled from 300°K down to 90°K.

a typical GaAs point-contact diode cooled by liquid nitrogen from room temperature, 300°K, down to 90°K. The excess noise temperature shown in Fig. 10 may be translated to noise figures in db, if desired, by use of the approximate rule that, in this range, 7 degrees excess noise temperature is equivalent to 1/10 db noise figure. The gain of the amplifier was held constant at 16 db.

It is interesting to note that the excess noise temperature decreased almost linearly with the diode temperature from 220°K down to 90°K. By extending the curve to the left, one can estimate that the noise contribution from the circuit only was about 10°K in this case. Uenohara has measured selected GaAs point contact diodes that are even better than the case plotted in Fig. 10. One diode, cooled to the temperature of liquid nitrogen, showed an excess noise temperature of only 12°K at 6 kMc.

## CONCLUSION

It is interesting to note that the excess noise temperature in a system using a cooled GaAs parametric amplifier is approaching that obtainable with our present-day masers operating at the same frequency. Because of its simplicity, such a parametric amplifier may become a reasonable competitor of the maser, especially when one considers the relatively large noise contributions from other portions of typical operating systems.



# Characterization of Microwave Variable Capacitance Diodes\*

SVERRE T. ENG†, MEMBER, IRE

**Summary**—This paper will describe the electrical characterization of microwave variable capacitance diodes. The importance of some of the diode parameters is discussed from the application point of view, and suitable measurement techniques for these parameters are described, together with actual measurement data on some diodes.

First, a general four-terminal transformation method is used, and some approximations lead to a fairly easy and accurate method of studying device characteristics. A resonant-cavity method is also considered, and it is explained under what condition it leads to a very simple test of the diode  $Q$ .

Finally, a method is presented which is based upon modifications of the Weissfloch canonical network. These simplifications can be used to get an easy interpretation of the junction impedance or the diode  $Q$ .

## I. INTRODUCTION

MICROWAVE variable capacitance diodes have recently been widely used in low-noise systems, microwave computers and harmonic generators; however, since the feasibility of using the diodes in these applications is fairly new, the problem of the characterization may be unfamiliar to the user. It should be pointed out that since we, in some instances, are touching the impedance measurement limit of the microwave instruments, the problem is not a simple one.

The techniques described in this paper should be sufficient for a device designer to evaluate the device parameters in the research laboratory as well as in production. The circuit designer will also find the measured parameters sufficient for the calculation of performance in many applications.

The first part of this paper describes the importance of the different diode parameters and the diode package. Then, together with some curves showing the actual behavior of a diode, different ways of measuring these characteristics at low as well as microwave frequencies are described. The transition capacitance which is one key parameter in all the applications, the capacitance nonlinearity coefficient, as well as the dc volt-ampere characteristic, and the breakdown voltage of a variable capacitance diode, are discussed.

Considerable attention is focused upon the measurement of the diode loss represented by the bulk series resistance of the wafer, since the losses are the most

undesirable parameter in circuit applications. Three different approaches are considered:

- a) a general four-terminal transformation method,
- b) a resonant-cavity method,
- c) a simplified canonical-network transformation method.

Some of the pertinent practical aspects of each of these methods are discussed.

## II. CIRCUIT CONSIDERATIONS

The most satisfactory electrical performance should be the guide in selecting the parameters useful in optimizing the physical structure of the device.

The capability of the parametric diodes is partially determined by the noise figure which can be achieved in microwave communication or radar and radio astronomy systems, by the transient response and input power requirements to establish oscillations in applications in binary computers, and by the efficiency in generating harmonics in harmonic generators.

First of all, these applications suggest low diode losses. The most common and convenient measure of the loss in a circuit element is the quality factor  $Q$  which measures the ratio of energy stored to energy lost per cycle. For an equivalent circuit of the diode consisting of the diode transition capacitance  $C_T$  in series with the bulk series resistance  $R_s$ , the  $Q$  is defined as

$$Q = \frac{1}{\omega R_s C_T} = \frac{f_c}{f}, \quad (1)$$

where  $f_c$  is defined as the cutoff frequency of the diode. The transition capacitance should be small for microwave impedance matching purposes when the diode is used in low-noise amplifiers.

The nonlinear capacitance coefficient  $(\partial C / \partial v)_{v=v_{dc}}$  should be high for good noise figure, for high-harmonic generator efficiency, and for low-rise time in computer applications. The nonlinearity coefficient is also important from pump-voltage considerations. A higher  $(\partial C / \partial v)_{v=v_{dc}}$  minimizes the necessary pump power. This is an important point in a frequency range where high power sources are not commercially available and especially in computer circuits where the same pump oscillator is driving several subharmonic generators.

The  $I$ - $V$  characteristics of the diode should show a reverse breakdown voltage of at least  $-5$  volts defined

\* Received by the PGMTT, July 5, 1960; revised manuscript received, August 19, 1960. This paper was presented at the 1960 IRE Symp. of the PGMTT, San Diego, Calif.

† Development Laboratory, Hughes Semiconductor Div., Newport Beach, Calif.



for 10  $\mu$ a leakage current. Several volts of pumping oscillator swing are sometimes required for amplifier operation. A low breakdown voltage might cause burn-out of the diode and shot noise effect. For harmonic generator application, it is especially desirable to have breakdown voltages of around -25 volts.

The range over which microwave diodes will operate satisfactorily is to a great extent determined by the electrical properties and the mechanical dimensions of the diode package. What is wanted is essentially as little package interaction as possible in different circuits. The diode package, therefore, should have low losses at the highest microwave frequencies, low stray capacitance and inductance, and mechanical dimensions fitted to coaxial, waveguide and strip-line circuits. A cylindrical package with quartz as insulating material and dimensions such as an 80-mil diameter and a 50-mil height with a stray capacitance of around 0.1  $\mu$ mf or less and an inductance measured at UHF of 1 m $\mu$ h, will meet most present requirements.

### III. LOW FREQUENCY AND DC CHARACTERIZATION

The transition capacitance  $C_T$  is a key parameter in all the applications and therefore should be measured accurately. A satisfactory frequency for measurement is 100 kc, because inductance effects are negligible in a high grade unit. A simple bridge circuit with an oscillator and an amplifier for null detection can be used. A suitable bridge for this purpose is the Boonton Electronics Capacitance Bridge 74CS4. A dc bias supply for measurements on diodes is built into the bridge. The signal voltage across the unknown capacitance should be less than 30 mv.

The transition capacitance at different frequencies as a function of voltage for a gold-bonded variable capacitance diode is plotted in Fig. 1. The measurement at 2 kMc was taken with a slotted line and agrees, within measurement error, with the 100 kc data. For the capacitance we can write:

$$C_T = C_0 \left(1 - \frac{v}{\phi}\right)^{-\gamma}, \quad (2)$$

where  $\phi$  is the contact potential and  $v$  is the applied voltage.  $C_0$  is the zero-bias capacitance and is a function of the impurity doping level and the geometrical configuration and structure of the diode. The exponent  $\gamma$  is a constant which is equal to  $\frac{1}{2}$  for the abrupt and  $\frac{1}{3}$  for the linear-graded junction.

When expanding the capacitance in a Taylor series, we get:

$$C_T = (C_1)_{v=v_{dc}} + \left(\frac{\partial C_T}{\partial V}\right)_{v=v_{dc}} V_{ac} + \frac{1}{2} \left(\frac{\partial^2 C_T}{\partial^2 V}\right)_{v=v_{dc}} V_{ac}^2 + \dots \quad (3)$$

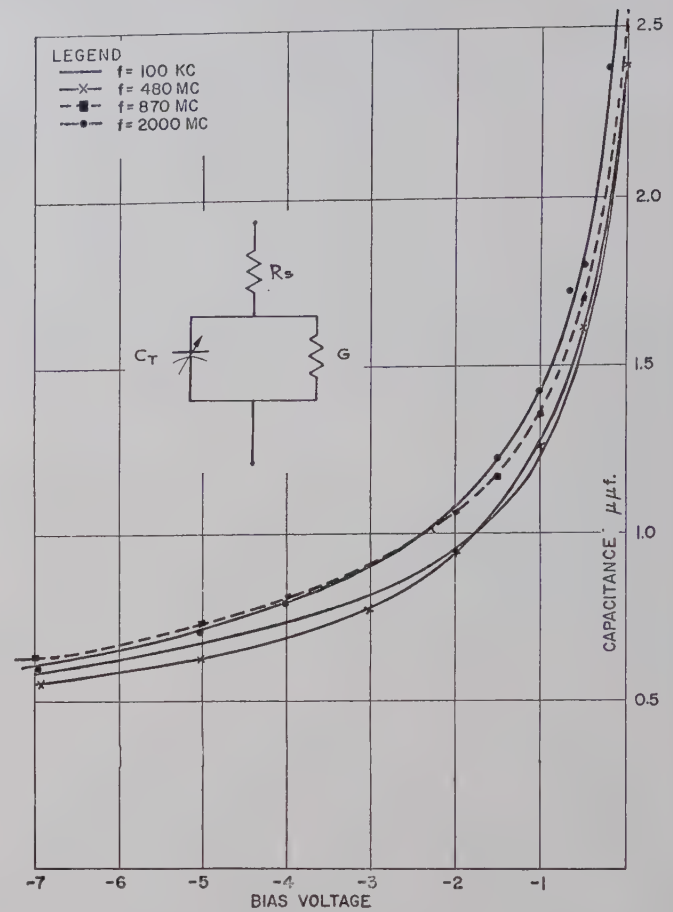


Fig. 1—Variation of junction capacitance with frequency; inset: the low frequency reverse-bias diode-equivalent circuit.

This is usually done in analytical work on amplifiers and subharmonic generators, and the first two terms are a fair enough approximation in these cases. The nonlinearity coefficient  $(\partial C/\partial V)_{v=v_{dc}}$  will then be an important parameter for the pump power requirement as well as for the optimum value of the negative conductance. There is no need for a special measurement of the coefficient, however, since it can be determined from (2):

$$\frac{\partial C_T}{\partial v} = \frac{\gamma C_0}{\phi} \left(1 - \frac{v}{\phi}\right)^{-\gamma-1}. \quad (4)$$

In second-harmonic generators, the second-order term has to be included in the analysis. Then we have

$$\frac{1}{2} \left(\frac{\partial^2 C_T}{\partial v^2}\right) = \frac{1}{2} \frac{C_0}{\phi^2} \gamma(\gamma+1) \left(1 - \frac{v}{\phi}\right)^{-\gamma-2}, \quad (5)$$

which is also determined by the diode structure, the contact potential and the bias voltage.

The volt-ampere characteristic of a Hughes HPA2800 diode is shown in Fig. 2. For a diode where the bulk re-



sistance is neglected, we have

$$I = I_s(e^{qV/kT} - 1), \quad (6)$$

where  $q/kT = 38.8 \text{ volt}^{-1}$  at  $25^\circ\text{C}$ . The measured value of the slope indicates a factor of  $37 \text{ volt}^{-1}$  and an exponential behavior which is in good agreement with theory. At very high currents, the slope indicates a bulk resistance of 2 ohms. This is a factor of 2 less than was obtained from microwave measurement. The discrepancy is most likely due to conductivity modulation. There is some correlation between the microwave series resistance and the series resistance measured by taking the slope of the dc curve at high forward currents. However, scatter diagrams show that a selection of devices by this method in the production line would not be possible.

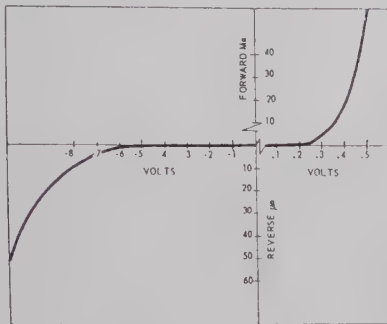


Fig. 2—The volt-ampere characteristic for a Hughes HPA2800 diode.

The diode conductance can be written

$$G = \frac{dI}{dV} = \frac{qI_s}{kT} \cdot e^{qV/kT}. \quad (7)$$

In the reverse direction, this conductance is in the order of micromhos. The reverse current in germanium, however, is mainly a surface leakage current. If a shot-noise contribution of 0.1 of the thermal noise contribution is tolerated when the diode is used in a low-noise amplifier, then we have for the leakage current  $I_c$

$$I_c = \frac{0.14kT_0}{2eR_s} = 1.25 \text{ ma}, \quad (8)$$

where  $k$  = Boltzmann's constant  $= 1.38 \times 10^{-23} \text{ per } ^\circ\text{K}$ ,  $T_0 = 290^\circ\text{K}$ ,  $R_s = 4 \text{ ohm}$ ,  $e = 1.6 \times 10^{-19} \text{ coulombs}$ . Thus, at room temperature, a fairly large leakage current can be tolerated if the  $Q$  of the diode was not degraded at the operating frequency. Since, however, the current is increasing very rapidly at the breakdown voltage, and the power dissipation in the diode increases the junction temperature, it would be wise to define the breakdown voltage,  $V_B$ , at  $10 \mu\text{a}$  current and to select breakdown voltages of minimum  $-5 \text{ volts}$  for diodes used in amplifiers and subharmonic generators. For harmonic

generators where substantially higher input power may be required, a breakdown voltage as high as  $-25 \text{ volts}$  is desirable.

The diode reverse-biased equivalent circuit at the low frequencies can be represented as in Fig. 1. The most convenient way to measure the series resistance  $R_s$  is at microwave frequencies where  $G$  is shunted out by  $C_T$ .

#### IV. MICROWAVE CHARACTERIZATION

The problem of measuring with reasonable accuracy a high  $Q$  impedance consisting of say  $1\text{--}2 \text{ ohms}$  resistance in series with a capacitance of  $1\text{--}2 \mu\text{mf}$ , is a difficult and tedious job at microwave frequencies, because we are at the limit of known microwave measurement technique. If, as in a diode, the above impedance is enclosed in a package with parasitic circuit elements, and the signal voltage across the diode should not exceed  $30 \text{ mv}$ , the measurement problem is still more complicated.

We may look at the interaction problem as shown schematically in Fig. 3(a), where  $Z_{in}$  is the measured impedance at the package terminals including the losses in the measurement jig, and  $Z_j$  is the diode junction impedance. The circuit designer is mostly concerned with  $Z_{in}$  and the device designer with  $Z_j$ .

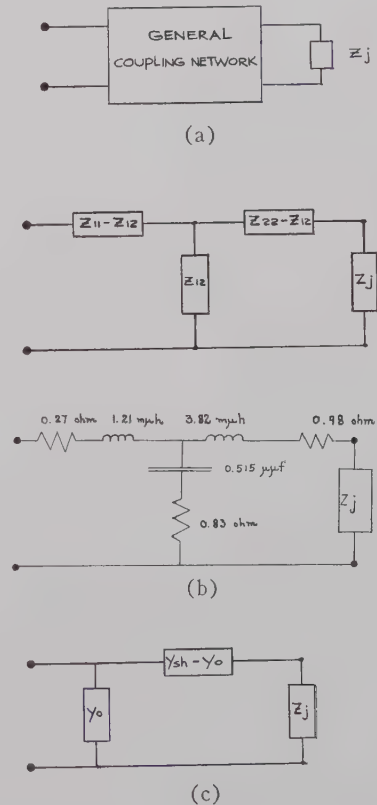


Fig. 3—(a) A four-terminal network representing the transformation from the diode junction impedance to the package terminal or the reference plane; (b) a four-terminal network represented by general  $Z$  parameters, and a typical equivalent circuit at  $4 \text{ kMc}$ ; (c) an approximate impedance transformation network which is valid up to  $2 \text{ kMc}$ .



### Approach 1

We can immediately see that the problem of referring the measurements to the active region of the device is one of determining the transformation from the transmission line in which the measurements are made to the interior of the device. The transformation can be represented in a number of ways, the most common of which is the impedance representation

$$\begin{aligned} V_1 &= I_1 Z_{11} + I_2 Z_{12} \\ V_2 &= I_1 Z_{21} + I_2 Z_{22} \\ Z_{12} &= Z_{21}, \end{aligned} \quad (9)$$

mainly because of its extensive use at lower frequencies. Then we get the equivalent circuit shown in Fig. 3(b) and the measured impedance is

$$Z_{in} = Z_{11} - \frac{Z_{12}^2}{Z_{22} + Z_j} \quad (10)$$

Since there are three parameters to be determined, we need, formally, three equations. If special terminations like  $Z_j = 0, \infty$ , and a standard impedance are used, the equations become simplified (Method A). It should be noted that this transformation will take care of all the defects of the diode holder as well as making corrections for the package losses and reactances.

One of the difficulties now is to make a good standard impedance. The impedance may consist of a small area contact to a resistive material. Assuming a perfectly hemispherical contact, one may easily integrate a spreading resistance of

$$r = \frac{1}{2\pi a \sigma}, \quad (11)$$

where  $\sigma$  is the conductivity of the material, and  $a$  is the radius of the contact. *P-P*- or *N-N*-type configuration is desirable. The resistance can be checked out by direct current, low frequencies, and microwave measurements. The diode itself can also be used as an impedance standard (Method B), since we know that the series resistance,  $R_s$ , is bias-independent at the higher microwave frequencies, and the reactance variation with bias is known from low-frequency measurements. We then need four instead of three equations to determine our three parameters,  $Z_{11}$ ,  $Z_{12}$ , and  $Z_{22}$ . The terminations may then be

$$\begin{aligned} Z_{j1} &= 0 \\ Z_{j2} &= \infty \\ Z_{j3} &= R_s + jX_1 \\ Z_{j4} &= R_s + jX_2. \end{aligned} \quad (12)$$

$X_1$  and  $X_2$  are the known reactances from low-frequency measurement of the capacitance at two different bias voltages.

From the physical considerations of the diode package and from measurement of the four terminal transformations, a simple transformation from  $Z_{in}$  to  $Z_j$  has been found to be valid up to 2 kMc (Method C). This simple transformation can be represented as in Fig. 3(c), and we get

$$Z_j = \frac{1}{Y_{in} - Y_o} - \frac{1}{Y_{sh} - Y_o}, \quad (13)$$

where  $Y_o$  and  $Y_{sh}$  are the open-circuited and short-circuited diode admittances. The transformation can easily be made on a Smith Chart, but because of the greater accuracy and ease with which a great number of measurements could be evaluated, the values of  $Z_j$  were usually computed using the IBM 704 computer.

Since exploration of the standing-wave pattern is one of the most convenient ways of measuring impedances, the slotted-line technique was used from 300 Mc to 5 kMc. The measurement setup shown in Fig. 4 can meas-

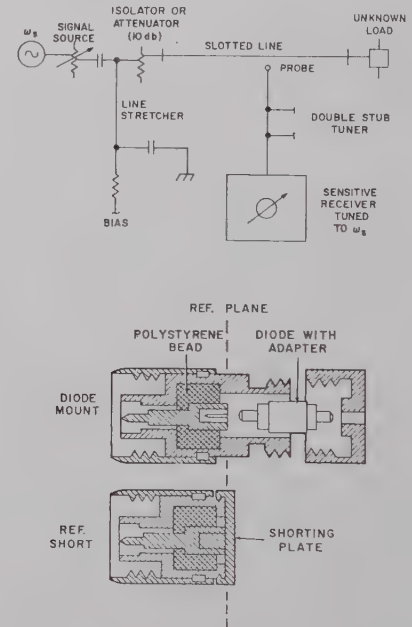


Fig. 4—Experimental measurement setup, used in Approach 1, for measuring very high-standing wave ratios.

ure standing-wave ratio as high as 500. The measurement procedure consists first of finding the value of the voltage minimum. Next, the distance is found between positions at which the output power at the probe is twice the minimum value. Then

$$VSWR = \rho = \frac{\lambda}{\pi \Delta x}, \quad (14)$$

where  $\lambda$  is the wavelength in the coaxial slotted-line section [2]. The shift in the minimum position,  $l$ , when the load is replaced by a short, is also recorded. Then, for instance, in the case of the transformation in (13), the admittance of the open diode package  $Y_o$ , the



shorted one  $Y_{sh}$ , and the actual diode admittance  $Y_{in}$ , are computed from

$$Y_{in,o,sh} = \frac{1}{Z_0} \frac{\rho - j \tan \frac{2\pi}{\lambda} l}{1 - j \tan \frac{2\pi}{\lambda} l}, \quad (15)$$

and substituted in (13). A slotted line with small probe width can be used together with a precision dial indicator as a standard test setup.

Measurement data taken at 2 kMc for a germanium diode junction impedance ( $R_s = 5.5$  ohms,  $C_T = 2.1 \mu\mu\text{f}$ ) using the general transformation Method A with a standard resistor of 15 ohms, according to (11), compared within 5 per cent with results obtained using the diode itself as a standard impedance (Method B). The standard resistors were measured at direct current, low frequency, and 1 kMc, and no noticeable frequency variation was found. Since both theory and measurements predict the same capacitance at microwave frequencies as at low frequency, and since the series resistance in the frequency range above 1 kMc does not show any change with bias voltage, the diode itself seems to be a very reliable standard. In computing the result, Method B is also easier to handle than Method A.

In Table I, Methods B and C are compared for dif-

TABLE I

Frequency (kMc)	Bias (volts)	Method B		Method C	
		$R_s$ (ohms)	$C_T$ ( $\mu\mu\text{f}$ )	$R_s$ (ohms)	$C_T$ ( $\mu\mu\text{f}$ )
2	0	6.32	0.787	5.21	0.840
	-1	6.1	0.520	4.79	0.569
3	0	6.55	0.776	4.40	1.045
	-1	6.1	0.522	4.40	0.702
4	0	5.79	0.775	2.60	2.110
	-1	5.27	0.499	2.60	1.36
6	0	5.14	0.80	0.05	—
	-1	5.9	0.531	0.06	—

The low-frequency capacitance at 0 volt = 0.786  $\mu\mu\text{f}$ ; at -1 volt = 0.530  $\mu\mu\text{f}$ .

ferent bias voltages and frequencies at and above 2 kMc. The errors in the results of Method B are estimated to be less than 15 per cent when the diode has a  $Q$  of 100 at the operating frequency and bias voltage, and the errors are on the order of 5 per cent for diode  $Q$ 's of 30 or less. Method B has been used extensively at 4 kMc as a comparison method in our laboratory. Below 2 kMc, earlier measurements showed very good agreement between these two methods. Thus, below 2 kMc, Method C is preferable for laboratory investigations of possible changes of  $R_s$  and  $C_T$  with, for instance, different surface treatments of the diode and so forth,

since no assumption is made with respect to resistance and capacitance changes.

Measurements were taken as low as 300 Mc on a gold-bonded germanium diode using Method C. Fig. 5 shows the variation of the equivalent series resistance with frequency and ambients, and the equivalent circuit in Fig. 6 is proposed to explain the variation of the re-

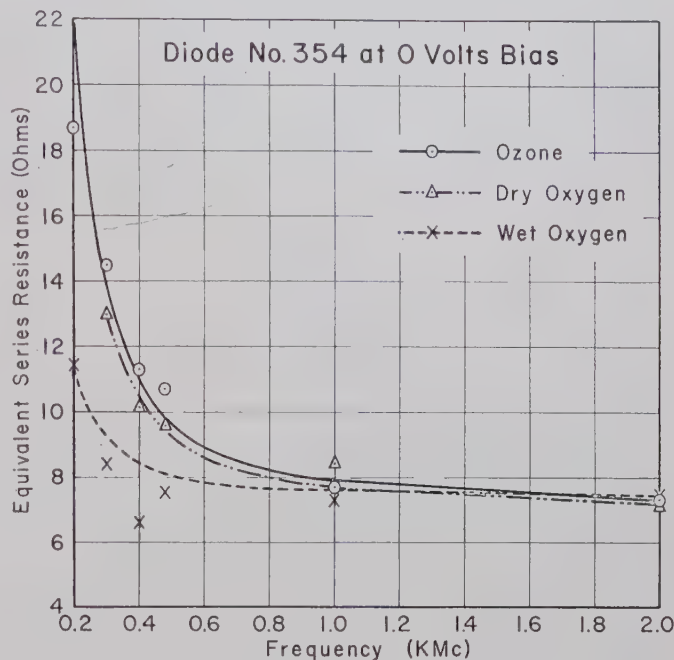


Fig. 5—The equivalent series resistance as a function of frequency and ambient for a Hughes HPA2800 germanium diode.

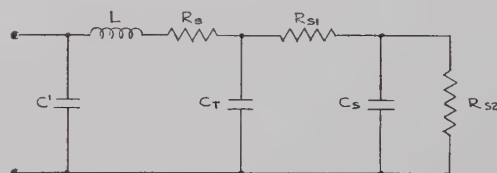


Fig. 6—Proposed equivalent circuit of a gold-bonded germanium diode in the high frequency and lower microwave range.

sistance.  $L$  is the lead and whisker inductance (4  $m\mu\text{h}$ ),  $C'$  (0.1  $\mu\mu\text{f}$ ) is the stray capacitance in the package,  $R_{s1}$  is the resistance along the surface which shunts the transition capacitance,  $C_T$ ; and  $C_s$  is the capacitance associated with the surface space-charge region. In addition, we have introduced a second surface resistance  $R_{s2}$  which expresses the dependence of the reverse current on the surface generation rate. The dc leakage current is mainly determined by  $R_{s2}$ , which is in the order of megaohm. At microwave frequencies,  $C_s$  effectively short circuits  $R_{s2}$  so that the equivalent series resistance can be expressed by

$$R_s' = R_s + \frac{1}{\omega^2 C_T^2 R_{s1}}. \quad (16)$$



The frequency dependence on the equivalent series resistance is only pronounced below 500 Mc. More detailed information about this experiment is reported elsewhere [3].

### Approach 2

We know that the microwave circuit can be described in a manner that closely resembles low frequency practice. Thus, a description of a cavity resonator from the low frequency point of view is complete if the shunt conductance  $G_0$ , together with the angular resonance frequency  $\omega_0$ , and the  $Q$ ,  $Q_0$ , are given. Since the ordinary low frequency concept of current and voltage, however, does not hold at microwave frequencies, we will define the shunt conductance as

$$G_0 = \frac{2W}{\left[ \int E dl \right]^2}, \quad (17)$$

where  $W$  is the power dissipated in the cavity and  $E$  is the electric field.

The method which will be described to find the  $Q$  of the diode will be deduced considering the cavity with input and output terminals used as a transmission device (Fig. 7). The output signal is measured as a function of frequency. If the bandwidth of the receiver is much smaller than the bandwidth of the cavity with and without the diode, the indicator traces a resonant curve from whose bandwidth the  $Q$  value of the cavity can be computed. By using a sweep generator as input and a broad-band detection system, we could make a dynamic observation of the cavity characteristic on a scope. Such a system has been made and the performance is very satisfactory. It should be noted that since the voltage across the diode should not exceed 25 mv and the input and output coupling should be very loose, a sensitive detection system is required. The equivalent circuit of the system is shown in Fig. 8(a) for the series resonant case. The cavity resonance is represented by  $L$ ,  $C$ , and  $R_s$ ; and  $Z_1$  and  $Z_2$  are the self-impedances of the coupling elements. Neglecting the self-impedances, we get a simple equivalent circuit referred to the middle loop as represented in Fig. 8(b). Then the unloaded  $Q$  of the cavity

$$Q_0 = \frac{\omega_0 L}{R_s}, \quad (18)$$

and the loaded  $Q$  of the system

$$Q_L = \frac{\omega_0 L}{R_s + N_1^2 R_g + N_2^2 R_L}. \quad (19)$$

The input and output coupling coefficients are defined as

$$\beta_1 = N_1^2 \frac{R_g}{R_s}$$

$$\beta_2 = N_2^2 \frac{R_L}{R_s}, \quad (20)$$

and we then get,

$$Q_0 = Q_L(1 + \beta_1 + \beta_2). \quad (21)$$

If we now consider the transmission through the cavity as a ratio of the power delivered to a matched load and the maximum power available from the generator, it is noted that the half-power points of transmission occur for

$$Q_L = \frac{\omega}{\Delta\omega}, \quad (22)$$

if the signal generator and detector impedances are both matched. The coupling coefficients should be adjusted to a minimum so that  $Q_0 \cong Q_L$ . Thus we have tried to obtain a high- $Q$ -cavity system in which the  $Q$  of the system can be determined by a measurement of the resonant frequency and the bandwidth.

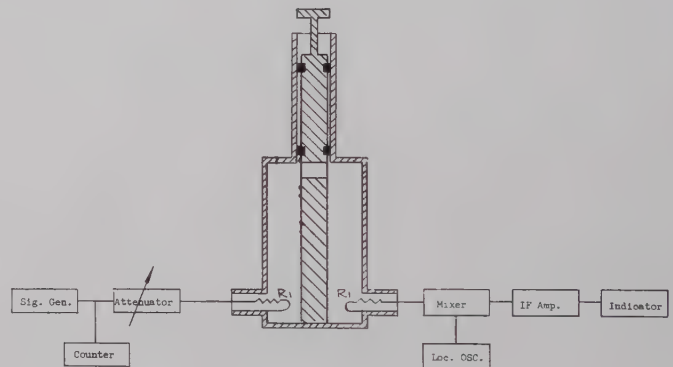


Fig. 7—Schematic diagram showing the measurement setup for the resonant cavity method.

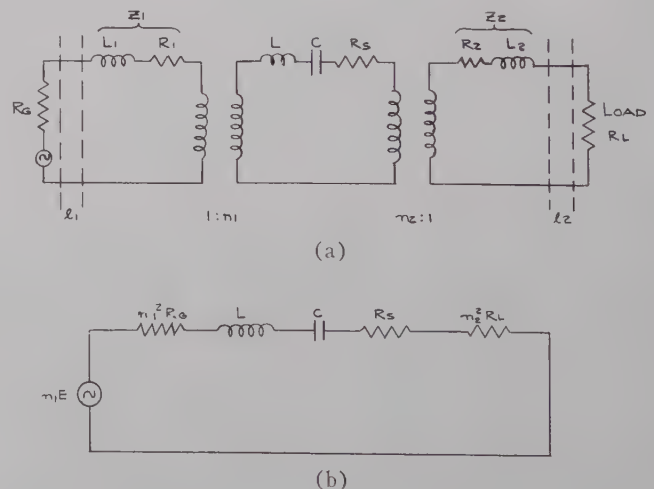


Fig. 8—(a) An equivalent circuit of the measurement system; (b) a reduced equivalent circuit of the measurement system.



We will now assume that the cavity as seen from the diode junction can be represented by a simple parallel resonant circuit. (A series representation may also be valid for cavity characteristics slightly different from those used in the experiment.)

The measuring procedure consists first of substituting an open diode in the cavity in order to include package- and bias-circuit losses and reactances as part of the cavity. Then we get

$$Q_0 = \frac{\omega_0 C_0}{G_0} \quad (23)$$

If an arbitrary diode is now inserted in the cavity we get a new  $Q$ ,  $Q_m$ , and a new angular resonance frequency  $\omega_m$ . Then,

$$Q_m = \frac{\omega_m(C_0 + C_T)}{G_0 + G_s}; \quad (24)$$

and since  $Q_d = (\omega_m C_T)/G_s$  is the real  $Q$  of the diode, we get

$$Q_d = \frac{C_T Q_m}{C_0 + C_T - \frac{G_0 Q_m}{\omega_m}} \quad (25)$$

where  $Q_m$  and  $\omega_m$  are measured quantities and  $C_T$  is known from low-frequency measurement of capacitance. If the cavity with the open diode inserted was completely characterized so that  $C_0$  and  $G_0$  were known, (25) would be a simple expression for the diode  $Q$ , especially

measured changes in resonance frequency of the cavity by a known amount of change in the diode capacitance according to

$$\left(\frac{\omega_1}{\omega_2}\right)^2 = \frac{C_{T_2} + C_0}{C_{T_1} + C_0} \quad (26)$$

from which  $C_0$  can be found. Then  $G_0$  can be calculated from (23). Procedure B uses a standard admittance diode,  $G_s + j\omega C_{T_s}$ , measured as in Approach 1, Method B. With this diode inserted in the cavity, we have

$$Q_s = \frac{\omega_s(C_0 + C_{T_s})}{G_0 + G_s} \quad (27)$$

which, combined with (23) gives

$$G_0 = \frac{G_s - \omega_s \frac{C_{T_s}}{Q_s}}{\frac{Q_0 \omega_s}{Q_s \omega_0} - 1} \quad (28)$$

and  $C_0$  can be found from (23). Table II shows the results obtained from both calibration procedures. Measurements on several diodes indicate the same behavior. Since Procedure A is independent of knowing the value of a standard impedance, we found it reasonable to use an average value of 1.1  $\mu\text{mf}$  for  $C_0$  and 11  $\mu\text{mhos}$  for  $G_0$ , according to the table.

Using this cavity resonance method in measurements on several Hughes silicon diodes (25), the results in Table III were obtained. A comparison with Method B in Approach 1 is also shown.

TABLE II

Bias (volts)	$C_T$ ( $\mu\text{mf}$ )	$Q$	Procedure A			Procedure B		
			$\omega/2\pi$ (Mc)	$C_0$ ( $\mu\text{mf}$ )	$G_0$ ( $\mu\text{mhos}$ )	$G_s$ ( $\mu\text{mhos}$ )	$G_0$ ( $\mu\text{mhos}$ )	$C_0$ ( $\mu\text{mf}$ )
+ .3	0.9	94	895	1.19	11.9	108	11	1.1
0	0.68	130	946			69	10.7	1.07
-1	0.48	182	1005	1.1	11	39	9.1	0.91
-4	0.34	340	1056			21.5	15.8	1.52
Open diode		750	1200					

if the cavity were designed so that the effect of the term  $(G_0 Q_m)/\omega_m$  is negligible. With this purpose in mind, the cavity in this experiment was designed for a high  $Q$  and with a characteristic impedance of 75 ohms. The resonant frequency was chosen to be as low as 1.2 kMc in order to facilitate ease of adjustment of the coupling loop, to escape higher modes, and to enable us to utilize equipment on hand in our laboratory.

The calibration of the cavity was accomplished by two different procedures. Procedure A makes use of the

TABLE III

Diode Number	Approach 1, Method B $f_c$ (kMc)	Approach 2 $f_c$ (kMc)
SM1-AA-2	52.7	50
SM1-AA-4	50.7	46.5
1008	54.9	50
1009	12.4	11.6
1011	32.2	36.2
1015	45.8	44.2



It can be concluded that the cavity resonance method is fairly accurate, and, if a sweeping technique was utilized, the method would be extremely useful for routine tests of diode cutoff frequency in the laboratory as well as in production.

### Approach 3

A general four-terminal coupling network can, at a particular frequency, be represented by a canonical network postulated by Weissfloch [1]. The equivalent circuit [Fig. 9(a)] is represented by a lossy and lossless part between the reference planes  $T_1$  and  $T_2$ , which define the ends of the physical structure representing the transformation.

We will now add stub tuners to the transformation between planes  $T_1$  and  $T_2$  so that when open and short circuits are substituted for the diode junction  $Z_j$ , the position of the minimum of the standing waves in the slotted line is shifted by a quarter wavelength. The reactive elements of the transformation have been tuned out and, with a precision package and diode holder, the equivalent circuit of the transformation will now be as shown in Fig. 9(b). The impedance transformation  $n^2/Z_0$ , the series resistance  $R$ , and the shunt resistance  $R_p$ , can be determined by measuring  $Z_{in}$  when  $Z_j$  is represented by a known standard capacitance, a short circuit, and an open circuit. The reference position for the minimum of the standing-wave pattern is estab-

lished for  $Z_j=0$  or  $\infty$ . Using the diode capacitance  $C_s$ , measured at low frequency as our standard capacitance, and when a measurement frequency is chosen so the effect of  $R_p$  is very small, we get

$$Z_{in_d} = R_{in_d} - jX_{in_d} = \frac{n^2}{Z_0} (R + R_s) - j \frac{n^2}{Z_0} X_s, \quad (29)$$

which gives

$$\frac{n^2}{Z_0} = \frac{X_{in_d}}{X_s}, \quad (30)$$

and from the open- and short-circuit measurements

$$R = \frac{Z_0}{n^2} R_{in_{sh}} \quad (31)$$

$$R_p = \frac{Z_0}{n^2} R_{in_{oc}}. \quad (32)$$

The measurement system is now fairly well calibrated, and we can write for the  $Q$  of the diode in terms of the measured  $Q$ ,  $Q_m$ , of the input impedance and the equivalent circuit parameters

$$Q_d = Q_m \left( 1 + \frac{R}{R_d} + \frac{(R + R_d)^2 + X_d^2}{R_p R_d} \right). \quad (33)$$

A measurement frequency was chosen high enough so that the third term in this expression is very small. In order to get an approximate idea of the correction term within the parenthesis at 9 kMc, it should be mentioned that the standing-wave ratio was in the order of 100 for an open diode and 10 for a shorted one. If we now take a silicon diode like SM1-AA-2 (see Table IV), with  $n^2/Z_0=0.1$ , we get  $R_p=1000$  ohms and  $R=1$  ohm, and with a normalized input impedance of  $0.5-j2.15$  (see Table IV), and zero-bias capacitance of  $0.82 \mu\mu f$ , we have at 9 kMc  $X_d=21.5$  ohms and  $R_d=4$  ohms, which gives

$$Q_d = Q_m (1 + 0.25 + 0.12) = \frac{f_c}{f}. \quad (34)$$

Thus, if  $Q_m$  is taken directly from the Smith Chart, the cutoff frequency of this diode should be in the order of 37 per cent higher than the cutoff frequency calculated from  $Q_m$ .

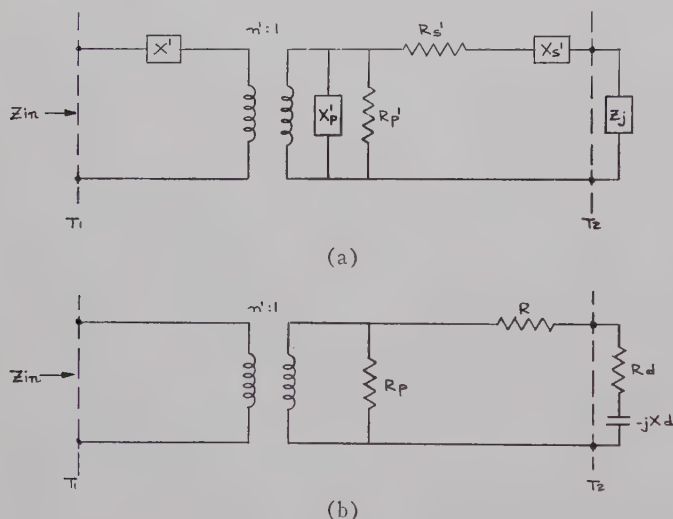


Fig. 9—(a) A general Weissfloch canonical network; (b) a simplification of the canonical network.

TABLE IV

Unit	$C_0$ ( $\mu\mu f$ )	VSWR	Phase Shift (Frac- tional Wavelength from Short)	$Z_{in_d}$ Normalized	$Q_m$	$f_c$ (kMc) (Correction Applied)	$n^2/Z_0$
SM-AA-1	0.69	13.0	0.169	$0.60-j2.40$	4.0	49.2	0.09
AA-2	0.82	13.0	0.183	$0.50-j2.15$	4.3	53.0	0.1
AA-3	0.37	18.0	0.210	$0.85-j3.7$	4.4	54.2	0.08
AA-4	0.95	9.5	0.156	$0.39-j1.65$	4.2	51.6	0.09



A block diagram of the equipment used in several measurements on Hughes silicon diodes is given in Fig. 10. The E-H tuner was adjusted according to two requirements. There must be a quarter-wave shift between open and shorted diodes and, further, the transformation ratio,  $n$ , must be such that  $Z_{in}$  can be plotted easily on a Smith Chart. The following procedure was found to be convenient:

- match a diode with tuners and sliding short,
- replace diode with open-circuit diode and note position of minimum,
- insert shorted diode and adjust sliding short to get quarter-wave shift in the minimum of the standing-wave pattern.

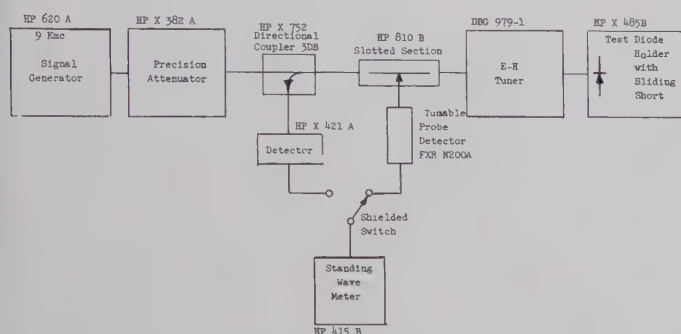


Fig. 10—Schematic diagram showing the measurement setup for the X-band measurement according to Approach 3.

Step a) is not absolutely necessary and it will be invalidated when the sliding short is readjusted in c). However, with most diodes tested, this procedure gave a usable impedance transformation without numerous readjustments of the tuners and the sliding short. After these adjustments, routine testing of diodes can be accomplished without retuning the elements.

In Table IV are the results of measurements on four silicon diodes. The measured impedances of the four diodes are plotted in Fig. 11, on page 20 using data from the table. These data are self-consistent in the respect that the measured reactances are nearly in the same proportion among units as the reactances calculated from low frequency  $C_0$ 's. This is indicated in the table by the calculated  $n^2/Z_0$  for each diode, which should be the same for all diodes, because the tuners were not touched during the set of measurements.

Fig. 12 on page 21 shows the measured impedances of a diode for various dc bias. According to our equivalent circuit, the points should fall on a circle of constant resistance, at least for the reverse and low forward biases. This plot supports the validity of the method. The points here are nearly on the circle of  $R/Z_0=1$ , which was only a coincidence in this particular experiment. However, as mentioned above, it was intended to transform the impedance to any convenient place in the middle of the Smith Chart. Also plotted are the impedances of four shorted packages with short no. 11 as the

phase reference. (It was also used as reference in plotting the diode impedance.) The reactance variation among shorted packages is about 3 ohms. Thus, it appears that the package is not quite good enough and causes errors from the assumption of identical packages. Several open circuit packages were measured, and they all had practically the same phase. The shorts were made by pressing the contacting posts against the diaphragms, and the opens were made by first contacting and then backing off a very slight amount.

Finally, in Table V is a comparison of the different approaches for five Hughes Silicon mesa diodes. The cutoff frequency is defined at zero-volt bias. Approach 3 is similar to Waltz's method [4]. The only difference is in the calibration procedure and that  $R_p$  is included in our equivalent circuit. The same measurement setup as in Fig. 10 was also used for Houlding's method [5]. The result is shown in the table to make the comparison as complete as possible. Since it has been experimentally verified that the loss resistance of the diode is also constant above 500 Mc, it can be concluded from the table and also from a large number of other measurements that the last two methods in the table sometimes can show a considerable error. The correction applied in Approach 3 is made according to (33).

TABLE V

Diode Number	Approach 1, Method B, at 4 kMc $f_c$ (kMc)	Approach 2 Around 1 kMc $f_c$ (kMc)	Approach 3 at 9 kMc, (Correction Applied) $f_c$ (kMc)	Houlding's Method [5] (No Correction Applied) $f_c$ (kMc)
SM1-AA-2	52.7	50	53.0	47.3
SM1-AA-4	50.7	46.5	51.6	44
1009	12.4	11.6	11.5	11
1011	32.2	36.2	10.0	14.2
1015	45.8	44.2	25.6	39.3

In the method used by Houlding [5], the effect of the parallel resistance  $R_p$  is neglected and the series resistance  $R$  is made part of the diode losses. Thus the source of error in this method is the circuit losses. Since both these two resistances are varying with the position of the E-H tuner and the sliding short settings, the measurements are also not quite repeatable when the tuner positions are changed. Thus, if the method is calibrated, the calibration will change from the measurement of one diode to another. Since each diode is matched individually in this method, the effect of variations in the diode packages is compensated for.

The reason for the discrepancy in  $f_c$  of diode 1011 and 1015 in Approach 3, compared with Approaches 1 and 2, is the fairly large diode capacitance of these two diodes compared with the other three diodes ( $C_T$  of SM1-AA-2 is  $0.82 \mu\mu\text{f}$  and  $C_T$  of 1011 is  $3.14 \mu\mu\text{f}$ ). The method assumed identical shorted packages. However, since the reactance variation among shorted packages

## IMPEDANCE OR ADMITTANCE COORDINATES

Units SM1-AA-1  
thru 4

Unit	C <sub>0</sub>
SM1AA-1	0.69 $\mu\text{yf}$
-2	0.82
-3	0.37
-4	0.95

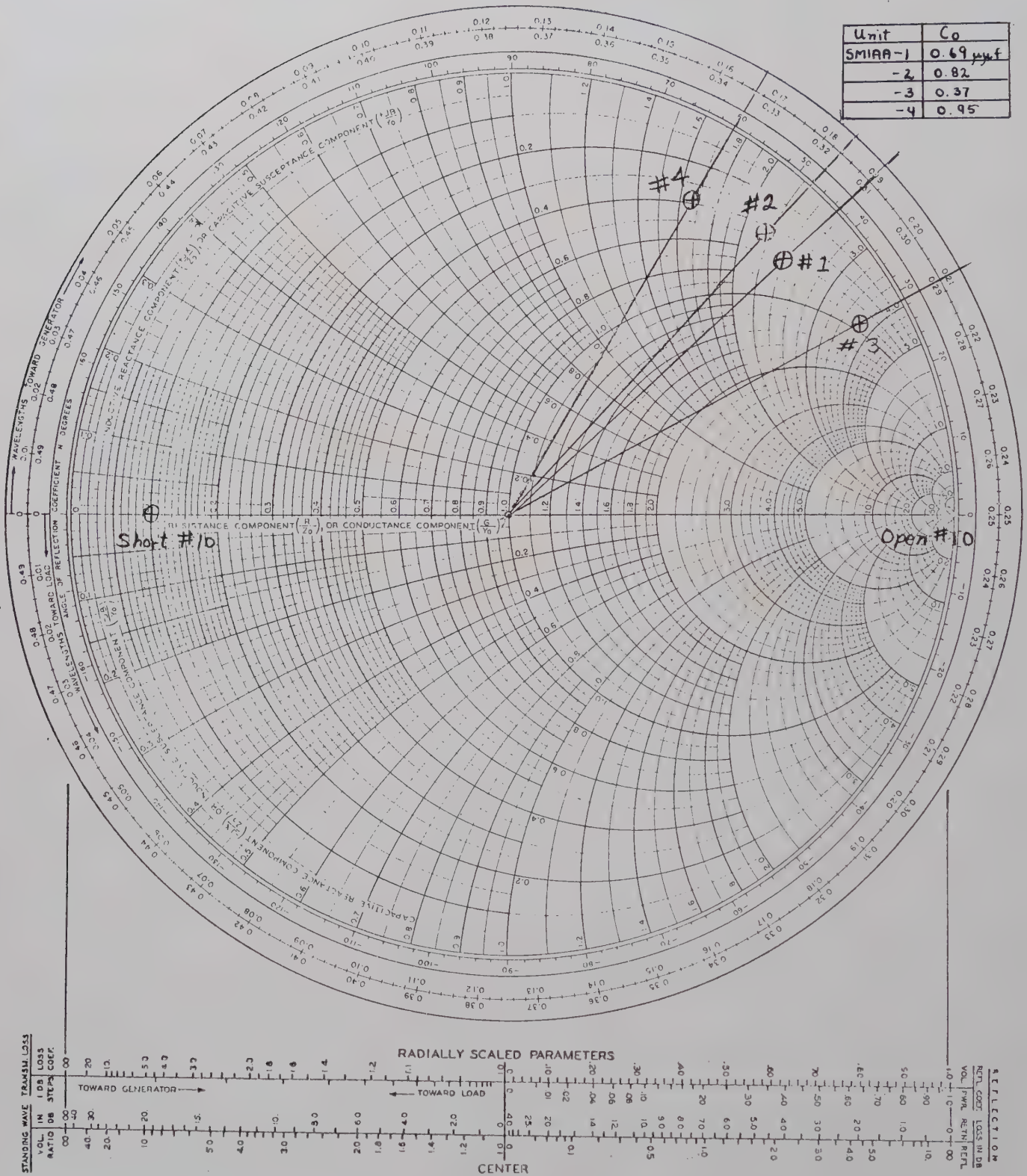


Fig. 11—The microwave impedance of four diodes plotted on the Smith Chart.



## IMPEDANCE OR ADMITTANCE COORDINATES

Bias	$C_t$
+0.5 V.	1.63 $\mu\text{pt}$
0.3 V.	0.98
0 V.	0.69
-1.0 V.	0.49
-4.0 V.	0.34

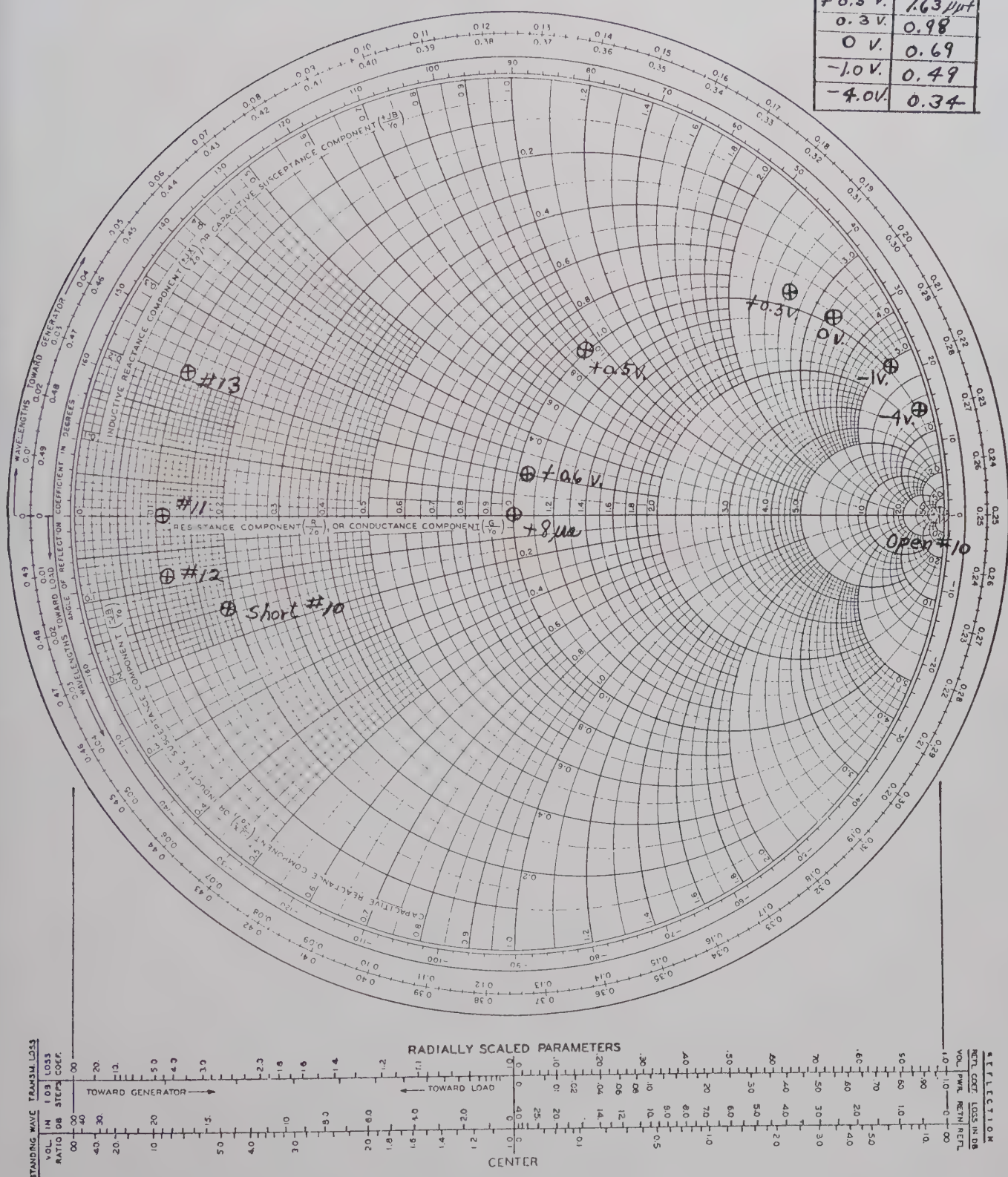


Fig. 12—The microwave impedance variation with bias voltage plotted on the Smith Chart.

can vary several ohms at 9 kMc (Fig. 12), the error in  $f_c$  for these high capacitance units can easily be understood.

Of the first two approaches which have given consistent results, the cavity-resonance method is by far the simplest and most adapted for very high  $Q$  diodes. The method is easy to calibrate and the measurement is not affected by variations in the diode packages, since the measurement frequency is chosen as low as 1 kMc. In Approach 3, if the diode  $Q$  is higher than 5 at 9 kMc, then a higher frequency of measurement is recommended in order to be able to neglect  $R_p$  in our equivalent circuit. A higher measurement frequency, however, requires extreme precision in package, in diode holder and in all respects of the measurements.

### V. CONCLUSIONS

A general representation has been given of the importance and requirements of the fundamental electrical parameters of microwave variable capacitance diodes. It is suggested that the following parameters be specified:

- 1) the breakdown voltage,
- 2) the capacitance at zero-volt bias,
- 3) the exact variation of the capacitance with bias voltage (from which the nonlinearity coefficient can be calculated),
- 4) the cutoff frequency or the  $Q$  at a particular frequency,
- 5) the dynamic back-biased resistance (because the diodes also have applications at the lower frequencies).

The  $Q$  of the diode is not an easy parameter to measure; therefore, three different approaches were considered in order to gain comparison. In the first method, a general four-terminal transformation is used from the active region of the device to the transmission line in which the measurements are made. Special termina-

tions such as open circuit, a short circuit, and a standard impedance were used instead of the active diode region when determining the general four-terminal coupling network. It was shown that a simple  $L$  network was a good approximation up to 2 kMc, and it led to a fairly accurate and easy method for measuring the diode junction impedance. In the second approach, the diode  $Q$  was deduced by placing the diode in a cavity resonator which is considered as a transmission device. From the measured bandwidth and the resonant frequency of the cavity with the diode inserted, the diode  $Q$  could be computed after the cavity, without the diode, was first calibrated by using a known capacitance change. Finally, a simplified form of a general Weissfloch canonical network was presented, which led to another  $Q$ -evaluation method.

The results obtained from all these methods compare fairly well. However, from measurement on several diodes, it can be concluded that the cavity resonance method (at around 2 kMc) may be the best for a specification test because of the ease with which these measurements can be accomplished, and the accuracy and the reproducibility of the results. In order to standardize this method, the cavity dimensions have to be specified for such a test.

### VI. ACKNOWLEDGMENT

The author wishes to thank D. English and R. Knox for their significant help in performing the measurements.

### BIBLIOGRAPHY

- [1] A. Weissfloch, *Hoch. und Electroakus.*, pp. 100-123; April, 1943.
- [2] E. L. Ginzton, "Microwave Measurements," McGraw-Hill Book Co., Inc., New York, N.Y.; 1957.
- [3] S. T. Eng and R. Solomon, "Frequency dependence of the equivalent series resistance for a germanium parametric amplifier diode," *PROC. IRE*; March, 1960.
- [4] M. C. Waltz, "A technique for the measurement of microwave impedance in the junction region of a semiconductor device," *Microwave J.*, vol. 2; May, 1959.
- [5] N. Houlding, "Measurement of varactor quality," *Microwave J.*, vol. 3; January, 1960.

## CORRECTION

W. H. Eggiman, author of "Scattering of a Plane Wave on a Ferrite Cylinder and Normal Incidence," which appeared on pp. 441-445 of the July, 1960, issue of these TRANSACTIONS, has brought the following to the attention of the *Editor*. By an oversight, the sponsoring agency of the work described in the paper was not mentioned. The author regrets the omission very much and wishes to express his sincere appreciation to the Electronics Research Directorate of the Air Force Cambridge Research Center, Air Research and Development Command, which supported the work under contract No. AF 19 (604)-3887.



# A Study of the Optimum Design of Wide-Band Parametric Amplifiers and Up-Converters\*

GEORGE L. MATTHAEI†, MEMBER, IRE

**Summary**—Single-diode parametric amplifiers or up-converters using multiple-resonator filters as coupling networks can be made to have considerably larger bandwidths than corresponding amplifiers having single-resonator coupling circuits. Data are presented from which the coupling-filter bandwidths required for given coupling network complexity, diode parameters, and required gain can be determined for both parametric amplifiers and up-converters. In the cases of nondegenerate parametric amplifiers and up-converters, the fact that the diode must be brought to resonance at more than one frequency has an added limiting effect on bandwidth. Some trial amplifier designs are shown, and important considerations in the synthesis of the coupling filters are noted. It is seen that for the case of upper-sideband up-converters, if a filter having  $n$  resonators is used in both the input and upper-sideband circuits, then the over-all response can be made to correspond to that of a filter with  $2n$  resonators. The gain characteristics of the trial amplifier designs as determined with a digital computer are included. Computed responses ranging in bandwidth from 9 to 27 per cent are obtained for multi-resonator designs having  $C_1/C_0=0.25$ .

## INTRODUCTION

IN THE PAST, most single-diode parametric and up-converter amplifiers have been designed with noise figure and gain as the prime consideration, and bandwidth has been of only secondary interest. Except for the paper of Seidel and Herrmann,<sup>1</sup> little attention appears to have been given to the possibility of increasing bandwidth by using coupling networks which are more complex than simple one-resonator tank circuits. In the work described herein, methods of network theory are used in order to predict the performance that can be obtained using coupling networks of any given complexity. In addition, some trial designs are tested by computing their responses with a digital computer.

The nature of the problem of wide-band design can be seen as follows: Suppose that the time variation of a variable-capacitance diode is given by the series<sup>2</sup>

$$C(t) = C_0 + 2C_1 \cos(\omega t + \phi_1) + \dots \quad (1)$$

The constant term  $C_0$  represents a fixed, parasitic capacitance which is responsible for the bandwidth limitations of parametric amplifiers and up-converters. Taking the case of parametric amplifiers, the capacitance  $C_0$  may be regarded as an intrinsic part of the input and

idler circuits. If, for example, the diode is connected so that  $C_0$  appears as a shunt element at the terminals of the input and idler circuits, then the real part of the impedance  $Z(j\omega)$  of each of these circuits is limited as indicated by the integral

$$\int_0^\infty \operatorname{Re} + Z(j\omega) d\omega = \frac{\pi}{2C_0} \quad (2)$$

which is derived by Bode.<sup>3</sup> Since in the operating band of a parametric amplifier it is necessary that the impedances of the input and idler circuits (including  $C_0$ ) be almost purely real, in view of (2), it is desirable that  $\operatorname{Re} Z(j\omega)$  go sharply to zero outside of the operating bands of these circuits so that bandwidth capability will not be wasted. Thus to conserve bandwidth capability and to obtain nearly constant gain across the band of interest, it is necessary to use filter structures as input and idler terminating networks.

In the case of nondegenerate parametric amplifiers, *i.e.*, the case where the signal and idler frequency bands do not overlap, two filters are required. In the case of so-called degenerate parametric amplifiers, the signal and idler frequency bands are the same, and one filter suffices for both. The paper of Seidel and Herrmann<sup>1</sup> treated the case of wide-band degenerate amplifiers using the viewpoint of setting derivatives of the gain function equal to zero at midband. The approach herein is quite different and rests directly on filter synthesis techniques.

## II. CIRCUITS FOR WIDE-BAND DEGENERATE AMPLIFIERS

From the work of Rowe,<sup>2</sup> it is seen that the operation of a shunt-connected, variable-capacitance diode being pumped at a frequency  $f_p$  can be represented by

$$\begin{bmatrix} I_1 \\ I_2^* \end{bmatrix} = \begin{bmatrix} jB_{11} & jB_{12} \\ j(-B_{21}) & j(-B_{22}) \end{bmatrix} \begin{bmatrix} V_1 \\ V_2^* \end{bmatrix} \quad (3)$$

where  $I_1$  and  $V_1$  are, respectively, the current into the diode and the voltage across the diode at the input signal frequency  $f$ , and where  $I_2^*$  and  $V_2^*$  are the conjugates of the analogous current and voltage at the idler frequency

$$f' = (f_p - f). \quad (4)$$

\* Received by the PGMTT, July 5, 1960; revised manuscript received, September 15, 1960. This research was supported by the Wright Air Dev. Div., Wright-Patterson AFB, Dayton, Ohio, under Contract AF 33(616)-5803.

† Stanford Res. Inst., Menlo Park, Calif.

<sup>1</sup> H. Seidel and G. F. Herrmann, "Circuit aspects of parametric amplifiers," 1959 WESCON CONVENTION RECORD, Pt. 2, pp. 83-90.

<sup>2</sup> This definition of  $C_0$  and  $C_1$  is consistent with the work of H. E. Rowe, "Some general properties of nonlinear elements. II. Small signal theory," *Proc. IRE*, vol. 46, pp. 850-860; May, 1958.

<sup>3</sup> H. W. Bode, "Network Analysis and Feedback Amplifier Design," D. Van Nostrand Co., Inc., New York, N. Y., pp. 280-281; 1945.

The various values of  $B_{mn}$  are given by

$$\begin{aligned} B_{11} &= 2\pi f C_0, & B_{12} &= 2\pi f C_1 \\ B_{21} &= 2\pi f' C_1, & B_{22} &= 2\pi f' C_0. \end{aligned} \quad (5)$$

Here,  $C_0$  and  $C_1$  are coefficients of the series in (1), and it is assumed that the diode sees short-circuits at the frequencies corresponding to all other harmonic and sideband frequencies. Examination of (3) to (5) shows that  $C_0$  acts like any other constant, linear capacitance at all frequencies,<sup>4</sup> and that the coupling between signals at frequencies  $f$  and  $f'$  occurs by way of  $C_1$ .

With the above background in mind, let us now examine the degenerate amplifier circuit in Fig. 1. It is shown using a circulator, which will give the largest gain and smallest noise figure; however, a circulator is not necessary as far as design for a given bandwidth is concerned. Neglecting the diode loss resistance for the moment, we see that the diode is represented by  $C_0$  and  $C_1$  in parallel, and  $C_0$  is treated as being incorporated into the first resonator of a band-pass filter circuit. The input admittances  $Y_b$  and  $Y_b'$  indicated in the figure are the input admittances of this filter at the signal frequency,  $f$ , and the idler frequency,  $f'$ , respectively. They are also the total admittances seen by  $C_1$  at frequencies  $f$  and  $f'$ . As a result of incorporating  $C_0$  into a filter structure,  $Y_b$  and  $Y_b'$  are almost purely real over an appreciable frequency band, a condition necessary for wide-band operation. In Fig. 1, the pump signal connections have been omitted for simplicity.

By matrix inversion, the relations of (3) to (5) can be expressed in the form

$$\begin{bmatrix} V_1 \\ V_2^* \end{bmatrix} = \begin{bmatrix} j(-X_{11}) & j(-X_{12}) \\ jX_{21} & jX_{22} \end{bmatrix} \begin{bmatrix} I_1 \\ I_2^* \end{bmatrix}, \quad (6)$$

where

$$\begin{aligned} X_{11} &= \frac{1}{2\pi f C_0(1 - a^2)} = \frac{1}{2\pi f C_0^s}, \\ X_{12} &= \frac{a}{2\pi f' C_0(1 - a^2)} = \frac{1}{2\pi f' C_1^s}, \\ X_{21} &= \frac{a}{2\pi f C_0(1 - a^2)} = \frac{1}{2\pi f C_1^s}, \\ X_{22} &= \frac{1}{2\pi f' C_0(1 - a^2)} = \frac{1}{2\pi f' C_0^s} \end{aligned} \quad (7)$$

and

$$a = \frac{C_1}{C_0}. \quad (8)$$

The square matrix defined by (6) and (7) gives the corresponding "open-circuit impedances" (for frequencies  $f$  and  $f'$ ) for a diode, *having all of its higher harmonics and unwanted sidebands short-circuited*. The

approach of Leenov<sup>5</sup> (who dealt with the case of up-converters) would give a somewhat different set of open-circuit impedances because his approach implies that the unwanted harmonics and sidebands are all open-circuited. In a given practical situation, usually, neither representation is entirely accurate, since the various unwanted frequencies usually all see different terminating impedances. For simplicity, the representation in (6) and (7) will be used herein.

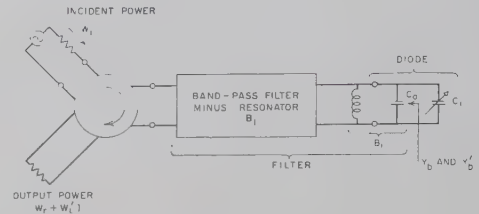


Fig. 1—Degenerate parametric amplifier with variable-capacitance diode resonated in shunt.

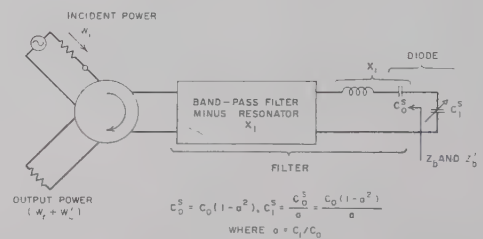


Fig. 2—Degenerate parametric amplifier with variable-capacitance diode resonated in series.

From the open-circuit impedance relations for the diode, we can obtain the series equivalent circuit for the diode as shown in Fig. 2. This representation is convenient when the diode is to become part of a series resonator as shown in this figure. This amplifier with the diode connected in series is essentially the dual of that in Fig. 1, and the same mathematical treatment applies for both. In the discussion to follow the series connection will be emphasized for the following reasons:

- 1) If the diode is resonated in series, the impedance level required for the associated filter will be lower than if the same diode is resonated in parallel at the same frequency. This makes possible the use of variable capacitance diodes with smaller capacitances which generally have better  $Q$ 's. It also may make the filter design more convenient.
- 2) The parasitic series inductance of the diode can be incorporated into the series resonator circuit.
- 3) Obtaining an  $a = C_1/C_0$  ratio which is as large as possible is vital if wide bandwidth is desired. If the diode is resonated in shunt, any stray shunt capacitances add directly to  $C_0$  and decrease the size of the ratio  $C_1/C_0$ . It appears probable that when the diode is resonated in series, the deleteri-

<sup>4</sup> Note that in (3), the second equation can also be expressed as  $I_2 = jB_{21}V_1^* + jB_{22}V_2$ . Thus, for  $V_1 = 0$ ,  $I_2/V_2 = jB_{22}$ .

<sup>5</sup> D. Leenov, "Gain and noise figure of a variable-capacitance up-converter," *Bell Sys. Tech. J.*, vol. 37, pp. 989-1008; July, 1958.



ous effects of stray capacitance can be minimized, since stray series capacitance should be easier to control.

### III. ANALYSIS OF PARAMETRIC AMPLIFIERS

It will be convenient to redraw the circuits in Fig. 1 as in Fig. 3, and the circuit in Fig. 2 as shown in Fig. 4. Note that in both Figs. 3 and 4 elements  $G_d$  or  $R_s$  have been added to account for diode losses. Considering the case of Fig. 4, the filter and circulator circuits are seen to have been drawn twice, once for the *signal frequency*  $f$ , and once for the *idler frequency*  $f'$ . Observe that the impedances evaluated at frequency  $f'$  are primed while the impedances evaluated at frequency  $f$  are unprimed.



Fig. 3—A parametric amplifier representation which is convenient for purposes of analysis (case of diode resonated in shunt).

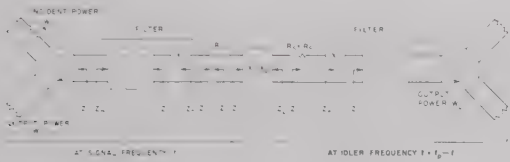


Fig. 4—A parametric amplifier representation which is convenient for purposes of analysis (case of diode resonated in series).

The coupling between the  $f$  and  $f'$  circuits is represented by the box labeled  $X_{12}X_{21}$ . Using (6) with  $X_{11}=X_{22}=0$  (the reactances  $X_{11}$  and  $X_{22}$  are removed from the  $X_{12}X_{21}$  box and lumped with  $Z_a$  and  $Z_a'$ ) and noting that  $Z_2$  in Fig. 4 is  $E_2/I_1$  while  $Z_a'$  in the figure would be  $-E_2/I_2$ , we readily obtain

$$Z_2 = \frac{-X_{12}X_{21}}{Z_a'^*}, \quad (9)$$

where  $X_{12}$  and  $X_{21}$  are positive quantities given by (7) and  $Z_a'^*$  is the complex conjugate of  $Z_a'$ . Thus, if  $Z_a'$  is real and positive,  $Z_2$  will be real and negative. As a result, this device operates as a negative resistance amplifier. It is also readily shown that  $Z_a$  in the figure is related to  $Z_2'$  by

$$Z_2' = \frac{-X_{12}X_{21}}{Z_a^*}. \quad (10)$$

In Fig. 4, the incident signal power (*i.e.*, available power) at frequency  $f$  is indicated by  $W_i$  (following Rowe's notation), while the output power at frequency  $f$  is the power  $W_r$  which is reflected into the circulator by the filter on the left in Fig. 4. (Of course, as has been mentioned previously, for the case of degenerate am-

plifiers there is actually only one filter. However, for purposes of analysis we may regard the filter on the right in Fig. 4 as being a second filter operating at frequency  $f'$ .) The power gain with respect to  $W_r$  is then

$$\frac{W_r}{W_i} = |\Gamma|^2 = \left| \frac{Z_m - Z_0}{Z_m + Z_0} \right|^2, \quad (11)$$

where  $\Gamma$  is the voltage reflection coefficient between the circulator impedance  $Z_0$  and the impedance  $Z_m$  seen looking in the left end of the left filter. For our purposes, however, it is much easier to deal with the impedances  $Z_b$  and  $Z_1$  rather than  $Z_0$  and  $Z_m$ . As is mentioned in Bode,<sup>6</sup>  $|\Gamma|$  may be computed by

$$|\Gamma| = \sqrt{\frac{W_r}{W_i}} = \left| \frac{Z_b - Z_1^*}{Z_b + Z_1} \right| \quad (12)$$

where  $Z_1^*$  is the complex conjugate of  $Z_1$ .<sup>7</sup> Using (9) we then obtain

$$\frac{W_r}{W_i} = \frac{\left| (Z_b - R_s) + \left( \frac{X_{12}X_{21}}{Z_a'^*} \right)^* \right|^2}{\left| (Z_b + R_s) - \left( \frac{X_{12}X_{21}}{Z_a'^*} \right) \right|^2}. \quad (13)$$

There is also power  $W_L'$  at frequency  $f'$  given out through the filter on the right in Fig. 4. To compute this we make use of the Manley-Rowe equations,<sup>2</sup> which say in effect that

$$\frac{W_2'}{W_2} = \frac{f'}{f}, \quad (14)$$

where  $W_2$  is defined as the power *into* the box  $X_{12}X_{21}$  from the left, and  $W_2'$  is defined as the power *into* the box from the right. (In this device  $W_2$  and  $W_2'$  are both negative.) The power *into*  $Z_1$  is  $W_i - W_r$ , so that the power *into*  $Z_2$  is

$$W_2 = (W_i - W_r) \frac{\text{Re } Z_2}{R_s + \text{Re } Z_2}, \quad (15)$$

which is a negative quantity in this case, since  $W_i < W_r$ ,  $\text{Re } Z_2 < 0$  and in practical cases  $R_s < |\text{Re } Z_2|$ . By (14), the power  $-W_2'$  out of the  $X_{12}X_{21}$  box is given by (15) times  $-f'/f$ . The power  $W_L'$  is that part of  $-W_2'$  which is absorbed in  $\text{Re } Z_b'$ , so that

$$\frac{W_L'}{W_i} = \left( 1 - \frac{W_r}{W_i} \right) \frac{\text{Re } Z_2}{R_s + \text{Re } Z_2} \left( \frac{-f'}{f} \right) \frac{\text{Re } Z_b'}{R_s' + \text{Re } Z_b'}, \quad (16)$$

where  $W_r/W_i$  is obtained from (13).

<sup>6</sup> Bode, *op. cit.*, p. 364.

<sup>7</sup> For (12) to be valid, it is necessary that the structure between the circulator and the reference plane of  $Z_b$  be lossless, or have negligible loss.

If  $f_0$  is the midband frequency for the filter in Fig. 2, then for the degenerate amplifier case it is required that

$$f_0 = f_p/2, \quad (17)$$

where  $f_p$  is the pump frequency. Then by (4), if

$$f = f_0 + \Delta \quad (18)$$

$$f' = f_0 - \Delta, \quad (19)$$

and if  $f$  is within the pass band of the filters,  $f'$  will also be within the pass band of the filter, but at the other side of  $f_0$ . As is indicated in Fig. 2, both the "reflected" power,  $W_r$ , at frequency  $f$ , and the idler power,  $W_{L'}$  at frequency  $f'$ , will emerge from the output port of the circulator. Since both the outputs at  $f$  and  $f'$  will carry the modulation, both represent useful power if the amplifier is followed either by a video detector or by another amplifier and then a video detector. Thus, the useful power gain of the device is equal to the sum of the gains given by (13) and (16), which is about 3 db more gain than is given by (13) alone. An exception occurs when  $f$  is almost equal to  $f'$ , so that the difference beat signal between  $f$  and  $f'$  falls within the pass band of the video amplifier following the crystal video detector. In this case the output power will vary between zero and a peak value of four times that of the signal output power alone, this variation being at a rate corresponding to the difference frequency  $|f-f'|$ . When  $|f-f'|$  exceeds the bandwidth of the video amplifier, this variation is no longer observable. Then the filtering effect of the amplifier averages out the  $|f-f'|$  variation so that the video power output is effectively the sum of the signal and idler video outputs (as taken separately).

By duality, equations analogous to (13) and (16) are readily obtained for the shunt diode case in Figs. 1 and 3. They are

$$\frac{W_r}{W_i} = \left| \frac{(Y_b - G_d) + \left( \frac{B_{12}B_{21}}{Y_a'^*} \right)^*}{(Y_b + G_d) - \left( \frac{B_{12}B_{21}}{Y_a'^*} \right)} \right|^2 \quad (20)$$

and

$$\frac{W_{L'}}{W_i} = \left( 1 - \frac{W_r}{W_i} \right) \frac{\text{Re } Y_2}{G_d + \text{Re } Y_2} \left( \frac{-f'}{f} \right) \frac{\text{Re } Y_b'}{G_d' + \text{Re } Y_b'}. \quad (21)$$

Herein, and for the parametric amplifier and up-converter discussions to follow, the loss elements  $R_s$ ,  $R_s'$ ,  $G_d$ , and  $G_d'$  in Figs. 3 and 4 will be defined as:

$$R_s = \frac{1}{Q_d 2\pi f_0 C_0^s} = \frac{(X_{11})_0}{Q_d} \quad (22)$$

$$R_s' = \frac{1}{Q_d' 2\pi f_0' C_0^s} = \frac{(X_{22})_0}{Q_d'} = R_s \quad (23)$$

$$G_d = \frac{2\pi f_0 C_0}{Q_d} = \frac{(B_{11})_0}{Q_d} \quad (24)$$

$$G_d' = \frac{2\pi f_0' C_0}{Q_d'} = \frac{(B_{22})_0}{Q_d'} = G_d \left( \frac{f_0'}{f_0} \right)^2, \quad (25)$$

where  $f_0$  is the center of the signal input band;  $f_0'$  is the band center of the idler band (of course, for degenerate amplifiers  $f_0 = f_0'$ );  $Q_d$  is the operating  $Q$  of the diode at frequency  $f_0$ ;  $Q_d' = Q_d(f_0/f_0')$  is the operating  $Q$  of the diode at frequency  $f_0'$ ;  $C_0^s$ ,  $X_{11}$ , and  $X_{22}$  are given by (7) and (8); and  $C_0$ ,  $B_{11}$ , and  $B_{22}$  are given by (5). The brackets and sub zeros are introduced to imply that

$$(X_{11})_0 = X_{11}|_{f=f_0}, \quad (X_{22})_0 = X_{22}|_{f=f_0'}, \text{ etc.} \quad (26)$$

Of course, the equations for  $R_s$  and  $R_s'$  are based on having the resistor and capacitor in series, while those for  $G_d$  and  $G_d'$  are based on having the conductance and capacitor in parallel. Computations indicate that the operating  $Q$ 's,  $Q_d$  and  $Q_d'$ , for typical graded junction diodes may be estimated by

$$Q_d = 0.71 \frac{f_c}{f_0} \quad \text{and} \quad Q_d' = 0.71 \frac{f_c}{f_0'} \quad (27)$$

where  $f_c$  is the usual "cutoff frequency" measured at a bias near the reverse breakdown voltage. These approximate formulas assume that the diode is pumped and biased so that the voltage swings from zero volts to negative voltages closely approaching breakdown.

#### IV. BAND-PASS FILTERS FROM LOW-PASS PROTOTYPES

Extensive tables of element values now exist for normalized maximally flat and Tchebycheff low-pass filter designs.<sup>8-10</sup> Fig. 5 shows the type of filter treated by these tables and a typical Tchebycheff response. A low-pass filter such as is shown in Fig. 5 is readily converted to an analogous band-pass filter by use of the transformation given in (a) to (c) in Fig. 6. Knowing the generator source impedance,  $R_0$ , the fractional bandwidth,  $w$ , and the center frequency,  $f_0$ , desired for the band-pass filter, we can compute the element values for the band-pass filter from the radian cutoff frequency,  $\Omega_1$ , and element values of the low-pass prototype (see Fig. 5), by use of (d), (e), and (f) in Fig. 6.

The filter shown in Fig. 6 has lumped elements, but filters for use with parametric amplifiers would probably consist of a mixture of semi-lumped and transmission-line elements. In such cases it is helpful to specify the resonators of a filter in terms of their resonant fre-

<sup>8</sup> L. Weinberg, "Network Design by Use of Modern Synthesis Techniques and Tables," Hughes Aircraft Co., Res. Labs., Culver City, Calif., Tech. Memo. 427; 1956. Also, *Proc. of NEC*, vol. 12; 1956.

<sup>9</sup> L. Weinberg, "Additional Tables for Design of Optimum Ladder Networks," Hughes Aircraft Co., Res. Labs., Culver City, Calif., Tech. Memo. 434; 1956.

<sup>10</sup> W. J. Getsinger, *et al.*, "Research on Design Criteria for Microwave Filters," SRI Project 2326, Contract DA 36-039 SC-74862, Stanford Res. Inst., Menlo Park, Calif. Tech. Rept. 4; December, 1958.



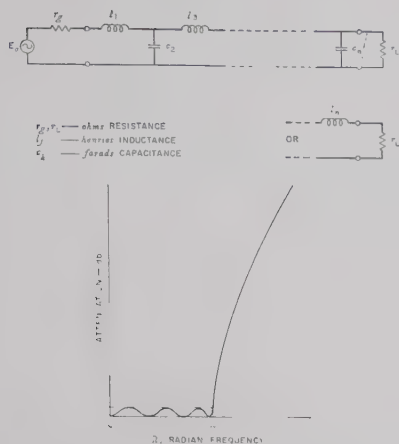


Fig. 5—Low-pass prototype filter and a typical Tchebycheff response.

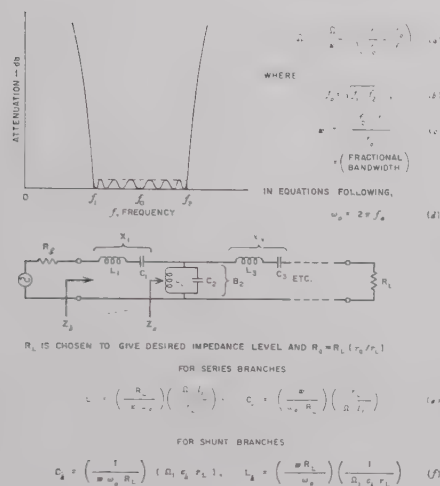


Fig. 6—Summary of relations for design of lumped-element band-pass filters from low-pass prototypes.

quency and their reactance or susceptance slopes, as is done in Fig. 7. Using this description, the exact nature of the resonators is unimportant, except that they must function similarly to series or shunt LC resonators in the vicinity of  $f_0$ . As is shown in the figure the parameters  $l_j$ ,  $c_k$ ,  $\Omega_1$ , and  $r_L$  from the low-pass prototype, along with  $R_0$ ,  $w$ , and  $f_0$  specified for the band-pass filter can be related directly to resonator slope parameters  $x_j$  and  $b_k$ . From these parameters the required reactance and susceptance slopes are obtained from the equations given. If the resonator boxes in Fig. 7 contain lumped-element resonators, as in Fig. 6, the slope parameters are given by

$$x_j = \frac{1}{\omega_0 C_j} = \omega_0 L_j, \quad \text{and} \quad b_k = \omega_0 C_k = \frac{1}{\omega_0 L_k}, \quad (28)$$

where the  $L$ 's and  $C$ 's are as defined in Fig. 6. Fig. 8 gives the equations for the circuit which is the dual of

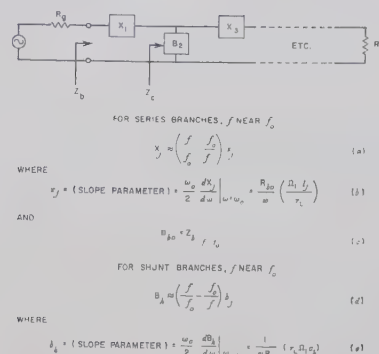


Fig. 7—General description of band-pass filters in terms of resonator slope parameters. ( $\Omega_1$ ,  $l_j$ ,  $c_k$  and  $r_L$  are defined in Fig. 5.)

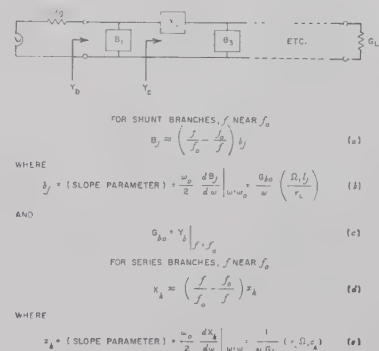


Fig. 8—Slope parameters for dual case to that in Fig. 7. ( $\Omega_1$ ,  $l_j$ ,  $c_k$ , and  $r_L$  are defined in Fig. 5.)

that in Fig. 7. If the circuit in Fig. 8 contains lumped-element resonators, then

$$b_j = \omega_0 C_j = \frac{1}{\omega_0 L_j}, \quad \text{and} \quad x_k = \omega_0 L_k = \frac{1}{\omega_0 C_k}. \quad (29)$$

## V. GAIN AND BANDWIDTH RELATIONS FOR DEGENERATE PARAMETRIC AMPLIFIERS

In the variable-capacitor amplifiers studied on this project, the capacitance  $C_0$  (or  $C_0^s$ ) of the diode represents a fixed parasitic element which cannot be eliminated. In the degenerate amplifier represented by Figs. 2 and 4,  $C_0^s$  is incorporated into the first resonator and by (28) fixes its minimum reactance slope. Thus for Fig. 2 and its representation in the form of Fig. 4, the slope parameters are restricted as follows:

$$x_1 = x_1' \geq (X_{11})_0 = (X_{22})_0 \quad (30)$$

for the case of degenerate amplifiers which, of course, have  $f_0 = f_0'$ . The inequality sign in (30) will usually hold as a result of extra reactance slope due to such things as  $L_1$  not being a truly lumped inductance, and reactance effects of the pump circuit coupling. However, for degenerate amplifiers, it should be possible to keep  $x_1$  nearly equal to  $(X_{11})_0$ .

In order to obtain equations which relate the mid-band gain of a degenerate amplifier to its filter band-

Solving for  $u$ , and then for  $w$  by use of (34) gives the filter fractional bandwidth

$$w = a \left( \frac{(X_{11})_0}{x_1} \right) \left( \frac{\Omega_1 l_1}{r_L} \right) \left[ \sqrt{\left[ \frac{1}{2aQ_d} \left( \frac{\Gamma_0 + 1}{\Gamma_0 - 1} + 1 \right) \right]^2 - \left( \frac{\Gamma_0 + 1}{\Gamma_0 - 1} \right) \left( \frac{1}{(aQ_d)^2} - 1 \right)} - \left[ \frac{1}{2aQ_d} \left( \frac{\Gamma_0 + 1}{\Gamma_0 - 1} + 1 \right) \right] \right]. \quad (37)$$

width, let us replace the impedances  $Z_b$  and  $Z_b'$  in Figs. 2 and 4 with the resistance  $(Z_b)|_{f=f_0} = R_{b0} = R_{b0}'$  defined in (c) of Fig. 7. In Fig. 7,  $R_{b0} = R_L$ , but the definition in (c) of that figure is used since for some kinds of transmission line filters,  $R_{b0}$  will not equal  $R_L$ . Then by (13) we can compute

$$|\Gamma_0| = \Gamma_0 = \frac{(R_{b0} - R_s)(R_{b0} + R_s) + (X_{12})_0(X_{21})_0}{(R_{b0} + R_s)(R_{b0} - R_s) - (X_{12})_0(X_{21})_0}, \quad (31)$$

where  $|\Gamma_0|^2 = (W_r/W_i)_0$  is the gain near midband *neglecting output due to the idler*. (The idler contributes about 3 db more of useful gain except, possibly, when the signal and idler frequencies are so close that their beat frequency is within the video detector bandwidth.) By (7), (8), and (26), we see that

$$(X_{12})_0 = a(X_{22})_0 \quad \text{and} \quad (X_{21})_0 = a(X_{11})_0. \quad (32)$$

By (31), (32), (22), and (23),

$$\Gamma_0 = \frac{\left( \frac{R_{b0}}{a(X_{11})_0} - \frac{1}{aQ_d} \right) \left( \frac{R_{b0}}{a(X_{11})_0} + \frac{1}{aQ_d} \right) + 1}{\left( \frac{R_{b0}}{a(X_{11})_0} + \frac{1}{aQ_d} \right)^2 - 1}, \quad (33)$$

where the fact that  $(X_{11})_0 = (X_{22})_0$  for degenerate amplifiers was also used. Now by (30) it is known that the slope parameter  $x_1$  for the first resonator  $X_1$  will be fixed largely by  $C_0^*$  for the diode. By (b) of Fig. 7,

$$\frac{R_{b0}}{x_1} = w \left( \frac{r_L}{\Omega_1 l_1} \right). \quad (34)$$

Thus, if we know  $r_L/(\Omega_1 l_1)$  from the low-pass prototype and have a value for  $R_{b0}/x_1$ , we can solve for the fractional bandwidth  $w$ . Introducing  $x_1$  in (33) as a cancelling factor we can obtain

$$|\Gamma_0| = \frac{\left( u - \frac{1}{aQ_d} \right) \left( u + \frac{1}{aQ_d} \right) + 1}{\left( u + \frac{1}{aQ_d} \right)^2 - 1}, \quad (35)$$

where

$$u = \frac{R_{b0} x_1}{a x_1 (X_{11})_0}. \quad (36)$$

If  $Q_d$  is very large, then (37) reduces to

$$w = a \left( \frac{(X_{11})_0}{x_1} \right) \left( \frac{\Omega_1 l_1}{r_L} \right) \sqrt{\frac{\Gamma_0 + 1}{\Gamma_0 - 1}}, \quad (38)$$

which is a convenient form for examining the significance of the various parameters. Note that  $w$  is directly proportional to  $a = C_1/C_0$  so that it is of great importance that the diode be pumped as hard as is allowable, if maximum bandwidth is desired. If the gain is low so that  $\Gamma_0$  is not much greater than one, then  $w$  is a strong function of gain. However, as the gain becomes larger, the quantity under the radical approaches one and the bandwidth becomes a very weak function of gain. Thus, it is seen that the gain-bandwidth product will not be constant as the gain is varied if the lumped-element prototype parameter  $\Omega_1 l_1/r_L$  remains fixed. Lombardo and Sard<sup>11</sup> report a gain-bandwidth product which is constant as the gain is varied, for the case of amplifiers with single-resonator filters. In their case the bandwidth is defined as the 3-db points and this bandwidth will decrease as the gain is increased for a single-resonator design. The analogous multiple-resonator Tchebycheff design situation is to vary the prototype (and hence,  $\Omega_1 l_1/r_L$ ) as the gain is varied so that the ripples of gain will always have the same db amplitude no matter what the average gain is. On that basis, something approaching a constant gain-bandwidth product vs gain may also result for multiple-resonator designs. However, if the prototype used remains fixed for a series of designs, having progressively increasing mid-band gains, the tendency will be for the size of the gain ripples to increase for designs with larger midband gains, while the equal-ripple bandwidth will change very little once gains of around 20 db or so are reached.

In order to facilitate the use of (37), the chart in Fig. 9 was computed. Using this chart, if a given gain in the vicinity of midband is desired (note that the abscissa is gain with respect to output at the signal frequency only), then knowing  $(aQ_d)$  for the diode to be used, the parameter  $h$  can be determined from the ordinate. If the diode is to be resonated in series, then the fractional bandwidth parameter for the filter can be computed by

$$w = ha \left( \frac{(X_{11})_0}{x_1} \right) \left( \frac{\Omega_1 l_1}{r_L} \right). \quad (39)$$

<sup>11</sup> P. P. Lombardo and E. W. Sard, "Low-noise microwave reactance amplifiers with large gain-bandwidth products," 1959 WESCON CONVENTION RECORD, Pt. 1, pp. 83-98.



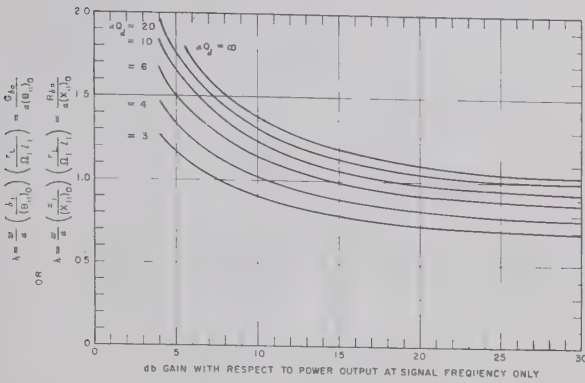


Fig. 9—Chart for relating degenerate parametric amplifier gain and filter bandwidth for a given low-pass prototype and for given diode parameters. (The idler contributes about 3 db additional gain to the gain indicated on the abscissa of this chart.)

If the diode is to be resonated in shunt, then the analogous relation

$$w = ha \left( \frac{(B_{11})_0}{b_1} \right) \left( \frac{\Omega_1 l_1}{r_L} \right) \quad (40)$$

applies.

From (39) and (40) it is seen that  $w$  depends strongly on  $(\Omega_1 l_1 / r_L)$  obtained from the lumped-element prototype. In order to obtain large fractional bandwidths,  $w$ , it is desirable that  $(\Omega_1 l_1 / r_L)$  be large. However, it will be found that prototype filters which will lead to amplifiers with more nearly constant gain throughout their operating band will tend to have smaller values of  $(\Omega_1 l_1 / r_L)$ , and hence, somewhat smaller bandwidths. Thus the choice of the lumped-element prototype involves a compromise between the objective of obtaining wide bandwidth and the objective of obtaining nearly constant gain. It should also be recognized that adding additional elements to the filter will also improve the performance. This is because additional elements facilitate holding the gain close to a desired value throughout the pass band, and they also permit a sharper cutoff, which improves the bandwidth capabilities, as was discussed with reference to (2).

If  $\Omega_1$  is the equal-ripple band edge of an ordinary low-pass Tchebycheff filter with resistor terminations, the fractional bandwidth  $w$  obtained with the aid of Fig. 9 and (39) or (40) will be the bandwidth of the corresponding band-pass filter for the amplifier when connected to resistor terminations corresponding to those of the prototype. As will be seen from the examples to follow, the negative-resistance type of termination presented by a pumped, variable-capacitance diode affects the response shape and bandwidth in a different way than does an ordinary resistor and, as a result, the actual operating bandwidth of the amplifier is somewhat larger than would be indicated by  $w$ . For  $w$  to predict the bandwidth of the amplifier with high accuracy,  $\Omega_1$  must be the band-edge frequency of the low-pass prototype when operated into a termination analogous to a pumped, variable-capacitance diode.

## VI. SOME DEGENERATE PARAMETRIC AMPLIFIER EXAMPLES

Fig. 10 shows a degenerate amplifier configuration having two resonators. The pump circuit is assumed to be so loosely coupled as to have negligible effect at frequencies away from the pump frequency,  $f_p$ . Design No. 1 listed in the figure was obtained using an  $n=2$  reactive-element, lumped-element prototype having 0.01-db Tchebycheff ripple.<sup>10</sup> The prototype elements as defined in Fig. 5 are  $r_0=1$ ,  $l_1=0.4488$ ,  $c_2=0.4077$ ,  $r_L=1.1008$ , and  $\Omega_1=1$ . If we hypothesize a diode having a cutoff frequency of  $f_c=85$  kMc, and if  $f_0=f_0'=1$  kMc then, by (27),  $Q_d=Q_d'=60$ . Let us assume that  $a=C_1/C_0=0.25$ , and that we desire about 15.5-db total gain near midband (including output at both the signal and idler frequencies). To obtain 15.5-db total gain near midband, we need 12.5-db gain near midband for the output at the signal frequency alone. For 12.5-db gain and  $(aQ_d)=0.25(60)=15$ , it is seen that  $h=1.17$ . If we assume that  $x_1/(X_{11})_0 \approx 1$ , then (39) calls for a fractional bandwidth  $w=0.121$  for the 0.1-db equal-ripple band of the filter (when connected to resistor terminations). Then by (b) and (c) of Fig. 7, the slope parameters for the two resonators are computed to be  $x_1=3.70$  and  $b_2=3.36$ , taking  $R_{b0}=r_L=1.1008$ .

Fig. 11 shows the computed input impedance,  $Z_b$ , for Design 1, and Fig. 12 shows its computed gain. Note that the equal-ripple band edges for the filter operated with normal resistor terminations extend from about  $f/f_0=0.94$  to  $f/f_0=1.06$ , corresponding to  $w=0.121$ , but these band-edge points have turned out to be points of peak gain when this filter is used in the variable-capacitance amplifier of Fig. 10. The reason for this will be clear by examination of Fig. 11 and (13). If  $Z_a'=Z_b+R_s=R$  and  $R=\sqrt{X_{12}X_{21}}$ , then the gain will be infinite and oscillation will result. When  $\text{Re } Z_b=R_b$  in Fig. 11 crosses  $\sqrt{X_{12}X_{21}}$ , oscillation is prevented by the fact that  $\text{Im } Z_b=X_b$  is not zero. Clearly, in order to lower the gain peaks in Fig. 12 it will be necessary to increase the input reactance at the points where  $R_b=\sqrt{X_{12}X_{21}}$ . This tendency for the gain to rise as  $\text{Re } Z_b$  starts to fall causes the bandwidth to tend to be larger for a degenerate parametric amplifier using a given filter than the bandwidth would be for the same filter operated in a passive circuit with normal resistive terminations.

The desired extra input reactance characteristic was obtained in Design No. 2 by reducing the slope parameter for the second resonator to  $b_2=2.35$ , while keeping the diode and Resonator 1 as they were previously. The resulting input impedance and gain is shown by the heavy lines in Figs. 11 and 12. As can be seen from the gain plot, the pass-band ripple has been reduced to about 1.6 db.

Using  $b_2=0$ , and  $x_1$  and the diode as before, a single-resonator design was obtained (Design No. 3). The response of this design is also plotted in Fig. 12. Note that

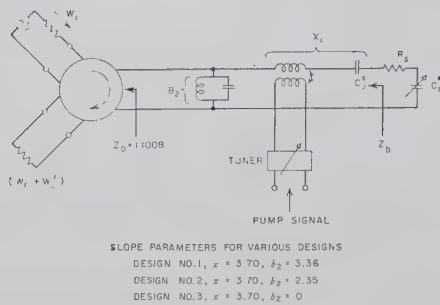


Fig. 10—Circuit for degenerate parametric amplifier examples using a two-resonator filter.

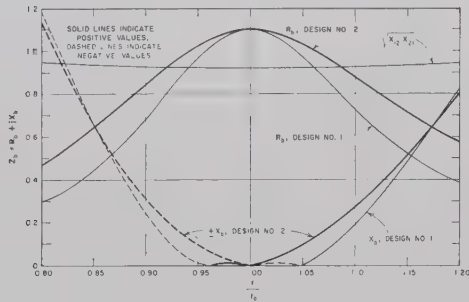


Fig. 11—Computed input impedance,  $Z_b$ , for Designs Nos. 1 and 2 in Fig. 10.

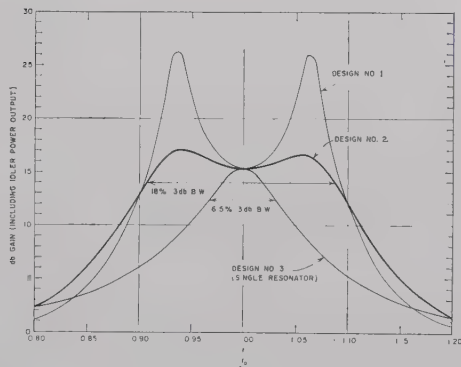


Fig. 12—Computed gain for Designs Nos. 1, 2, and 3 in Fig. 10 using a diode having  $a = C_1/C_0 = 0.25$  and  $Q_d = 60$ .

increasing the number of resonators from one to two makes possible an increase in 3-db bandwidth from 6.5 per cent to 18 per cent. Adding additional resonators can increase the potential bandwidth even further, but the amount of improvement per additional resonator will decrease rapidly as the number of resonators is increased.

Fig. 13 shows another design using a five-resonator filter. The transmission-line portion of the filter was designed using a 0.10-db Tchebycheff-ripple, four-reactive-element prototype having an infinite impedance current generator at one end.<sup>9</sup> If the current of the generator is  $I_g$ , then the power delivered into the filter (and to the load resistor at its other end) is

$$P = |I_g|^2 \text{Re } Z_b \quad (41)$$

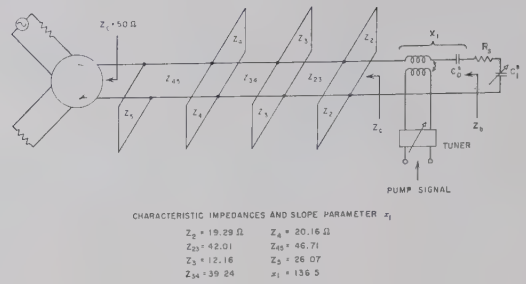


Fig. 13—A five-resonator, degenerate, parametric amplifier design example.

where  $Z_b$  is the input impedance of the filter. It is thus seen that for a Tchebycheff filter of this type, the real part of the input impedance will be a Tchebycheff approximation of a constant value in the pass band. Since a nearly constant  $\text{Re } Z_b$  is desirable to obtain a constant gain, this type of prototype appears to be useful for parametric amplifier design. The four-resonator transmission line portion of the filter was designed from the prototype<sup>12</sup> using microwave filter design techniques developed at this laboratory<sup>13,14</sup>. As is seen from the  $R_c/Z_0 = Z_b/Z_0$  curve in Fig. 14, it has a very nearly Tchebycheff approximation to a constant  $\text{Re } Z_b$  throughout the pass band. As is shown by the  $X_c/Z_0$  curves, the input impedance of the transmission line filter has an excessive amount of imaginary part. The slope parameter  $x_1$  of the resonator  $X_1$  was chosen so as to largely cancel this imaginary part while leaving a sizable reactance at the points where  $\text{Re } Z_b = \sqrt{X_{12}X_{21}}$ , and it was assumed again that  $a = C_1/C_0 = 0.25$ . Since the impedance function,  $Z_c$ , for the transmission-line portion of the filter has arithmetic symmetry, while the reactance of the diode resonator,  $X_1$ , does not, resonator  $X_1$  was tuned about one per cent low so that the total net reactances in the vicinity of cutoff on both sides will be of nearly equal amplitude.

Using  $a = 0.25$  and  $Q_d = 60$ , as for Designs Nos. 1 to 3, the gain was computed and plotted in Fig. 15. In this case the design gain is lower (roughly 10 db including signal and idler power). Since the gain of high-gain parametric amplifiers is a hypersensitive function of their input impedance, in the case of wide-band parametric amplifiers it may be necessary to use lower gains so that the adjustments will not be so critical. If the parametric amplifier is being used simply as a relatively

<sup>12</sup> In this case the slope parameters of the shunt transmission line resonators cannot be obtained from the prototype by the relations in Figs. 7 or 8, as a result of the selectivity effects of the connecting lines. However, it would be possible to relate Resonator 1 to a prototype as is done in Fig. 7, since  $X_1$  has no  $\lambda_0/4$  connecting line.

<sup>13</sup> G. L. Matthaei and P. S. Carter, Jr., "Design Criteria for Microwave Filters and Coupling Structures," Tech. Rept. 7, SRI Project 2326, Contract DA 36-039 SC-74862, Stanford Res. Inst., Menlo Park, Calif.; July, 1959.

<sup>14</sup> G. L. Matthaei, "Band-pass microwave filter design—a new method and its relation to other methods," 1960 IRE NATIONAL CONVENTION RECORD, pt. 3, pp. 95-122.



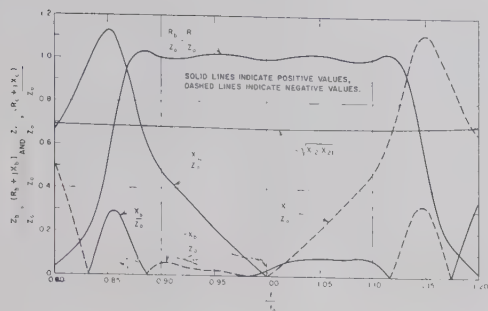


Fig. 14—Computed input impedances  $Z_b$  and  $Z_o$  for the circuit in Fig. 13.

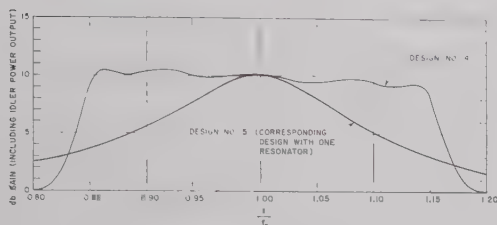


Fig. 15—Computed gain for the amplifier in Fig. 13 and also for an analogous one-resonator amplifier both using a diode having  $a = C_1/C_0 = 0.25$  and  $Q_d = 60$ .

low-noise first-stage amplifier, then gains as low as 10 db may be acceptable in many cases. Of course, lower gain also gives larger bandwidth. Note that in this case the gain is very flat, with only about 0.5-db ripple. If the design had been carried out to give larger gain ripples, a larger minimum gain could probably have been obtained for the same bandwidth. Observe that the gain has a slight slope to it throughout the operating band. This is due to the  $f'/f$  factor in (16). The bandwidth of the equal-ripple portion of the response is seen to be about 29 per cent in this case.<sup>15</sup>

Note that in Fig. 13 it would have also been possible to resonate the diode in shunt and use a  $\lambda_0/4$  line between the diode resonator and shunt stubs  $Z_2$ . Besides other possible disadvantages of resonating the diode in shunt, such a scheme would yield a smaller operating bandwidth because of the selectivity of the  $\lambda_0/4$  line between resonators 1 and 2. As a result of this extra selectivity, the slope parameter of the diode resonator would have to be less for a given bandwidth or, putting it another way, the bandwidth would have to be less for a given slope parameter. As a result, it is advantageous to have the first resonator in series and the second one in shunt, or vice versa, so that  $\lambda_0/4$  coupling lines are not required adjacent to the diode resonator.

## VII. CHOICE OF LUMPED-ELEMENT PROTOTYPES FOR AMPLIFIER FILTERS

As can be seen from the preceding examples, the requirements on filters for parametric amplifiers are some-

what different than for filters used in more conventional applications. Assuming that the diode is being resonated in series, for a given db ripple in gain, the real part of the input impedance must be much more nearly constant for a parametric amplifier filter than for a conventional filter. It is also very important that there be a sizable reactive component when  $\text{Re } Z_b$  starts to fall at the band edge.

The input impedances of several common types of filters were computed to investigate their usefulness for amplifier applications. Conventional Tchebycheff filters having resistive terminations at both ends were found to have the characteristic that  $\text{Re } Z_b$  ranges above the generator resistance value,  $R_0$ , for frequencies near  $\Omega = 0$ , but ranges below the  $R_0$  value at frequencies approaching cutoff. In this respect,  $\text{Re } Z_b$  for a prototype having an infinite impedance generator (as discussed with respect to Design No. 4) is different, since for that type of prototype  $\text{Re } Z_b$  has equal ripples about a constant value. A maximally flat filter design having resistive terminations at both ends had a relatively small reactive component at frequencies where  $\text{Re } Z_b$  was falling. As previously noted, this is undesirable.

Further investigation is desirable to determine general methods for obtaining optimum filter designs for parametric amplifiers. Working back from Design No. 2, we obtain the prototype elements  $r_0 = 1$ ,  $l_1 = 0.592$ ,  $c_2 = 0.376$ ,  $r_L = 1.1008$ ,  $\Omega_1 = 1$  where in this case  $\Omega_1$  is the low-pass prototype radian frequency corresponding to equal-ripple band-edge points in the response of Design No. 2 in Fig. 12. It is seen that these prototype element values differ significantly from those of the 0.01-db ripple, two-reactive-element prototype used for Design No. 1. Although Design No. 4 has a very flat response, a design from a somewhat different prototype could probably have given a little more bandwidth for the same gain and gain ripple (or more gain for the same bandwidth and gain ripple).

## VIII. NONDEGENERATE PARAMETRIC AMPLIFIERS

Fig. 16 shows a circuit for a nondegenerate parametric amplifier analogous to the degenerate amplifier in Fig. 10. In this case  $f_0$ , the center of the signal band, and  $f_0'$ , the center of the idler band, are widely separated and two filters are required in order to obtain the proper performance. In Fig. 16, the resonator  $B_2$  belongs to the signal filter which is terminated by the circulator. The resonator  $B_2'$  belongs to the idler filter, while  $R_L'$  provides the idler termination. The series branch in this circuit contains the diode which introduces the parameters  $C_0^s$ ,  $C_1^s$ ,  $R_s$  as previously discussed, and in this case the parasitic series inductance  $L_d$  of the diode is also shown. The diode is brought to series resonance at both  $f_0$  and  $f_0'$  by introduction of a length of series transmission line short-circuited at the end. Thus, the series branch in Fig. 16 operates as resonator  $X_1$  for the signal filter at frequencies near  $f_0$ , while it operates as resonator  $X_1'$  for the idler filter at frequencies near  $f_0'$ . Using

<sup>15</sup> The transmission line filter was designed for 25 per cent equal-ripple bandwidth when driven by a current generator.

a semistripline construction, the series transmission line stub might be realized to a satisfactory approximation as fine wire transmission line between the ground plates.

The circuit in Fig. 16 can also be represented as in Fig. 4, but care must be used in relating the two forms. Branch  $X_1 + R_s$  in Fig. 4 should contain the impedance of the entire circuit to the right of resonator  $B_2$  in Fig. 16 (except for  $C_1^s$ ) measured at the signal frequency  $f$ . Meanwhile, the branch  $R_s' + X_1'$  in Fig. 4 should contain the impedance of the entire circuit to the left of resonator  $B_2'$  in Fig. 16 (again, except for  $C_1^s$ ) measured at the idler frequency  $f' = f_p - f$ . Since the impedance of  $B_2'$  is very low at the signal frequency  $f$ , while the impedance of  $B_2$  is very low at the idler frequency  $f'$ , the impedances  $X_1 + R_s$  and  $R_s' + X_1'$  in Fig. 4 are, for most practical purposes, the impedances of the series arm in Fig. 16 (minus  $C_1^s$ ) at frequencies  $f$  and  $f'$ , respectively. For the case of nondegenerate amplifiers, the circulator on the right in Fig. 4 should, of course, be replaced by a load resistor.

Fig. 17 shows a typical reactance characteristic such as might result from the  $C_0^s$ ,  $L_d$ , and series line combination in Fig. 16. Frequency  $f_{01}$  is defined as the resonant frequency of resonator  $X_1$ , while  $f_{01}'$  is the resonant frequency of resonator  $X_1'$ . At frequency  $f_{01}$  the series line would usually look inductive, while at  $f_{01}'$  it may look either capacitive or inductive depending on the relative sizes of  $C_0^s$  and  $L_d$ . The line is  $\lambda/4$  long at frequency  $f_R$ , and hence causes infinite reactance at that frequency, while the line would be close to  $\lambda/2$  long at frequency  $f_{01}'$ .

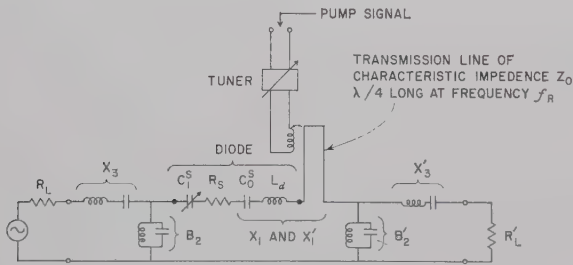


Fig. 16—Example of a nondegenerate parametric amplifier using a two-resonator filter in the signal circuit and also in the idler circuit.

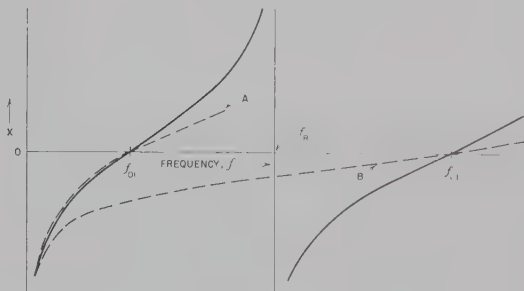


Fig. 17—An approximate reactance curve for the resonator circuit formed by  $C_0^s$ ,  $L_d$  and the transmission line in Fig. 16.

Some previous writers have assumed, in effect, that the diode capacitance  $C_0^s$  (or  $C_0$  for the shunt case) can be resonated out independently at the frequencies  $f_{01}$  and  $f_{01}'$ . If that were possible, the reactance curve for resonator  $X_1$  in Fig. 4 would be approximately as shown by the dashed curve marked A in Fig. 17, while the reactance curve for resonator  $X_1'$  would be as shown by the dashed curve marked B. (Each of the curves corresponds approximately to  $C_0^s$  in series with a lumped inductance.) Curves A and B would yield considerably smaller reactance slope in the vicinity of  $f_{01}$  and  $f_{01}'$ , and hence, would yield greater bandwidth than would the solid, multiple resonance curve in Fig. 17. However, since resonators  $X_1$  and  $X_1'$  must both contain the same element  $C_0^s$ , their circuitry is necessarily interconnected and there appears to be no way of avoiding the use of multiple resonances in the reactance curve for resonators  $X_1$  and  $X_1'$ . This extra reactance slope which occurs in the nondegenerate amplifier case increases the slope parameters  $x_1$  and  $x_1'$  and tends to reduce the bandwidth possible as compared with a corresponding degenerate amplifier.

For maximum amplifier bandwidth the signal and idler filters should have the same bandwidth. If  $w$  is the signal filter fractional bandwidth while  $w'$  is the idler filter fractional bandwidth, then we require that

$$\frac{w'}{w} = \frac{f_0}{f_0'} \quad (42)$$

Assuming that both the signal and idler filters are to be designed from the same lumped-element prototype, we may use (b) in Fig. 7 to derive the equation:

$$\frac{x_1}{R_{b0}} = \frac{x_1'}{R_{b0'}} \left( \frac{f_0}{f_0'} \right), \quad (43)$$

or

$$R_{b0'} = (R_{b0}) \left( \frac{f_0}{f_0'} \right) \left( \frac{x_1'}{x_1} \right). \quad (44)$$

If the diode is resonated in shunt, the analogous relation

$$G_{b0'} = (G_{b0}) \left( \frac{f_0}{f_0'} \right) \left( \frac{b_1'}{b_1} \right) \quad (45)$$

applies. Using Fig. 4 as a model, by use of (13) we may relate the design bandwidth of the filters to the mid-band gain for given  $x_1$ ,  $x_1'$ ,  $a$ ,  $Q_d$  and filter prototype parameters. Using (13) and (43) and the fact that

$$(X_{12})_0 = a(X_{22})_0 = a(X_{11})_0 \left( \frac{f_0}{f_0'} \right), \quad (46)$$

$$(X_{21})_0 = a(X_{11})_0, \quad (47)$$

and

$$Q_d' = Q_d \left( \frac{f_0}{f_0'} \right), \quad (48)$$



we obtain after considerable manipulation

$$u = \sqrt{\left[ \frac{1}{2q} \left( \frac{\Gamma_0 + 1}{\Gamma_0 - 1} + \gamma \right) \right]^2 + \frac{\Gamma_0 + 1}{\Gamma_0 - 1} \left( 1 - \frac{\gamma}{q^2} \right)} - \left[ \frac{1}{2q} \left( \frac{\Gamma_0 + 1}{\Gamma_0 - 1} + \gamma \right) \right] \quad (49)$$

where

$$\Gamma_0 = \sqrt{\frac{W_r}{W_i}} \bigg|_{f=f_0} \quad (50)$$

$$\gamma = \frac{f_0'}{f_0} \frac{x_1}{x_1'} \quad (51)$$

$$q = aQ_d \sqrt{\frac{x_1}{x_1'}} \quad (52)$$

$$u = \frac{R_{b0}}{ax_1} \frac{\sqrt{x_1 x_1'}}{(X_{11})_0} = \frac{w}{a} \left( \frac{r_L}{\Omega_1 l_1} \right) \frac{\sqrt{x_1 x_1'}}{(X_{11})_0} \quad (53)$$

If the diode is resonated in shunt, (49) and (50) still apply but

$$\gamma = \left( \frac{f_0'}{f_0} \right)^3 \left( \frac{b_1}{b_1'} \right) \quad (54)$$

$$q = aQ_d \sqrt{\frac{b_1}{b_1'}} \left( \frac{f_0'}{f_0} \right) \quad (55)$$

and

$$u = \frac{G_{b0}}{ab_1} \frac{\sqrt{b_1 b_1'}}{(B_{11})_0} \frac{f_0}{f_0'} = \frac{w}{a} \left( \frac{r_L}{\Omega_1 l_1} \right) \frac{\sqrt{b_1 b_1'}}{(B_{11})_0} \frac{f_0}{f_0'} \quad (56)$$

Using (49), charts were prepared of  $u$  vs  $\gamma$  for various values of  $q$  and  $\Gamma_0$ . Figs. 18(a), (b), and (c) show such charts for the cases of  $\Gamma_0 = 3.162$  (10-db gain);  $\Gamma_0 = 5.623$  (15-db gain); and  $\Gamma_0 = 10$  (20-db gain), respectively. To use these charts (for the series resonance case) one first designs the diode circuitry to give the resonances for  $X_1$  and  $X_1'$  so that  $x_1$  and  $x_1'$  can be computed. Then knowing  $a$ ,  $Q_d$ , and  $f_0'/f_0$ ,  $\gamma$  and  $q$  are determined by (51) and (52). From the chart for the desired gain we obtain  $u$ , and then by (53) the fractional

bandwidth of the input filter must be

$$w = ua \left( \frac{(X_{11})_0}{\sqrt{x_1 x_1'}} \right) \left( \frac{\Omega_1 l_1}{r_L} \right). \quad (57)$$

If the diode is resonated in shunt the corresponding equation is

$$w = ua \left( \frac{f_0' (B_{11})_0}{f_0 \sqrt{b_1 b_1'}} \right) \left( \frac{\Omega_1 l_1}{r_L} \right). \quad (58)$$

Note that in the nondegenerate parametric amplifier case it is important to keep  $\sqrt{x_1 x_1'}$  (or  $f_0/f_0' \sqrt{b_1 b_1'}$ ) as small as possible if the bandwidth is to be maximized.

## IX. NONDEGENERATE PARAMETRIC AMPLIFIER EXAMPLES

A normalized design example was worked out on the basis of the circuit in Fig. 16. To facilitate comparison with the degenerate amplifier Design No. 2 (where  $x_1 = (X_{11})_0 = 3.70$ ), in this case  $(X_{11})_0$  was also chosen as 3.70. Taking  $f_0 = 500$  Mc and  $f_0' = 2500$  Mc we have  $f_0'/f_0 = 5$ . For simplicity it was assumed that the diode's internal inductance  $L_d$  causes the diode to be self-resonant at 2500 Mc. This, then, calls for  $(X_L)_0 = 3.70 / (5)^2 = 0.148$ , where  $(X_L)_0$  is the reactance of  $L_d$  at frequency  $f_0$ . Since the diode is self-resonant at frequency  $f_0'$ , the series line in Fig. 16 is chosen to be  $\lambda/2$  long at frequency  $f_0'$ , so as to also be resonant. This gives  $f_R/f_0 = 2.5$ , where  $f_R$  was defined in Fig. 17. (Note that here we have taken  $f_{01} = f_0$  and  $f_{01}' = f_0'$ .) Then to bring the diode to resonance at frequency  $f_0$  it is required that the series line have a normalized characteristic impedance of  $Z_0 = 4.90$ . Having thus defined the series reactance branch in Fig. 16, the resonator slope parameters  $x_1$  and  $x_1'$  were computed to be 4.27 and 8.42, respectively, by use of (b) in Fig. 7. Note that these values are considerably larger than the values  $x_1 = (X_{11})_0 = 3.70$  and  $x_1' = (X_{22})_0 = 0.740$  which they could assume if it were possible to resonate the diode at the two frequencies  $f_0$  and  $f_0'$  independently.

The diodes for Designs Nos. 1, 2, and 3 were taken to have  $a = C_1/C_0 = 0.25$ , with  $Q_d = 60$  for  $f_0 = 1000$  Mc. In this case  $a = 0.25$  was used with  $Q_d = 120$ , corresponding to an identical diode operated with  $f_0 = 500$  Mc. The lumped-element prototype values used were the values  $r_0 = 1$ ,  $l_1 = 0.592$ ,  $c_2 = 0.376$ ,  $r_L = 1.1008$ , and  $\Omega_1 = 1$  discussed in Section VII. Using Fig. 18(b) and (57), the signal filter fractional bandwidth for 15-db gain was found to be  $w = 0.091$ . By (b) of Fig. 7

$$R_{b0} = wx_1 \left( \frac{r_L}{\Omega_1 l_1} \right) \quad (59)$$

was obtained for the computation of  $R_{b0}$ , and  $R_{b0}'$  was computed by use of (44). Slope parameters  $b_2$  and  $b_2'$  were obtained by (e) in Fig. 7,<sup>16</sup> and the entire design is tabulated in Table I under Design No. 6.

<sup>16</sup> Note that  $w'$  from (42) and  $R_{b0}'$  must be used in computing  $b_2'$ .

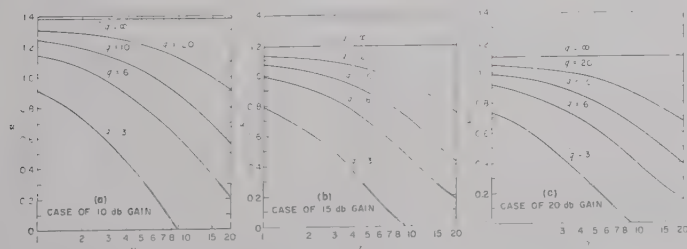


Fig. 18—Charts for determining the filter bandwidths of nondegenerate parametric amplifiers. [The definition and use of quantities  $u$ ,  $\gamma$ , and  $q$  will be found in (49) to (58) and the accompanying discussion.]

TABLE I

NORMALIZED DESIGN PARAMETERS FOR DESIGNS NOS. 6, 7, AND 8  
(Nondegenerate Parametric Amplifiers of Form in Fig. 16)

Design No. 6	
Frequencies:	
$f_o'/f_o = 5$ ,	$f_p/f_o = 6$
For Diode:	
$(X_{11})_0 = 3.700$ ,	$a = C_1/C_0 = 0.25$
$(X_L)_0 = 0.1480$ ,	$Q_d = 120$
For Series Transmission Line:	
$Z_0 = 4.889$ ,	$f_R/f_o = 2.5$
Resonator Slope Parameters and Other Filter Parameters:	
$x_1 = 4.271$ ,	$b_2 = 6.282$
$x_1' = 8.420$ ,	$b_2' = 79.66$
$f_{01}/f_o = 1$ ,	$f_{02}/f_o = 1$
$f_{01}'/f_o = 5$ ,	$f_{02}'/f_o = 5$
(where $f_{01}$ , $f_{02}$ , $f_{01}'$ and $f_{02}'$ are the resonant frequencies of resonators $X_1$ , $B_2$ , $X_1'$ , and $B_2'$ , respectively)	
$R_{b0} = R_L = 0.7233$ ,	$R_{b0}' = R_L' = 0.2852$
Design No. 7	
Same as Design No. 6 except that:	
$f_{02}/f_o = 0.9970$ ,	$f_{02}'/f_o = 5.0006$
$f_p/f_o = 5.9976$	
Design No. 8	
Same as Design No. 6 except that:	
$b_2 = b_2' = 0$	
to give single-resonator filters.	

The dashed line in Fig. 19 shows the response of Design No. 6 as computed with a digital computer by methods based on (13). Its midband gain is nearly 15 db, as expected, while its 3-db bandwidth is about 9 per cent. This is somewhat less than anticipated since, as mentioned in Section VII,  $\Omega_1$  for the prototype was derived from the equal-ripple band edge for Design No. 2. Thus an equal-ripple bandwidth of about 9 per cent was at first expected. The difference between the anticipated and computed results is probably related to the fact that Design No. 2 was operating with about 12.5 midband gain with respect to the signal frequency, while this design is operating with 15-db gain midband gain with respect to the signal frequency. This corresponds to the  $\sqrt{X_{12}X_{21}}$  line in Fig. 11 crossing the  $R_b$  curve at a higher level in this latter case, which would tend to narrow the bandwidth.

Due to the relatively large slope of  $\sqrt{X_{12}X_{21}}$  vs frequency for nondegenerate amplifiers, the response for Design No. 6 tilts down towards higher frequencies. Design No. 7 listed in Table I has the No. 2 resonators of the filters detuned slightly to compensate for this. The results are as indicated by the heavy solid curve in Fig. 19. Design No. 8 has the slope parameters  $b_2$  and  $b_2'$  set to zero to give a design with single resonators.<sup>17</sup>

<sup>17</sup> Of course for a practical circuit with single resonators some means would have to be provided to short out  $R_L'$  at signal frequencies  $f$ , and  $R_L$  at idler frequencies  $f'$ .

As with the degenerate amplifier case in Fig. 12, use of two-resonator filters gives slightly over three times the bandwidth which would result if single resonator filters were used. Observe that the fractional bandwidth achieved with the degenerate amplifier is twice that achieved with the nondegenerate amplifier, mostly as a result of the relatively large values of  $x_1$  and  $x_1'$  in the latter case.

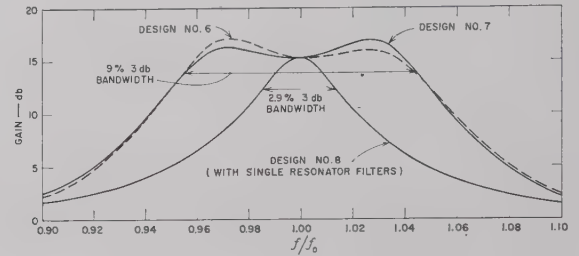


Fig. 19—Computed responses of some trial nondegenerate parametric amplifier designs of the form in Fig. 16 using the parameters listed in Table I.

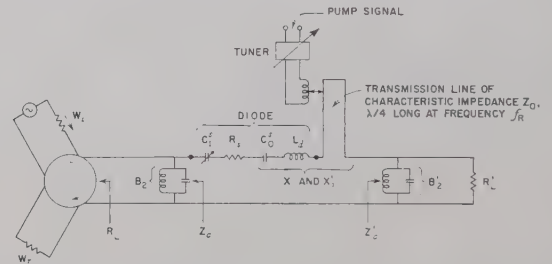


Fig. 20—Up-converter circuit having three input resonators and three upper-sideband resonators.

## X. THEORY OF WIDE-BAND UP-CONVERTERS

Fig. 20 shows an up-converter circuit using circuitry similar to that in Fig. 16. In this case the lower-sideband frequency ( $f_p - f$ ) is suppressed and the primed resonators comprise a filter which passes upper-sideband frequencies  $f'$ , where in this case  $f'$  is defined as

$$f' = f_p + f. \quad (60)$$

The circuit can again be analyzed in the form in Fig. 4 (the circulators, of course, are not needed since the output and input are at separate ports). In this case, however, it can easily be shown from Rowe's work<sup>2</sup> [in a manner similar to the derivation of (9) and (10)] that if  $f'$  is defined by (60) then

$$Z_2 = \frac{X_{12}X_{21}}{Z_a'} \quad (61)$$

and

$$Z_2' = \frac{X_{12}X_{21}}{Z_a} \quad (62)$$

apply instead of (9) and (10). According to the Manley Rowe equations,<sup>2</sup> (14) becomes for this case



$$\frac{W_2'}{W_2} = -\frac{f'}{f} \quad \text{or} \quad \frac{-W_2'}{W_2} = \frac{f'}{f}, \quad (63)$$

which implies that whatever power enters the left side of the  $X_{12}X_{21}$  box in Fig. 4 will be emitted from the right side of the box amplified by the ratio  $f'/f$ . In a manner paralleling (12) to (16), we obtain for this case

$$\frac{W_r}{W_i} = \left| \frac{(Z_b - R_s) - \left( \frac{X_{12}X_{21}}{Z_a'} \right)^*}{(Z_b + R_s) + \left( \frac{X_{12}X_{21}}{Z_a'} \right)} \right|^2 \quad (64)$$

and

$$\frac{W_L'}{W_i} = \left( 1 - \frac{W_r}{W_i} \right) \frac{\text{Re } Z_2}{R_s + \text{Re } Z_2} \left( \frac{f'}{f} \right) \frac{\text{Re } Z_b'}{R_s' + \text{Re } Z_b'}. \quad (65)$$

It can be shown that at midband the gain becomes

$$\begin{aligned} \left( \frac{W_L'}{W_i} \right)_0 &= \left( \frac{f_0'}{f_0} \right) \frac{4R_{b0}R_{b0'}(X_{12}X_{21})_0}{[(R_{b0} + R_s)(R_{b0'} + R_s') + (X_{12}X_{21})_0]^2} \quad (66) \end{aligned}$$

where, as before, the subzeros are used to indicate that the various quantities are to be evaluated at frequencies  $f_0$  or  $f_0'$  as is appropriate. Corresponding equations for the case where the diode is resonated in shunt are easily obtained by duality.

Eqs. (61) and (62) indicate that when  $f'$  is the upper-sideband frequency given by (60), then the  $X_{12}X_{21}$  box in Fig. 4 simply operates as an impedance inverter,<sup>18</sup> and no negative resistance is involved. Some thought on the matter will show that the response for a circuit like that in Fig. 20 which has three input resonators and three upper-sideband resonators will give a six-resonator filter response. Because of this property, it is advantageous to design the three resonators of the input filter in Fig. 20 as though they were the first three resonators of a six-resonator filter, and likewise for the three resonators of the upper-sideband filter.

To understand the basis for the procedure suggested above, consider the low-pass prototype with six reactive elements shown in Fig. 21(a). The ordinary Tchebycheff or maximally-flat prototypes of this sort having an even number of elements and one or more frequencies of perfect transmission are antimetric—i.e., half the network is the dual of the other half. Because of this property such networks can always be put into the form shown in Fig. 21(b). The box marked  $K$  is an idealized impedance inverter which operates at all frequencies like a quarter-wavelength line of characteristic im-

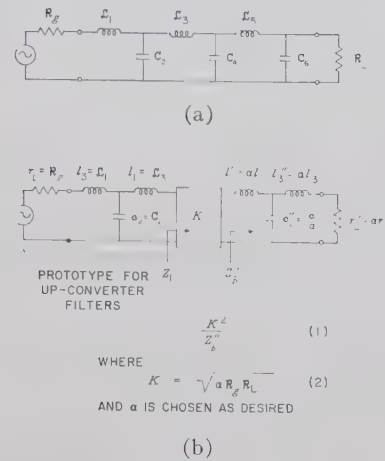


Fig. 21—Manner in which a three-reactive-element low-pass prototype for design of three input and three upper-sideband resonators of an up-converter is obtained from a six-reactive-element antimetric prototype.

pedance  $K$ . Thus, (1) in Fig. 21 applies at all frequencies, where the size of  $K$  is specified by (2) in the figure. Note that the parameter  $\alpha$  is available to adjust the impedance level of the right half of the network, and if  $\alpha$  is chosen equal to one, the network in Fig. 21(b) will be symmetrical. In order to correspond to the resonator notation used in the preceding amplifier examples, we redesignate the elements on the left half of the modified circuit  $l_1, c_2, l_3$ , as shown in Fig. 21(b). The circuit on the left of Fig. 21(b) is then used as the prototype for both the input and the upper-sideband filter circuits.

It will be found that the approach described above can yield a much larger value of  $l_1$  for the prototype than would be obtained if  $l_1$  were taken as the end element of a complete, three-reactive-element prototype.<sup>19</sup> As in the preceding examples a larger value of  $l_1$  will mean a larger bandwidth for the corresponding band-pass filters for the amplifier. Unfortunately, this same procedure will not work when  $f'$  is given by (4). In that case the imaginary part of  $Z_2$  in Fig. 4 tends to have the same sign as the imaginary part of  $Z_b$ , while for this design procedure to work, the signs of the imaginary parts should be opposite so as to cause reactance cancellation. This happens when (60) and (61) apply.<sup>20</sup>

Ignoring  $R_s'$  in Fig. 4 and using (61) we obtain for  $f=f_0$

$$(Z_2)_0 = \frac{(X_{12}X_{21})_0}{R_{b0}'} \quad (67)$$

<sup>19</sup> Examination of tables of prototype filter element values<sup>8-10</sup> shows that this statement holds for prototype filters having two times an odd number (but not two times an even number) of reactive elements.

<sup>20</sup> To verify these statements it is important to note that when (4) and (9) apply, if  $f < f_0$ , then  $f' > f_0'$  and in Fig. 4  $\arg Z_b \approx -\arg Z_b'$ . When (60) applies, if  $f < f_0$ , then  $f < f_0'$  and  $\arg Z_b \approx \arg Z_b'$ . These facts along with (9) and (61) lead to the conclusions above.

<sup>18</sup> S. B. Cohn, "Direct-coupled-resonator filters," PROC. IRE, vol. 45, pp. 187-196; February, 1957.

where  $R_{b0}'$  is, as before,  $Z_{b0}'$  evaluated at  $f_0'$ . Now  $(Z_2)_0$  should equal  $\mathcal{R}_L$  shown in Fig. 21(a) scaled to the impedance level of  $R_{b0}$ . Thus

$$(Z_2)_0 = \frac{R_{b0} \mathcal{R}_L}{\mathcal{R}_g} \quad (68)$$

Equating (67) and (68), and introducing the equal-bandwidth constraint given by (43), we obtain

$$R_{b0} = \sqrt{\frac{(\bar{X}_{12}\bar{X}_{21})_0}{\frac{\mathcal{R}_L}{\mathcal{R}_g} \left(\frac{f_0}{f_0'}\right) \left(\frac{x_1'}{x_1}\right)}} \quad (69a)$$

$$= a(X_{11})_0 \sqrt{\left(\frac{\mathcal{R}_g}{\mathcal{R}_L}\right) \left(\frac{x_1}{x_1'}\right)} \quad (69b)$$

and

$$R_{b0}' = R_{b0} \left(\frac{f_0}{f_0'}\right) \left(\frac{x_1'}{x_1}\right), \quad (70)$$

which establish the impedance levels of the input and upper-sideband filters. Then by (b) in Fig. 7 the fractional bandwidth of the input filter is

$$w = \frac{R_{b0}}{x_1} \left(\frac{\Omega_1 l_1}{r_L}\right) \quad (71a)$$

$$= \frac{a(X_{11})_0}{\sqrt{x_1 x_1'}} \sqrt{\frac{\mathcal{R}_g}{\mathcal{R}_L}} \left(\frac{\Omega_1 l_1}{r_L}\right), \quad (71b)$$

and by (42) the fractional bandwidth of the output filter is

$$w' = \frac{w f_0}{f_0'}. \quad (72)$$

The design procedure may then be summarized as follows. First the  $f_0$  and  $f_0'$  values must be selected to give adequate gain. In this case the idealized power gain ratio for any input frequency  $f$  and output frequency  $f'$  is given simply by  $f'/f$ ; however, in a practical situation the actual gain will be less as a result of diode loss (and losses in the filters). An estimate of the actual midband gain can be obtained using the equation<sup>5</sup>

$$\left(\frac{W_L}{W_i}\right)_0 = \left(\frac{f_0'}{f_0}\right) \frac{1}{(u + \sqrt{1 + u^2})^2} \quad (73)$$

where

$$u = \frac{R_s}{\sqrt{(X_{12}X_{21})_0}} = \frac{1}{aQ_d} \sqrt{\frac{f_0'}{f_0}}. \quad (74)$$

Eqs. (73) and (74) give the maximum midband power gain possible for a given  $f_0'/f_0$  and diode operating  $Q$ . As a result of the introduction of bandwidth considerations into the design process, the actual gain for an amplifier of maximum bandwidth will be a little less.

Having selected values for  $f_0$  and  $f_0'$  which will yield adequate gain, the diode resonator circuit giving resonators  $X_1$  and  $X_1'$  should be designed first so that resonator slope parameters  $x_1$  and  $x_1'$  can be computed from the derivative expression in (b) of Fig. 7 evaluated at  $\omega_0 = 2\pi f_0$  and  $\omega_0' = 2\pi f_0'$ , respectively. Then obtaining  $\mathcal{R}_g$  and  $\mathcal{R}_L$  from the unmodified form of the low-pass prototype shown in Fig. 21(a) and having values for  $X_{12}X_{21}$  and  $f_0'/f_0$ ,  $R_{b0}$  and  $R_{b0}'$  are computed by (69b) and (70). Then knowing  $\Omega_1$ ,  $r_L$ , and  $l_1$  for the modified prototype shown in Fig. 21(b),  $w$  and  $w'$  can be computed by use of (71a) and (72). Having values for  $R_{b0}$ ,  $w$ ,  $R_{b0}'$ , and  $w'$ , the remaining resonator slope parameters for the input and upper-sideband filters are computed by use of (b) and (e) in Fig. 7, using the element values of the modified prototype filter shown in Fig. 21(b). The midband gain including diode loss can then be checked by use of (22), (23), and (66).

If the diode is resonated in shunt the procedure is essentially the same on the dual basis. The corresponding equations are

$$G_{b0} = a(B_{11})_0 \frac{f_0'}{f_0} \sqrt{\frac{\mathcal{R}_g}{\mathcal{R}_L} \frac{b_1}{b_1'}} \quad (75)$$

$$G_{b0}' = G_{b0} \frac{f_0}{f_0'} \frac{b_1'}{b_1} \quad (76)$$

$$w = \frac{a(B_{11})_0}{\sqrt{b_1 b_1'}} \frac{f_0'}{f_0} \sqrt{\frac{\mathcal{R}_g}{\mathcal{R}_L}} \left(\frac{\Omega_1 l_1}{r_L}\right). \quad (77)$$

Eq. (72) applies as before, and the prototype is still defined as in Fig. 21. The extra  $f_0'/f_0$  factor appearing in (75) and (77) but not in (69b) and (71b) occurs as a result of the fact that  $(X_{12}X_{21})_0 = a^2(X_{11})_0^2(f_0/f_0')$  while  $(B_{12}B_{21})_0 = a^2(B_{11})_0^2(f_0'/f_0)$ .

## XI. EXAMPLES OF WIDE-BAND UP-CONVERTERS

A trial up-converter design was worked out assuming that  $f_0 = 500$  Mc,  $f_0' = 7600$  Mc, and that the normalized diode parameters are as indicated in Table II. As before,  $(X_L)_0$  is the reactance of the parasitic inductance  $L_d$  in Fig. 20 at frequency  $f_0$ . Using the series transmission line parameters shown in the table, the diode is brought to resonance at  $f_0$  with a slope parameter of  $x_1 = 4.260$  and at frequency  $f_0'$  with a slope parameter of  $x_1' = 24.670$ . The filters were then designed from a six reactive element, 0.5-db Tchebycheff ripple, lumped-element prototype of the form shown in Fig. 21(a)<sup>8-10</sup> having the element values  $\mathcal{R}_g = 1.0000$ ,  $\mathcal{L}_1 = 1.7254$ ,  $C_2 = 1.2479$ ,  $\mathcal{L}_3 = 2.6064$ ,  $C_4 = 1.3137$ ,  $\mathcal{L}_5 = 2.4758$ ,  $C_6 = 0.8696$ ,  $\mathcal{R}_L = 1.9840$ , and the cutoff frequency  $\Omega_1 = 1$ . The element values for the converted form in Fig. 21(b) are  $l_1 = 2.6064$ ,  $c_2 = 1.2479$ ,  $l_3 = 1.7254$ , and  $r_L = 1.000$ . Carrying out the design as described in the preceding



TABLE II

NORMALIZED DESIGN PARAMETERS FOR DESIGNS NO. 9, 10, 11, AND 12  
(Up-Converters of the Form in Fig. 20)

Design No. 9		
Frequencies:		
$f_0'/f_0 = 15.2125,$	$f_p/f_0 = 14.2125$	
For Diode:		
$(X_{11})_0 = 3.700,$	$a = C_1/C_0 = 0.25$	
$(X_L)_0 = 0.03700,$	$Q_d = 1/(\ 2\pi f_0 C_0 R_s) = 120$	
For Series Transmission Line:		
$Z_0 = 5.180,$	$f_R/f_0 = 2.5521$	
Resonator Slope Parameters and Other Filter Parameters:		
$x_1 = 4.260,$	$b_2 = 27.421,$	$x_3 = 2.820$
$x_1' = 24.670,$	$b_2' = 1095.6,$	$x_3' = 16.333$
All unprimed resonators resonate at $f_0$ and all primed resonators resonate at $f_0'$		
$R_{b0} = R_L = 0.2727, \quad R_{b0}' = R_L' = 0.1038$		
(The three-resonator input and output filter designs were derived from a six-reactive-element low-pass prototype with 0.5 db Tchebycheff ripple.)		
Design No. 10		
Same as Design No. 9 except that:		
$b_2 = x_3 = b_2' = x_3' = 0$		
$R_{b0} = R_L = 0.2355, \quad R_{b0}' = R_L' = 0.08968$		
(The designs for the single-resonator input and output filters were derived from a two-reactive-element low-pass prototype with 1.0-db Tchebycheff ripple.)		
Design No. 11		
Same as Design No. 9 except that:		
$b_2 = x_3 = b_2' = x_3' = 0$		
$R_{b0} = R_L = 0.3877, \quad R_{b0}' = R_L' = 0.1478$		
(The designs of the single-resonator input and output filters were worked out to give maximum gain at midband under the constraint that the input and output filters have the same bandwidth.)		
Design No. 12		
Same as Design No. 9 except that:		
$b_2 = x_3 = b_2' = x_3' = 0$		
$R_{b0} = R_L = R_{b0}' = R_L' = 0.2392$		
(The designs of the single-resonator input and output filters were worked out in this case to give maximum mid-band gain regardless of bandwidth considerations.)		

section, impedance levels and slope parameters as indicated for Design No. 9 in Table II are obtained. The fractional bandwidths of the input and upper-sideband filters are  $w = 0.1669$  and  $w' = 0.01097$ .

The response of an amplifier of the form in Fig. 20 with the circuit parameters as indicated for Design No. 9 in Table II was computed using a digital computer and (64) and (65). The results are shown by the curve marked Design No. 9 in Fig. 22. With  $f_0'/f_0 = 15.2$  the theoretical midband gain of a lossless amplifier would be 11.8 db. As is seen from the figure, the actual midband gain including the diode loss is about 10.2 db. If the diode had been lossless, a 0.5-db ripple, Tchebycheff response with six peaks and an equal-ripple bandwidth of 16.7 per cent would be expected. However, as a result of diode loss the band edges are rounded and the equal-

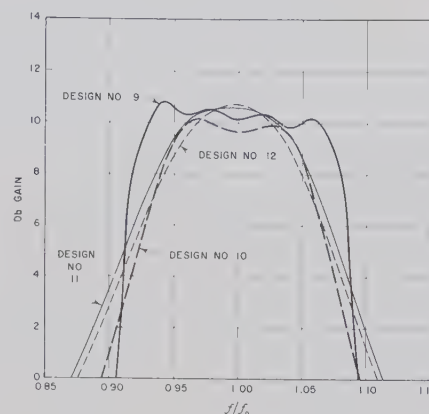


Fig. 22—The responses of some trial up-converter designs determined with a digital converter.

ripple bandwidth is narrowed to about 14 per cent, though the 3-db bandwidth is still somewhat over 16 per cent.

The curve marked Design No. 10 in Fig. 22 was computed using the corresponding parameters indicated in Table II. This design is for an analogous amplifier with a single input resonator and a single upper-sideband resonator with the design worked out from a two-reactive-element, 1.0-db ripple, Tchebycheff low-pass prototype. In this case a lossless amplifier should give an equal-ripple bandwidth of 10 per cent. As in the preceding example, the diode loss narrows the equal-ripple bandwidth and reduces the height of the ripples.

Design No. 11 in Table II and Fig. 22 was worked out so as to give maximum midband gain using single-resonator input and upper-sideband filters whose design was constrained by (43) so as to give equal input and upper-sideband filter bandwidths. Design No. 12 in Table II and Fig. 22 was worked out to give maximum midband gain regardless of any bandwidth considerations while using single-resonator input and upper-sideband filters.<sup>5</sup>

## XII. NOISE FIGURE

The noise figure of several of the trial designs was computed assuming that the only degradation of the noise figure from the ideal is due to thermal noise in the diode loss resistance. On this basis Design No. 2 in Figs. 10 and 12 has a noise figure of 3.3 db when  $f$  is near  $f_0$ , as compared with an ideal noise figure of 3.0 db (as measured by the signal generator method<sup>21</sup>). Design No. 6 in Figs. 16 and 19 has a computed noise figure of 1.1 db (as measured by either the signal generator or noise source methods<sup>21</sup>), while Design No. 9 in Figs. 20 and 22 has a computed noise figure of 0.97 db. From these examples it is evident that design for maximum bandwidth (for given gain, etc.) is quite compatible with good noise figures.

<sup>21</sup> S. B. Cohn, "The noise figure muddle," *The Microwave J.*, vol. 2, pp. 7-11; March, 1959.

## XIII. CONCLUSIONS

The use of lumped-element, low-pass prototype filters in the design of the band-pass filters for parametric amplifiers and up-converters is found to simplify the problem greatly. This is because once the lumped-element, low-pass prototype is specified, only the fractional bandwidths and impedance levels of the band-pass filters remain to be specified. Reducing the problem to this number of degrees of freedom is seen to make the design problem quite tractable. In the case of up-converters, ordinary lumped-element Tchebycheff or maximally-flat prototypes are found to be quite appropriate, but in the case of parametric amplifiers with the negative-resistance type of operation, such prototypes should be modified as indicated in Sections VI and VII in order to prevent high peaks of gain at the band edges. The two-reactive-element prototype given in the last paragraph of Section VII should be suitable for many cases where two-resonator filters are desired.

As can be seen from (37), (49) to (58), and (71b), the fractional bandwidths called for in the design of the band-pass filters of parametric amplifiers and up-converters are directly proportional to  $a = C_1/C_0$ . Further, it will be noted that in all of the equations in this paper the degradation of performance due to diode loss is always controlled by the parameter  $(aQ_d) = (C_1/C_0)Q_d$  rather than by  $Q_d$  alone. [In the case of up-converters see (74).] Thus the size of  $C_1/C_0$  is of vital importance in determining the bandwidth capabilities of a parametric amplifier or up-converter. At present little information is available as to the largest practical values that  $C_1/C_0$  can take without overdriving the diode so

as to degrade the noise figure. The value  $a = C_1/C_0 = 0.25$  used in the examples of this paper is probably practical, though perhaps on the optimistic side.

In the case of degenerate parametric amplifiers the fractional bandwidth of the band-pass filter is *inversely* proportional to the resonator slope parameter  $x_1$  (or  $b_1$  for the diode resonated in shunt). For nondegenerate amplifiers and up-converters the fractional bandwidth  $w$  is inversely proportional to  $\sqrt{x_1 x_1'}$  (or  $\sqrt{b_1 b_1'}$  for the shunt resonance case). Thus it is of great importance to design the diode resonator circuit so as to minimize the reactance (or susceptance) slope at  $f_0$  and  $f_0'$ . Stub tuners and the like must be avoided since they introduce unnecessary resonances and, as a result, large reactance slopes. If the diode resonator is a series resonator, it is desirable that it be followed immediately by a shunt resonator (or vice versa if the diode resonator is a shunt resonator). If the diode resonator and the next resonator of the filter are separated by a connecting line, part of the selectivity of the connecting line must be charged to the diode resonator, thus increasing the effective size of the diode resonator slope parameter and reducing the bandwidth which can be used in the filter.

In summary, the bandwidths which can be achieved in engineering practice will be influenced very much by the usable  $C_1/C_0$  ratio of available diodes, and by the degree to which the slope parameters of the diode resonators can be minimized using practical circuitry. Though the examples presented herein involve a guess as to what  $C_1/C_0$  should be and are idealized in some respects, they should be strongly suggestive of the performance that can be expected.

## CORRECTION

G. R. Valenzuela, author of "Impedances of an Elliptic Waveguide (For the  $H_1$  Mode)," which appeared on pp. 431-435 of the July, 1960, issue of these TRANSACTIONS, has brought the following to the attention of the Editor.

On page 433, read:

into  $H_z$ , and then integrating, it can be easily shown that

$$V = i\omega\mu \int_0^{u_0} \int_{-\pi/2}^{\pi/2} H_z(u, v) ds_1 ds_2 = 2 \int_0^{u_0} E_u \left( u, \frac{\pi}{2} \right) ds_1.$$

Also on page 433, pertaining to (4), read:

Now the impedances can be easily obtained. Let

$$Z_0 = 120\pi \left( \frac{\lambda g}{\lambda} \right) \quad \text{and} \quad h = q(k^2 - \beta^2)^{1/2},$$

then

$$Z_{WV} = \frac{h^4 I_1^2}{I_2} Z_0$$

and

$$Z_{WI} = \frac{I_2}{4J_{c1}^2(u_0)} Z_0. \quad (4)$$

On page 435, for (8) read:

The expression for the approximate impedances are

$$\begin{aligned} Z_{WV} &= \frac{32}{3\pi} \frac{r(3+r^2)}{(5+2r^2)} Z_0 \\ Z_{WI} &= \frac{3\pi}{32} \frac{r(15+11r^2+2r^4)}{(2+r^2)^2} Z_0. \end{aligned} \quad (8)$$



# A Low-Noise X-Band Parametric Amplifier Using a Silicon Mesa Diode\*

R. D. WEGLEIN†, SENIOR MEMBER, IRE, AND F. KEYWELL‡

**Summary**—This paper summarizes a cooperative effort to develop silicon mesa variable-capacitance diodes and to evaluate their potential for achieving low-noise amplification in the high microwave frequency range. Cutoff frequencies of about 70 kMc at zero-bias voltage (corresponding to 140 kMc at maximum reverse bias voltage) with a total permissible voltage swing in excess of 5 volts have been obtained.

A versatile degenerate X-band parametric amplifier was developed which, when used in conjunction with these silicon mesa diodes, achieved a radiometer noise temperature of 130°K at 8.5 kMc with a 50-Mc bandwidth at 17-db gain. The measured performance of the diode (figure of merit) is compared with the first-order theory in an operating radar system. The over-all performance of the amplifier improved the observed system sensitivity by 6 db.

IN this section, we present a first-order design theory which suggests that practical silicon-mesa-diode cutoff frequencies measured at zero bias have a theoretical upper limit well in excess of 200 kMc. In the laboratory, approximately 30 per cent of this theoretical value has been achieved; however, it is important to note that the measured value of the cutoff frequency has been remarkably substantiated by the measurement of noise temperature at X band.

The objective is to derive an expression for the cutoff frequency at zero bias from the definition

$$f_c(0) = \frac{1}{2\pi R_s C(0)} \quad (1)$$

in terms of pertinent parameters: parent material resistivity  $\rho$ , diameter of the mesa  $d$ , and the diffusion length in forming the junction  $L$ . The total series resistance of the mesa is approximately the sum of the axial length of the mesa  $l$  and the constriction resistance at the base of the mesa. In terms of volume resistivity  $\rho$ , this is given by

$$R_s \simeq \frac{\rho}{d} \left( \frac{1}{2} + 1.27 \frac{l}{d} \right) \text{ ohms.} \quad (2)$$

Since in practice the  $l/d$  ratio is of the order unity, (2) is approximately given by

$$R_s \simeq 0.70 \frac{\rho}{d} \text{ ohms,} \quad (3)$$

where  $\rho$  is in units of  $10^{-3}$  ohm-cm and  $d$  is in units of  $10^{-3}$  inches. The capacitance per unit area of a linearly graded junction in silicon is found from Shockley's expression<sup>1</sup> in terms of practical units:

$$C(0) = 2.53 \times 10^{-3} a^{1/3} V_0^{1/3} \mu\text{mf}, \quad (4)$$

where  $V_0$  is the total voltage across the junction and the concentration gradient  $a$  at the junction is given by

$$a = \frac{N_s}{\sqrt{\pi} L} \exp \left( -\frac{x_j^2}{4L^2} \right), \quad (5)$$

where  $N_s$  is the constant surface concentration,  $L$  is the diffusion length, and  $x_j$  is the junction depth. Substituting (5) into (4) yields for the capacitance

$$C(0) = 1.75 d^2 L^{-1/3} \mu\text{mf} \quad (6)$$

where

$$N_s = 4 \times 10^{20} \text{ cm}^{-3}$$

$$V_0 = 0.6 \text{ volt}$$

and

$$L \text{ is in units of microns}$$

has been assumed for the silicon parent material. We may now express the zero-bias cutoff frequency (1) in terms of the design parameters:

$$f_c \simeq 131 \frac{L^{1/3}}{\rho d} \text{ kMc} \quad (7)$$

Inspection of (7) shows that the cutoff frequency is increased by starting with the lowest resistivity silicon feasible from the standpoint of crystal growth and yet consistent with the ability to overcompensate the parent material by diffusion to form a  $p$ - $n$  junction. The mesa structure should be reduced to the minimum diameter to achieve reasonable admittance levels for high microwave frequency applications, but it cannot be reduced without limit because of practical considerations, some of the more important of which are strength and contact resistance. Because of the cube-root dependence, the diffusion length is not critical. Since, in practice, an etched mesa has a conical shape, deeper diffusion causes a greater increase in capacitance than can be offset by an

\* Received by the PGMTT, July 15, 1960; revised manuscript received, September 19, 1960.

† Res. Labs., Hughes Aircraft Co., Malibu, Calif.

‡ Semiconductor Devices, Inc., Newport Beach, Calif. Formerly with Semiconductor Div., Hughes Aircraft Co., Newport Beach, Calif.

<sup>1</sup> W. Shockley, "The theory of  $p$ - $n$  junctions in semiconductors and  $p$ - $n$  junction transistors," *Bell Syst. Tech. J.*, vol. 28, pp. 435-489; July, 1949.

increase in diffusion length. For these reasons, we have found it practical to form a mesa of  $8 \times 10^{-4}$  inches in diameter in  $10^{-3}$  ohm-cm silicon parent material with a diffusion length of about 3 microns. This resistivity and diffusion length are also in keeping with the minimum reverse breakdown voltage, as can be seen from Fig. 1. Eq. (7), which incidentally shows a dependence of the cutoff frequency on the mesa diameter not heretofore appreciated, is plotted for these parameters as a function of the concentration gradient, or diffusion length. Although this curve shows continued improvement in cutoff frequency at high diffusion lengths, the above practical considerations tend to establish a maximum value for this type of geometry not too far from the 3-micron value, which is the diffusion length of our choice. Four measured points are shown in Fig. 1. The dot represents a low-frequency estimate of the cutoff frequency at zero bias which we obtained by using the capacitance measured at 100 kc and the resistance corresponding to the slope of the I-V diode characteristic at large forward currents. The crosses denote measured cutoff frequencies at 9 kMc for three different diodes. In practice, a cutoff frequency of about 30 per cent of the predicted value or about 70 kMc (as measured by standard techniques described in the recent literature) has been obtained. It is not at all surprising that the obtained cutoff frequency is considerably less than the predicted one, when it is recognized that the calculations of the cutoff frequency apply strictly to a low-frequency model and

do not account for losses which may be limiting factors at very high frequencies. These factors are presently under investigation. It is for this reason that accurate prediction of noise performance demands that the cut-off frequency be measured in the vicinity of the expected operating range. The change between the dc measurement and one conducted at 9.0 kMc is indicated in the figure, and it is this latter value that must be used to predict performance.

#### FIGURE OF MERIT AND PREDICTED PERFORMANCE

The cutoff frequency at zero bias and maximum voltage swing without the current flow in either direction through the diode are a measure of the figure of merit. This figure of merit is valid in predicting the noise performance of a parametric amplifier, if it can be shown that the noise sources are entirely resistive. The figure of merit which has been suggested<sup>2,3</sup> and previously used to predict the performance of parametric amplifiers at various microwave and UHF frequencies is given by

$$K = \left( \frac{\Delta C}{2\bar{C}} \right) \left( \frac{f_c}{f_s} \right), \quad (8)$$

where

$\Delta C$  is the capacitance swing at maximum voltage swing,

$\bar{C}$  is the mean capacitance,

$f_s$  is the operating frequency,

$f_c$  is the cutoff frequency at optimum bias voltage.

To evaluate the quality of a variable-capacitance diode in terms of this figure of merit, we have built a parametric amplifier at X band in which both signal and idler frequencies are supported in the same cavity. As will be described later, this type of amplifier can be made very flexible and is uniquely suited for this measurement. This figure of merit enters into performance as follows: The radiometer noise temperature<sup>4</sup> of such an amplifier is given by

$$T_{n2} = \frac{1}{\mu_{s2}} T_d, \quad (9)$$

where  $\mu_{s2} \leq K - 1$ ,  $T_d$  is the diode body temperature, and the equality holds for maximum available capaci-

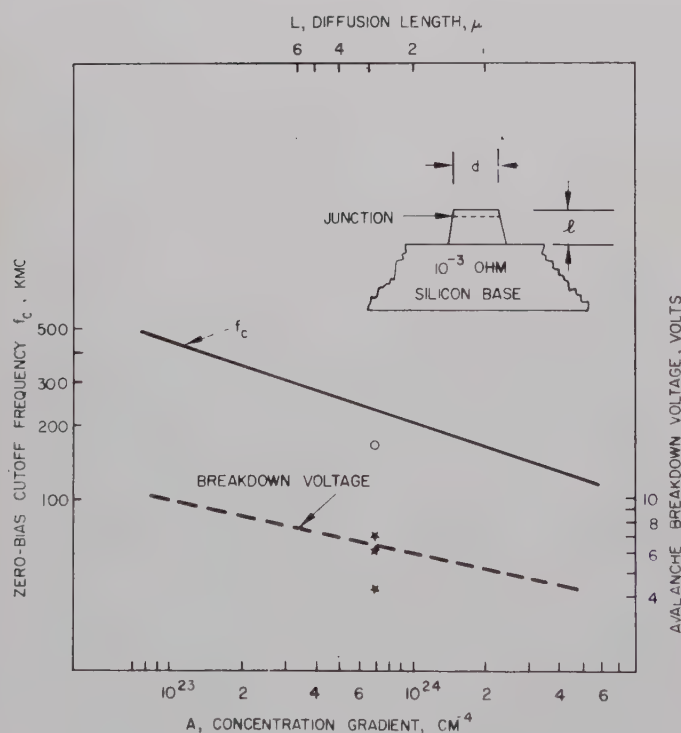


Fig. 1—Cutoff frequency of silicon mesa diode as a function of diffusion length  $L$  (microns) and concentration gradient  $A$  ( $\text{cm}^{-4}$ ) at the junction for  $\rho = 10^{-3}$  ohm-cm,  $N_0 = 4 \times 10^{20} \text{ cm}^{-3}$ , and  $V_0 = 0.6$  volt.

<sup>2</sup> R. C. Knechtli and R. D. Weglein, "A Lower Limit on the Noise Temperature of a Parametric Amplifier," presented at the 17th Conf. on Electron Tube Res., Mexico D. F., Mexico, June 24, 1959.

<sup>3</sup> R. C. Knechtli and R. D. Weglein, "Low noise parametric amplifier," PROC. IRE, vol. 48, pp. 1218-1226; July, 1960.

<sup>4</sup> Two kinds of noise temperatures are commonly referred to in connection with parametric amplifiers. When signal and idler frequencies are relatively near each other, as in this example, both frequency ports are approximately equally loaded by the source conductance, and we speak of a radiometer noise temperature, indicating that all available frequency ports are connected to the source. The alternative method of reception, where the signal source is connected to one frequency port, though others may receive and generate noise, is often characterized by the term, "radar noise temperature."



tance swing. The pump power required to maintain high gain and this noise temperature is given by

$$\frac{P_2}{(\omega_s \bar{C}) \left( \frac{\Delta C}{2C} \right) (\Delta V)^2} \geq \frac{1}{2K}, \quad (10)$$

where the equality applies to optimum conditions of matching and maximum utilization of the available capacitance swing. The pump power has been normalized to the design parameters, *viz.*, admittance level, normalized capacitance, and the maximum voltage swing.

The capacitance-voltage characteristic of a typical silicon mesa diode as measured at 100 kc is shown in Fig. 2; the package parasitic capacitance is also included. In Fig. 3, the dc characteristic of this diode shows the maximum voltage swing for less than 1  $\mu$ a current in either direction to be 5.5 volts. The normalized capacitance swing  $\Delta C/2\bar{C}$  corresponding to this voltage

swing was computed from Fig. 2,<sup>5</sup> and the cutoff frequency was measured at 9 kMc. The resulting figure of merit and the derived predicted performance are shown in Table I. These numbers represent the best anticipated behavior under the previously stated optimum conditions. The diode body temperature has been assumed to be the ambient (300°K) temperature.

TABLE I

DC bias voltage	2.5v
$\Delta C/2C$	0.26
$f_c$ (0 bias)	68 kMc
$f_c$ (operating bias)	108 kMc
Signal frequency	8.5 kMc
Figure of merit	3.1
Noise temperature	140° K
Pump power	75 Mw

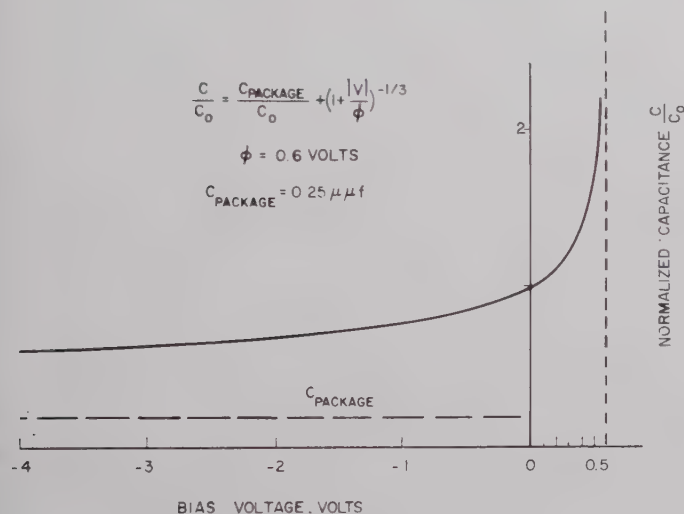


Fig. 2—Capacitance-voltage curve of X-band silicon mesa diode as measured at 100 kc.  $C_{\text{package}} = 0.25$  pf;  $\phi = 0.6$  volt is the built-in voltage.

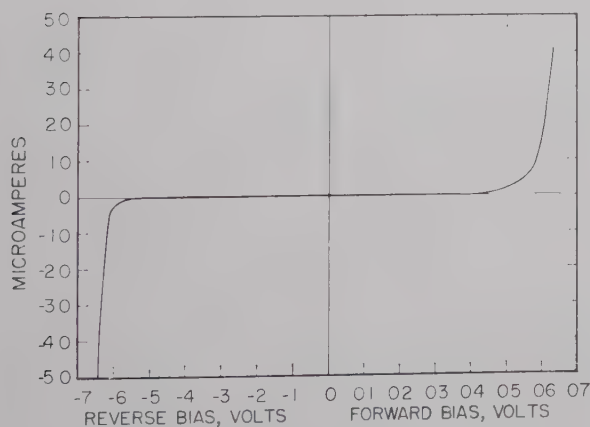


Fig. 3—Measured dc characteristic of silicon mesa diode used in experiment.

#### PHILOSOPHY OF AMPLIFIER CIRCUIT DESIGN

There is little doubt that in order to obtain low-noise broad-band performance from a parametric amplifier at a given frequency, not only is it necessary to use a diode with the best available  $Q$ , but also the circuit in which the diode is to be used must offer those complementary features which permit the achievement of the optimum performance. Thus, either the circuit design must take the exact parameters of the diode into account or, if these are not accurately known, sufficient flexibility must be built in to cope with the expected range of the variables. This last feature of flexibility is of particular importance in an amplifier circuit which is to perform at X band. Here, the diode has a self-resonant frequency, most likely below the signal frequency, and measures must be taken to raise this resonance to a more favorable place, if possible above the idler frequency. If this is not done and the cavity is relied upon to tune out the inductance at the signal frequency, not only is the noise performance likely to be impaired because of the added resonance losses but also the bandwidth will surely be curtailed. An additional consideration is the ratio of the diode mean capacitive susceptance to the cavity characteristic admittance. It can be shown that the susceptance variation through the amplification band is minimized when this ratio is of the order of unity. In many cases, it is not practical to fulfill this requirement. For example, in this amplifier the lowest practical characteristic impedance of the X-band cavity was about 100 ohms, while the diode reactance at the operative bias was approximately 30 ohms.

<sup>5</sup> S. Sensiper and R. Weglein, "Capacitance and charge coefficients for parametric diode devices," *PROC. IRE*, vol. 48, p. 1482; August, 1960.

The size of the signal and idler cavities is a final consideration in achieving a desired bandwidth. For maximum bandwidth, they should be as small as possible and should resonate in the fundamental mode to keep the reactance variation across the band at a minimum. To achieve the desired flexibility, we designed the diode holder to permit an arbitrary diode position in the signal and pump cavities and incorporated a coaxial tuner as an extra degree of freedom in order to manage the diode self-resonance. The actual circuit configuration which resulted from the incorporation of these features is shown in Fig. 4. While little mention has been made of circuit properties which yield a minimum noise performance, the above features, which ensure flexibility and bandwidth, also tend to ensure low-noise performance if the circuit losses are kept at a minimum. The built-in flexibility then permits sufficient overcoupling of the source or antenna conductance to minimize the contributions from diode losses without seriously restricting the bandwidth criteria.

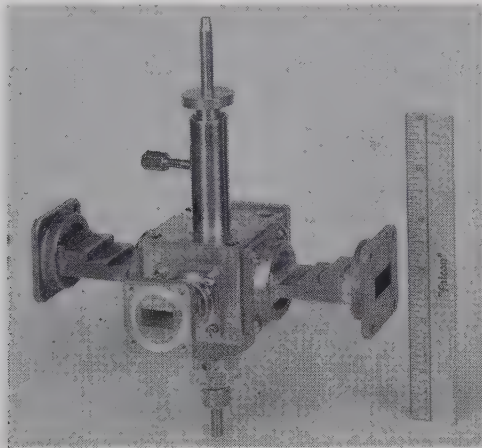


Fig. 4—Degenerate X-band amplifier showing transformers to standard waveguide sizes.

## RESULTS

The performance of this amplifier with a number of these diodes was measured by use of the arrangement illustrated in Fig. 5. Provisions were made for observing both bandwidth and noise performance at separate switch positions. Because of the pitfalls in measuring noise figures of negative resistance amplifiers, considerable precautions were taken to make the noise measurements as accurate as possible. All losses were carefully determined, and the noise figure of the balanced mixer following the parametric amplifier was measured. The quoted noise temperatures of the parametric amplifier were then referred to its input terminals. In Table II, the measured performance is compared with the predicted one; the numbers with an asterisk are the measured values in each case. The best performance was obtained with diode No. 2, which gave a radiometer noise temperature of 130°K and a gain-bandwidth product of

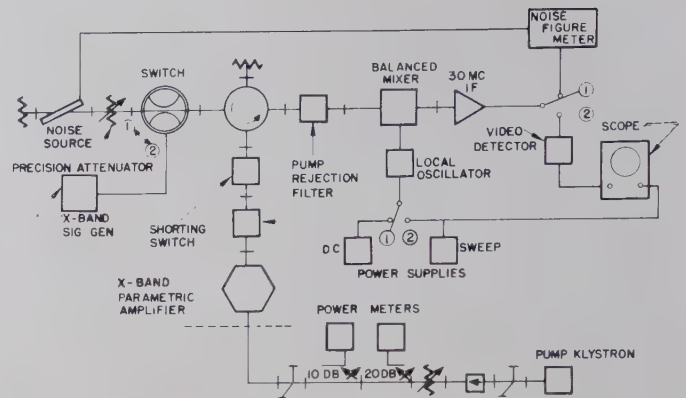


Fig. 5—Schematic of circuit arrangement to measure gain-bandwidth (position ②) and noise performance (position ① shown).

TABLE II

Diode No.	1		2		3	
Cutoff frequency $f_c$ kMc, 0-bias voltage	62		68		44	
Figure of merit K	2.8		3.1		1.2	
Noise temperature, °K	170	240*	140	130*	250	260*
Pump Power, Mw	80	150*	74	145*	100	180*
Gain, db	17		17		19	
Bandwidth, Mc	56		50		10	

350 Mc, *i.e.*, a bandwidth of 50 Mc at 17-db insertion gain.

The performance of the amplifier was checked for compatibility with existing radar systems. Before the parametric amplifier was included, the system noise figure was measured and found to be about 10 db. From the measured performance of the parametric amplifier, the increase in sensitivity of the over-all system was estimated to be between 5 db and 6 db. Fig. 6 shows an A-scope display, from which the actual improvement in sensitivity can be estimated. This presentation shows amplitude of the reflected signal vs range; the large amplitude at the left is the transmitted pulse. The top portion of the figure represents the receiver sensitivity prior to the inclusion of the parametric amplifier. For the same background noise level, it is seen that in the bottom picture, where the low-noise parametric amplifier increases the sensitivity, the low-level signals appear to be decidedly stronger. A particularly good example is indicated by the arrow, from which an approximate increase in sensitivity commensurate with the prediction can be seen.

After the initial evaluation of these silicon mesa diodes was completed and their potential in low-noise parametric amplifiers had been well established, a compact amplifier was designed. It was specifically made compatible with these particular diodes in order to bring out their optimum features with a minimum of



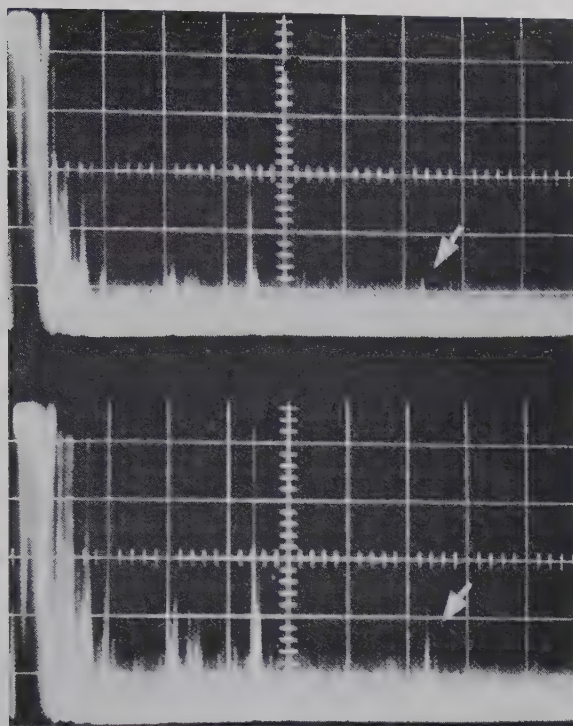


Fig. 6—Radar presentation showing improvement of sensitivity through inclusion of parametric amplifier.

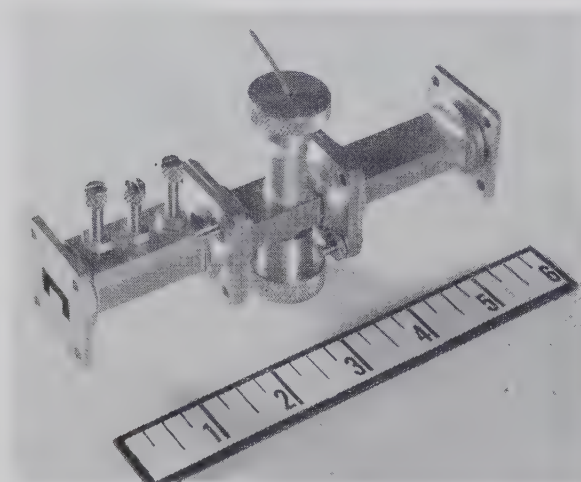


Fig. 7—Developmental model of degenerate X-band parametric amplifier specifically adapted to silicon mesa diode.

TABLE III

Frequency	8.5 kMc
Power gain	15 db
Bandwidth	20 Mc
Radiometer	1.0 db (80°K)
Noise figure	
Pump power	45 Mw

adjustments. Thus, the flexibility of the previously described experimental amplifier was sacrificed. An early developmental model is seen in Fig. 7. Both the noise performance and the pump power requirement improved, as Table III reveals. This enhancement can be directly related to the fairly precise knowledge of the particular diode characteristics which were used in arriving at the compatible circuit design. Although the gain-bandwidth product in this model was somewhat less than expected, further modifications of this design are expected to yield considerable improvements.

#### CONCLUSIONS

The design of silicon mesa variable-capacitance diodes has successfully led to devices with cutoff frequencies and figures of merit that make low-noise reception at X band a practical reality. Zero-bias cutoff frequencies of nearly 70 kMc led to a noise temperature of 130°K in an X-band parametric amplifier which had a gain-bandwidth product of 350 Mc. Compatibility with ex-

isting radar systems was demonstrated. Precise knowledge of the diode characteristics is mandatory to achieving the optimum performance. As a corollary, in order to maintain uniformly high performance in a particular circuit design, where many similar units are involved, such as in a production model or in traveling-wave parametric amplifiers, uniform diode characteristics (capacitance-voltage curve as well as cutoff frequency) are of the utmost importance.

#### ACKNOWLEDGMENT

The authors wish to acknowledge the assistance of R. Burchart, E. Hail, and D. Rice in the development and assembly of the diode devices, as well as the help of F. Bacon in performing many of the X-band measurements reported here. R. Steinkolk designed the developmental model. Finally, the authors are indebted to R. S. Jamison who supplied the measurement data contained in Table III.

# Design and Operation of Four-Frequency Parametric Up-Converters\*

J. A. LUKSCH†, MEMBER, IRE, E. W. MATTHEWS†, SENIOR MEMBER, IRE,  
AND G. A. VERWYST†, MEMBER, IRE

**Summary**—A theoretical analysis of a four-frequency parametric-diode up-converter is presented, retaining both sum and difference frequencies generated by mixing of pump and signal. Upper and lower sideband up-converters are compared, and it is shown that the gain limitations of the former can be overcome by combination with the latter, without appreciable loss of stability. Three different parametric amplifier configurations utilizing this four-frequency mode of operation have been designed, fabricated, and tested. These designs utilize sum-frequency up-conversion from 400 to 9400 Mc., and have exhibited noise figures below 1.5 db, gain in excess of 12 db, and bandwidths greater than 8 Mc.

## I. INTRODUCTION

THE OBJECTIVE of this parametric amplifier development was to achieve low-noise operation of a UHF monopulse radar receiver. This type of radar operates by comparison of signals received on four separate antenna lobes slightly displaced from the antenna boresight axis. Sum and difference signals derived from these four through hybrids are compared after amplification to determine the location of a target with respect to the antenna axis. Accuracy of the system depends on relative stability of all components in the four amplifier channels preceding the point of comparison. It was decided to concentrate development on a sum-frequency parametric up-converter for this system, since it presumably does not involve regeneration and is therefore potentially the most stable mode of paramp operation.

## II. PRELIMINARY DEVELOPMENT

The first up-converter constructed which yielded promising results was in the form of two crossed-waveguides, as shown in Fig. 1, with the diode mounted in an aperture between them. This configuration incorporates sufficient tuning flexibility that it should be possible to match the pump, sum, and signal frequencies and short circuit the difference frequency simultaneously, as assumed in the usual theoretical analysis for this mode of operation. A signal around 400 Mc was introduced coaxially through a double-stub tuner, and a pump frequency of 9 kMc was used, so the output sum-filter was tuned to 9400 Mc. After adjusting the short circuit in the pump waveguide to yield a good match for the pump input, the sum-frequency output

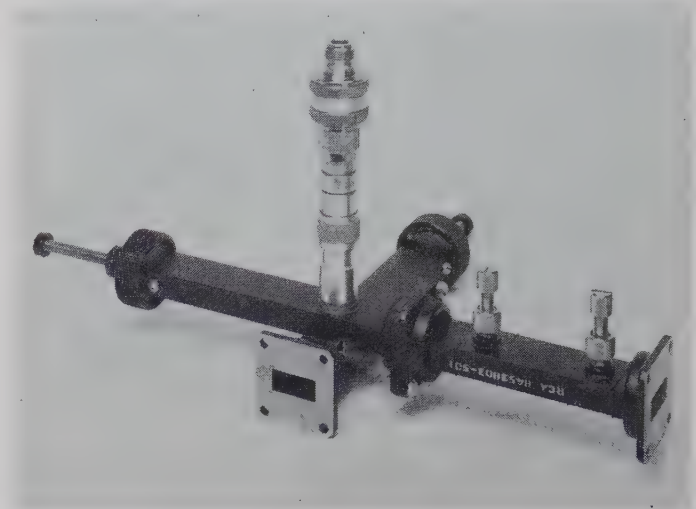


Fig. 1—Crossed waveguide amplifier.

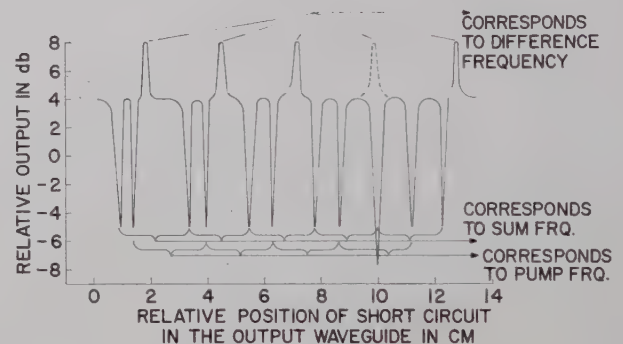


Fig. 2—Tuning of sum-frequency mode of operation of parametric amplifier.

was found to vary, as shown in Fig. 2, with movement of the short circuit in the output waveguide. It was observed that the peaks of maximum output were separated by one-half wavelength at the *difference* frequency (8600 Mc), and the maximum gain was found to be *more* than the 13-db maximum predicted by the Manley-Rowe energy relations. This indicated that internal regeneration was taking place, and that a more complete theoretical investigation was needed to understand the phenomenon.

## III. THEORETICAL INVESTIGATION

Some insight into the operation of a four-frequency parametric amplifier may be gained by consideration

\* Received by the PGMTT, June 15, 1960; revised manuscript received, September 21, 1960.

† Missile and Surface Radar Div., Defense Electronic Products, Radio Corp. of America, Moorestown, N. J.



of the Manley-Rowe<sup>1</sup> power relations as they apply to a lossless diode. If transfer of power is allowed only at signal, pump, sum, and difference frequencies, these relations reduce to

$$\begin{aligned} \frac{W_s}{f_s} + \frac{W_+}{f_+} - \frac{W_-}{f_-} &= 0 \quad (a) \\ \frac{W_p}{f_p} + \frac{W_+}{f_+} + \frac{W_-}{f_-} &= 0 \quad (b), \end{aligned} \quad (1)$$

where positive values of  $W$  represent power absorbed by the diode. The first equation may be rearranged to obtain the up-converter power gain  $G_p^+$ , as<sup>2</sup>

$$G_p^+ = -\frac{W_+}{W_s} = \frac{f_+}{f_s} - \left(\frac{W_-}{W_s}\right)\left(\frac{f_+}{f_-}\right). \quad (2)$$

This indicates that the gain at the sum frequency is increased if power is removed at the difference frequency, and if the regeneration is controlled so that  $W_s$  remains positive (*i.e.*, the signal input conductance remains positive). Eq. 1(b) indicates that the pump power will have to increase to supply the additional output at both sum and difference frequencies.

The equivalent circuit shown in Fig. 3 may be considered for this four-frequency mode of operation. The equations for the 3-port diode network of Fig. 3, considering it to be lossless, can be expressed as

$$\begin{aligned} I_s &= jB_{11}V_s + jB_{12}V_+ + jB_{13}V_- \\ I_+ &= jB_{21}V_s + jB_{22}V_+ + jB_{23}V_- \\ I_- &= jB_{31}V_s + jB_{32}V_+ + jB_{33}V_- \end{aligned} \quad (3)$$

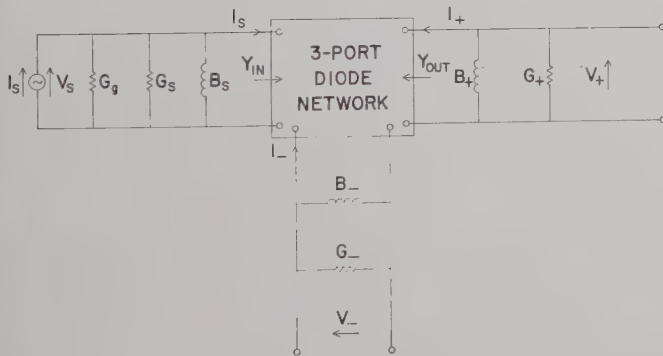


Fig. 3—Four-frequency paramp equivalent circuit.

<sup>1</sup> J. M. Manley and H. E. Rowe, "Some general properties of nonlinear elements—Part I. General energy relations," *PROC. IRE*, vol. 44, pp. 904-913; July, 1956.

<sup>2</sup> E. M. T. Jones and J. S. Honda, "A low noise up-converter parametric amplifier," 1959 IRE WESCON CONVENTION RECORD, pt. I, pp. 99-107, with proper corrections. Parts of the theoretical development which follows also closely parallels that of D. K. Adams, "An analysis of four-frequency nonlinear reactance circuits," *IRE TRANS. ON MICROWAVE THEORY AND TECHNIQUE*, vol. 8, pp. 274-283; May, 1960.

With the terminal loads indicated in Fig. 3 connected to the diode network, the circuit equations can be solved for the signal input admittance  $Y_{in}$  as

$$Y_{in}(s) = \frac{I_s}{V_s} = jB_{11} + \frac{B_{13}B_{31}Y_2 + B_{12}B_{21}Y_3 - j(B_{12}B_{23}B_{31} + B_{13}B_{32}B_{21})}{Y_2Y_3 + B_{32}B_{23}}, \quad (4)$$

where  $Y_2 = G_+ + jB_+ + jB_{22}$  and  $Y_3 = G_- + jB_- + jB_{33}$ . Now if  $B_+$  and  $B_-$  are adjusted for tuning the amplifier so that  $B_+ = -B_{22}$  and  $B_- = -B_{33}$ , then  $Y_2 = G_+$  and  $Y_3 = G_-$  and (4) becomes

$$Y_{in}(s) = jB_{11} + \frac{B_{13}B_{31}G_+ + B_{12}B_{21}G_- - j(B_{12}B_{23}B_{31} + B_{13}B_{32}B_{21})}{G_+G_- + B_{32}B_{23}}. \quad (5)$$

The available power gain of the amplifier for sum-frequency up-conversion, defined as the ratio of power output at  $f_+$  to the power absorbed at  $f_s$ , is given by

$$G_p^+ = \left| \frac{V_+}{V_s} \right|^2 \frac{G_+}{G_{in}} \quad (6)$$

where

$$G_{in} = \text{R.P.}(Y_{in}) = \frac{B_{13}B_{31}G_+ + B_{12}B_{21}G_-}{G_+G_- + B_{32}B_{23}} \quad (7)$$

and  $B_s$  is adjusted to tune out the susceptive part of  $Y_{in}$ .

$\frac{V_+}{V_s}$  can be obtained from the network equations (3) as

$$\frac{V_+}{V_s} = \frac{-B_{23}B_{31} - jB_{21}G_-}{G_+G_- + B_{23}B_{32}}, \quad (8)$$

so that (6) becomes

$$G_p^+ = \frac{G_+(B_{23}^2B_{31}^2 + B_{21}^2G_-^2)}{(G_+G_- + B_{23}B_{32})(B_{13}B_{31}G_+ + B_{12}B_{21}G_-)} \quad (9)$$

This choice of gain definition is perhaps most representative of the amplifier capabilities, since it represents the power gain which can be obtained if the generator is matched to the amplifier input.

The diode network coefficients in (3) can be obtained according to the procedure outlined by Leenov, *et al.*,<sup>3</sup> assuming a lossless diode being driven by a large pump voltage  $v_p(t)$  and a small signal voltage  $v_s(t)$  so that the voltage across the diode is

$$v(t) = V_{dc} + v_p(t) + v_s(t) \quad (10)$$

where  $V_{dc}$  is the bias voltage and  $v_s(t)$  includes small amplitude modulation products.

<sup>3</sup> D. N. Leenov, A. Uhlir, Jr., and A. E. Bakanowski, Bell Tel. Labs. Interim Rept. on Task 8, Signal Corps Contract No. DA-36-034-SC 65589; 1954 to present.

The charge on the capacitor is some function of this voltage  $v(t)$ . If the pump voltage is much larger than the signal voltage, this charge function may accurately be expanded in a Taylor's series about  $v_p(t)$ , and  $v_s(t)$  may be considered a small variation about this expansion point, or

$$Q(t) = f(v) = f(v_p) + f'(v_p)v_s(t) + 1/2f''(v_p)v_s^2(t) + \dots \quad (11)$$

Neglecting terms in  $v_s^2(t)$  and higher, the coefficient  $f'(v_p)$  represents the variable capacitance  $C(t)$  seen by  $v_s(t)$  and produced by  $v_p(t)$ . If  $v_p(t)$  is expressed as a Fourier series of fundamental frequency  $b$ ,

$$v_p(t) = \sum_{n=-\infty}^{\infty} v_n e^{j2\pi nbt}, \quad (12)$$

$f'(v_p)$  may be similarly expanded as

$$f'(v_p) = C(t) = \sum_{n=-\infty}^{\infty} C_n e^{j2\pi nbt}, \quad (13)$$

where  $C_{-n} = C_n$  if  $C(t)$  is assumed to be an even function.

The small signal voltage  $v_s(t)$  includes all frequencies which result from the conversion process, except the pump and its harmonics, so that

$$v_s(t) = \sum_{k=\pm 1} \sum_{m=-\infty}^{\infty} v_{km} e^{j2\pi(mb+ks)t}. \quad (14)$$

The small-signal charge variations are given by

$$Q_s(t) = C(t)v_s(t) = \sum_{k=\pm 1} \sum_{m=-\infty}^{\infty} \sum_{n=-\infty}^{\infty} C_n v_{km} e^{j2\pi[(m+n)b+ks]t} \quad (15)$$

and the corresponding current is obtained from

$$i_s(t) = \frac{dQ_s(t)}{dt}. \quad (16)$$

The current components of interest are those at the signal, sum, and difference frequencies, which may be found from (15) and (16):

$$\begin{aligned} I_s &= jw_s C_0 V_s + jw_s C_1 V_+ + jw_s C_1 V_-^* \\ I_+ &= jw_+ C_1 V_s + jw_+ C_0 V_+ + jw_+ C_2 V_-^* \\ I_-^* &= -jw_- C_1 V_s - jw_+ C_2 V_+ - jw_- C_0 V_-^*. \end{aligned} \quad (17)$$

Comparing (17) with (3) yields the following values for the diode network parameters:

$$\begin{aligned} B_{11} &= w_s C_0 & B_{12} &= w_s C_1 & B_{13} &= w_s C_1 \\ B_{21} &= w_+ C_1 & B_{22} &= w_+ C_0 & B_{23} &= w_+ C_2 \\ B_{31} &= -w_- C_1 & B_{32} &= -w_- C_2 & B_{33} &= -w_- C_0. \end{aligned} \quad (18)$$

Substituting these values into the gain and input conductance expressions, (7) and (9), yields

$$G_p^+ = \left( \frac{w_+}{w_s} \right) \frac{1}{1 - \left( \frac{w_-}{w_+} \right) \left( \frac{G_-}{G_+} \right) \left( \frac{G_+^2 + w_+^2 C_2^2}{G_-^2 + w_-^2 C_2^2} \right)} \quad (19)$$

$$G_{in} = (w_s C_1^2) \frac{w_+ G_- - w_- G_+}{G_+ G_- - w_+ w_- C_2^2}. \quad (20)$$

The corresponding gain expression for operation in the difference-frequency mode (power output at  $w_-$ , power dissipated at  $w_+$ ) is

$$G_p^- = \left( \frac{w_-}{w_s} \right) \frac{1}{\left( \frac{w_+}{w_-} \right) \left( \frac{G_+}{G_-} \right) \left( \frac{G_-^2 + w_-^2 C_2^2}{G_+^2 + w_+^2 C_2^2} \right) - 1}. \quad (21)$$

The negative term in the denominator of each of the gain expressions indicates the presence of regeneration in both the sum and difference frequency types of operation. The input conductance expression (20), with difference terms in both numerator and denominator, suggests the possibility of obtaining stable operation with positive input conductance at the signal terminals while operating with appreciable regeneration and consequent high gain for either sum or difference frequency output. If the signal input conductance is negative, the above gain expressions are meaningless, since no net signal power is absorbed by the amplifier. In this case, the transducer gain may be used; this is defined as the ratio of the up-converter power output to the power available from the signal source. For the sum-frequency type of operation, this transducer gain is given by

$$\begin{aligned} G_t^+ &= \frac{|V_+|^2 G_+}{I_0^2 / 4G_g} = \frac{4G_g G_+}{I_0^2} \left| \frac{V_+}{V_s} \right|^2 \left| \frac{I_s}{G_{in}} \right|^2 \\ &= \frac{4G_g G_+}{(G_g + G_s + G_{in})^2} \left| \frac{V_+}{V_s} \right|^2 = \frac{4G_g |G_{in} G_p^+|}{(G_g + G_s + G_{in})^2} \end{aligned} \quad (22)$$

where  $G_g$  and  $G_s$  are as shown in Fig. 3, and  $G_p^+$  is the value obtained from (19), which is actually negative.

The diode losses can be included in the analysis if the self-admittance terms in (3) are assumed to contain an added conduction component ( $jB_{11} \rightarrow G_{11} + jB_{11}$ ). The input conductance then becomes

$$G_{in} = G_{11} + (w_s C_1^2) \frac{w_+(G_- + G_{33}) - w_-(G_+ + G_{22})}{(G_+ + G_{22})(G_- + G_{33}) - w_+ w_- C_2^2}. \quad (23)$$

The available power gain for sum-frequency output becomes

$$\begin{aligned} G_p^+ &= \left( \frac{w_+}{w_s} \right) \left( \frac{G_+}{G_+ + G_{22}} \right) \left[ 1 + \left( \frac{G_{11}}{G_+ + G_{22}} \right) \frac{[(G_+ + G_{22})(G_- + G_{33}) - w_+ w_- C_2^2]^2}{w_s w_+ C_1^2 [w_- C_2^2 + (G_- + G_{33})^2]} \right. \\ &\quad \left. - \left( \frac{G_- + G_{33}}{G_+ + G_{22}} \right) \left( \frac{w_-}{w_+} \right) \frac{w_+^2 C_2^2 + (G_+ + G_{22})^2}{w_-^2 C_2^2 + (G_- + G_{33})^2} \right]^{-1}. \end{aligned} \quad (24)$$



If  $G_{11}$  can be neglected (since the diode  $Q$  will be the greatest at the signal frequency), (24) becomes

$$G_p^+ = \left( \frac{w_+}{w_s} \right) \left( \frac{G_+}{G_+ + G_{22}} \right) \frac{1}{1 - \left( \frac{G_- + G_{33}}{G_+ + G_{22}} \right) \left( \frac{w_-}{w_+} \right) \frac{w_-^2 C_2^2 + (G_+ + G_{22})^2}{w_-^2 C_2^2 + (G_- + G_{33})^2}} \quad (25)$$

These equations including moderate diode loss are of the same form as the original equations neglecting loss, the primary difference being an increase in each of the circuit conductance components by the amount of the diode conductance at the respective frequencies.

The variation of gain and input conductance of a four-frequency upper-sideband up-converter are plotted in Figs. 4, 5, and 6 as functions of the difference-frequency loading ( $G_-$ ), for typical values of  $G_+$ ,  $C_1$ , and  $C_2$  and a lossless diode. The fundamental pump-frequency component of capacitance variation  $C_1$  does not appear in the gain expression (19) and does not affect the sign of the input conductance (20). The second-harmonic capacitance variation  $C_2$ , together with the conductances  $G_+$  and  $G_-$ , control both gain and input conductance. The equations are plotted for pump and signal frequencies of 9000 and 400 Mc, respectively, corresponding to the frequencies used in the experi-

mental amplifiers described later. The three figures represent progressively increasing values of  $G_+$ , with the same value of  $C_1$  and  $C_2$ . Figs. 4 and 6 show positive regions of input conductance for large and small values of  $G_-$ , separated by a region of negative input conductance. The transitions between these regions coincide with the points of infinite gain and represent the points where either the numerator or denominator of the input conductance expression (20) changes sign. These points can be made to coincide by the proper choice of  $G_+$  and  $C_2$ , as shown approximately in Fig. 5; in this case, no negative input conductance will be observed for any value of  $G_-$  (except the one singular point), and the amplifier will be unconditionally stable. Otherwise, there will be two regions of stable operation separated by one of unstable operation, as in Figs. 4 and 6. In either case, the possibility definitely exists of a choice of operating conditions which will yield high

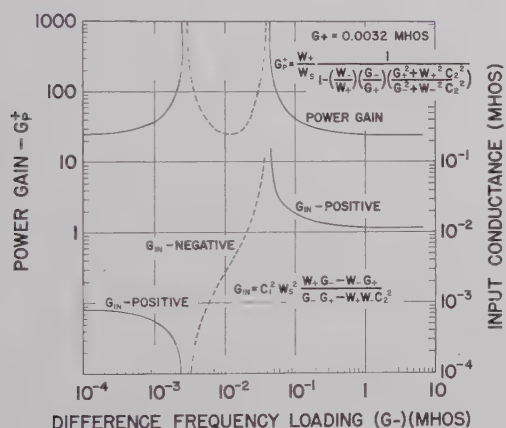


Fig. 4—Characteristics of sum-frequency up-converter.

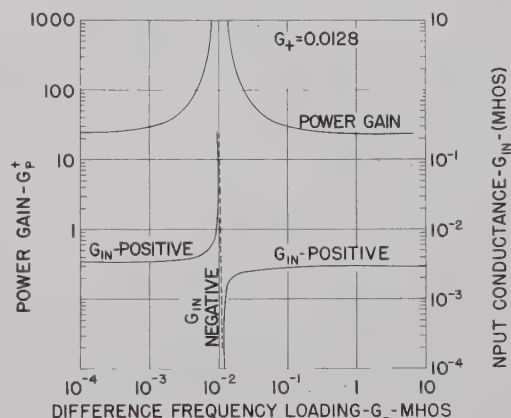


Fig. 5—Characteristics of sum-frequency up-converter.

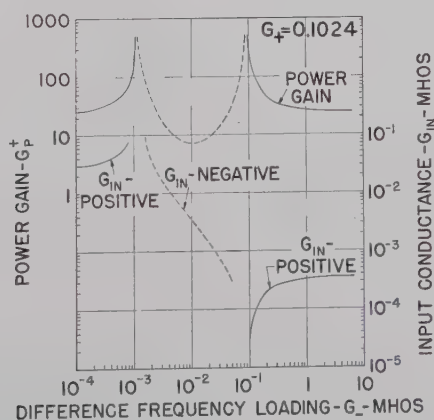


Fig. 6—( $G_+ = 0.1024$ ) Characteristics of sum-frequency up-converter.

gain, with regeneration, but without negative input signal conductance, and consequently stable operation.

The form of the gain equation (21) for difference-frequency output is the same as that for sum-frequency operation (19), and the same input conductance expression (20) applies, so that the two types of operation would exhibit similar characteristics, with slightly higher gain for the sum frequency because of the greater up-conversion ratio. It is interesting to note that while absorption of power at the difference frequency produces increased gain for the sum-frequency up-converter, absorption of power at the sum frequency tends to stabilize the operation of the difference-frequency up-converter. Furthermore, since the diode resistance dissipates power at all frequencies, this may produce both effects naturally.

The effect of pump power variation on the gain of the sum-frequency mode is shown in Fig. 7. The primary effect of pump power is to change the diode coefficients  $C_0$ ,  $C_1$  and  $C_2$ . A change of  $C_0$  will affect amplifier tuning at all frequencies, while a change of  $C_1$  will affect match conditions at all frequencies. The variation of  $C_2$  will alter the regeneration condition, and thus will be most important in determining over-all performance.

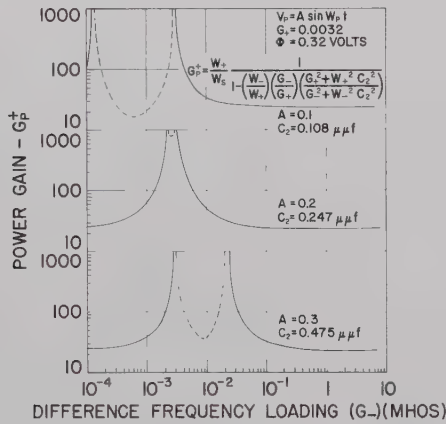


Fig. 7—Pump-power gain variation of up-converter.

Fig. 7 shows the variation of gain as a function of  $G_-$  for three different values of  $C_2$ , representing three different pump-power levels. The characteristics of these curves are the same as those in Figs. 4–6, showing two gain peaks, one of which remains fixed with varying  $C_2$ , while the other moves, and can coincide with the first for a critical value of  $C_2$ . The values of the diode coefficients can be obtained numerically as a function of pump-power level, if the diode characteristic is known. The values shown in Fig. 7 assume the usual relation for a linearly-graded junction diode:

$$C = \frac{C'}{\sqrt[3]{1 - \frac{V}{\phi}}} \quad (26)$$

with  $C' = 1$  pfd,  $V_{Bias} = 0$ , and  $\phi = 0.32$  volt.

The importance of including  $C_2$ , the second harmonic variation of the variable capacitance, in the analysis of this four-frequency operation is apparent from the major role it plays in determining input conductance, gain, and consequently stability. In fact, control of the amplifier characteristics by direct injection of a second harmonic component of pump voltage has been suggested. It may be necessary to consider even higher pump harmonics in order to obtain ultimate agreement with experiment.

Experimental results have shown that the dissipation of power at the fourth frequency in the up-converter operation does not degrade the noise performance to any measurable extent. Jones and Honda<sup>2</sup> have derived noise figure equations for this four-frequency mode, neglecting the  $C_2$  terms, with similar conclusions.

The noise figure equation for sum-frequency up-conversion is most easily derived if the network equations (3) are altered to include the terminating impedances, so that

$$jB_{11} \rightarrow G_g + G_s + G_{ds} + jB_s + jB_{11}, \text{ etc.}, \quad (27)$$

where  $G_{ds}$  is the diode loss at the signal frequency. If the susceptances are tuned out, the real coefficients remaining on the principal diagonal may be identified as

$$\begin{aligned} G_1 &= G_g + G_s + G_{ds} \\ G_2 &= G_+ + G_{d+} \\ G_3 &= G_- + G_{d-} \end{aligned} \quad (28)$$

The matrix currents now represent externally applied currents.

The noise figure may be defined as

$$F = \frac{\text{Total noise power delivered to the load } (G_+)}{\text{Noise power delivered to the load from } G_g}$$

Using (28) and the previous notation, this can be derived as

$$\begin{aligned} F = 1 + \frac{G_{ds}}{G_g} + \frac{G_3}{G_g} \frac{(C_2^2 G_1^2 + w_s^2 C_1^4)}{C_1^2 (G_3^2 + w_-^2 C_2^2)} \\ + \frac{G_2}{G_g} \frac{(G_1 G_3 - w_s w_- C_1^2)^2}{w_+^2 C_1^2 (G_-^2 + w_-^2 C_2^2)} \end{aligned} \quad (29)$$

Neglecting diode losses and loss due to signal input loading  $G_s$ , this may be evaluated for the high-gain condition<sup>4</sup> as

$$\begin{aligned} F = 1 + \frac{w_+ G_+ (w_s^2 C_1^4 + G_g^2 C_2^2)}{w_- G_g C_1^2 (w_+^2 C_2^2 + G_+^2)} \\ + \frac{G_+ \left( \frac{G_g G_+}{w_+} - w_s C_1^2 \right)^2}{G_g C_1^2 (w_+^2 C_2^2 + G_+^2)} \end{aligned} \quad (30)$$

<sup>4</sup> Since the poles of the gain expression (19) coincide with the poles and zeros of the input conductance (20), the high-gain condition may be arbitrarily identified with the zero-input conductance condition. This condition may be used to relate  $G_-$  to  $G_+$  and eliminate the former from (29).



Examination of (30) reveals that the noise figure decreases for decreasing  $G_+$  and increasing  $w_+$ , and that there is an optimum relationship among the parameters which will eliminate the last term in (30).

If the following set of typical values is substituted into (30), the potential noise figure neglecting losses is under 0.2 db:  $C_1 = 0.25$  pfd./ $C_2 = 0.05$  pfd./ $f_s = 400$  Mc,  $f_p = 9$  kMc,  $G_+ = 10^{-4}$  mhos, and  $G_s = 10^{-2}$  mhos.

The operating characteristics of an actual four-frequency up-converter depend on the individual control of each of the four frequencies involved. The extent to which such independent control is possible depends on the configuration chosen. In the following section, experimental results will be presented for three different physical configurations, and a comparison of their performances will be made.

#### IV. EXPERIMENTAL RESULTS

##### A. Crossed-Waveguide Type

The crossed-waveguide UHF up-converter on which four-frequency operation was first observed was incorporated into a complete receiver system according to the block diagram of Fig. 8. The  $X$ -band local oscillator signal was derived by combining a UHF local oscillator signal with the pump frequency; this produces an IF output independent of pump frequency, and is the first step towards stable up-converter operation. The necessary filters and isolators were incorporated as shown to prevent undesired interaction between various parts of the system. The balanced mixer and 60-Mc IF preamplifier had a combined noise figure of about 9 db, and with the amplifier tuned to a center frequency of around 400 Mc, the system had an over-all gain and noise figure variation with frequency as shown in Fig. 9.<sup>5</sup> This represents a tuning condition for a maximum up-converter gain of about 22 db, with a 3-db bandwidth of 8 Mc, and a system noise figure at midband of less than 1 db. The varactor diodes used were Micro-wave Associates MA-460F or Sylvania D4110D, for which a pump power of under 10 mw was required. The variation of gain and noise figure with pump power for this amplifier are shown in Fig. 10; both variations are fairly linear with pump power near the specified operating point, and a change of  $\pm 5$  per cent in pump power causes a change in gain of  $\pm 3.5$  db.

Equivalent performance of this amplifier could be obtained over a 50-Mc band with only two tuning adjustments required—position of the short circuit in the output waveguide (tuning the difference frequency) and adjustment of the UHF input tuner. By completely re-

tuning filters and mixers (whose bandwidths were about 100 Mc), it was possible to achieve nearly equivalent performance at  $L$ -band (1000 Mc), with only a slight degradation of noise figure to about 1.5 db.

##### B. Balanced Type

A balanced diode mount utilizing a pair of varactor diodes with an  $X$ -band hybrid as shown in Fig. 11 was constructed for operation as a four-frequency up-converter. The advantage expected from this type of operation is isolation between pump and sideband signals produced by the hybrid because of the relative phases involved. This isolation, however, is strongly dependent upon balancing of the two diodes and their associated input circuits. Additional isolation of the sum-frequency output from the pump was provided by means of a movable cutoff-type high-pass filter consisting of a section of small-size waveguide designed to slide within the standard waveguide, as shown in Fig. 11. This adjustability provides for reflective tuning of the difference frequency to control the internal regeneration. The individual diode mounts were designed for a good match to the pump and sum frequencies, while a double-tuned lumped constant circuit was used to match the diodes to the coaxial input.

Measured characteristics of this amplifier, incorporated into the same system described for the crossed-waveguide unit, are shown in Fig. 12. The maximum gain obtained was only about 12 db, and the minimum noise figure about 3 db, nearly half of which was contributed by the mixer IF stages following. This reduced performance in comparison with the crossed-waveguide type was partially caused by the fact that only one reversed pair of MA-460D diodes (60 kMc cutoff) was available for these tests. Furthermore, the balance conditions of the two diodes in actual operation could not be checked easily and would certainly affect the regenerative operation considerably.

The stability of this configuration against changes in pump power are shown in Fig. 13. The operation appears extremely stable—a pump power of 10 mw produced optimum noise figure, while an increase to 40 mw did not produce oscillation. The noise figure was under 4.0 db, for pump powers between 5 and 25 mw, a remarkable range.

##### C. Circulator Type

The third up-converter configuration investigated utilized an  $X$ -band circulator to separate the pump and sum-frequency output signals as shown in Fig. 14. A single varactor diode is used in an  $X$ -band mount, which is matched for both pump and sum frequencies; this is coupled to one arm of the circulator through a movable cutoff-type high-pass filter which reflects the difference frequency to provide the internal regeneration. Input signal tuning was by means of a coaxial double stub tuner. The performance obtained with an

<sup>5</sup> Gain of the up-converter was measured by the standard technique of inserting a known attenuation in the  $X$ -band output line and measuring the change in combined amplifier-mixer noise figure. The gain thus measured corresponds to the transducer gain as defined in (22), which is by its definition equal to or less than the available power gain, depending upon conditions of input match.

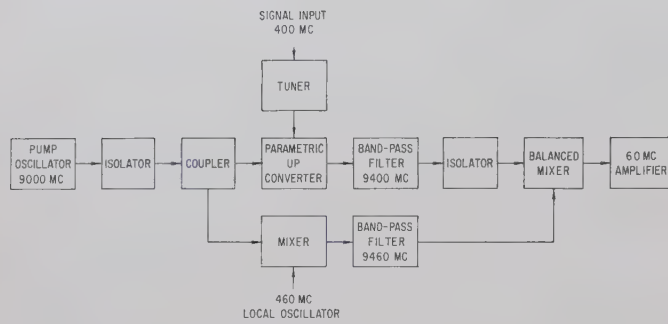


Fig. 8—Receiver system block diagram.

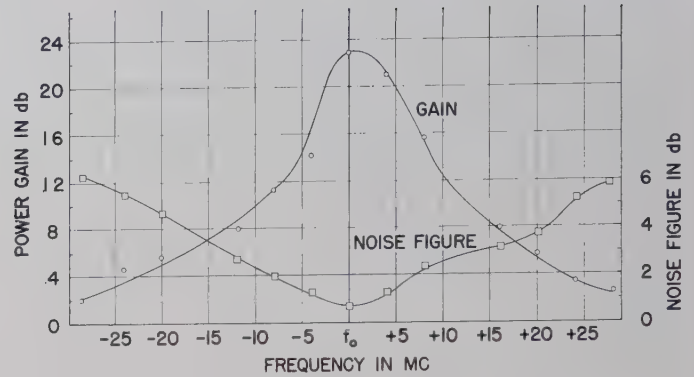


Fig. 9—Gain and noise figure of crossed-waveguide up-converter.

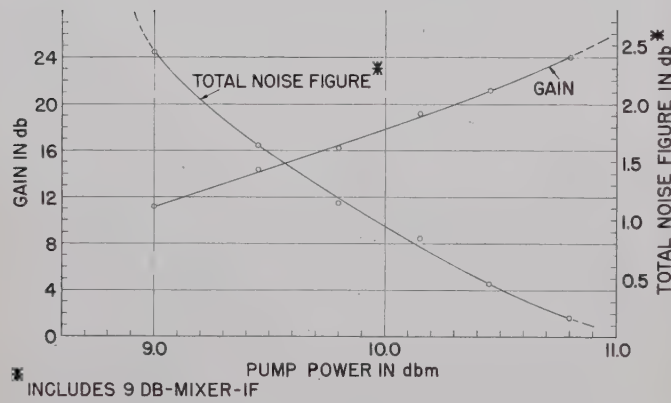


Fig. 10—Variation of gain and noise figure of parametric amplifier vs pump power (crossed-guide).

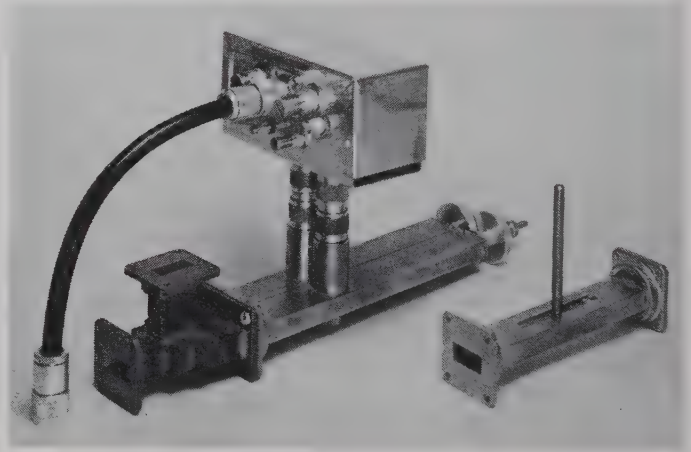


Fig. 11—Balanced amplifier.

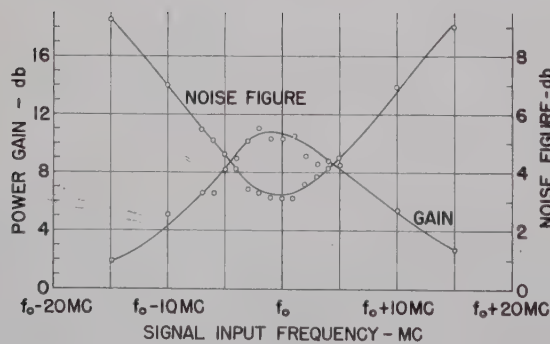


Fig. 12—Band-pass characteristics, balanced amplifier.

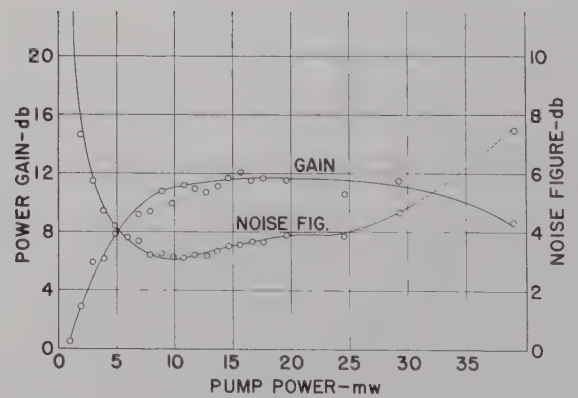


Fig. 13—Gain and noise figure vs pump power level, balanced amplifier.



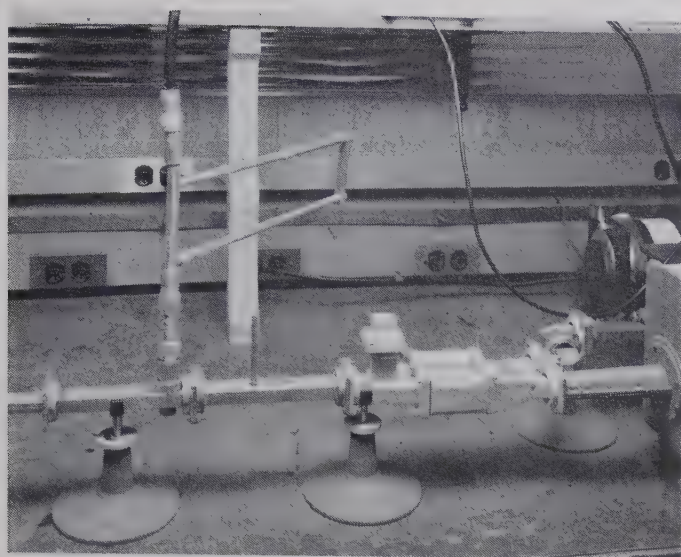


Fig. 14—Circulator-type amplifier.

MA-460F varactor is shown in Fig. 15. A maximum up-converter gain of 20 db was achieved, with a 3-db bandwidth of 12 Mc and a receiver noise figure under 1 db at midband. Tuning of this unit was extremely easy and involved readjustment of signal input tuner and movable high-pass filter.

Equivalent performance could be achieved over a range of at least 50 Mc. The stability with pump-power variation is shown in Fig. 16. Nominal pump power required was about 25 mw, higher than the other configurations because of circulator loss and mismatch of the high-pass sliding filter. This power could fluctuate  $\pm 25$  per cent ( $\sim 1$  db) with very little change in amplifier gain or noise figure. Further increase in pump power did not produce oscillation.

A summary of the operating characteristics of the three up-converters is shown in Table I. The dynamic range for linear operation of all three types appears to be from the noise level to the point where the output approaches a level 25 to 30 db below the pumping level. This represents a range of about 75 db for a system bandwidth of the order of 5 Mc.

The over-all stability of these up-converter systems was investigated by building two of the crossed-waveguide types, operating them from common pump and signal sources, and comparing their outputs at IF. Operation of the two was adjusted in phase and amplitude to produce a null in the comparison circuit. This null was maintained to within  $\pm 3^\circ$  in phase and  $\pm 0.5$  db in amplitude over a period of several hours without adjustment, using a temperature-stabilized reflex klystron with a well-regulated power supply for the pump source.

#### D. Correlation with Theory

Correlation between the above experimental results

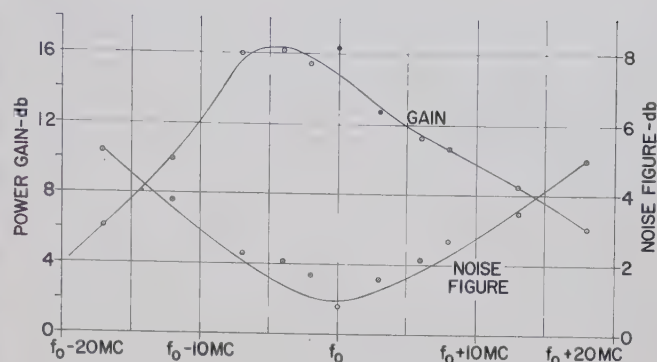


Fig. 15—Band-pass characteristics, circulator-type amplifier.

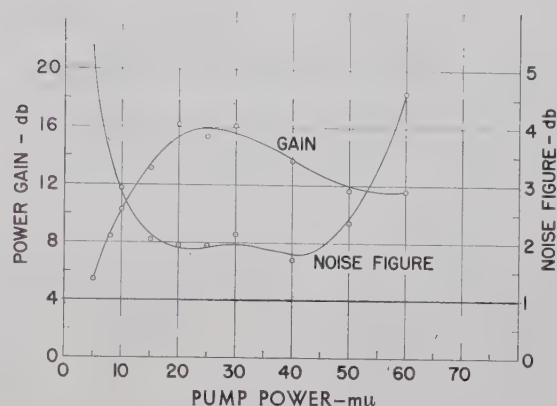


Fig. 16—Gain and noise figure vs pump-power level, circulator-type amplifier.

TABLE I  
CHARACTERISTICS OF FOUR-FREQUENCY UHF PARAMETRIC UP-CONVERTERS

Type	Signal Frequency Mc	Gain db	Noise* Figure db	Bandwidth Mc	Pump Power mw
Crossed Waveguide	400	22	1.0	8	10
	1000	20	1.5	—	20
Balanced	400	12	3	9	10
Circulator	400	16	1	12	25

\* Mid-band noise figure including contribution of 9 db mixer—IF combination.

and the theoretical results derived in the previous section is exceedingly difficult to make. First of all, it is necessary to know the equivalent circuit parameters for the configuration tested, such as  $G_+$ ,  $G_-$ ,  $G_0$ , and  $G_s$ . Next, the diode parameters  $C_1$  and  $C_2$  must be determined under actual operating conditions, as they depend on pump power level, bias, diode characteristics, and relative loading at each harmonic of the pump frequency. Diode losses would complicate the analysis tremendously. An analysis similar to that of Knechtli

and Weglein<sup>6</sup> would assist in the evaluation, but would be considerably more complicated for the four-frequency type of operation.

Consequently, the authors feel that the theoretical results are most useful in predicting the type of operation which might be expected from a four-frequency parametric amplifier (and which might explain some inconsistencies in supposedly three-frequency operation). Meanwhile, the experimental results represent typical values obtained in the laboratory. Other configurations, particularly those which permit more independent control of tuning and loading of each of the four frequencies, and which perhaps allow some measure of independent control of the diode coefficients  $C_1$  and  $C_2$ , may produce superior results and may be easier to correlate with theory.

Further experiments with the crossed-guide and circulator type paramps mentioned above have shown that for best noise performance the amplifier adjustments seem to produce a regenerative gain at the signal

input port of about 8 db, when the up-converter gain is about 20 db. The difference of 12 db is within 2 db of the theoretical gain due to up-conversion alone. This appears to indicate that best noise performance is obtained in the potentially-unstable region of negative input conductance, in Figs. 4 and 6. Correlation with theory would have to be made in terms of transducer gain, as in (22). Because of the negative input conductance, it has been found very necessary to operate these amplifiers with an isolator on the signal input port to provide stability against input mismatch over the entire frequency band of the amplifier, particularly for use with a radar having many wavelengths of transmission line between the actual antenna and the parametric amplifier.

#### V. ACKNOWLEDGMENT

The authors wish to thank V. Stachejko for his excellent design and experimental work on the crossed-waveguide unit and R. M. Scudder for his guidance and suggestions. Portions of this paper have been incorporated into a master's thesis submitted to the University of Pennsylvania by two of the authors.

<sup>6</sup> R. C. Knechtli and R. D. Weglein, "Low-noise parametric amplifier," Proc. IRE, vol. 48, pp. 1218-1226; July, 1960.

## Ferrites with Planar Anisotropy at Microwave Frequencies\*

ISIDORE BADY†, SENIOR MEMBER, IRE

**Summary**—Materials with an easy plane of magnetization (planar anisotropy) have recently been discovered. The large anisotropy field that tends to keep the magnetization in the easy plane reduces the field required to cause ferromagnetic resonance, which makes the material promising for microwave applications. Equations are derived for the susceptibility, taking into account losses and a finite medium. Propagation in a longitudinal and transverse static field is considered. The location of a slab in a rectangular waveguide for minimum loss in the forward direction, and the use of the material as a phase shifter, are discussed. Experimental microwave data on some materials are given, and also data on an isolator and phase shifter incorporating these materials.

#### I. INTRODUCTION

FOR most ceramic magnetic materials used in the microwave frequency range, the magnetic anisotropy field is sufficiently small so that it can be neglected in deriving equations for engineering applications. However, there are two groups of materials that have very large anisotropy fields that cannot be neglected. Both of these groups have a hexagonal crystal structure; the first has an easy direction of magnetization along the  $C$  axis, and the second has an easy plane of magnetization perpendicular to the  $C$  axis (planar anisotropy). The first group includes the ceramic permanent magnetic material, barium ferrite, marketed under various trade names such as Ferroxdure, Magnadur, Indox, Ceramagnets, etc. The latter group is called Ferro-

\* Received by the PGMTT, June 10, 1960; revised manuscript received, August 1, 1960.

† United States Army Signal Res. and Dev. Lab., Fort Monmouth, N. J.



plana and has been discovered more recently. Both of these materials are described in the new book by Smit and Wijn<sup>1</sup> which itself contains numerous references.

Some articles describing microwave applications of ceramic permanent magnet materials have appeared in the literature;<sup>2-5</sup> however, though there have been articles discussing the ferromagnetic resonance of ferrites with planar anisotropy,<sup>6,7</sup> the author is not aware of any publication discussing the microwave applications of these ferrites. It is the purpose of this paper to develop some general equations for the microwave applications of ferrites with planar anisotropy and to present some experimental data on the material and devices incorporating this material. It will be assumed that the materials are polycrystalline and are oriented so that all easy planes of magnetization are mutually parallel. The only magnetic anisotropy field that will be considered will be the one that tends to hold the magnetization vector in the easy plane. The term planar ferrites will frequently be used as a short way of saying ferrites with planar anisotropy.

## II. EQUATIONS OF MAGNETIZATION AND SUSCEPTIBILITY: APPLIED FIELD IN EASY PLANE

### A. Infinite Medium, No Losses

In the absence of anisotropy fields, the equation of magnetization is simply

$$\frac{1}{\gamma} \frac{d\vec{M}}{dt} = \vec{M} \times \vec{H},$$

where  $\gamma$  is the gyromagnetic ratio,  $\vec{M}$  the magnetization vector, and  $\vec{H}$  the magnetic field. The quantity  $\vec{M} \times \vec{H}$  constitutes a torque. The anisotropy field of the planar ferrites produces an additional torque  $\vec{T}_a$  that tends to keep magnetization vector in the easy plane. The equation of magnetization now becomes

$$\frac{1}{\gamma} \frac{d\vec{M}}{dt} = \vec{M} \times \vec{H} + \vec{T}_a. \quad (1)$$

<sup>1</sup> J. Smit and H. P. Wijn, "Ferrites," John Wiley and Sons, New York, N. Y.; 1959.

<sup>2</sup> M. T. Weiss and F. A. Dunn, "A 5-mm resonance isolator," IRE TRANS. ON MICROWAVE THEORY AND TECHNIQUES, vol. 6, p. 331; July, 1958.

<sup>3</sup> M. T. Weiss, "The behavior of Ferroxdure at microwave frequencies," 1955 IRE CONVENTION RECORD, vol. 3, pt. 8, p. 95.

<sup>4</sup> D. J. DeBitetto, F. K. DuPre, and F. G. Brockman, "Highly Anisotropic Materials for Millimeter Wave Applications," presented at the Symp. on Millimeter Waves, Polytechnic Inst. of Brooklyn, New York; March 31-April 2, 1959.

<sup>5</sup> L. C. Kravitz and G. S. Heller, "Resonance isolator at 70 kMc," PROC. IRE, vol. 47, p. 331; February, 1959.

<sup>6</sup> H. S. Belson and C. J. Kriessman, "Microwave resonance in hexagonal ferromagnetic single crystals," J. Appl. Phys., supplement to vol. 30, no. 4, p. 175S; April, 1959.

<sup>7</sup> E. Schlömann and R. V. Jones, "Ferromagnetic resonance in polycrystalline ferrites with hexagonal crystal structure," J. Appl. Phys., supplement to vol. 30, no. 4, p. 177S; April, 1959.

It is now proposed to develop the equation for  $\vec{T}_a$  and to expand (1) in Cartesian coordinates. (See Fig. 1.) The easy plane of magnetization will be taken as the  $XY$  plane.

The anisotropy energy of materials with one axis of symmetry is given by<sup>8</sup>

$$E_a = K_1 \sin^2 \theta + K_2 \sin^4 \theta \cdots \quad (2)$$

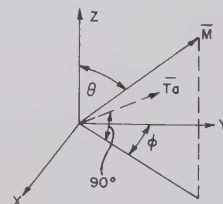


Fig. 1—Representation of magnetization and torque vectors.

The torque caused by this anisotropy is equal to minus the derivative of the energy. Thus,

$$\vec{T}_a = - (2K_1 \sin \theta \cos \theta + 4K_2 \sin^3 \theta \cos \theta) \hat{\theta},$$

where the symbol  $\hat{\theta}$  over a letter denotes a unit vector.

In this paper we will consider only cases where the magnetization will be in, or very close to, the easy plane; i.e.,  $\theta \approx \pi/2$ . Therefore,

$$\sin \theta \approx 1, \quad \cos \theta \approx \frac{M_z}{M_s};$$

$$\vec{T}_a = - (2K_1 + 4K_2) \frac{M_z}{M_s} \hat{\theta}.$$

The magnetic anisotropy field is defined as<sup>9</sup>

$$H_a = - \frac{2(K_1 + 2K_2)}{M_s}.$$

We thus have

$$\vec{T}_a = H_a M_s \hat{\theta} \quad (3)$$

where  $\hat{\theta}$  is in the  $XY$  plane and is perpendicular to  $\vec{M}_s$ . It points in the direction a right-hand screw moves in turning  $\vec{M}$  towards the  $XY$  plane. Thus,  $\hat{\theta} = -\cos \phi \hat{x} + \sin \phi \hat{y}$  where  $\phi$  is the angle between the  $XY$  component of  $\vec{M}$  and the torque. For the case where  $\theta$  is almost equal to  $\pi/2$ , we can write

$$\cos \phi = \frac{M_y}{M_s}; \quad \sin \phi = \frac{M_x}{M_s}. \quad (4)$$

Eq. (3) thus becomes

$$\vec{T}_a = \frac{H_a M_s}{M_s} (-M_y \hat{x} + M_x \hat{y}). \quad (5)$$

<sup>8</sup> Smit and Wijn, *op. cit.*, p. 48.

<sup>9</sup> *Ibid.*, p. 49.

We now assume that we apply a static biasing field  $H_0$  in the  $Y$  direction and saturate the material in that direction. Thus, we can take  $M_y$  as approximately equal to  $M_s$ . The applied RF magnetic fields will be taken as lying in the  $XZ$  planes. Thus, the  $\vec{M}$  and  $\vec{H}$  of (1) can be written as

$$\vec{M} = (M_s \hat{y} + m_x \hat{x} + m_z \hat{z})$$

$$\vec{H} = (H_0 \hat{y} + h_x \hat{x} + h_z \hat{z}).$$

Note that dc components here and in the remainder of this paper will be expressed in capital letters, whereas RF components will be expressed in small letters.

Eq. (1) can now be written as follows:

$$\frac{j\omega m_x}{\gamma} = M_s h_x - m_z H_0 - H_a m_z \quad (6a)$$

$$\frac{j\omega m_y}{\gamma} = m_z h_x - m_x h_z + H_a m_z \frac{m_x}{M_s} \quad (6b)$$

$$\frac{j\omega m_z}{\gamma} = -M_s h_x + m_x H_0. \quad (6c)$$

Eq. (6b) can be omitted from further consideration since the quantities involved are much smaller than the quantities in the other two equations. Eqs. (6a) and (6c) can now be solved as follows:

$$\begin{aligned} m_x &= \frac{M_s}{D_1} [(H_0 + H_a) h_x - j H_i h_z] \\ m_z &= \frac{M_s}{D_1} [j H_i h_x + H_0 h_z] \end{aligned} \quad (7)$$

where

$$\begin{aligned} D_1 &= H_0(H_0 + H_a) - H_i^2 \\ H_i &= \frac{\omega}{|\gamma|}. \end{aligned}$$

The flux  $\vec{b}$  is given by the equation

$$\begin{aligned} \vec{b} &= \vec{h} + 4\pi\vec{m} = \vec{h} + \begin{vmatrix} \chi_{xx} & -j\chi_{xz} & 0 \\ j\chi_{xz} & \chi_{zz} & 0 \\ 0 & 0 & 1 \end{vmatrix} \begin{vmatrix} h_x \\ h_z \\ h_y \end{vmatrix} \\ &= (1 + [\chi])\vec{h} \end{aligned} \quad (8)$$

$$\begin{aligned} \chi_{xx} &= \frac{4\pi M_s}{D_1} (H_0 + H_a) \\ \chi_{zz} &= \frac{4\pi M_s}{D_1} H_0 \\ \chi_{xz} &= \frac{4\pi M_s}{D_1} H_i. \end{aligned} \quad (9)$$

We note that the  $H_0$  required for resonance is much smaller than in the case of conventional ferrites, and that  $\chi_{xx} \neq \chi_{zz}$ .

The extent to which the anisotropy field decreases the magnitude of the external field required for resonance is illustrated in Table I. ( $\gamma$  is taken as 2.8 Mc per oersted.) The advantage of this for microwave devices is obvious.

TABLE I

Frequency (Mc)	$H_a$ (oe)	Field for Resonance	
		Isotropic (oe)	Planar (oe)
3000	5000	1070	230
5000	5000	1780	580
10,000	5000	3580	1800
5000	10,000	1780	330
10,000	10,000	3580	1100
20,000	10,000	7160	3700

### B. Finite Medium, No Losses

Assuming that the sample is in the shape of an ellipsoid, demagnetizing factors  $N_x$ ,  $N_y$ ,  $N_z$  can be introduced. Eq. (6) can then be rewritten as

$$\begin{aligned} \frac{j\omega m_x}{\gamma} &= M_s(h_x - N_z m_z) - m_z(H_0 - N_y M_s) - H_a m_z \\ \frac{j\omega m_z}{\gamma} &= -M_s(h_x - N_x m_x) + m_x(H_0 - N_y M_s). \end{aligned} \quad (10)$$

The terms in the tensor relating magnetization to externally applied fields are

$$\begin{aligned} \chi_{xx} &= \frac{4\pi M_s H_x}{D_2} \\ \chi_{zz} &= \frac{4\pi M_s H_z}{D_2} \\ \chi_{xz} &= \frac{4\pi M_s H_i}{D_2}, \end{aligned} \quad (11)$$

where

$$\begin{aligned} H_x &= H_0 + H_a + M_s(N_z - N_y); \quad D_2 = H_x H_z - H_i^2 \\ H_z &= H_0 + M_s(N_x - N_y); \quad H_i = \frac{\omega}{|\gamma|}. \end{aligned}$$

From (11) we note that the anisotropy field operates in the same way as the fields caused by the inequality of the demagnetizing factors. However, the anisotropy field may be as high as 30,000 oersteds, whereas the field caused by the inequality of demagnetizing factors cannot exceed the saturation magnetization, which can be as high as 6000 with present materials.

The demagnetizing fields caused by the inequality of the demagnetizing factors can of course be used to supplement the anisotropy field in reducing the external



biasing field required for resonance. Two instances where this is accomplished are shown in Fig. 2, where it is assumed that the slab is very thin. The greatest reduction in external field required will be for the slab in Figure 2(b). Thus, for a material with an anisotropy field of 10,000 oersteds and a saturation magnetization of 2000 oersteds, the fields required for resonance at 15,000 Mc would be 600, 2000, and 2200 oersteds for the geometry shown in Fig. 2(b), for the geometry shown in Figure 2(a), and for the infinite medium, respectively. In an infinite isotropic medium the field required would be 5300 oersteds.

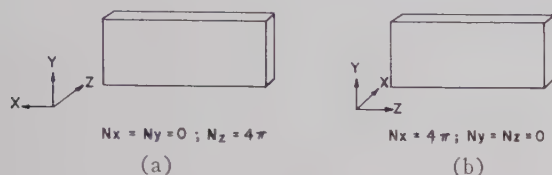


Fig. 2—Planar ferrite slabs. (a) Easy plane in plane of slab. (b) Easy plane perpendicular to plane of slab.

### C. Infinite Medium, With Losses

Losses (or damping) will be introduced, through the Landau-Lifshitz formulation. From (1), we note that there are two torque terms to be considered. The first is  $\vec{M} \times \vec{H}$ . The loss term corresponding to this torque will be a vector that is proportional to this torque and is perpendicular to both the torque and the magnetization vector. The loss term for this torque can thus be represented as

$$\frac{\alpha \vec{M}}{M_s} \times (\vec{M} \times \vec{H}),$$

where  $\alpha$  is the proportionality constant. This can be expanded to give

$$\alpha[(H_0 m_x - M_s h_x) \hat{x} + (H_0 m_z - M_s h_z) \hat{z}].$$

The second torque term is  $-H_0 m_z \hat{x}$ . (See (5); the term  $M_x \hat{y}$  can be neglected.) The loss term for this torque can thus be represented by

$$-\frac{\alpha H_0 m_z}{M_s} (\vec{M}_x \hat{x}) = \alpha H_0 m_z \hat{z}.$$

The equation of magnetization thus becomes

$$\begin{aligned} \frac{j\omega m_z}{\gamma} &= M_s h_z - m_z H_0 - H_0 m_z + \alpha(H_0 m_x - M_s h_x) \\ \frac{j\omega m_x}{\gamma} &= m_x H_0 - M_s h_x + \alpha(H_0 m_z - M_s h_z + H_0 m_z). \end{aligned} \quad (12)$$

The terms of the susceptibility tensor for this case are shown in (13). The single prime denotes the reactive part and the double prime the dissipative part of the complex term; i.e.,  $\chi^* = \chi' - j\chi''$ .

$$\chi'_{xx} = \frac{4\pi M_s}{D_3} \{ [1 + \alpha^2][H_0 + H_a][(1 + \alpha^2)(H_0 + H_a)H_0 - H_i^2] + \alpha^2(2H_0 + H_a)H_i^2 \}$$

$$\chi''_{xx} = \alpha \frac{4\pi M_s H_i}{D_3} \{ (1 + \alpha^2)(H_0 + H_a)^2 + H_i^2 \}$$

$$\chi'_{xz} = \frac{4\pi M_s}{D_3} \{ [1 + \alpha^2]H_0[(1 + \alpha^2)(H_0 + H_a)H_0 - H_i^2] + \alpha^2(2H_0 + H_a)H_i^2 \}$$

$$\chi''_{xz} = \alpha \frac{4\pi M_s H_i}{D_3} \{ (1 + \alpha^2)H_0^2 + H_i^2 \}$$

$$\chi'_{zx} = \frac{4\pi M_s H_i}{D_3} \{ (1 + \alpha^2)(H_0 + H_a)H_0 - H_i^2 \}$$

$$\chi''_{zx} = \alpha \frac{4\pi M_s}{D_3} \{ H_i^2(2H_0 + H_a) \}$$

$$D_3 = [(1 + \alpha^2)(H_0 + H_a)H_0 - H_i^2]^2 + [\alpha H_i(2H_0 + H_a)]^2$$

$$H_i = \frac{\omega}{|\gamma|}. \quad (13)$$

### D. Finite Medium, With Losses

Taking into consideration both a finite ellipsoid and losses, the terms in the susceptibility tensor are shown in (14). Terms in  $\alpha^2$  have been omitted in this equation.

$$\chi'_{xx} = \frac{4\pi M_s}{D_4} H_x(H_x H_z - H_i^2)$$

$$\chi''_{xx} = \frac{\alpha 4\pi M_s H_i}{D_4} [H_x(H_x + H_z) - (H_x H_z - H_i^2)]$$

$$\chi'_{xz} = \frac{4\pi M_s}{D_4} H_z(H_x H_z - H_i^2)$$

$$\chi''_{xz} = \frac{\alpha 4\pi M_s H_i}{D_4} [H_z(H_x + H_z) - (H_x H_z - H_i^2)]$$

$$\chi'_{zx} = \frac{4\pi M_s}{D_4} H_i[H_x H_z - H_i^2]$$

$$\chi''_{zx} = \frac{\alpha 4\pi M_s H_i^2}{D_4} [H_x + H_z]$$

$$D_4 = [H_x H_z - H_i^2]^2 + [\alpha H_i(H_x + H_z)]^2. \quad (14)$$

$H_x$ ,  $H_z$ , and  $H_i$  have been defined in connection with (11).

### E. Linewidth

Linewidth can be defined as the difference in the two values of the biasing field at which the loss term of the susceptibility is one-half its maximum value. (For the purposes of this discussion any of the terms  $\chi''_{xx}$ ,  $\chi''_{zz}$ , or  $\chi''_{xz}$  may be used.) For materials in which  $\alpha$  is very much less than 1, the loss term of the susceptibility will be one-half of its maximum value when

the two terms in the denominator  $D_3$  of (13) are equal. Disregarding terms in  $\alpha^2$  we thus have (see Fig. 3),

$$H_{01/2}(H_{01/2} + H_a) - H_i^2 = \alpha H_i(2H_{01/2} + H_a)$$

$$\text{Let } H_{01/2} = H_{0r} \pm \Delta H_{1/2}.$$

Disregarding second-order terms, we get  $\Delta H_{1/2} = \alpha H_i$ , or  $\Delta H = 2\alpha H_i$  where  $H_i$  is the field at which an isotropic ferrite would be resonant.

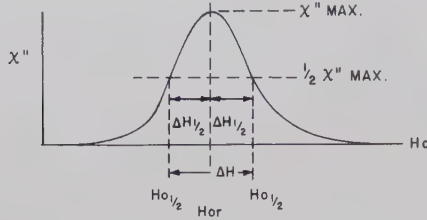


Fig. 3—Resonance curve.

The conclusion thus is that the linewidth for the isotropic ferrite and planar ferrites will be the same. In general, the entire theoretical resonance-loss curve of planar ferrites is very similar to that of the isotropic ferrites.

It is also of interest to compare the maximum of the loss-term of susceptibility in the two cases. In the case of isotropic ferrites, we have (disregarding terms in  $\alpha^2$ ),

$$\chi''_{\max} = \frac{4\pi M_s}{2\alpha H_i}.$$

In the case of planar ferrites we have

$$\chi''_{\max} = \frac{4\pi M_s}{\alpha H_i} \frac{(H_0 + H_a)^2 + H_i^2}{(2H_0 + H_a)^2}.$$

For  $H_a \gg H_0$ , we have

$$\chi''_{\max} = \frac{4\pi M_s}{\alpha H_i} = 2\chi''_{\max}.$$

Thus, the maximum value of susceptibility  $\chi''_{xx}$  in the case of planar ferrites may double that in the case of isotropic ferrites. However, the maximum value of  $\chi''_{zz}$  will be very much smaller, as shown below:

$$\frac{\chi''_{\max}}{\chi''_{\max}} = \frac{(H_0 + H_a)^2 + H_0(H_0 + H_a)}{H_0^2 + H_0(H_0 + H_a)} = \frac{H_0 + H_a}{H_0}. \quad (15)$$

### III. APPLIED FIELD PERPENDICULAR TO EASY PLANE

If the biasing field is applied perpendicular to the easy plane of magnetization, and if its magnitude is less than the anisotropy field  $H_a$ , the material will not be saturated, and the type of analysis applied above is completely inapplicable. There will very likely be do-

main in the easy plane, and susceptibility will then be caused by domain wall motion. Moreover, the anisotropies in the basal plane will now be important and complicate the picture further. There may possibly be some useful applications for such a case, but it is not intended to analyze this case in this paper.

If the biasing field is perpendicular to the easy plane and its magnitude exceeds the anisotropy field, then the material will be saturated and a straightforward analysis can be made. However, it is not intended to make this analysis in this report, as the principal attraction of planar ferrites for linear applications in the microwave region appears to lie in the fact that, by virtue of its anisotropy, the field required for resonance or other applications is much smaller than in isotropic ferrites. In the above case, the field for resonance will be much greater than that required for isotropic ferrites.

### IV. PLANE-WAVE PROPAGATION

#### A. Longitudinal Magnetization

1) *Determination of Phase Constants for Plane Waves:* From Maxwell's equations, we readily obtain

$$\nabla \times \nabla \times \vec{h} = \omega^2 \epsilon \mu_0 \vec{h} (1 + [\chi]). \quad (16)$$

The easy plane of magnetization will be taken in the  $XY$  plane, and the biasing field applied in the  $Y$  direction. Assume a plane wave propagating in the  $Y$  direction with a propagation constant  $j\beta$ . (Assume the medium to be lossless.) Then

$$\frac{\partial}{\partial x} = \frac{\partial}{\partial z} = 0$$

$$\nabla \times \nabla \times \vec{h} = \hat{x}\beta^2 h_x + \hat{z}\beta^2 h_z. \quad (17)$$

Combining (16) and (17) we get

$$\begin{aligned} \beta^2 h_x &= \beta_d^2 [h_x(1 + \chi_{xx}) + j\chi_{xz}h_z] \\ \beta^2 h_z &= \beta_d^2 [h_z(1 + \chi_{zz}) - j\chi_{xz}h_x], \end{aligned} \quad (18)$$

where  $\beta_d = \omega^2 \epsilon \mu_0$ .

Solving for  $\beta^2$  by setting the determinant of (18) to zero, yields,

$$\begin{aligned} \beta_+^2 &= \beta_d^2 \left\{ 1 + \frac{1}{2} \frac{4\pi M_s}{H_0(H_0 + H_a) - H_i^2} \cdot [2H_0 + H_a + (H_a^2 + 4H_i^2)^{1/2}] \right\} \\ \beta_-^2 &= \beta_d^2 \left\{ 1 + \frac{1}{2} \frac{4\pi M_s}{H_0(H_0 + H_a) - H_i^2} \cdot [2H_0 + H_a - (H_a^2 + 4H_i^2)^{1/2}] \right\} \end{aligned} \quad (19)$$

where

$$H_i = \frac{\omega}{|\gamma|}.$$



For a numerical example, let us take the following values:

$$\begin{aligned} f &= 10,000 \text{ Mc} & H_0 &= 300 \text{ oersteds} \\ 4\pi M_s &= 2000 \text{ gauss} & H_a &= 10,000 \text{ oersteds} \end{aligned}$$

We then obtain

$$\beta_+ = -1.3\beta_d; \quad \beta_- = 1.16\beta_d.$$

If a conventional ferrite with the same  $4\pi M_s$  value were used, the values obtained would be  $\beta_+ = 0.39\beta_d$ ;  $\beta_- = 1.5\beta_d$ . A biasing field of about 2700 and 9000 oersteds would be required for  $\beta_+$  and  $\beta_-$  respectively to reach the values given for the case of the planar ferrites.

2) *Normal Modes*: In conventional ferrites, the normal modes of propagation are the circularly polarized modes, *i.e.*,  $h_x = \pm jh_z$ , as has been shown in the literature. The normal modes of propagation in the case of planar ferrites can be obtained by substituting the values of  $\beta$  given in (19) into (18), thereby obtaining the corresponding ratios of  $h_z$  and  $h_x$ :

$$\left(\frac{h_z}{h_x}\right)_{\pm} = \frac{-j}{2H_i} [H_a \mp (H_a^2 + 4H_i^2)^{1/2}]. \quad (20)$$

We note, by multiplying out, that

$$\left(\frac{h_z}{h_x}\right)_+ \cdot \left(\frac{h_z}{h_x}\right)_- = 1.$$

Thus we see that the normal modes in planar ferrites are elliptically polarized, and the ratios of  $h_z$  and  $h_x$  for the two modes are reciprocal. It can be shown that if  $h_z$  and  $h_x$  have the ratios indicated in (20), the relation between  $\vec{b}$  and  $\vec{h}$  is scalar; *i.e.*,  $\vec{b} = \mu_{\pm} \vec{h}$  where  $\mu_{\pm}$  are the values in the parentheses in (19).

It can be readily shown that it is not possible to have Faraday rotation with planar ferrites. Faraday rotation requires that there be circular symmetry in the plane perpendicular to the direction of propagation. In the case of planar ferrites, this is manifestly not true. The nonexistence of Faraday rotation can be shown explicitly by considering a plane-polarized wave existing at one point along the direction of propagation. Numerical computation will show that the wave will be elliptically polarized at all other points except for discrete points at regular intervals along the direction of propagation.

### B. Transverse Magnetization

There are two cases to consider, depending on whether the direction of propagation is perpendicular to the plane of easy magnetization, or whether it is in the plane. Consider the former first; *i.e.*, the  $XY$  plane is the easy plane,  $H_0$  is in the  $Y$  direction, and propaga-

tion is in the  $Z$  direction. Then  $\partial/\partial x = \partial/\partial y = 0$ , and  $\partial/\partial z = -j\beta$ , where  $j\beta$  is the propagation constant:

$$\nabla \times \nabla \times \vec{h} = \hat{x}\beta^2 h_x.$$

Combining (16) and (20) we get

$$\begin{aligned} \beta^2 h_x &= \beta_d^2 [h_x(1 + \chi_{xx}) + j\chi_{xz}h_z] \\ 0 &= \beta_d^2 [h_x(1 + \chi_{xz}) - j\chi_{xx}h_z] \\ \beta^2 &= \beta_d^2 \left[ \frac{(1 + \chi_{xx})(1 + \chi_{xz}) - \chi_{xz}^2}{1 + \chi_{xz}} \right]. \end{aligned} \quad (21)$$

For propagation in the  $X$  direction we get

$$\beta^2 = \beta_d^2 \left[ \frac{(1 + \chi_{xx})(1 + \chi_{xz}) - \chi_{xz}^2}{1 + \chi_{xx}} \right]. \quad (22)$$

The quantities in brackets in (21) and (22) define an effective relative permeability for the medium for the two cases considered above.

## V. MICROWAVE APPLICATIONS

### A. Resonance Isolator: Location of Slab in Rectangular Waveguide for Minimum Absorption at Resonance for One Direction of Propagation

In the following discussion it is assumed that the volume of the slab is small, so that perturbation theory is applicable. Starting with (10), we readily derive the following:

$$\begin{aligned} \frac{m_x}{M_s} &= \frac{(H_0 + R)h_x - jH_i h_z}{(H_0 + R)(H_0 + S) - H_i^2} \\ \frac{m_z}{M_s} &= \frac{jH_i h_x + (H_0 + S)h_z}{(H_0 + R)(H_0 + S) - H_i^2} \\ R &= H_a + M_s(N_x - N_y); \quad H_i = \frac{\omega}{|\gamma|} \\ S &= M_s(N_x - N_y). \end{aligned} \quad (23)$$

The denominator in (23) will equal zero at a value of  $H_0$  given in (24):

$$H_0 = -\frac{R+S}{2} + \frac{1}{2} [(R+S)^2 - 4(RS - H_i^2)]^{1/2}. \quad (24)$$

For the above value of  $H_0$ ,  $m_x$  and  $m_z$  will tend to be extremely large. However, for a particular ratio of  $h_x$  to  $h_z$ , the numerators of (23) will be zero. Let  $b$  be defined so that  $h_z = -jbh_x$ . Setting the numerator of either of the equations in (23) to zero, and substituting the value of  $H_0$  given in (24), we get

$$b = \frac{1}{2H_i} [\sqrt{(R+S)^2 - 4(RS - H_i^2)} + (R-S)]. \quad (25)$$

Assuming a thin slab in the configuration of Fig. 4(a), we have  $N_x = N_y = 0$ ;  $N_z = 4\pi$ ;

$$b = \frac{1}{2H_i} [H_a + 4\pi M_s + \sqrt{(H_a + 4\pi M_s)^2 + 4H_i^2}]. \quad (26)$$

As a numerical example, let  $H_a = 10,000$  oersteds,  $4\pi M_s = 3000$  gauss, with an operating frequency of 15,000 Mc. The value of  $b$  comes out to be 2.78. The distance  $d$  can now be readily determined by finding the location in the (unperturbed) waveguide at which  $h_z$  and  $h_x$  have the desired ratio.

If  $H_a = 0$ , then  $b = 1.31$ . Thus, in the case of planar ferrites, the location of the slab is considerably closer to the center of the waveguide than in the case of isotropic ferrites.

Consider next the slab shown in Fig. 4(b). The easy plane is perpendicular to the plane of the slab. Eq. (25) applies in this case, too. However, whereas in the first case,  $b$  is the ratio of transverse to longitudinal RF magnetic fields, in the second case,  $b$  is the ratio of the longitudinal to transverse fields. For a thin slab,  $N_x = 4\pi$ ,  $N_y = N_z = 0$ . Eq. (25) now becomes

$$b = \frac{1}{2H_i} [H_a - 4\pi M_s + \sqrt{(H_a - 4\pi M_s)^2 + 4H_i^2}]. \quad (27)$$

The location of the slab for a resonance isolator will now be closer to the narrow wall than in the case of isotropic ferrites.

The third and fourth cases are illustrated in Figs. 4(c) and 4(d). Eq. (25) applies,  $N_x = N_z = 0$ ;  $N_y = 4\pi$ ;

$$b = \frac{1}{2H_i} [H_a + \sqrt{H_a^2 + 4H_i^2}]. \quad (28)$$

As in the case of isotropic ferrites, the ratio of transverse to longitudinal  $h$  fields for minimum absorption is the same as in the infinite medium.

It is of interest to consider how the location for minimum absorption at resonance for the third and fourth cases varies as a function of frequency. To do this, it is necessary to decompose the RF magnetic fields in the waveguide into the normal modes given in (20):

$$h_x + jh_z = P(b + j) + Q(1 - jb).$$

$(b + j)$  corresponds to the plus sign in (20) and will be designated as positive polarization;  $(1 - jb)$  then corresponds to negative polarization:

$$P = \frac{bh_x + h_z}{1 + b^2}, \quad Q = \frac{h_x - bh_z}{1 + b^2}.$$

A plot of the distribution of positive and negative polarization ( $P$  and  $Q$ ) as a function of frequency is shown in Fig. 5.<sup>10</sup>  $H_a$  was taken as 10,000 oersteds; all the curves have been normalized so that  $Q = 1$  when  $P = 0$ .

<sup>10</sup> For isotropic ferrites compare Fig. 26 in, A. G. Fox, S. E. Miller and M. T. Weiss, "Behavior and applications of ferrites in the microwave region," *Bell Syst. Tech. J.*, vol. 34, p. 5; January, 1955.

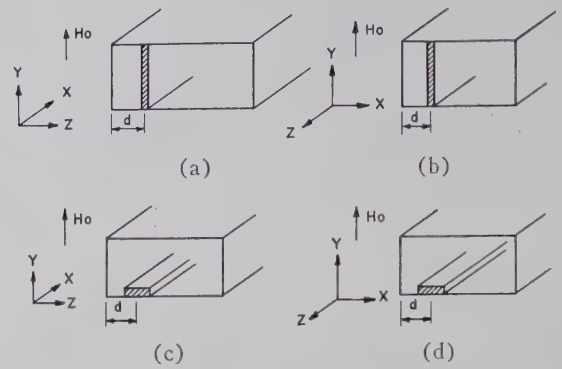


Fig. 4—Planar ferrite slabs in rectangular waveguide;  $XY$  plane is easy plane.

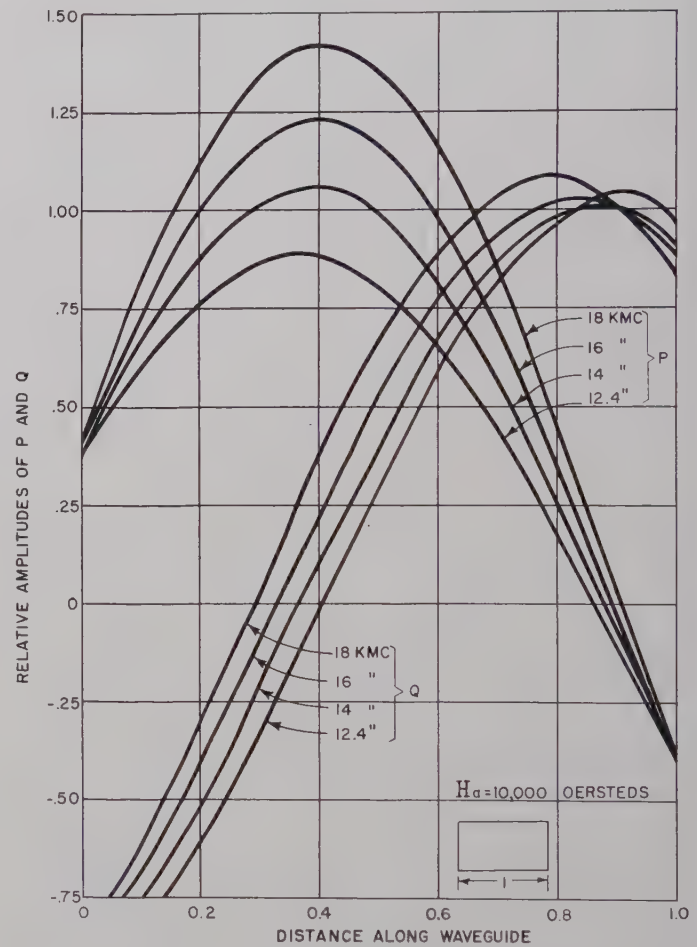


Fig. 5—Distribution of positive and negative elliptical polarization, in rectangular waveguide.

When the easy plane is oriented as in Fig. 4(c) (easy plane parallel to waveguide axis), then the location of the point of minimum absorption is given by the intersection of the  $Q$  curves with the horizontal zero axis. When the easy plane is oriented as in Fig. 4(d) (easy plane perpendicular to waveguide axis), the location of the point of minimum absorption is given by the intersection of the  $P$  curves with horizontal zero axis. It is apparent that the spread in the  $P$  curve intersections is far less than that of the  $Q$  curves, and also less



than the corresponding spread for isotropic ferrites. This means that an isolator using planar ferrites with the easy plane perpendicular to the waveguide axis will be more broad-band than an isolator using isotropic ferrites, with respect to the shift in the location of the absorption minimum. Schlömann arrived at the same conclusion by a somewhat different approach.<sup>11</sup>

### B. Phase Shifter

We will consider only the case of a thin slab in the geometry shown in Fig. 4(a), where the easy plane of magnetization is in the plane of the slab. We will also assume that the slab is thin enough so that perturbation theory can be applied. In this case, the phase shift will be proportional to the change in susceptibility, and we need therefore consider only the change in susceptibility as a function of applied field.

Using (11) we can write,

$$\chi_{xx} = 4\pi M_s \frac{H_0 + H_a + 4\pi M_s}{H_0(H_0 + H_a + 4\pi M_s) - H_i^2}.$$

Consider first that we are operating well below resonance. Then

$$\frac{\Delta\chi_{xx}}{\Delta H_0} = - \frac{4\pi M_s}{H_i^2}. \quad (29)$$

This is the same as for an isotropic ferrite with the same magnetization. However,  $H_0$  will be limited to smaller values in the case of planar ferrites, and so the total possible phase shift is smaller. Thus, planar ferrites are not as desirable as isotropic ferrites in this manner of operation.

Eq. (29) assumes the material is saturated. If  $H_0$  is zero, the material will be unsaturated, and the susceptibility will be zero, or close to zero. The application of a small field that is just enough to saturate the material will change the susceptibility to

$$\frac{4\pi M_s(H_a + 4\pi M_s)}{H_i^2}.$$

The ratio of this change of susceptibility to applied field will be much greater than that indicated in (29). This mode of operation may lead to more efficient phase shifters. The slab should be up against the narrow wall for this mode of operation.

Suppose now that we are operating well above resonance. Then

$$\chi_{xx} = \frac{4\pi M_s}{H_0}. \quad (30)$$

$\Delta\chi_{xx}/\Delta H_0$  will be much larger for planar ferrites than for isotropic ferrites, since  $H_0$  is smaller in the case of

planar ferrites. However, the more interesting comparison is between planar ferrites above resonance and isotropic ferrites below resonance. Let us call the ratio of change of susceptibility to change of applied field, the sensitivity of the phase shifter. The ratio of the sensitivity of the planar ferrite phase shifter to that of an isotropic ferrite phase shifter is equal to  $(H_i/H_0)^2$ , where  $H_i$  is equal to  $\omega/|\gamma|$  and  $H_0$  is the applied field for planar ferrites. Since  $H_i$  will be generally greater than  $H_0$ , the planar ferrite phase shifter will be more sensitive.

### C. Switches

Planar ferrites may be advantageous for use in switches that operate on the principle of biasing the ferrite to resonance for the OFF position and removing the bias for the ON position, since the switching field is considerably smaller than for isotropic ferrites.

### D. Harmonic Generation

Jepsen<sup>12</sup> shows that the efficiency of a ferrite in generating harmonics can be greatly enhanced if the ferrite is asymmetrical in the plane perpendicular to the direction of magnetization. He gives a formula quantitatively expressing this enhancement<sup>13</sup> and shows that it is proportional to the saturation magnetization multiplied by the difference in the demagnetizing factors in the plane perpendicular to the direction of magnetization. It has been noted above (Sec. II-B) that the anisotropy field behaves in the same way as does the inequality of demagnetizing factors. However, since the anisotropy field can greatly exceed the maximum field due to the inequality of demagnetizing factors, it is apparent that planar ferrites with high anisotropies are much more efficient harmonic generators than are isotropic ferrites.

Jepsen's equation<sup>13</sup> can be rewritten to take anisotropy into account. The result is

$$F = \frac{2}{\alpha} [H_a + M_s(N_z - N_x)] \cdot \frac{H_0 + H_a + M_s(N_z - N_y)}{(2H_0 + H_z + M_s(N_x + N_z - 2N_y))^2}. \quad (31)$$

$F$  is the ratio of second-harmonic amplitude when there is asymmetry in the plane perpendicular to the direction of magnetization, to the amplitude when there is symmetry. The demagnetizing factors can be used to augment the anisotropy field to obtain efficient harmonic generation. Best results are obtained when  $N_z = 4\pi$ ,  $N_x = N_y = 0$ . For this case,

$$F = \frac{2}{\alpha} \times \frac{G(H_0 + G)}{(2H_0 + G)^2}, \quad (32)$$

<sup>11</sup> E. Schlömann, "On the theory of the ferrite resonance isolator," IRE TRANS. ON MICROWAVE THEORY AND TECHNIQUES, vol. 8, p. 199; March, 1960.

<sup>12</sup> R. L. Jepsen, "Harmonic Generation and Frequency Mixing in Ferromagnetic Insulators," Gordon McKay Lab., Harvard University, Cambridge, Mass., Scient. Rept. No. 15; 1958.

<sup>13</sup> *Ibid.*, eq. 5-31, p. 54.

where  $G = (H_a + 4\pi M_s)$ . At a frequency of 70 kMc, and taking  $G = 30,000$  gauss (approximate values for  $\text{Co}_2\text{Y}$ ),  $\alpha = 0.02$ ,  $F$  comes out to be 39. If  $G$  were 15,000 gauss,  $F$  would be approximately one half the above value.

## VI. EXPERIMENTAL DATA

The experimental data given in this section are intended primarily to illustrate the equations derived above. It is not intended to give comprehensive data on the properties of available planar ferrites or to detail design data on devices. As noted previously, all polycrystalline samples were oriented.

### A. Measurement of Material Properties

1) *Preparation and Mounting of Samples:* Measurements were made using small spheres and wafers. The spheres were ground from rough-cut cubical samples by placing them in a glass tube perpendicular to a rapidly rotating abrasive wheel, as described by Carter, *et al.*<sup>14</sup> The diameter was approximately 40 mils. As might be expected from the magnetic anisotropy, there was also an anisotropy in the hardness, and the samples had ellipticities of approximately 10 per cent. This degree of ellipticity has only a very small effect and so it was disregarded.

The spheres were mounted on small polystyrene rods with the easy plane parallel to the axis of the rod. This was accomplished as follows: The sphere was placed on a glass platform and a permanent magnet placed underneath; the sphere thus automatically oriented itself so that the easy plane was perpendicular to the platform. A very small amount of vinyl adhesive was placed on the tip of the rod and the rod placed on top of the sphere. The magnet was removed and the rod could now pick up the sphere. The magnet was then placed on top of the platform and the rod, with the sphere on it, was placed underneath and remained there until the adhesive hardened.

The dimensions of the wafers were approximately  $50 \times 50 \times 10$  mils. They were mounted on rods in the same way as were the spheres.

2) *Determination of Ferromagnetic Resonance Curves:* Ferromagnetic resonance curves were obtained for both the spheres and wafers. Measurements were generally made in a rectangular cavity, using the setup shown in Fig. 6. The signal generators used were the Hewlett-Packard Models 626A and 628A, which contained accurate variable attenuators.

In the case of the sphere, the rod containing the ferrite was inserted in the opening on the broad face of the cavity. Since the sphere was oriented on the rod so that

the easy plane was parallel to the rod, rotating the rod could bring the easy plane parallel or perpendicular to the RF magnetic field, as desired. The proper rotation of the rod for these conditions was determined by setting the biasing field to the value required for resonance and rotating the rod so as to bring the transmitted power to a minimum (easy plane parallel to RF field) or to a maximum (easy plane perpendicular to RF field).

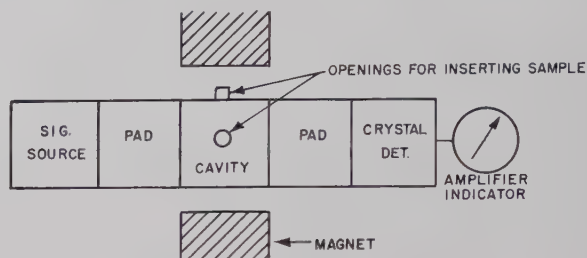


Fig. 6—Test setup for ferromagnetic resonance.

Two wafers were tested. One had the easy plane in the plane of the wafer. This was mounted on a rod with the plane of the wafer parallel to the rod. The rod was inserted through the opening on the broad face of the cavity and rotated so that the easy plane was parallel to the RF magnetic field. This was designated Case 1. The second wafer had the easy plane perpendicular to the plane of the wafer. This wafer was mounted on a rod with the plane of the wafer and the easy plane both parallel to the rod. This wafer was inserted in the opening on the broad face of the cavity and rotated so that the easy plane was parallel to the RF magnetic field. (See discussion above.) This was designated Case 2. The same wafer was then inserted in the opening on the narrow face of the cavity and rotated so that the easy plane was parallel to the biasing field. This was designated Case 3.

In some cases, where the losses at resonance were too high, the sample was measured by placing it at a position of maximum  $h$  field in a shorted transmission line, and by measuring the VSWR as a function of applied field. The shorted transmission line had openings for inserting the ferrite on the broad and narrow walls, as did the cavity.

Some of the curves obtained are shown in Figs. 7–9. The other curves are similar.

3) *Anisotropy Field:* The anisotropy was determined from the resonance curves of spheres or wafers. For spheres, the resonance condition given in (7) is used; *i.e.*,  $H_0(H_0 + H_a) = (\omega/\gamma)^2$ . The wafer tested had the easy plane in the plane of the wafer and was oriented so that the RF field was parallel to the easy plane. Taking into account the geometry of the wafer, the resonance condition is given by  $H_0[H_0 + H_a + 0.62(4\pi M_s)] = (\omega/\gamma)^2$ . The value of  $\gamma$  was taken as 2.8 Mc/oersted.

<sup>14</sup> J. L. Carter, E. V. Edwards and I. Reingold, "Ferrite sphere grinding technique," *Rev. Sci. Instr.*, vol. 30, p. 946; October, 1959.



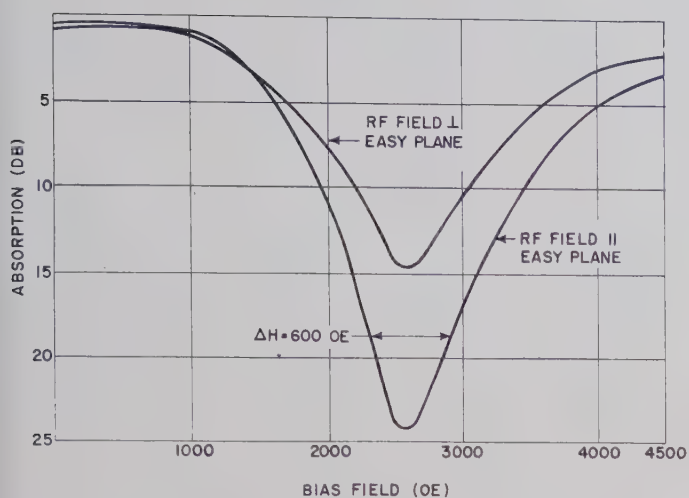


Fig. 7—Ferromagnetic resonance curves of  $\text{Zn}_2\text{Y}$  sphere at 14.9 kMc.

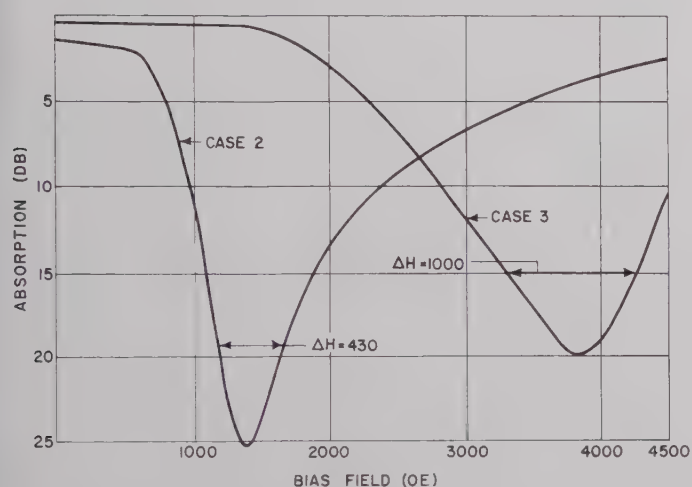


Fig. 8—Ferromagnetic resonance curves of wafers of  $\text{Zn}_2\text{Y}$  at 14.9 kMc.

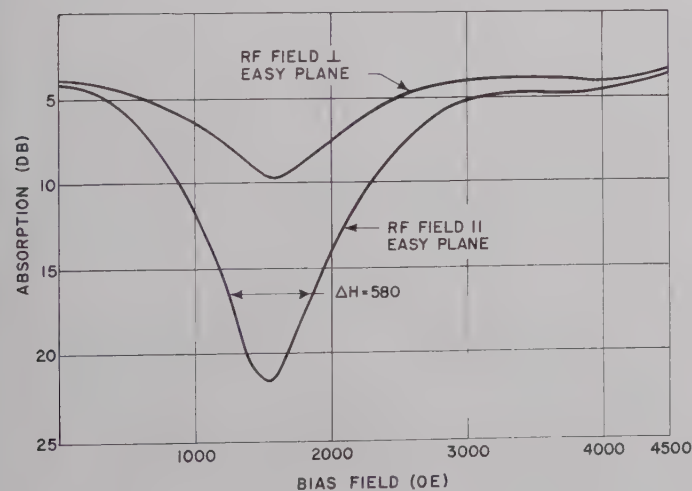


Fig. 9—Ferromagnetic resonance curves of  $\text{Ni}_2\text{Y}$  sphere at 14.9 kMc.

In Table II is a tabulation of the results obtained on polycrystalline samples. The  $\text{Co}_2\text{Y}$  was in the shape of a wafer; the others were spheres.

Single crystals of  $\text{Zn}_2\text{Y}$  were also measured.<sup>15</sup> Apparently the crystals were not perfect, since the measured values ranged from 8900 to 10,000 oersteds. Values of anisotropy field of  $\text{Zn}_2\text{Y}$ ,  $\text{Ni}_2\text{Y}$ , and  $\text{Co}_2\text{Y}$  given by Smit and Wijn<sup>1</sup> are 9000, 14,000, and 28,000 oersteds, respectively. A torsion pendulum was used to obtain these values. Chemical compositions of the above materials are also given by Smit and Wijn.<sup>1</sup>

4) *Susceptibility Ratio*: Eq. 15 gives a theoretical formula for the ratio  $\chi''_{xx}/\chi''_{zz}$  at resonance. This formula was checked experimentally. The formula used to calculate the experimental ratio is given below:

$$\left(\frac{\chi''_{xx}}{\chi''_{zz}}\right)_{\text{exper}} = \frac{\left(\frac{V_0}{V_r}\right)_{xx} - 1}{\left(\frac{V_0}{V_r}\right)_{zz} - 1}, \quad (33)$$

where  $20 \log_{10} (V_0/V_r)$  is equal to the decrease in transmitted output at resonance, expressed in decibels. The results are in Table III.

TABLE II

Material	Frequency (kMc)	$H_a$ (oe)
$\text{Zn}_2\text{Y}$	10.8	9200
$\text{Zn}_2\text{Y}$	13.0	8400
$\text{Zn}_2\text{Y}$	14.9	8500
$\text{Zn}_2\text{Y}$	17.0	8400
$\text{Ni}_2\text{Y}$	13.0	17,100
$\text{Ni}_2\text{Y}$	14.9	17,200
$\text{Ni}_2\text{Y}$	17.0	16,700
$\text{Co}_2\text{Y}$	20.0	40,000

TABLE III

Material	Frequency (kMc)	Theoretical Ratio	Experimental Ratio	Theoretical/Experimental
$\text{Zn}_2\text{Y}$ (polyxtal)	10.8	7.6	4.3	1.76
$\text{Zn}_2\text{Y}$ (polyxtal)	13.0	5.2	4.2	1.24
$\text{Zn}_2\text{Y}$ (polyxtal)	14.9	4.3	3.5	1.23
$\text{Zn}_2\text{Y}$ (polyxtal)	17.0	3.7	3.0	1.23
$\text{Ni}_2\text{Y}$ (polyxtal)	14.9	12.3	6.9	1.78
$\text{Ni}_2\text{Y}$ (polyxtal)	17.0	9.5	5.4	1.75
$\text{Zn}_2\text{Y}$ (singlextal)	14.9	4.95	4.95	1.00
$\text{Zn}_2\text{Y}$ (singlextal)	14.9	5.35	4.95	1.08

It is noted that the theoretical ratio is always equal to or larger than the experimental ratio. This to be expected, since any misalignment will tend to decrease  $\chi''_{xx}$  and increase  $\chi''_{zz}$ . The single crystals show much better agreement between theoretical and experimental ratios since they are much better aligned.

<sup>15</sup> The single crystals were grown at USADRD, and are the results of the first attempt at preparing them. The work is continuing.

In the case of  $\text{Ni}_2\text{Y}$  there was a considerable amount of absorption not associated with the main resonance. This spurious absorption was excluded in calculating the experimental ratio (Fig. 9).

5) *Linewidth*: Linewidth was measured on the spheres and wafers. The results for the polycrystalline samples are tabulated in Table IV. In all cases the samples were aligned so that the easy plane was parallel to the RF magnetic field. The sphere and wafers of the  $\text{Zn}_2\text{Y}$  came from the same parent body.

It may be noted that the linewidth changes appreciably with frequency, particularly in the case of  $\text{Ni}_2\text{Y}$ . Also, there is a more than 2:1 change in the linewidth of a given wafer when measured per Case 2 or Case 3.

The linewidth of spheres of single crystals of  $\text{Zn}_2\text{Y}$  varied from 210 to over 300. The linewidth of a wafer of a single crystal  $\text{Zn}_2\text{Y}$  was 170 and 330 oersteds when measured per Case 2 and Case 3, respectively.

### B. Measurement on Devices

1) *Phase Shifter*: A phase shifter was made using  $\text{Zn}_2\text{Y}$ . The sample was 1.5 inches long, 0.290 inch high, and 0.20 inch wide. The easy plane was parallel to the length of the sample. The sample was placed against the narrow wall of the waveguide. The test frequency was 15 kMc. The results are shown in Table V. Phase shift is with respect to phase at zero magnetic field.

2) *Isolator*: An isolator was made using  $\text{Zn}_2\text{Y}$ . The sample was 5/8 inch long and 0.05×0.05 inch in cross section. The easy plane was perpendicular to the waveguide axis. The optimum location of the sample for best front-to-back ratio over the full waveguide band was found to be such that the center of the cross section was 0.078 inch from the waveguide wall. The test results are shown in Table VI. The field was tuned for resonance in the reverse direction in each case.

A similar sample of  $\text{Zn}_2\text{Y}$ , but with the easy plane parallel to the waveguide axis, was also tested. It was not possible to find any location for the sample where the forward loss was low for the entire band. If the center of the sample was 0.177 inch from the narrow waveguide wall, the forward losses were low from 15 to 18 kMc, but high at the low frequencies. If the center of the sample was 0.204 inch from the narrow waveguide wall, the forward losses were low from 12.4 to 15 kMc, but high at the higher frequencies.

The above test data corroborate the discussion in Sec. V of this paper concerning the effect of the orientation of the easy plane on the broad-banding of the isolator.

TABLE IV

Material	Frequency (kMc)	Shape	Case	Line Width (oe)
$\text{Zn}_2\text{Y}$	10.8	Sphere	—	530
$\text{Zn}_2\text{Y}$	13.0	Sphere	—	570
$\text{Zn}_2\text{Y}$	14.9	Sphere	—	600
$\text{Zn}_2\text{Y}$	17.0	Sphere	—	600
$\text{Zn}_2\text{Y}$	14.9	Wafer	1	520
$\text{Zn}_2\text{Y}$	14.9	Wafer	2	430
$\text{Zn}_2\text{Y}$	14.9	Wafer	3	1000
$\text{Ni}_2\text{Y}$	13.0	Sphere	—	500
$\text{Ni}_2\text{Y}$	14.9	Sphere	—	580
$\text{Ni}_2\text{Y}$	17.0	Sphere	—	640
$\text{Ni}_{1.2}\text{Cu}_{0.2}\text{Zn}_{1.6}\text{Y}$	13.7	Wafer	1	325

TABLE V

Field (oe)	Phase Shift (degrees)
225	6
340	8
430	10
530	12

TABLE VI

Frequency (kMc)	Forward Loss (db)	Reverse Loss (db)	Field (oe)
12.4	0.10	1.55	1850
13	0.09	1.57	2050
14	0.08	1.60	2350
15	0.08	1.70	2650
16	0.10	1.82	3000
17	0.10	1.82	3350
18	0.10	1.95	3750

### ACKNOWLEDGMENT

RCA, Princeton, N. J. has a contract with the Signal Corps for the development of planar ferrites, and the polycrystalline materials described herein were prepared by them. The author is grateful for the cooperation of R. L. Harvey, I. Gorden, and R. Braden, and the many stimulating discussions with them. Some of the measurements were made at RCA. The Contract number is DA36-039 sc-78288.

This material, though part of a regular Signal Corps project, is also being used by the author in connection with graduate studies in the Electrical Engineering Department at Rutgers University, New Brunswick, N. J. The cooperation and assistance of Professor M. Sirkis of Rutgers is appreciated.

The author was assisted in "getting off the ground" by notes given him by Professor R. V. Jones of Harvard. Sections II-A and IV-A are based on these notes.



# Wide-Band Resonance Isolator\*

W. W. ANDERSON†, MEMBER, IRE, AND M. E. HINES‡, MEMBER, IRE

**Summary**—A parallel-plate transmission line loaded with capacitors or high dielectric constant material along a narrow strip has a circularly polarized RF magnetic field everywhere external to the loading over a very broad band. The magnetic resonance line of a narrow linewidth ferrite was inhomogeneously broadened by a very inhomogeneous magnetic field to provide resonance absorption over a wide frequency range. A prototype structure has given better than 15 db per inch attenuation in the reverse direction over a bandwidth from 1.5 kMc to 6.0 kMc. The forward loss caused by the ferrite is about 0.2 db to 0.4 db over this range of operation.

## I. INTRODUCTION

A GENERAL rule for developing microwave devices is—once it works, broad-band it. Isolators are no exception to this rule. The development of broad-band resonance isolators is characterized by the work of Weiss<sup>1</sup> and Duncan, Swern, Tomiyasu, and Hannwacker.<sup>2</sup> The latter authors describe a device which operates over an octave bandwidth beginning at 2 kMc. Recently, Jones, Matthaei and Cohn<sup>3</sup> described a broad-band isolator using the Faraday rotation effect in a ferrite.

In studying the propagation of TE waves between parallel plates, it is found that the RF magnetic field is elliptically polarized if the wave is slowed down by some smooth or fine-grained structure along the direction of propagation. In particular, the polarization may be made to approach arbitrarily close to circular polarization for sufficient slowing of the wave. The ratio of transverse to longitudinal components of the RF magnetic field is given by

$$\frac{H_x}{H_z} = \frac{-j}{\sqrt{1 - \frac{k^2}{\beta^2}}}, \quad (1)$$

where  $\beta$  is the propagation constant along the structure and  $k$  is the free-space propagation constant. For infinite parallel plates, this relation holds everywhere external to the slowing structure! Thus, for all frequencies for which  $\beta \gg k$ , we will have nearly perfect circular polarization.

\* Received by the PGM-TT, June 28, 1960; revised manuscript received, August 25, 1960.

† Electronics Lab., Stanford University, Stanford, Calif. Formerly Bell Telephone Labs., Murray Hill, N. J.

‡ Microwave Associates, Burlington, Mass. Formerly Bell Telephone Labs., Murray Hill, N. J.

<sup>1</sup> M. T. Weiss, "Improved rectangular waveguide resonance isolators," IRE TRANS. ON MICROWAVE THEORY AND TECHNIQUES, vol. MTT-4, pp. 240-243; October, 1956.

<sup>2</sup> B. J. Duncan, L. Swern, K. Tomiyasu, and J. Hannumacher, "Design considerations for broadband ferrite coaxial line isolators," Proc. IRE, vol. 45, pp. 483-490; April, 1957.

<sup>3</sup> E. M. T. Jones, G. L. Matthaei, and S. B. Cohn, "A nonreciprocal, TEM-mode structure for wide band gyrator and isolator applications," IRE TRANS. ON MICROWAVE THEORY AND TECHNIQUES, vol. MTT-7, pp. 453-460; October, 1959.

Given circular polarization, how do we obtain broad-band resonance isolation? This problem is considered in Section III of this paper. Fortunately, it is possible to broaden inhomogeneously the ferrimagnetic resonance line of a ferrite in such a way that strong absorption takes place at locations in the structure where the various frequency RF components are strong.

## II. THE SLOW WAVE STRUCTURE

Two possible slow wave structures have been considered for this isolator. They are shown in Fig. 1. In all cases, we will only be interested in the lowest order TE mode. All field quantities will be assumed to vary as  $\exp [j(\omega t - \beta z) - \sqrt{\beta^2 - k^2} |x|]$ . For the capacitively loaded line, we find

$$\beta \approx \frac{\omega^2 \mu_0 h C}{2}, \quad (2)$$

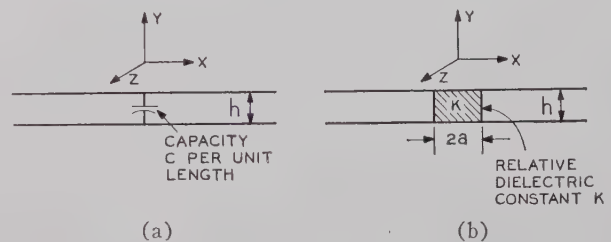


Fig. 1—Slow wave structures in parallel-plane transmission line.

where  $\mu_0$  is the permeability of the medium external to the capacity loading,  $h$  is the height of the guide, and  $C$  is the capacitance per unit length. Note that

$$\frac{\beta}{k} = \sqrt{\frac{\mu_0}{\epsilon_0}} \frac{\omega C h}{2}, \quad (3)$$

so that by (1), the circularity of the polarization improves with increasing frequency. However, by the  $x$  dependence of the field quantities,  $\exp [-\sqrt{\beta^2 - k^2} |x|]$ , it is seen that the higher frequency fields are bound more closely to the center of the line.

Several authors have derived expressions for the RF fields for the dielectric loaded line.<sup>4,5</sup> In this case, the expression for the propagation constant,  $\beta$ , involves the solution of the transcendental equation

<sup>4</sup> D. Fleri and G. Hanley, "Nonreciprocity in dielectric loaded TEM mode transmission lines," IRE TRANS. ON MICROWAVE AND TECHNIQUES, vol. MTT-7, pp. 23-27; January, 1959.

<sup>5</sup> M. Cohn, "Propagation in a dielectric-loaded parallel plane waveguide," IRE TRANS. ON MICROWAVE THEORY AND TECHNIQUES, vol. MTT-7, pp. 202-208; April, 1959.

$$\tan \sqrt{K - \frac{\beta^2}{k^2}} ka = \sqrt{\frac{\frac{\beta^2}{k^2} - 1}{K - \frac{\beta^2}{k^2}}} \quad (4)$$

for the lowest-order TE mode. The ratio  $\beta/k$  is shown as a function of  $\sqrt{K} ka$  with  $K$  as a parameter in Fig. 2.  $K$  is the relative dielectric constant of the center section of the guide. Higher-order TE modes occur for

$$\sqrt{K - 1} ka = \frac{n\pi}{2} \quad (5)$$

which reduces to

$$\sqrt{K} ka \approx \frac{n\pi}{2} \quad (6)$$

for  $K \gg 1$ . Hybrid modes may be removed to an arbitrarily high frequency by reducing the height of the guide.<sup>5</sup>

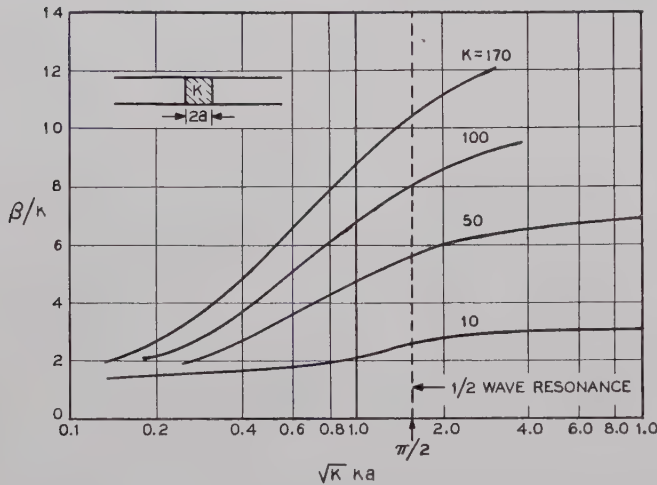


Fig. 2—Slowing factor  $\beta/k$  for various degrees of dielectric loading of parallel-plane transmission line.

For the case of  $K=100$  (typical of  $\text{TiO}_2$  in ceramic form), it is possible to obtain  $\beta/k > 3$  over more than two octaves before problems of higher order modes come in. This type of moding problem does not exist for a guide loaded with ideal capacitors. As in the capacitively loaded guide, high frequency fields are bound closer to the dielectric than low frequency fields.

Expressions for the RF field components and the effects of finite guide width are given in the Appendix. The presence of open-circuit or short-circuit walls at the edge of the guide has little effect if

$$\exp[-\sqrt{\beta^2 - k^2} b] \ll 1,$$

where  $b$  is the halfwidth of the guide. Short-circuit walls introduce a low-frequency cutoff in the propagation characteristic.

An approximation to the capacitively loaded line may be made by capacitive posts. The heavily dielectric-loaded structures may use  $\text{TiO}_2$  ( $K \approx 100$ ), for the dielectric. This material may have a loss tangent of the order of  $10^{-3}$  at microwave frequencies.<sup>6</sup>

### III. THE FERRITE STRUCTURE

The high-frequency RF fields are concentrated near the slowing structure while the lower frequency fields may extend to large distances from the center of the transmission line. It is possible to introduce ferrite slabs next to the slowing structure and bias them in such a way that high-frequency resonance absorption occurs near the center of the line and low-frequency resonance absorption occurs away from the center of the line.

Consider the magnetic pole configuration of Fig. 3.

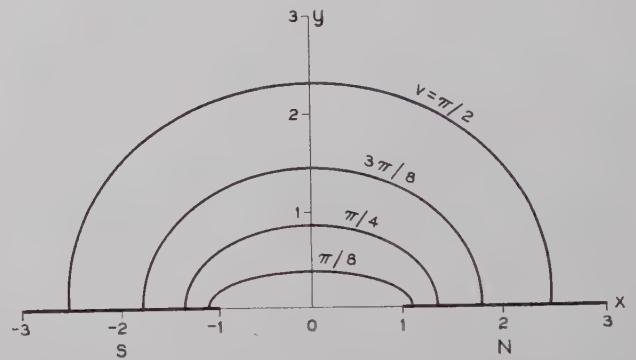


Fig. 3—Magnetic-pole shape and lines of constant magnetic field intensity.

The lines of flux,  $v = \text{constant}$ , are given by<sup>7</sup>

$$\frac{x^2}{\cosh^2 v} + \frac{y^2}{\sinh^2 v} = 1. \quad (7)$$

At  $y=0$  the magnetic field is perpendicular to the plane of the poles, and the relative magnetic field intensity as a function of  $x$ , the distance from the center, is given by

$$H_0(x) = \frac{M_0}{2 \times E}, \quad (8)$$

where  $M_0$  is the pole strength and  $E$  is the complete elliptic integral

$$E = \int_0^{\pi/2} \sqrt{1 - \tanh^2 v \sin^2 \theta} d\theta \quad (9)$$

and

$$v = \cosh^{-1} x. \quad (10)$$

For a "thin" ferrite slab directly above the magnetic poles, the magnetic field will be perpendicular to the ferrite slab and of intensity given by (8). When the

<sup>6</sup> A. R. Von Hippel, "Dielectric Materials and Applications," John Wiley and Sons, Inc., New York, N. Y., pp. 304-305; 1954.

<sup>7</sup> S. Ramo and J. R. Whinnery, "Fields and Waves in Modern Radio," John Wiley and Sons, Inc., New York, N. Y., p. 136; 1953.



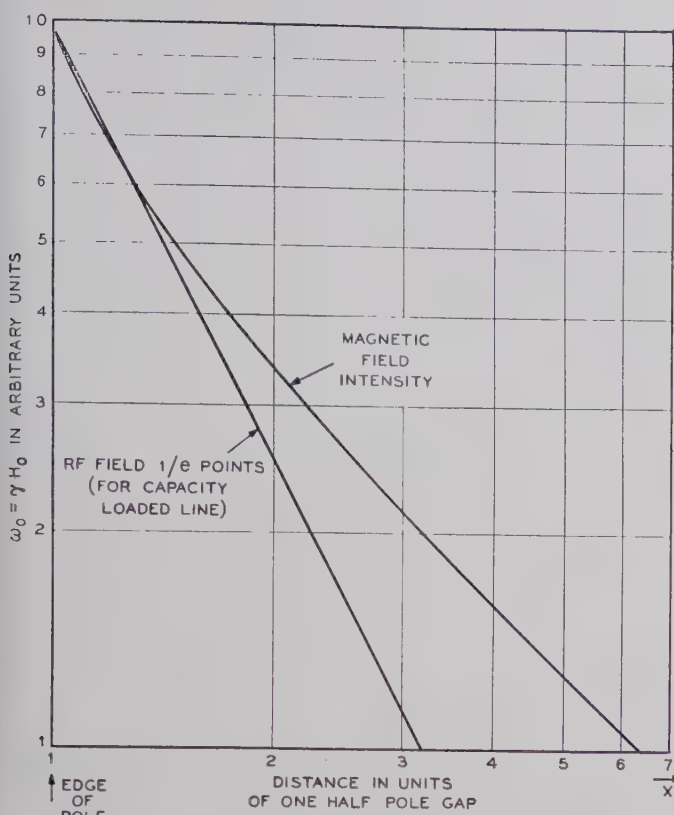


Fig. 4—Relative magnetic field intensity for pole configuration of Fig. 3.

demagnetizing factor for a flat plate<sup>8</sup> is included, the resonance condition is given by

$$\omega_0 = \gamma[H_0(x) - 4\pi M_s], \quad (11)$$

where  $4\pi M_s$  is the saturation magnetization. A plot of  $H_0$  as a function of distance from the edge of the magnetic pole gap is given in Fig. 4. Also, a line is shown representing the  $1/e$  amplitude points of the RF field in the  $\beta \gg k$  region for  $\beta \sim \omega^2$ .

#### IV. EXPERIMENTAL RESULTS

Isolators using both capacitive and dielectric slowing have been constructed and tested. The resultant structures are shown in Fig. 5. The capacitively-loaded structure consisted of a parallel plate line 0.025 inch high with an  $8 \mu\mu\text{f}$  post spaced every 0.065 inch which gave an upper cutoff frequency of about 7 kMc, as would be expected from (3). To obtain this high capacity, it was necessary to have a gap between the post and bottom plate of only 0.00025 inch. A thin sheet of mylar was used to give this spacing. The dielectric-loaded structure used a slab of ceramic rutile ( $\text{TiO}_2$ ,  $K \approx 100$ ), 0.075 inch wide by 0.025 inch high.

The ferrites used in these experiments were flat plates in the shape of isosceles trapezoids with bases of 1.25 inches and 2.0 inches, an altitude of 0.375 inch, and

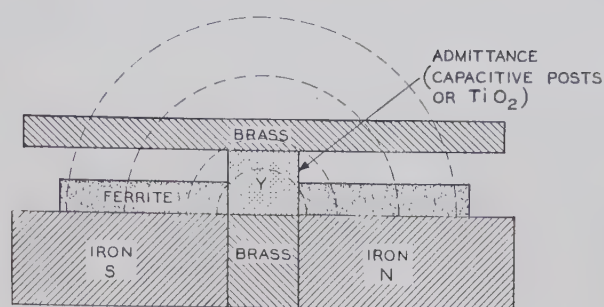


Fig. 5—Cross section of isolator.

a thickness of 0.020 inch. Three ferrite materials were used. All were polycrystalline and had a saturation magnetization,  $4\pi M_s$ , of the order of 500 gauss. The first sample was a magnesium aluminum-manganese ferrite ( $\text{Mg}_{1.0}\text{Al}_{0.6}\text{Fe}_{1.35}\text{Mn}_{0.1}\text{O}_4$ ) with a linewidth of 500 oersteds. The other two samples were aluminum substituted yttrium-iron garnet ( $3\text{Y}_2\text{O}_3 \cdot \text{Al}_2\text{O}_3 \cdot 4\text{Fe}_2\text{O}_3$ ). One YIG sample had a linewidth of 15 oersteds and the other a linewidth of 50 oersteds.

The behavior of all three ferrite materials was remarkably similar. The forward and reverse transmission through the structure as a function of magnetic field (arbitrary units) are shown in Fig. 6. This is data for the capacitive post structure with ferrite slabs on both sides of the posts. The ferrite in this case is the YIG sample with a 15-oersted linewidth. This material seemed to give slightly better results than the other materials. If we choose an operating magnetic field corresponding to the arrow in Fig. 6, an isolation vs frequency curve results, as shown in Fig. 7. Reverse attenuation curves for all three ferrites are shown in Fig. 8. For this last set of data the ferrite was placed on only one side of the structure, resulting in about one-half the isolation shown in Fig. 7.

The very low forward loss indicated in Figs. 7 and 9 is caused by the presence of the ferrite alone. This forward loss was determined by observing the change in transmitted power as the ferrite was removed from the structure. In all this work, it is important to realize that only the characteristics of the isolation mechanism are under consideration. Thus, a 0.3- to 0.5-db copper loss has been subtracted from the data, as well as input and output mismatch losses. We did not attempt to build a broad-band match into the test structures. At frequencies where high input and output VSWR's tended to mask the transmission characteristics of interest, tuning stubs were used to reduce input and output reflection coefficients.

The experiments to date with the dielectric-loaded isolator have yielded data similar to that of the capacity-loaded structure. A typical set of data for this case is shown in Fig. 9. The YIG sample with a 15-oersted linewidth was used here. Short tapers were used to provide some impedance matching, but the reflections from the structure were still appreciable.

<sup>8</sup> C. Kittel, "On the theory of ferromagnetic resonance absorption," *Phys. Rev.*, vol. 73, pp. 155-161; January, 1948.

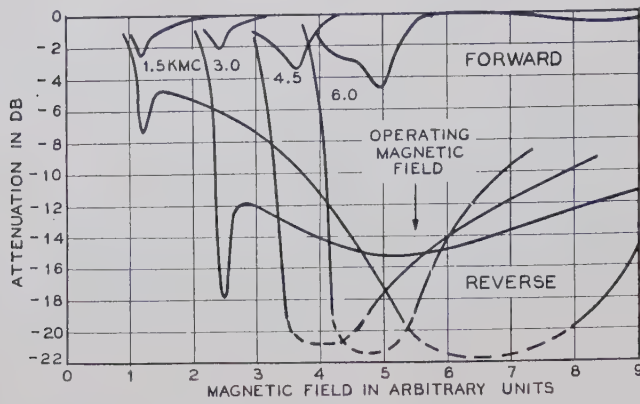


Fig. 6—Capacitively-loaded isolator characteristics as a function of magnetic field.

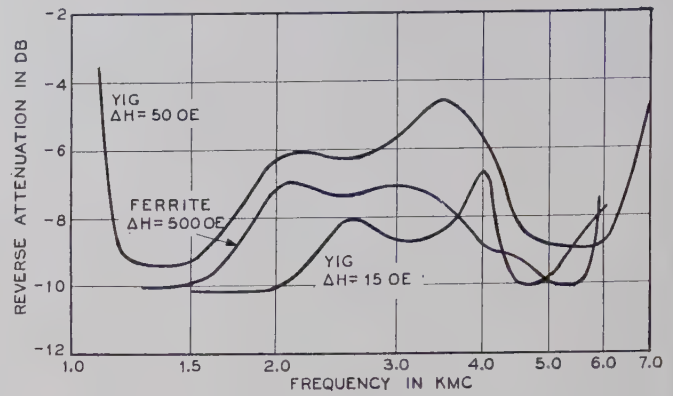


Fig. 8—Comparison of isolator characteristics for various ferrite materials.

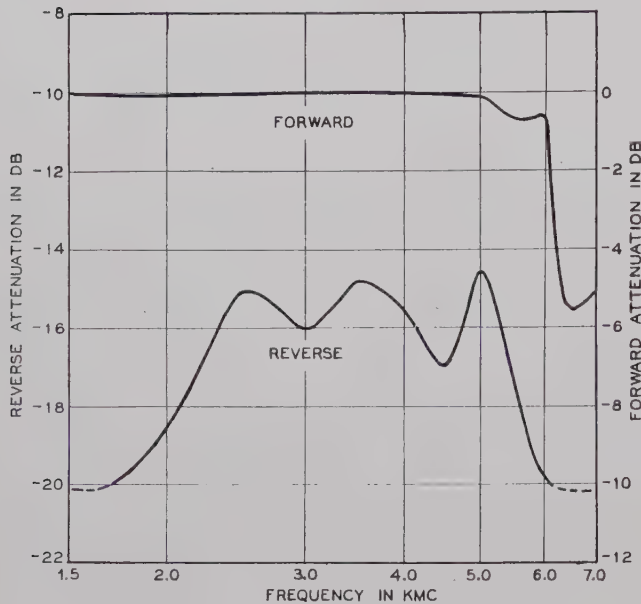


Fig. 7—Capacitively-loaded isolator characteristic for a fixed magnetic field.

## V. CONCLUSION

A design technique for obtaining wide-band resonance isolation has been described. Experiments to date indicate that the concepts presented in Sections II and III of this paper are correct and useful.

Several interesting problems have yet to be solved. The first is to obtain a good broad-band match to either of the structures described. This probably can be done by a long taper into the slowing structure. The second problem is a thorough experimental investigation to find the optimum dc magnetic-field shape for broad-band isolation. Preliminary experiments indicate that the isolation-frequency characteristic is rather sensitive to dc magnetic-field shape at the edge of the ferrite next to the slowing structure. A third problem is associated with the second problem, namely, a theoretical treatment of wave propagation in an inhomogeneously magnetized ferrite medium.

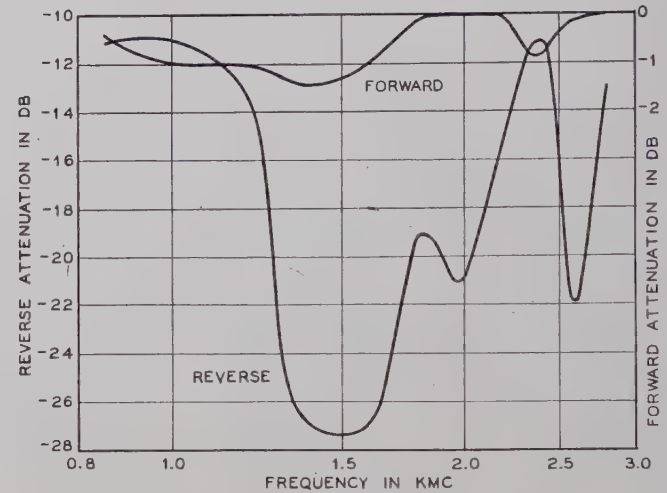


Fig. 9—Isolation characteristic of dielectric-loaded line.

## APPENDIX

### FIELDS IN SLOW WAVE STRUCTURE

#### A. The Capacity-Loaded Guide

For a parallel-plate transmission line of infinite width, height  $h$ , and capacity  $C$  per unit length along the center of the line, we find

$$E_y = E_0 e^{j(\omega t - \beta z) - p|x|} \quad (12)$$

$$H_x = -\frac{\beta}{\omega \mu_0} E_y, \quad (13)$$

$$H_z = -\frac{j p}{\omega \mu_0} E_y. \quad (14)$$

The coordinate system used here is shown in Fig. 1. The transverse propagation constant  $p$  must satisfy the wave equation, giving the relation

$$-\beta^2 + p^2 = -k^2 \quad (15)$$

where  $k$  is the propagation constant of free space (or the material filling the volume of the guide). The boundary condition at  $x=0$  determines the longitudinal propagation constant  $\beta$  through the equation



$$p = \sqrt{\beta^2 - k^2} = \frac{\omega^2 \mu_0 h C}{2}. \quad (16)$$

Eqs. (13)-(15) then give (1)

$$\frac{H_x}{H_z} = \frac{-j}{\sqrt{1 - \frac{k^2}{\beta^2}}}. \quad (1)$$

For the case of  $\beta \gg k$ , (16) reduces to (2)

$$\beta \approx \sqrt{\beta^2 - k^2} = \frac{\omega^2 \mu_0 h C}{2}. \quad (2)$$

If we add impedance side walls at  $x = \pm b$ , the RF fields are given by

$$E_y = E_0 e^{j(\omega t - \beta z)} (e^{-p|x|} + A e^{p|x|}), \quad (17)$$

$$H_x = -\frac{\beta}{\omega \mu_0} E_0 e^{j(\omega t - \beta z)} (e^{-p|x|} + A e^{p|x|}), \quad (18)$$

$$H_z = -\frac{j\beta}{\omega \mu_0} E_0 e^{j(\omega t - \beta z)} (e^{-p|x|} - A e^{p|x|}). \quad (19)$$

The presence of the side walls degrades the circular polarization of the RF magnetic field since we now have

$$\frac{H_x}{H_z} = \frac{-j}{\sqrt{1 - \frac{k^2}{\beta^2}}} \frac{e^{-p|x|} + A e^{p|x|}}{e^{-p|x|} - A e^{p|x|}}. \quad (20)$$

For open circuit walls at  $x = \pm b$ , the transverse propagation constant is determined by the equation

$$pb \tanh pb = \frac{\omega^2 \mu_0 Chb}{2}, \quad (21)$$

while for short circuit walls, the propagation constant  $p$  is found from

$$\frac{pb}{\tanh pb} = \frac{\omega^2 \mu_0 Chb}{2}. \quad (22)$$

In this later case, there is a low-frequency cutoff, given approximately by

$$\omega_c = \sqrt{\frac{2}{\mu_0 Chb}}. \quad (23)$$

To improve the circular polarization as given in (20), the quantity  $A$  should be as small as possible. For an open circuit wall at  $x = \pm b$ , the constant  $A$  in (20) is given by

$$A = e^{-2pb}, \quad (24)$$

while for short circuit walls at  $x = \pm b$  we find

$$A = -e^{-2pb}. \quad (25)$$

### B. The Dielectric Loaded Guide

Cohn<sup>5</sup> has given the complete expressions for the even and odd electric field modes in an infinite, parallel-plane, dielectric-loaded transmission line. We will only add the effects of open or short circuit walls at the edge

of the transmission line. In the dielectric region, the electric fields are

$$E_y = E_0 \begin{pmatrix} \cos k_d x \\ \sin k_d x \end{pmatrix} e^{j(\omega t - \beta z)}, \quad (26)$$

where  $k_d = k\sqrt{K - (\beta^2/k^2)}$ . The even electric field modes are the  $\cos k_d x$  terms, and the odd field modes are the  $\sin k_d x$  terms. In the region external to the dielectric, the fields are

$$E_y = E_0 \begin{pmatrix} \cos k_d a \\ \sin k_d a \end{pmatrix} \frac{e^{-p|x|} + A e^{p|x|}}{e^{-pa} + A e^{pa}} e^{j(\omega t - \beta z)}. \quad (27)$$

The ratio of transverse-to-longitudinal magnetic field is then given by (20) and the constant  $A$  by (24) or (25).

The propagation constant  $\beta$  for the various mode and wall configurations is given by the following transcendental equations:

1) Even electric field, open circuit walls

$$\begin{aligned} & \tan \sqrt{K - \frac{\beta^2}{k^2}} ka \\ &= \sqrt{\frac{\frac{\beta^2}{k^2} - 1}{K - \frac{\beta^2}{k^2}}} \tanh \sqrt{\frac{\beta^2}{k^2} - 1} k(b - a). \end{aligned} \quad (28)$$

2) Even electric field, short circuit walls

$$\begin{aligned} & \tan \sqrt{K - \frac{\beta^2}{k^2}} ka \\ &= \sqrt{\frac{\frac{\beta^2}{k^2} - 1}{K - \frac{\beta^2}{k^2}}} \coth \sqrt{\frac{\beta^2}{k^2} - 1} k(b - a). \end{aligned} \quad (29)$$

3) Odd electric field, open circuit walls

$$\begin{aligned} & -\cot \sqrt{K - \frac{\beta^2}{k^2}} ka \\ &= \sqrt{\frac{\frac{\beta^2}{k^2} - 1}{K - \frac{\beta^2}{k^2}}} \tanh \sqrt{\frac{\beta^2}{k^2} - 1} k(b - a). \end{aligned} \quad (30)$$

4) Odd electric field, short circuit walls

$$\begin{aligned} & -\cot \sqrt{K - \frac{\beta^2}{k^2}} ka \\ &= \sqrt{\frac{\frac{\beta^2}{k^2} - 1}{K - \frac{\beta^2}{k^2}}} \coth \sqrt{\frac{\beta^2}{k^2} - 1} k(b - a). \end{aligned} \quad (31)$$

# Maser Operation at Signal Frequencies Higher than Pump Frequency\*

FRANK R. ARAMS†, SENIOR MEMBER, IRE

**Summary**—Methods using harmonic spin coupling for operating solid-state masers with signal frequencies higher than the pump frequency are discussed. Expressions for the population inversion ratios are presented, and the maximum signal-to-pump-frequency ratios are calculated.

Experimental data is presented on a ruby maser which is operated using the symmetrical method. Amplification was obtained at signal frequencies from 10,320 to 10,740 Mc, using pump frequencies ranging from 9580 to 9670 Mc.

An experiment in which maser operation is obtained simultaneously at two frequencies is described.

SOLID-STATE masers are ordinarily operated with the pump frequency two to ten times the signal frequency. This relationship—a relatively high pump frequency—permits good spin-population inversion (and hence satisfactory gain-bandwidth products) at the signal frequency.<sup>1</sup>

A major obstacle to the development of masers with very high signal frequencies has been the lack of availability of satisfactory pump power sources in the millimeter-wave and submillimeter-wave regions. One approach toward circumventing the unavailability of satisfactory millimeter pump sources has been the pulsed maser. With the pulse technique, transient maser amplification of signals up to 70 kMc has been obtained.<sup>2</sup>

Because transient methods have obvious disadvantages, there is a need for a continuous-wave maser in which the pump frequency is kept as low as possible relative to the signal frequency.

One method of keeping the pump frequency low is the method used in the "X-X maser." In this maser, the pump frequency is only about 15 per cent higher than the signal frequency.<sup>3</sup> This method of operation can probably be used in the millimeter-wave region by using maser materials which have suitably large zero-field splittings—for example, emerald, and Cr<sup>+++</sup> or Fe<sup>+++</sup> doped titania.

As the signal frequency is raised higher and higher, it becomes increasingly desirable to use a pump frequency

lower than the signal frequency. Several methods for achieving continuous-wave maser operation with a signal frequency higher than the pump frequency will be discussed in this paper. Operating data on a maser operating in such a manner will be given.

The low-pump-frequency maser operation discussed here involves spin-coupling of transitions that are equal in frequency or harmonically related. In the harmonic-spin-coupling process, simultaneous spin flips cause energy transfer between transitions that are harmonically related in frequency; all, or almost all, of the Zeeman energy of the spin system is conserved.<sup>4-8</sup> Saturation of the lowest-frequency transition by applied pump power will result in a simultaneous saturation effect in the harmonically related transition. This spin-coupling mechanism will alter the spin population distribution between the energy levels in such a manner that a negative temperature is obtained at a signal frequency higher than the pump frequency.

## THE SYMMETRICAL METHOD

A maser material is required having four (or more) energy levels. Let these energy levels be numbered from 1 to 4 in order of increasing energy, and let the notation  $f_{ij}$  represent the frequency corresponding to the energy difference between the  $i$ th and the  $j$ th levels. An operating point (in terms of magnetic field strength and orientation with respect to the crystal  $C$ -axes) is chosen at which  $f_{14} = 2f_{23}$ . The method of operation is as follows.

The spin population distribution among the various levels before application of pump power is approximately as shown in Fig. 1(a). The  $f_{23}$  transition is saturated by means of pump power from an external pump source at frequency  $f_{23}$ . The saturation of the  $f_{23}$  transition will result in the simultaneous saturation (at least partial) of the  $f_{14}$  transition through the mechanism of harmonic spin coupling. Thus, the spin populations of

\* Received by the PGMTT, July 15, 1960. This work is part of a doctoral dissertation at the Polytechnic Inst. of Brooklyn, Brooklyn, N. Y.

† Airborne Instruments Lab., Cutler-Hammer, Inc., Melville, L. I., N. Y.

<sup>1</sup> N. Bloembergen, "Proposal for a new type solid-state maser," *Phys. Rev.*, vol. 109, pp. 324-327; October 15, 1956.

<sup>2</sup> S. Foner, L. Momo, A. Mayer, and R. Myers, "Pulsed field millimeter wave maser," in "Quantum Electronics," Columbia University Press, New York, N. Y., p. 487; 1960.

<sup>3</sup> F. R. Arams, "Low field X-band ruby maser," *PROC. IRE*, vol. 46, p. 1373; August, 1959.

<sup>4</sup> N. Bloembergen, S. Shapiro, P. Pershan, and J. O. Artman, "Cross-relaxation in spin systems," *Phys. Rev.*, vol. 144, pp. 445-459; April 15, 1959.

<sup>5</sup> W. H. Higa, "Excitation of an L-band ruby maser," in "Quantum Electronics," Columbia University Press, New York, N. Y., p. 298; 1960.

<sup>6</sup> J. E. Geusic, "Harmonic spin coupling in ruby," *Phys. Rev.*, vol. 118, pp. 129-130; April 1, 1960.

<sup>7</sup> W. S. C. Chang, "Spin lattice relaxation via harmonic coupling," in "Quantum Electronics," Columbia University Press, New York, N. Y., p. 346; 1960.

<sup>8</sup> W. B. Mims and J. McGee, "Spin-spin energy transfer and the operation of three-level masers," *PROC. IRE*, vol. 47, p. 2120; December, 1959.



levels 2 and 3 have been equalized to the average value of their equilibrium populations. The same will be true of levels 1 and 4. The spin population distribution, assuming that all spin-lattice relaxation times are equal, is shown in Fig. 1(b). Note that a negative temperature is obtained in the  $f_{12}$  transition.<sup>5,6</sup>

The negative temperature at  $f_{12}$  and the saturated  $f_{23}$  transition combine to produce a negative temperature at a frequency  $f_{13}$ , which is higher than the pump frequency  $f_{23}$ . In terms of the spin populations of the various energy levels, since  $n_2 > n_1$ , and  $n_2 = n_3$ , it follows that  $n_3 > n_1$ , so that maser action can be obtained at  $f_{13}$ . Thus, a way has been found to obtain operation with a signal frequency higher than the pump frequency. Maser amplification can thus be obtained simultaneously at two signal frequencies,  $f_{12}$  and  $f_{13}$ , which are related by the expression  $f_{\text{sig1}} + f_{\text{pump}} = f_{\text{sig2}}$ . (This circumstance will be discussed further later on.)

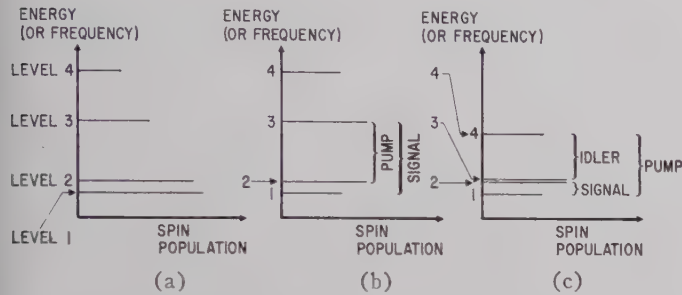


Fig. 1—Population distribution in symmetrical method. (a) Thermal equilibrium, pump power off. (b) Pump power (at  $f_{23}$ ) on. (c) Analogous three-level technique illustrating that  $f_{34}$  is idler transition.

Comparison of this symmetrical method with the standard Bloembergen three-level maser<sup>1</sup> shows that  $f_{34}$  plays the role of the idler transition, and that Fig. 1(b) is analogous to the Bloembergen three-level maser technique if we think of the  $f_{23}$  transition as the degenerate intermediate energy level; this is shown in Fig. 1(c) and is verified by the following analysis.

#### Analysis:

We can solve for the steady-state (negative) population difference,  $\Delta n_{13} = n_1 - n_3$ , using the usual linearized rate equations<sup>1</sup> and the conditions  $n_2 = n_3$  caused by pump saturation and  $n_1 = n_4$  caused by saturation by second-harmonic spin coupling. A more general procedure is to add to each of the standard rate equations one term representing the spin coupling between the harmonically related transitions. (All other possible simultaneous multiple spin-flip processes are neglected.) Let  $w_c$  be the harmonic-spin-coupling transition probability;  $w_{ij}$ , the spin-lattice transition probability between the  $i$ th and  $j$ th energy levels; and  $n$ , the order of the spin-coupling harmonic. The condition  $n_1 = n_4$  is not used, since the degree of saturation of the  $f_{14}$  transition will depend upon the parameter  $w_c/w_{ij}$ . For  $w_c/w_{ij} = \infty$ , the results are identical with those calculated for the

first method. The two pertinent rate equations (since we are pumping between levels 2 and 3) are

$$\frac{dn_1}{dt} = -w_{12} \left[ \Delta n_{12} - \frac{Nh}{4kT_0} f_{12} \right] - w_{13} \left[ \Delta n_{13} - \frac{Nh}{4kT_0} f_{13} \right] - w_{14} \left[ \Delta n_{14} - \frac{Nh}{4kT_0} f_{14} \right] - w_c [\Delta n_{14} - n \Delta n_{23}] \quad (1a)$$

$$\frac{dn_4}{dt} = w_{14} \left[ \Delta n_{14} - \frac{Nh}{4kT_0} f_{14} \right] + w_{24} \left[ \Delta n_{24} - \frac{Nh}{4kT_0} f_{24} \right] + w_{34} \left[ \Delta n_{34} - \frac{Nh}{4kT_0} f_{34} \right] + w_c [\Delta n_{14} - n \Delta n_{23}]. \quad (1b)$$

In these equations  $N$  is the total spin population,  $h$  is Planck's constant,  $k$  is Boltzmann's constant, and  $T_0$  is the bath temperature. The form of the harmonic spin coupling terms in (1) is obtained by linearizing (for second-harmonic) terms of the form<sup>4</sup> ( $n_2^2 n_4 - n_3^2 n_1$ ). For all  $w_{ij}$  equal, we obtain for the steady-state

$$\Delta n_{13} = -\frac{Nh}{4kT_0} \frac{\left[ w_{ij}(f_{23} - 2f_{13}) + w_c \left[ \left( \frac{n+1}{2} \right) f_{23} - f_{13} \right] \right]}{2w_{ij} + w_c}. \quad (2)$$

For  $w_c/w_{ij} = \infty$ , this reduces to

$$\Delta n_{13} = -\frac{Nh}{4kT_0} \left( \frac{f_{34} - f_{\text{signal}}}{2} \right). \quad (3)$$

This expression is independent of  $n$  and has the same form as that for a standard Bloembergen three-level maser, which—for all  $w_{ij}$  equal—is

$$\Delta n_{\text{signal}} = -\frac{Nh}{4kT_0} \left( \frac{f_{\text{idler}} - f_{\text{signal}}}{2} \right). \quad (4)$$

Hence, it is evident that  $f_{34}$  and  $f_{12}$  act as the idler and signal transitions, respectively [Fig. 1(c)], and that we wish to maximize  $f_{34}$ .

Taking (2), normalizing it to the Boltzmann thermal equilibrium population difference  $(\Delta n_{13})_0$ , and rewriting it in terms of the signal frequency,  $f_{13}$ , and pump frequency,  $f_{23}$ , we obtain

$$\frac{\Delta n_{13}}{(\Delta n_{13})_0} = \frac{T_0}{T_{s13}} = 1 - \frac{\left( n + 1 + 2 \frac{w_{ij}}{w_c} \right) \frac{f_{23}}{f_{13}}}{2 \left( 1 + 2 \frac{w_{ij}}{w_c} \right)} \quad (5)$$

where  $T_{s13}$  is the spin temperature of the  $f_{13}$  transition.  $T_0/T_{s13}$  must be negative in order to obtain amplification, and the obtainable gain is proportional to  $T_0/T_{s13}$ . As (5) shows, for  $n > 1$ , amplification can be obtained with a signal frequency  $f_{13}$  larger than the pump frequency  $f_{23}$ .

Using (5) we solve for the maximum ratio of signal-

frequency-to-pump-frequency, with  $n$  and  $w_c/w_{ij}$  as parameters, by setting  $T_0/T_{s13}$  equal to zero. The results are shown in Table I. As can be seen, for  $w_c/w_{ij} = \infty$ , the maximum ratio of signal-frequency-to-pump-frequency is 1.5 for  $n=2$ , and 2.0 for  $n=3$ . The maximum signal frequency is seen to be dependent upon  $w_c/w_{ij}$ . This is intuitively reasonable, because the  $f_{14}$  (second-harmonic) transition is not saturated for finite  $w_c/w_{ij}$ . As expected, the maximum ratio increases with  $n$ . It is seen that  $w_c/w_{ij}$  need not be very high to permit maser amplification at frequencies higher than the pump frequency. However, because  $w_c$  is an implicit function of  $n$ , it may be difficult to achieve high signal-frequency-to-pump-frequency ratios. To maximize  $w_c/w_{ij}$ , it is desirable to go to as low a bath temperature as possible, since  $w_c$  is independent of and  $w_{ij}$  is proportional to bath temperature. This parameter—the ratio of the  $w$ 's—can also be changed by varying the concentration of the paramagnetic ion in the maser crystal.

TABLE I

SYMMETRICAL METHOD: MAXIMUM RATIO OF SIGNAL FREQUENCY TO PUMP FREQUENCY

	$w_c/w_{ij} = \infty$	10	4	2	1
$n=2$	1.5	1.33	1.17	1.0	0.83
3	2.0	1.75	1.5	1.25	1.0
4	2.5	2.17	1.83	1.5	1.17
	$n+1$	$n+1.2$	$n+1.5$	$n+2$	$n+3$
$n$	2	2.4	3	4	6

Eq. (5) also shows that the inversion improves as the signal-frequency-to-pump-frequency ratio is decreased. In fact, it continues to increase even when the signal frequency becomes lower than the pump frequency. When the signal frequency is less than the pump frequency, the energy-level arrangement could be called harmonic push-pull pumping (Fig. 2). Thus, even when the signal is less than the pump frequency, the improved inversion (and hence increased gain-bandwidth product) makes the harmonic-coupling technique attractive in comparison with the standard three-level Bloembergen maser technique.

#### ALTERNATIVE SYMMETRICAL METHOD

Suppose the energy levels are arranged in such a manner that  $f_{14} = 2f_{23}$  (as previously), but  $f_{34} < f_{12}$  (rather than  $f_{34} > f_{12}$ , as previously). It is still possible to obtain maser amplification at a signal frequency (now  $f_{24}$ ) higher than the pump frequency ( $f_{23}$ ). Here,  $f_{12}$  is the idler transition. Thus, just as in the standard Bloembergen three-level maser, maser operation can be obtained with the idler transition higher in energy than the signal transition, or vice versa.

#### THE ASYMMETRICAL METHOD

In this method, we again require four (or more) energy levels numbered from 1 to 4 in order of increasing

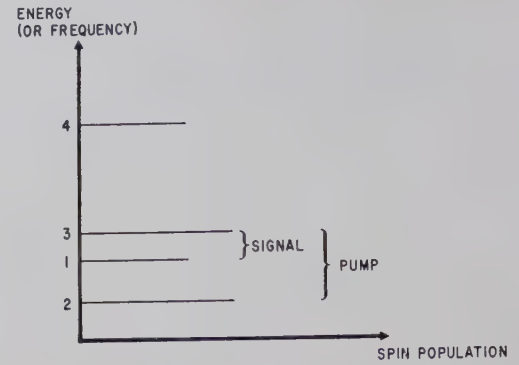


Fig. 2—Population distribution for harmonic push-pull pumping.

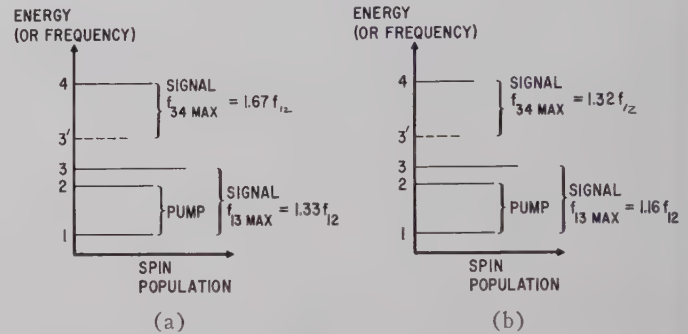


Fig. 3—Population distribution for asymmetrical method. (a) Complete saturation of  $f_{24}$  transition. (b) Incomplete saturation of  $f_{24}$  transition  $w_c/w_{ij}=10$ ;  $n=z$ .

energy. We chose an operating point at which  $f_{24} = 2f_{12}$ . The method of operation is as follows (see Fig. 3).

The  $f_{12}$  transition is saturated by means of pump power from an external pump source at frequency  $f_{12}$ . The harmonic spin-coupling mechanism results in the simultaneous saturation (at least partial) of the  $f_{24}$  transition. The populations of levels 1, 2, and 4 will be essentially equalized to their average value. The spin population distribution will then be as shown in Fig. 3(a).

A negative temperature can be obtained at a signal frequency  $f_{13}$  (and  $f_{23}$ ) or  $f_{34}$ , depending upon the location of energy level 3. The signal frequency  $f_{13}$  will be, and the signal frequency  $f_{34}$  may be, higher than the pump frequency  $f_{12}$ .

#### Analysis:

We can solve for the steady-state (negative) population differences,  $\Delta n_{13}$  and  $\Delta n_{34}$ , using the usual linearized rate equations and the saturation condition  $n_1 = n_2 = n_4$ .

Again, the more general procedure is to add the harmonic spin-coupling terms to the rate equations. In the steady state, assuming that all  $w_{ij}$  are equal, we obtain for the population inversion ratios,

$$\frac{T_0}{T_{s13}} = 1 - \frac{\left(n + 2 + 4 \frac{w_{ij}}{w_c}\right) \frac{f_{12}}{f_{13}}}{3 + 8 \frac{w_{ij}}{w_c}} \quad (6)$$

and



TABLE II  
ASYMMETRICAL METHOD: MAXIMUM RATIO OF SIGNAL FREQUENCY TO PUMP FREQUENCY

	$w_c/w_{ij} = \infty$		10		4		2	
	$f_{13}$	$f_{34}$	$f_{13}$	$f_{34}$	$f_{13}$	$f_{34}$	$f_{13}$	$f_{34}$
$n=2$	1.33	1.67	1.16	1.32	1.0	1.0	0.86	0.71
3	1.67	2.33	1.42	1.84	1.2	1.4	1.0	1.0
4	2.0	3.0	1.74	2.37	1.4	1.8	1.14	1.29
$n$	$n+2$	$2n+1$	$n+2.4$	$2n+1$	$n+3$	$2n+1$	$n+4$	$2n+1$
	3	3	3.8	3.8	5	5	7	7

$$\frac{T_0}{T_{s_{34}}} = 1 - \frac{(2n+1) \frac{f_{12}}{f_{34}}}{3 + 8 \frac{w_{ij}}{w_c}} \quad (7)$$

The maximum ratios of signal-frequency-to-pump-frequency as functions of  $n$  and  $w_c/w_{ij}$  for the asymmetrical method are shown in Table II. The maximum signal-to-pump ratio is different for the  $f_{13}$  and  $f_{34}$  transitions, being 1.33 and 1.67, respectively, for second-harmonic spin coupling, and 1.67 and 2.33, respectively, for third-harmonic spin coupling. Eqs. (6) and (7) also show that, as in the symmetrical method, harmonic spin coupling significantly improves maser operation over the three-level Bloembergen maser, even when the signal frequency is lower than the pump frequency.

The population ratio of the pump transition  $f_{14}$  was calculated assuming that the  $f_{12}$  transition is saturated by externally applied pump power. We obtain

$$\frac{T_0}{T_{s_{14}}} = \frac{8 - \frac{4}{n+1}}{8 + 3 \frac{w_c}{w_{ij}}} \quad (8)$$

for the dependence of the degree of saturation of the  $f_{14}$  transition upon the  $w_c/w_{ij}$  parameter. As expected,  $T_0/T_{s_{14}} \rightarrow 0$  for  $w_c/w_{ij} \rightarrow \infty$ . How incomplete saturation of the spin-coupled second-harmonic transition reduces the maximum signal frequency is shown in Fig. 3(b). The reduction in population of level 4 combines with an increase of the level 1 and 2 populations to yield only a limited frequency range where inverted populations are obtainable.

#### THE PUSH-PUSH MASER

This may be considered as a special case of the asymmetrical method with  $n=1$ . Since  $f_{12}=f_{24}$ , both transitions are saturated directly by the applied pump power.<sup>9</sup> The population inversion ratios can be obtained directly from (6) and (7) by setting  $w_c/w_{ij} = \infty$  and  $n=1$ . The result shows that the push-push maser produces a significant improvement in population inversion ratio over the three-level Bloembergen maser. However, maser operation at a signal frequency higher than the pump

frequency can be obtained for unequal spin-lattice relaxation times only.

#### EXPERIMENTAL DATA

Continuous-wave maser operation with the signal frequency about 1000 Mc higher than the pump frequency was successfully achieved using the symmetrical method. By using the four energy levels in ruby (chromium-doped aluminum oxide), maser amplification was first obtained at  $f_{13}=10,590$  Mc, using a pump frequency of  $f_{23}=9595$  Mc. The magnetic field of 1675 oersteds was oriented at 90 degrees to the ruby  $C$ -axis. The energy levels used are indicated in Fig. 4; they were so arranged that  $f_{14}=2f_{23}$ .

We established experimentally that the  $f_{14}$  transition is saturated because of the pump power applied at frequency  $f_{23}$ , and that the frequency ratio need not be exactly integral.<sup>10</sup> It was possible, using a constant pump frequency of  $f_{23}=9650$  Mc, to saturate the  $f_{14}$  transition over a 600-Mc frequency range (centered near 19,300 Mc) with an optimized magnetic field.

The experimental result that the second-harmonic,  $f_{14}$ , transition can be saturated over a range of frequencies with constant pump frequency, is attributable in part to the fact that the frequency of the  $f_{23}$  transition varies very little with magnetic field (Fig. 4), changing by less than 40 Mc per 100 oersteds in the region of interest.

The experimental setup consisted of a doubly resonant tunable cavity operating in the  $TE_{10}$  waveguide mode. The ruby crystal had a nominal 0.05-per cent residual chromium content. The pump power was 8 milliwatts at a liquid helium bath temperature of 4.2 degrees K. To ascertain that the saturation of the  $f_{14}$  transition was primarily caused by harmonic spin coupling, we measured the second-harmonic power output of the pump power source in the 18 to 26 kMc range and found it to be less than 1 microwatt.

A voltage-gain bandwidth product of 11 Mc was measured at a liquid helium bath temperature of 4.2 degrees K. It is expected that larger gain-bandwidth products can be obtained, since the ruby occupied only a small portion of the cavity. The filling factor is estimated to be 50 per cent. The spin population inversion ratio was also measured, and was found to be  $-0.37$ .

<sup>9</sup> "Solid-State Research," MIT Lincoln Lab. Quarterly Progress Rept., p. 65; July 15, 1959.

<sup>10</sup> F. R. Arams, "Maser operation with signal frequency higher than pump frequency," PROC. IRE, vol. 47, p. 108; January, 1960.

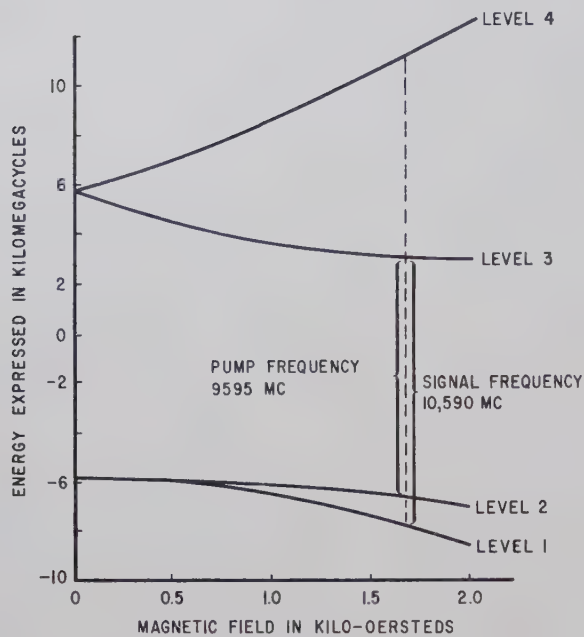


Fig. 4—Energy levels used in ruby in symmetrical method experiment.

The tuning range was 420 Mc with optimized pump frequency and magnetic field and a liquid helium bath temperature of 4.2 degrees K. Maser amplification was obtained over the 10,320- to 10,740-Mc range, using pump frequencies ranging from 9580 to 9670 Mc. The data are plotted in Fig. 5. The tuning range obtained is also of interest in view of the frequency difference between the pump frequency  $f_{23}$  and  $\frac{1}{2}f_{14}$ , but it is consistent with the observed wide-range harmonic saturation of  $f_{14}$  previously described. A greater tuning range should be obtainable at 1.5 degrees K.

An attempt was also made at obtaining maser operation using the asymmetrical method. The orientation of  $60^\circ$  between ruby C-axis and applied magnetic field is of particular interest, since the harmonic relationship  $f_{24}=f_{12}$  is maintained over a wide range of frequencies,<sup>8</sup> that is, a pump frequency  $f_{12}=8.3$  to 12.7 kMc, and a signal frequency  $f_{34}=10$  to 15 kMc.  $Q$  improvement was observed, but inversion has not yet been obtained, indicating the possibility that additional factors (such as other spin-flip processes) may need to be included that were not considered in the present analysis.

#### TWO-FREQUENCY MASER OPERATION

In the symmetrical method, a negative spin temperature was obtained at two frequencies simultaneously. One of these is at a relatively low frequency, designated  $f_{s1}$ . The second frequency  $f_{s2}$  is numerically related to  $f_{s1}$  via the pump frequency  $f_p$ —that is,  $f_{s2}=f_{s1}+f_p$ .

A triply resonant cavity experiment was set up, and it was possible to obtain maser amplification at  $f_{s1}$  and  $f_{s2}$  simultaneously. Operating conditions were: magnetic field = 1650 gauss at 90 degrees to the ruby C-axis;  $f_p=9600$  Mc;  $f_{s1}=1005$  Mc; and  $f_{s2}=10,605$  Mc. When

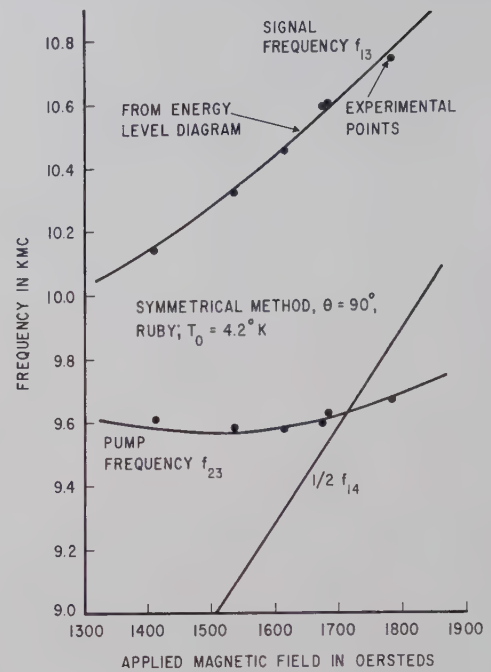


Fig. 5—Frequency tuning range of ruby maser using symmetrical method.

the liquid helium bath temperature was reduced to 1.5 degrees K, maser action was obtained at  $f_{s1}$  and  $f_{s2}$ , simultaneously. Maser action would get better or worse at both frequencies concurrently as adjustments—such as angular orientation and magnetic field strength—were being made.

The condition  $f_{s2}=f_p+f_{s1}$  used here is also used in the parametric amplifier up-converter. In that application,  $p$ - $n$  junction diodes or ferromagnetic materials are used, and the input is at frequency  $f_{s1}$ , the output is at frequency  $f_{s2}$ , and the obtainable power gain is equal to the frequency ratio  $f_{s2}/f_{s1}$ .

In the experimental double-frequency maser setup, no interaction between the  $f_{s1}$  and  $f_{s2}$  signals was observable except when the input power level approached saturation. An input signal at  $f_{s1}$  did not affect the  $f_{s2}$  output, and vice versa. It is concluded that the absence of coherence between the  $f_{12}$  and  $f_{13}$  transitions prevents the realization of a maser amplifier up-converter.

#### CONCLUSIONS

Several methods for obtaining CW maser operation with a signal frequency higher than the pump frequency were analyzed. Performance data on the symmetrical method were presented. This maser was tuned over a 420-Mc range. Using the methods described, millimeter-wave masers having pump frequencies lower than signal frequencies should become available in the foreseeable future.

#### ACKNOWLEDGMENT

The author wishes to thank Professor Milton Birnbaum of the Polytechnic Institute of Brooklyn, Brooklyn, N. Y. for valuable advice and discussions.



# A Solid-State Microwave Source from Reactance-Diode Harmonic Generators\*

T. M. HYLTI<sup>†</sup>, MEMBER, IRE AND K. L. KOTZEBUE<sup>‡</sup>, MEMBER, IRE

**Summary**—The generation of harmonics with reasonable efficiencies has been made possible by the application of high  $Q$  nonlinear reactance diodes. An approximate solution for the conversion loss of harmonic generators utilizing these devices has been obtained and design curves relating conversion loss with harmonic number, diode  $Q$ , and voltage-capacitance coefficient are presented. Harmonic generators have been operated with silicon and gallium-arsenide mesa diodes in the UHF region and conversion losses approaching the theoretical value have been obtained. Three harmonic generation stages in miniature modular packages were cascaded to obtained 7-mw output at  $S$  band. These stages were driven by a transistorized crystal-controlled oscillator and power amplifier which supplied 200 mw at 140 Mc from 1.3-w dc.

## INTRODUCTION

THE generation of microwave frequencies at the milliwatt power level has in the past been the exclusive domain of klystrons and similar electron-beam devices. Unfortunately, in many satellite, missile, and portable ground equipment applications, the weight, size, reliability, and power consumption of these devices and their associated power supplies have proved to be a severe handicap. At lower frequencies these problems have often been solved by using semiconductor devices; for example, by replacing vacuum tubes with transistors. The upper frequency limit at which such transistor operation is practical is steadily increasing and is now approaching the microwave range.

Laboratory transistors have operated as oscillators at  $S$  band, and there are commercially available transistors capable of power output in the milliwatt range at 1000 Mc. As we go lower in frequency the power capabilities greatly increase; for example, power levels to 1 w are now available from transistors at as high as 150 Mc. Because of this relatively large power available in the VHF region, it is now possible to obtain useful power at microwave frequencies from an all-solid-state source by combining transistors with high-efficiency harmonic generators constructed from low-loss semiconductor diodes. This paper discusses the theoretical performance of harmonic generators and the design and performance of such a microwave source which weighs 13 ounces and is capable of an output power of 7 mw at 2520 Mc when connected to a 28-v, 1.3-w power source.

## THEORY OF HARMONIC GENERATION

Previous harmonic generators have made use of standard microwave mixer diodes. Page has shown that

even an ideal nonlinear resistance generates harmonics with a conversion efficiency of  $1/n^2$ , where  $n$  is the desired harmonic.<sup>1</sup> A review of microwave components catalogs will show the realizable efficiency with presently available diodes to be an order of magnitude poorer than the  $1/n^2$  expression indicates. It seems reasonable that harmonic generation by nonlinear reactance should have greatly enhanced efficiency, for a perfect reactance without dissipative loss can only transfer or store energy.

Indeed, it can be shown from the Manley-Rowe relations that the efficiency of generation of any harmonic can approach unity.<sup>2</sup> In practice, however, power flow at unwanted frequencies, and the inevitable loss of realizable circuit elements, will reduce that efficiency.<sup>3,4</sup>

An approximate solution for the conversion loss of a nonlinear reactance harmonic generator is not too difficult to obtain, provided we restrict ourselves sufficiently. Even though high efficiencies can be expected in many instances, we will assume the harmonic voltage to be small in order to keep the mathematics under control. Experimental results indicate that the error involved will normally be small in designs of practical interest. We will start with the fundamental equation for current:

$$i = \frac{dq}{dt} = \frac{dq}{dv} \frac{dv}{dt} \\ = c(v) \frac{dv}{dt} \quad (1)$$

We will assume that the ac voltage is composed of a large fundamental voltage,  $v_1$ , and small harmonic voltages,  $v_2$ . With this assumption we can expand the capacitance function,  $c(v)$ , in a Taylor series about  $v_1$ :

$$c(v) = c(v_1) + \left. \frac{dc}{dv} \right|_{v=v_1} v_2 + \dots \quad (2)$$

We can also write the identity

$$\frac{dc}{dt} = \frac{dc}{dv} \frac{dv}{dt}; \quad (3)$$

<sup>1</sup> C. H. Page, "Harmonic generation with ideal rectifiers," *PROC. IRE*, vol. 46, pp. 1738-1740; October, 1958.

<sup>2</sup> J. M. Manley and H. E. Rowe, "Some general properties of nonlinear elements," *PROC. IRE*, vol. 44, pp. 904-913; July, 1956.

<sup>3</sup> D. Leenov and A. Uhler, "Generation of harmonics and subharmonics at microwave frequencies with  $p$ - $n$  junction diodes," *PROC. IRE*, vol. 47, pp. 1724-1729; October, 1959.

<sup>4</sup> D. Leeson and S. Weinreb, "Frequency multiplication with nonlinear capacitors—a circuit analysis," *PROC. IRE*, vol. 47, pp. 2076-2084; December, 1959.

\* Received by the PGMTT, July 26, 1960; revised manuscript received, September 26, 1960.

<sup>†</sup> Texas Instruments, Inc., Dallas, Tex.

<sup>‡</sup> Watkins-Johnson Co., Palo Alto, Calif.

therefore,

$$\frac{dc}{dv} \bigg|_{v=v_1} = \frac{\left( \frac{dc}{dt} \right)_{v=v_1}}{\left( \frac{dv}{dt} \right)_{v=v_1}} \quad (4)$$

Substituting (4) and (2) into (1), we get

$$i = c(v_1) \left[ \frac{dv_1}{dt} + \frac{dv_2}{dt} \right] + \frac{dc(v_1)}{dt} v_2 \left[ 1 + \frac{\frac{dv_2}{dt}}{\frac{dv_1}{dt}} \right] + \dots \quad (5)$$

To obtain linear equations, we assume that

$$\frac{\frac{dv_2}{dt}}{\frac{dv_1}{dt}}$$

is small compared to unity. With this approximation, the expression for current becomes

$$i = c(v_1) \left[ \frac{dv_1}{dt} + \frac{dv_2}{dt} \right] + \frac{dc(v_1)}{dt} v_2. \quad (6)$$

In the evaluation of (6) we will use exponential representations. Let

$$\begin{aligned} v_1 &= V_1 e^{j\omega_1 t} + V_1^* e^{-j\omega_1 t}, & V_1 &= V_1^* \\ v_2 &= \sum_{\substack{n=-\infty \\ n \neq \pm 1}}^{\infty} V_n e^{jn\omega_1 t} \\ c(v_1) &= C_0 \sum_{n=-\infty}^{\infty} \gamma_n e^{jn\omega_1 t} & \gamma_n &= \gamma_{-n} \\ i &= \sum_{n=-\infty}^{\infty} I_n e^{jn\omega_1 t}. \end{aligned} \quad (7)$$

Substituting these values into (6), we obtain the following expression for the  $n$ th harmonic current:

$$I_n = j\omega C_0 [\gamma_{n-1} - \gamma_{n+1}] V_1 + jn\omega C_0 \sum_{\substack{k=-\infty \\ k \neq \pm 1}}^{\infty} \gamma_{n-k} V_k. \quad (8)$$

From this equation we can construct an admittance matrix which will describe the "small-signal" harmonic generator. Before carrying the analysis further, let us assume that our circuit is so constructed as to allow sig-

nificant voltages to exist across the capacitor only at the fundamental and  $n$ th harmonic. This is a reasonable assumption for many practical circuits, since the diodes will be of relatively high  $Q$ . With only  $V_1$  and  $V_n$  not equal to zero, we can then obtain from (8) the following equations for  $I_1$  and  $I_n$ :

$$\begin{aligned} I_1 &= j\omega C_0 [1 - \gamma_2] V_1 + j\omega C_0 \gamma_{n-1} V_n \\ I_n &= j\omega C_0 [\gamma_{n-1} - \gamma_{n+1}] V_1 + jn\omega C_0 V_n. \end{aligned} \quad (9)$$

In matrix notation we have,

$$\begin{bmatrix} I_1 \\ I_n \end{bmatrix} = j\omega C_0 \begin{bmatrix} 1 - \gamma_2 & \gamma_{n-1} \\ \gamma_{n-1} - \gamma_{n+1} & n \end{bmatrix} \begin{bmatrix} V_1 \\ V_n \end{bmatrix}. \quad (10)$$

This matrix represents the admittance of the lossless, small-signal harmonic generator. We will approximate the effect of series loss by inverting the admittance matrix and by adding a series resistance. The *lossless* inverted matrix equation is:

$$\begin{bmatrix} V_1 \\ V_n \end{bmatrix} = \begin{bmatrix} Z_{11} & Z_{12} \\ Z_{21} & Z_{22} \end{bmatrix} \begin{bmatrix} I_1 \\ I_n \end{bmatrix}, \quad (11)$$

where

$$\begin{aligned} Z_{11} &= \frac{n}{j\omega C_0 D} \\ Z_{12} &= -\frac{\gamma_{n-1}}{j\omega C_0 D} \\ Z_{21} &= -\frac{\gamma_{n-1} - \gamma_{n+1}}{j\omega C_0 D} \\ Z_{22} &= \frac{1 - \gamma_2}{j\omega C_0 D} \\ D &= n(1 - \gamma_2) - \gamma_{n-1}(\gamma_{n-1} - \gamma_{n+1}) \\ &\approx n(1 - \gamma_2). \end{aligned}$$

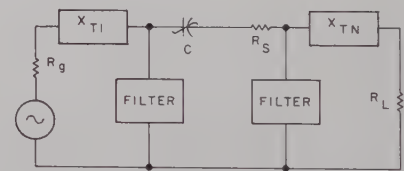


Fig. 1—Circuit model used in the analysis of harmonic generation.

The circuit model used in the derivation of gain (actually a loss) is shown in Fig. 1. We can write the transducer gain for this circuit as

$$g_T = \frac{4R_g R_L |Z_{21}|^2}{|(Z_{11} + Z_{T1})(Z_{22} + Z_{Tn}) - Z_{12} Z_{21}|^2}. \quad (12)$$

Substituting the matrix values we have,

$$g_T = \frac{4R_g R_L \left( \frac{\gamma_{n-1} - \gamma_{n+1}}{1 - \gamma_2} \right)^2 \frac{1}{(n\omega C_0)^2}}{\left| \left( \frac{1}{j\omega C_0 (1 - \gamma_2)} + Z_{T1} \right) \left( \frac{1}{j\omega n C_0} + Z_{Tn} \right) + \frac{\gamma_{n-1}(\gamma_{n-1} - \gamma_{n+1})}{(1 - \gamma_2)^2} \frac{1}{(n\omega C_0)^2} \right|^2}. \quad (13)$$



Now, let us assume that we impose the tuning conditions

$$\text{Imag } X_{+1} = \frac{1}{\omega C_0(1 - \gamma_2)},$$

and

$$\text{Imag } X_{Tn} = \frac{1}{n\omega C_0}. \quad (14)$$

Further, let us assume that all circuit loss, exclusive of source or load resistance, is series loss associated with the nonlinear capacitor. Therefore,  $R_{T1} = R_g + R_s$  and  $R_{Tn} = R_L + R_s$ . Eq. (13) then becomes

$$g_T = \frac{4R_g R_L \left( \frac{\gamma_{n-1} - \gamma_{n+1}}{1 - \gamma_2} \right)^2 \frac{1}{(n\omega C_0)^2}}{\left[ (R_g + R_s)(R_L + R_s) + \frac{\gamma_{n-1}(\gamma_{n-1} - \gamma_{n+1})}{(1 - \gamma_2)^2} \frac{1}{(n\omega C_0)^2} \right]^2}. \quad (15)$$

We can maximize the gain by choosing the proper values for the source and load resistances. A little calculus will show the values to be

$$R_g = R_L = R_s \sqrt{1 + \bar{\gamma}^2 Q_n^2} \quad (16)$$

where

$$\bar{\gamma}^2 = \frac{\gamma_{n-1}(\gamma_{n-1} - \gamma_{n+1})}{(1 - \gamma_2)^2}$$

and

$$Q_n = \frac{1}{n\omega C_0 R_s}.$$

Substituting this optimum value into the expression for transducer gain we get, after some manipulation,

$$g_T = \frac{\gamma_{n-1} - \gamma_{n+1}}{\gamma_{n-1}} \frac{\bar{\gamma}^2 Q_n^2}{[1 + \sqrt{1 + \bar{\gamma}^2 Q_n^2}]^2}. \quad (17)$$

Notice that as we allow the loss to approach zero (by making  $Q$  large), the transducer gain approaches unity. That it will never quite reach unity may be attributed to our initial small-signal approximations.

Using computed values for the capacitance Fourier coefficients, we can readily obtain curves which show how much loss can be expected in harmonic generators using semiconductor diodes. Several such sets of curves are shown in Figs. 2-7 (next page). Here we have plotted conversion loss in db as a function of the diode  $Q$  at the fundamental frequency for the second, third, fourth, sixth, and eighth harmonics. Figs. 2, 3, and 4 show results applicable to diodes which have  $1/\sqrt{V}$  capacitance variations (such as the alloy-junction diodes), while Figs. 5, 6, and 7 show results applicable to  $1/\sqrt[3]{V}$  capacitance variations (such as the diffused-junction diodes). The parameter,  $a$ , is the ratio of ac voltage amplitude to dc bias (including contact potential). The proper value of  $a$  cannot at this time be precisely stated. A combination of theory and experiment indicates that

for peak ac voltages of around 5 volts or less, a value of  $a=0.90$  is reasonable. For lower or higher drive levels the insertion-loss curves corresponding to  $a=0.85$  and  $a=0.95$  are included as well as those for  $a=0.90$ .

If we follow the change in conversion efficiency as a function of drive level, we will observe that at high efficiencies the curves predict saturation phenomena. For example, Fig. 2 indicates that doubling with a diode of  $Q=100$  will yield a conversion loss of 1.6 db, while Fig. 4 indicates a loss of 2.1 db. Although such a saturation characteristic is actually observed in practice<sup>5,6</sup> it is likely that the saturation effect predicted by the curves

is actually due to errors introduced by the original small-signal approximation. The saturation effects encountered experimentally can probably be attributed to a decrease in the effective  $Q$  of the diode caused by forward or reverse conduction.

Several conclusions may be drawn from Figs. 2 through 7. One is that for efficient generation, particularly at the higher harmonics, diode and circuit  $Q$ 's must be quite high. It should also be noted that the generation of higher harmonics with this type of circuit is best accomplished in stages. As an example, let us assume that we wish to generate the sixth harmonic with a diode of  $Q=100$  at the fundamental frequency in circuits having negligible losses. Fig. 3 shows that if we go directly to the sixth harmonic we should expect a conversion loss of 15.5 db. If we choose to double and then to triple with two diodes of the same quality as used in the previous example, we find a conversion loss of 1.8 db in doubling, and 4.5 db in tripling ( $Q=50$  for the tripler), which gives a total conversion loss of only 6.3 db, an improvement of 9.2 db over the single-stage conversion efficiency. If we triple first and then double, we get even better efficiency: only a 5.4-db conversion loss. This is one order of magnitude improvement over the single-stage conversion efficiency.

The example above used the curves corresponding to abrupt-junction diodes for which the capacitance variation is proportional to  $1/\sqrt{V}$ . For a linearly-graded junction, those with a capacitance proportional to  $1/\sqrt[3]{V}$ , the predicted efficiencies are lower. Direct conversion to the sixth harmonic, as in the above example with a linearly-graded diode, will result in a 22-db loss, 6.5 db below the output with a comparable abrupt

<sup>5</sup> R. Lowell and M. J. Kiss, "Solid-state microwave power sources using harmonic generation," *PROC. IRE*, vol. 48, pp. 1334-1335; July, 1960.

<sup>6</sup> D. Leenov and J. W. Rood, "UHF harmonic generation with silicon diodes," *PROC. IRE*, vol. 48, p. 1335; July, 1960.

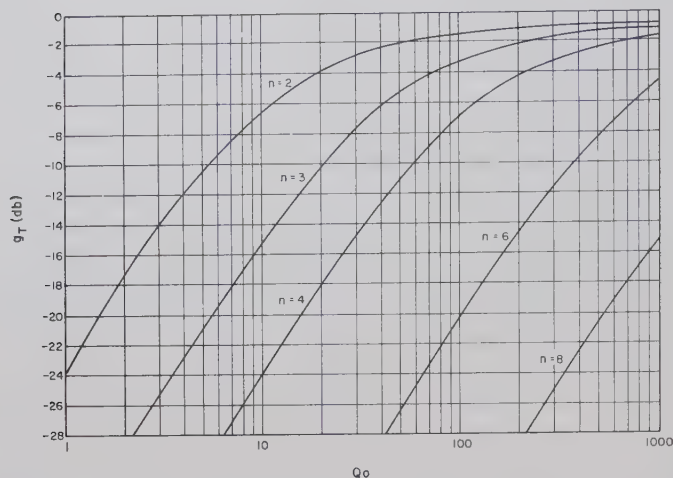


Fig. 2—Computed conversion loss of harmonic generation as a function of diode  $Q$  at the fundamental frequency.  $a=0.85$ . Inverse square-root capacitance variation with voltage.

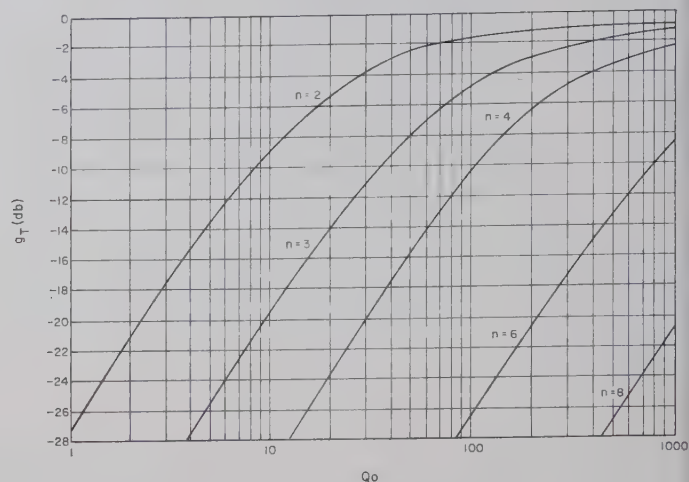


Fig. 5—Computed conversion loss of harmonic generation as a function of diode  $Q$  at the fundamental frequency.  $a=0.85$ . Inverse cube-root capacitance variation with voltage.

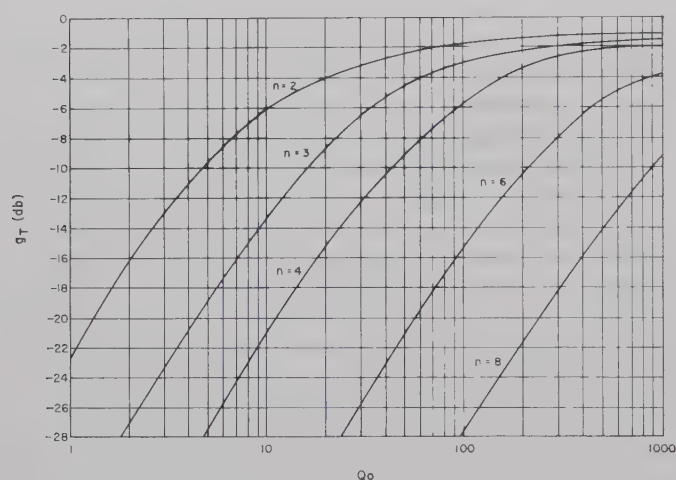


Fig. 3—Computed conversion loss of harmonic generation as a function of diode  $Q$  at the fundamental frequency.  $a=0.90$ . Inverse square-root capacitance variation with voltage.

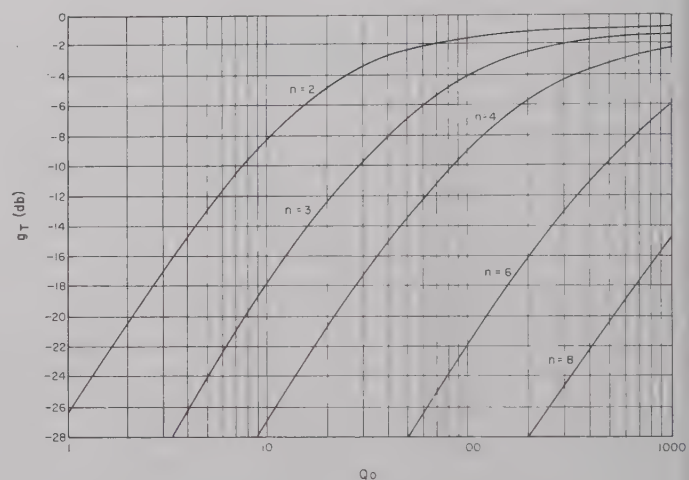


Fig. 6—Computed conversion loss of harmonic generation as a function of diode  $Q$  at the fundamental frequency.  $a=0.90$ . Inverse cube-root capacitance variation with voltage.

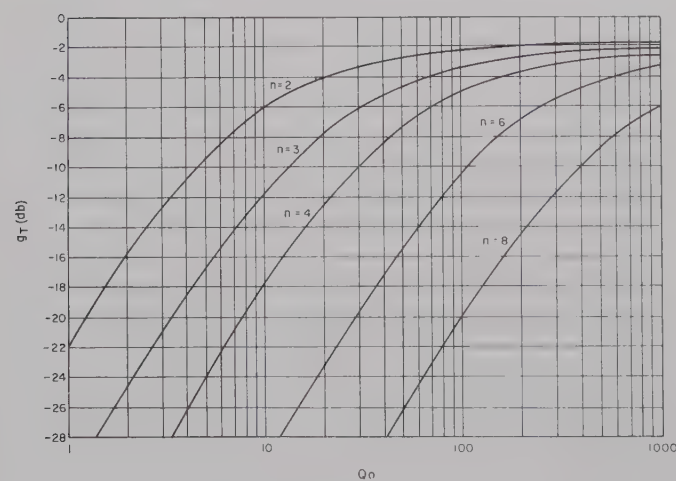


Fig. 4—Computed conversion loss of harmonic generation as a function of diode  $Q$  at the fundamental frequency.  $a=0.95$ . Inverse square-root capacitance variation with voltage.

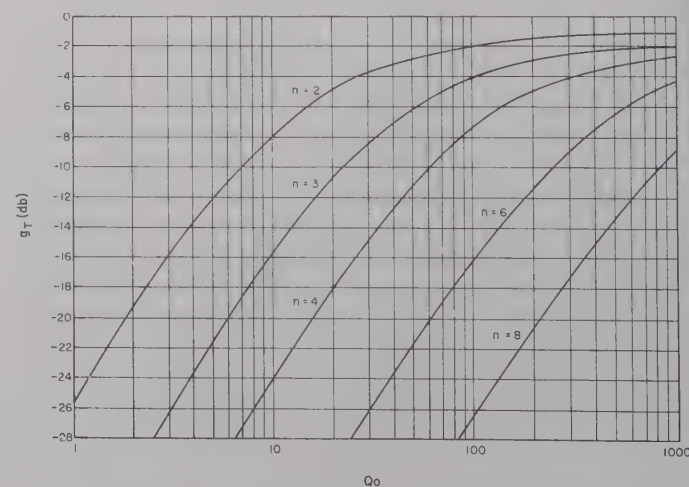


Fig. 7—Computed conversion loss of harmonic generation as a function of diode  $Q$  at the fundamental frequency.  $a=0.95$ . Inverse cube-root capacitance variation with voltage.



junction. A tripler, followed by a doubler, will have a combined loss of 7.4 db, a 2-db greater loss than the previous example using abrupt junction diodes. At the present time, though, diffused silicon diodes are available with a greater reverse breakdown voltage than diodes having abrupt junction characteristics and, therefore, have greater power handling capabilities.

### EXPERIMENTAL RESULTS

To apply harmonic generation to a specific task, considerable attention must be given to the choice of input frequency and to the number and type of multiplier stages. When designing for maximum power output at some desired frequency these factors will be determined by the quality and capabilities of the transistors and re-

actance diodes available at the time of design. This design procedure may best be illustrated by describing a crystal-controlled local oscillator source that supplies 5 to 10 mw of power at 2520 Mc.

To best utilize the reactance diodes available at the time of design, the sequence of multiplication chosen was: triple from 140 to 420 Mc, double from 420 to 840 Mc, and triple again from 840 to 2520 Mc. The last tripler stage was justified by the high-quality reactance diodes available for use at low power levels. A crystal-controlled oscillator, a doubler, and a power amplifier was designed using three 2N1141 transistors which had an output of 200 mw at 140 mc. This circuit, shown in Fig. 8, required 1.3 watts input at 28 volts.

The application of harmonic generation to many microwave problems depends upon the successful packaging of these circuits. A miniature modular construction was used which is light and rugged, yet retains the flexibility of cascading stages to achieve various frequencies and power from common modules. The transistor crystal-controlled oscillator, doubler, and power amplifier were readily adapted to this modular construction. A circuit for the tripler from 140 to 420 Mc is suggested by the circuit model used in the theoretical study (Fig. 1). The actual circuit used is shown in Fig. 9(a). By using miniature piston capacitors and a subminiature potentiometer in this tripler circuit, the size was reduced for packaging in a one cubic inch module. An input of 200 mw at 140

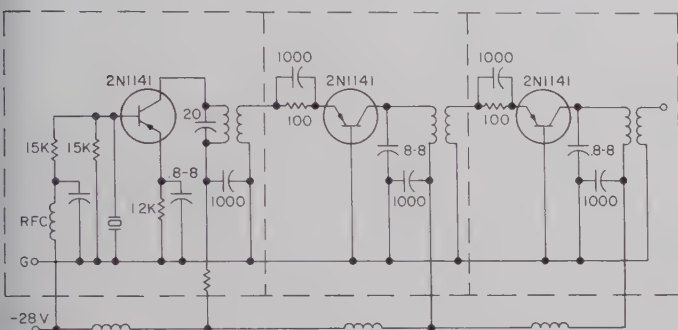
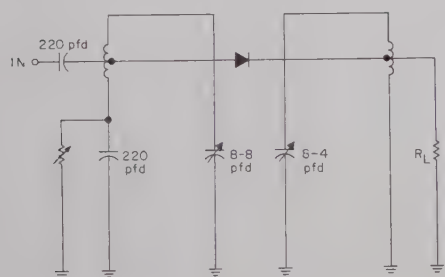
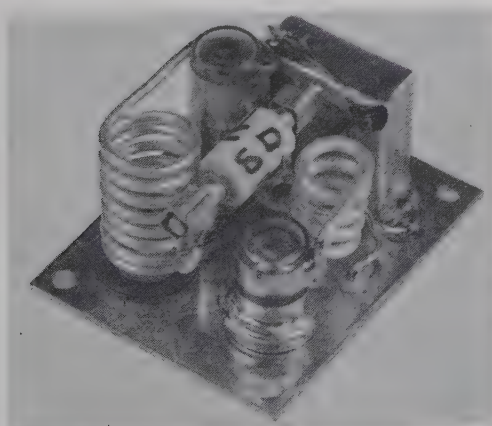


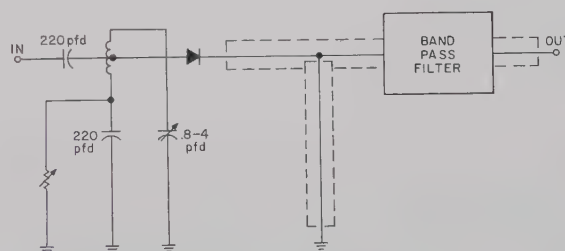
Fig. 8—Schematic diagram of the transistorized crystal-controlled oscillator, doubler, and power amplifier.



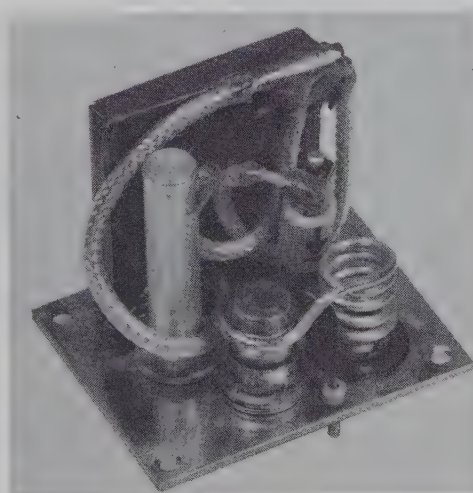
(a)



(b)



(a)



(b)

Fig. 9—(a) Schematic diagram of the reactance-diode tripler from 140 Mc to 420 Mc. (b) Photograph of the reactance-diode tripler from 140 Mc to 420 Mc.

Fig. 10—(a) Schematic diagram of the reactance-diode doubler from 420 Mc to 840 Mc. (b) Photograph of the reactance-diode doubler from 420 Mc to 840 Mc.

Mc produced 80 mw output at 420 Mc. All spurious outputs were suppressed a minimum of 15 db. This 4-db conversion loss was obtained with a diode having a 4-picofarad capacitance at 2-v reverse bias, and a 2.5-ohm series resistance. As reverse breakdown of this diode occurred at approximately 80 volts, considerably more power could be handled by this tripler.

For the doubler to 840 Mc the circuit shown in Fig. 10(a) was evolved which consisted of both lumped and distributed elements. Circuit elements as used in the preceding tripler formed the input of the doubler and miniature coaxial components were developed for use in the output. A stub tuner 3/16-inch in diameter and 7/8-inch long was employed for output tuning and a "Triplate" filter 0.8 inch wide, 0.9 inch high and 1/8 inch thick provided output filtering. A diffused silicon diode with a 0.95-picofarad junction capacitance and 9-ohm series resistance was used in this circuit as shown assembled in Fig. 10(b). An input of 80 mw at 420 Mc produced an output of 30 mw at 840 Mc.

The final tripler to 2520 Mc was designed with distributed circuits at both input and output as shown in Fig. 11. This was reduced to the required 0.8 inch by 0.9 inch by 1 inch size by using Microdot cable to form the resonant lines and a subminiature teflon-loaded filter as the output filter. Approximately 7 mw output was obtained with 30 mw input for a 6.3-db conversion

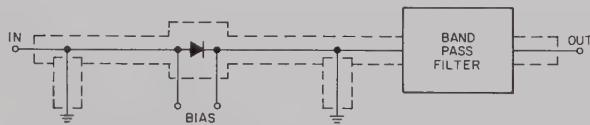


Fig. 11—Schematic diagram of the reactance-diode tripler from 840 Mc to 2520 Mc.

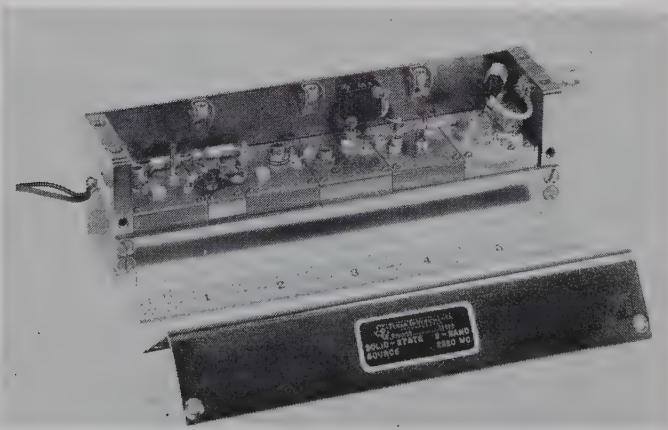


Fig. 12—Photograph of assembled solid-state S-band signal source.

loss. This is 3 db below the theoretical output associated with a 45-kMc cutoff diode. One and one-half-db loss is due to the output filter, and the remaining loss is attributed to losses in the Microdot cable and to tuning problems. The assembled S-band source is shown in Fig. 12.

### CONCLUSION

It is now possible to design a crystal-controlled local oscillator source at microwave frequencies which is light, rugged, and requires only about 1/10 the input power required by other means of local oscillator generation. There are several operating characteristics that should be noted. Since harmonic generators operate with relatively constant efficiency from very low power up to saturation, a lower output power may be accompanied by a corresponding reduction in input power. The power supply problem is greatly simplified, both by the elimination of the heater supply and by the self-limiting characteristic of the harmonic generator as shown in Fig. 13. A 10-per cent deviation from the 28-volt input will cause less than 1-db output variation. This should permit the operation of such microwave sources from unregulated supplies, solar cells, or batteries.

The harmonic generation stages may be considered to be a series of high- $Q$  coupled resonant circuits, and as such, the band-pass is very narrow. Future research might lead to broad-banding techniques but, at present, cascaded harmonic generators have only sufficient band-pass for simple AFC.

Harmonic generation to higher frequencies is limited only by the quality of the reactance diodes. With diodes having a cutoff frequency in the range of 100 to 200 kMc, solid-state power sources to  $K_u$  band should now be possible.

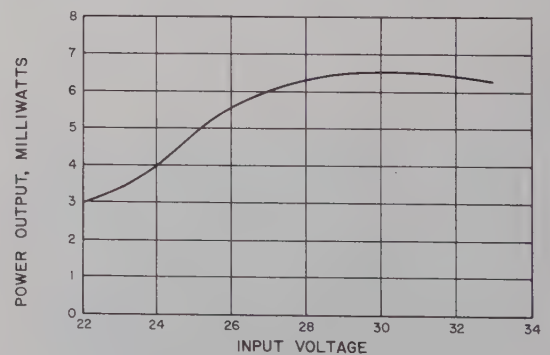


Fig. 13—Plot of the measured of RF power output at 2520 Mc as a function of the applied direct voltage.



# Propagation of Waves in a Plasma in a Magnetic Field\*

WILLIAM P. ALLIS†

**Summary**—The propagation of electromagnetic waves in a plasma in a magnetic field as given by the Appleton-Hartree theory is discussed in terms of the wave normal surfaces instead of the more conventional propagation vector plots, and the “ordinary” and “extraordinary” waves are defined in terms of their polarizations instead of using a continuity argument. This gives a different picture of “a wave” which has some advantages. In particular, “whistlers” become obvious, as are regions of high reflection and high absorption.

The Appleton-Hartree theory is then extended to include the effect of electron temperature, and this results in a third wave whose velocity is of the order of electron thermal motions.

THE propagation of electromagnetic waves through an ionized gas in a magnetic field has been studied<sup>1</sup> since Appleton and Hartree derived the magneto-ionic equations, and most of what is said here can be obtained from their equations although taken from a somewhat different point of view. The remainder comes from the Russian literature,<sup>2</sup> although that has to be re-worked considerably to be understood. The medium to be discussed is a collisionless plasma in which the ions are assumed to be stationary.

Let us first discuss propagation in a plasma without a magnetic field (Fig. 1). It differs from that in a dielectric in that bound electrons generally oscillate in phase with the applied force, whereas a free electron oscillates out of phase. Consequently, the phase velocity  $u$  of an electromagnetic wave in a dielectric is slower than the velocity  $c$  in free space, whereas it is faster in a plasma. This does not violate relativity as the group velocity  $w$  is always less than  $c$ .

It is conventional to represent the dispersion of electromagnetic waves by a plot of the propagation constant  $k$  against  $\omega$ , and for a field free plasma this gives a hyperbola which “cuts off” below the plasma frequency  $\omega_p^2 = Ne^2/\epsilon_0 m$  (Fig. 2). Consequently, radio waves of frequency less than the  $\omega_p$  appropriate for the

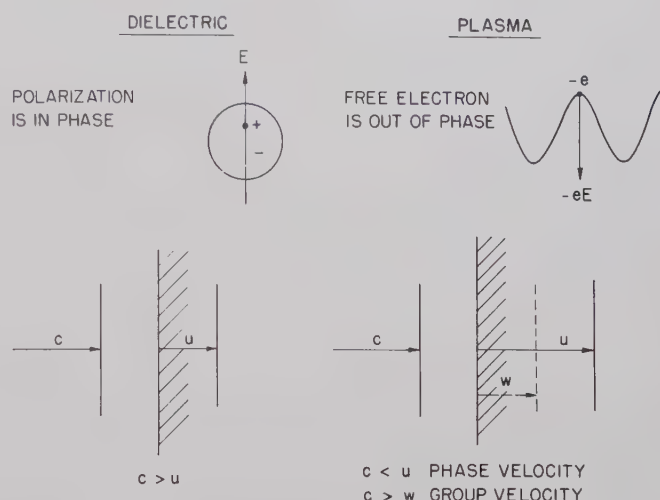


Fig. 1—Contrast of polarization due to bound and free electrons.

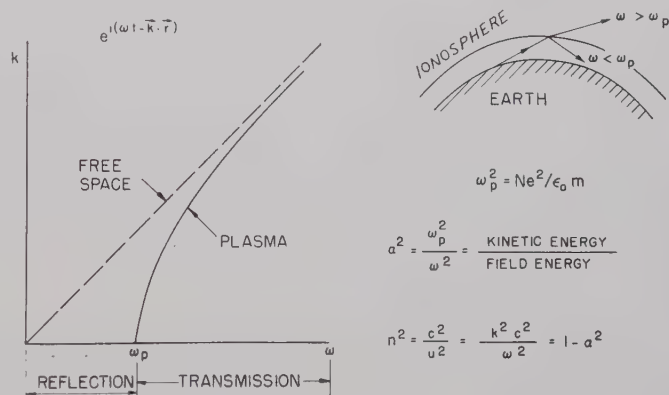


Fig. 2—Propagation constant plot for a plasma without magnetic field.

ionosphere are reflected back to earth. In terms of the ratio

$$\alpha^2 = \frac{\omega_p^2}{\omega^2} = \frac{\text{Kinetic Energy}}{\text{Field Energy}} = \frac{Nmv^2}{\epsilon_D E^2}$$

the index of refraction  $n = c/u$  is given by

$$n^2 = \frac{c^2}{u^2} = \frac{k^2 c^2}{\omega^2} = 1 - \alpha^2.$$

The symbols  $\alpha^2$  and  $\beta$  which are used correspond to  $X$  and  $Y$  in the accepted URSI international notation.

\* Received by the PGM-TT, July 19, 1960; revised manuscript received, November 7, 1960. This work was performed in cooperation with Dr. S. J. Buchsbaum of the Bell Telephone Labs., and was supported in part by the U. S. Army (Signal Corps), the U. S. Air Force (Office of Scientific Res., Air Res. and Dev. Command), the U. S. Navy (Office of Naval Res.); and in part by the Atomic Energy Commission and the National Science Foundation.

† Res. Lab. of Electronics, Mass. Inst. Tech., Cambridge.

<sup>1</sup> J. A. Ratcliffe, "The Magneto-Ionic Theory and Its Applications to the Ionosphere," Cambridge University Press, London, Eng.; 1959. This work provides most of the pertinent references.

<sup>2</sup> A. G. Sitenko and K. N. Stepanov, *Soviet Phys., JETP*, vol. 4, pp. 512-520; 1957.

In the presence of a magnetic field, the conductivity  $\sigma$  becomes a tensor  $\mathbf{\sigma}$ ; and from that, one obtains an equivalent dielectric tensor  $\mathbf{K}$ ,

$$\mathbf{K} = 1 + \frac{\mathbf{\sigma}}{j\omega\epsilon_0} = \begin{vmatrix} K_T & K_H & 0 \\ -K_H & K_T & 0 \\ 0 & 0 & -K_P \end{vmatrix}$$

$$K_r = 1 - \frac{\alpha^2}{1 - \beta}$$

$$K_l = 1 - \frac{\alpha^2}{1 + \beta}$$

$$2K_T = K_r + K_l$$

$$2jK_H = K_r - K_l$$

which turns out to have only three distinct components,  $K_{\text{Parallel}}$ ,  $K_{\text{Transverse}}$ , and  $K_{\text{Hall}}$ —the subscripts referring to the directions of the electric field relative to the magnetic field. The components  $K_T$  and  $jK_H$  are the sum and difference of  $K_{\text{right}}$  and  $K_{\text{left}}$  which refer to circular polarizations of the electric field.

For a plane wave, the wave equation may be written

$$\mathbf{n} \times (\mathbf{n} \times \mathbf{E}) + \mathbf{K} \cdot \mathbf{E} = 0,$$

where  $\mathbf{n}$  is a vector normal to the wave whose magnitude is the index of refraction  $n = c/u$ . This equation is linear homogeneous and hence the determinant of its coefficients must vanish. This yields the dispersion relation

$$\tan^2 \theta = - \frac{K_p(n^2 - K_r)(n^2 - K_l)}{(n^2 - K_p)(K_T n^2 - K_r K_l)}.$$

It is convenient to have this equation solved for  $\tan^2 \theta$ , as setting the numerator equal to zero gives the indices of the two waves (right- and left-handed) which can propagate along  $\mathbf{B}_0$  and setting the denominator equal to zero gives the two waves (ordinary and extraordinary) which propagate across  $\mathbf{B}$ .

$$\begin{aligned} \text{Propagation Along } \mathbf{B}_0: & \begin{cases} n_r^2 = K_r \\ n_l^2 = K_l \end{cases} \\ \theta &= 0 \\ \text{Propagation Across } \mathbf{B}_0: & \begin{cases} n_o^2 = K_p \\ K_T n_x^2 = K_r K_l \end{cases} \\ \theta &= \pi/2 \end{aligned}$$

The polarizations of these four waves in the principal directions are shown in Fig. 3, as are the dispersion equations, which are expressed by giving the index of refraction as a function of  $\alpha = \omega_p/\omega$  and  $\beta = \omega_b/\omega$ ,  $\omega_b = eB/m$ . These relations can be shown by propagation constant plots in Fig. 4.

The *cutoff* for any of these waves occurs when  $k=0$  or  $n=\infty$ , and they have a *resonance* when  $k=\infty$  or  $n=0$ . These differ in that a wave in an inhomogeneous medium which is approaching a cutoff gets refracted away from the cutoff, whereas one approaching a resonance gets refracted towards it. The four singular situations are named in Table I.

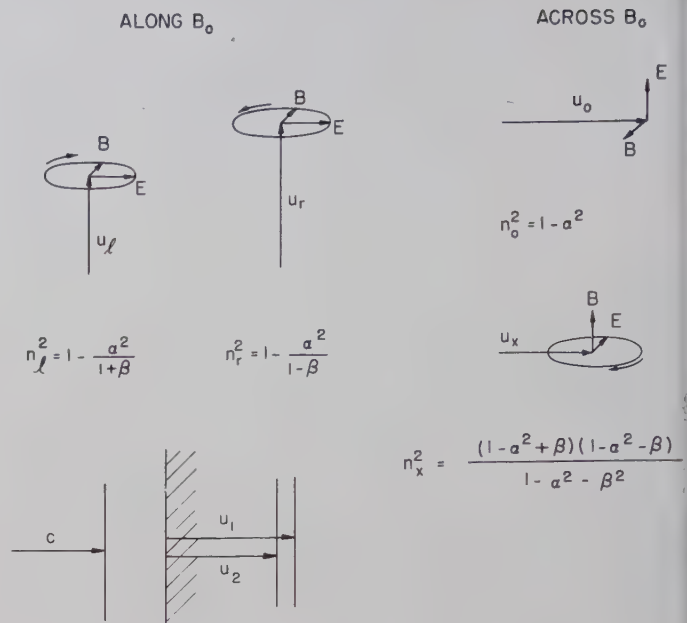


Fig. 3—Polarization of the principal waves.

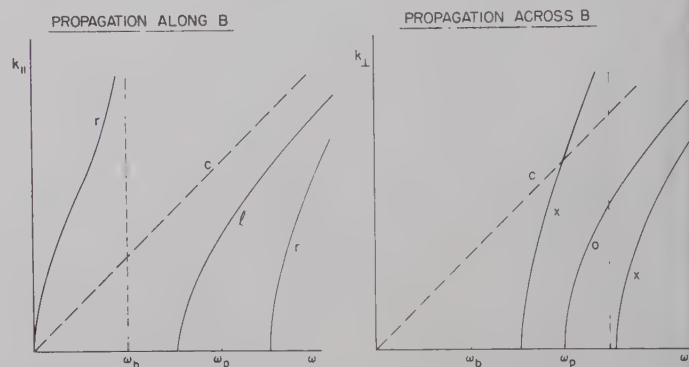


Fig. 4—Propagation constants in a magnetic field.

TABLE I

	Cutoff $u = \infty$	Resonance $u = 0$
Cyclotron:	$(\omega \pm \omega_b)^2 = \omega_b^2 + \omega_p^2$	$\omega^2 = \omega_b^2$
Plasma:	$\omega^2 = \omega_p^2$	$\omega^2 = \omega_p^2 + \omega_b^2$

These four equations are represented by lines, three straight and one parabolic, on a plot of  $\beta^2$  against  $\alpha^2$  (Fig. 5). As  $n^2$  changes sign when one crosses a cutoff or resonance line,  $n$  changes from real to imaginary, and the corresponding wave ceases to propagate. Accordingly, the four lines bound 8 areas on the  $\alpha^2$ - $\beta^2$  plot, in each of which the set of principal waves which propagate is different. It is interesting to show not only the principal waves ( $\theta=0$  and  $\theta=\pi/2$ ) but also the propagation at an arbitrary angle  $\theta$  to the magnetic field, and this is done by plotting the velocity  $u$  against  $\theta$  in a polar plot. Such a diagram is shown in the figure for



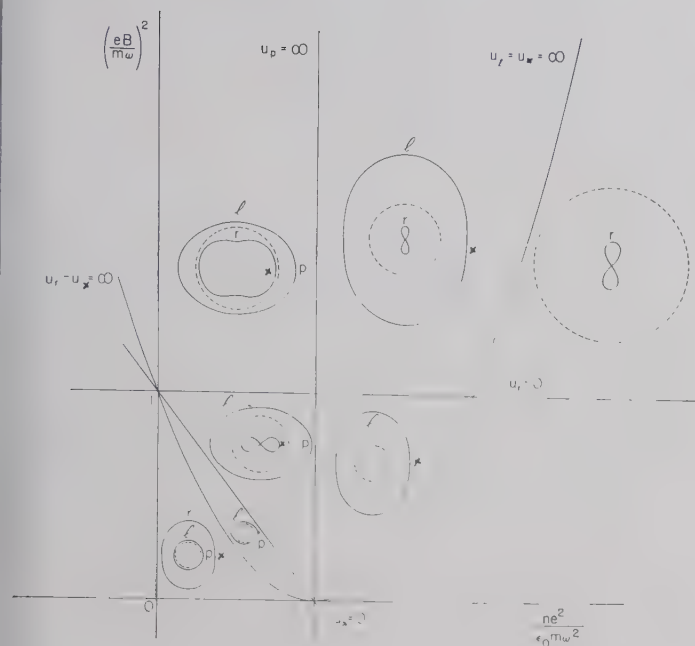


Fig. 5—Wave normal surfaces in a plasma in a magnetic field.

some representative point in each area. In each diagram, the magnetic field is directed up and the “wave normal surface” is obtained by rotating the diagram around this direction as an axis. Unfortunately, the scale of each diagram is different, and this is shown by the dotted circles which represent the velocity of light in free space for each diagram.

One sees that there is one area in the  $\alpha^2$ - $\beta^2$  plane at low magnetic fields ( $\beta^2 < 1$ ) for which no wave can propagate; two areas at low densities ( $\alpha^2 < 1$ ) where there is complete propagation in all directions; and three areas where the wave surface crosses itself at the origin, that is for which there is a resonant cone. When this cone has a small angle with respect to the magnetic field, waves are guided by the magnetic field and this is responsible for the phenomenon of “whistlers.”

Consider the region of the  $\alpha^2$ - $\beta^2$  plot near the  $\beta^2$  axis. If one performs experiments at increasing magnetic fields, which correspond to vertical displacements on the plot, with a right-hand polarized wave, one expects a sharp resonance absorption in the region where the  $r$  wave does not propagate. If one repeats the experiment at a higher plasma density (further to the right on the plot), one expects a resonance broadened on the high-frequency side because the area in which the  $r$  wave does not propagate is broader here. The calculated results with no collisions, and with few collisions, are shown in Fig. 6 (next page). Experimental results, taken both in emission and absorption, are shown in Fig. 7.

This completes what must be said here about the simple plasmas considered by Appleton and Hartree.

We must now consider plasmas in which the thermal motions are not negligible, although we shall still consider them as small. The dielectric tensor now fills out so that there are six independent components

$$K = 1 + \frac{\mathbf{d}}{j\omega\epsilon_0} = \begin{vmatrix} K_{11} & K_{12} & K_{13} \\ -K_{12} & K_{22} & K_{23} \\ K_{13} & -K_{23} & K_{33} \end{vmatrix} \quad \alpha^2 = \frac{Ne^2}{m\epsilon_0\omega^2}, \quad \beta^2 = \left(\frac{eB}{m\omega}\right)^2$$

and each component is considerably more complicated. As an example,

$$K_{11} = 1 - \frac{\alpha^2}{1 - \beta^2} - \epsilon n^2 \left[ \frac{1 + 3\beta^2}{(1 - \beta^2)^3} \xi^2 + \frac{3\zeta^2}{(1 - \beta^2)(1 - 4\beta^2)} \right]$$

where  $\xi$  and  $\zeta$  are the direction cosines of  $\mathbf{k}$  and the dispersion equation is now bi-cubic.

$$-\epsilon a n^6 + A n^4 - B n^2 + C = 0, \quad \epsilon = \left(\frac{kT}{mc^2}\right) \alpha^2,$$

so that there are three wave surfaces. In general, two of these are substantially the same as the ones studied previously and will be called “electromagnetic.” The third has a phase velocity of the order of electron speeds and will be called the “plasma electron” wave.

For propagation along  $B_0$  the three indices are

$$\begin{aligned} \text{Fast Waves} \quad \begin{cases} n_r^2 = \frac{1 - \alpha^2/(1 - \beta)}{1 + \epsilon/(1 - \beta)^3} \\ n_l^2 = \frac{1 - \alpha^2/(1 + \beta)}{1 + \epsilon/(1 + \beta)^3} \end{cases} \\ \text{Plasma Wave } n_p^2 = \frac{1 - \alpha^2}{3\epsilon} \end{aligned}$$

The plasma wave  $n_p$  has the dispersion relation given by Vlasov and by Bohm and Gross and its propagation plot is given in Fig. 8.

For propagation across  $B_0$  the dispersion is more complicated, the extraordinary electromagnetic and plasma waves being coupled in one equation as their polarizations are similar.

There is now a new resonance at  $\beta^2 = 1/4$  or  $\omega = 2\omega_b$ , so that there are now 13 regions on the  $\alpha^2$ - $\beta^2$  plot. The wave surfaces have been calculated by R. Papa and are shown in Figs. 9 and 10. The plasma wave surfaces are shown here considerably enlarged, as they are, in fact, generally much smaller than the electromagnetic waves.

When one also includes the ion temperature, a fourth wave will appear, but this has not been worked out in detail. There is an amazing variety to the possible waves in a plasma in a magnetic field.

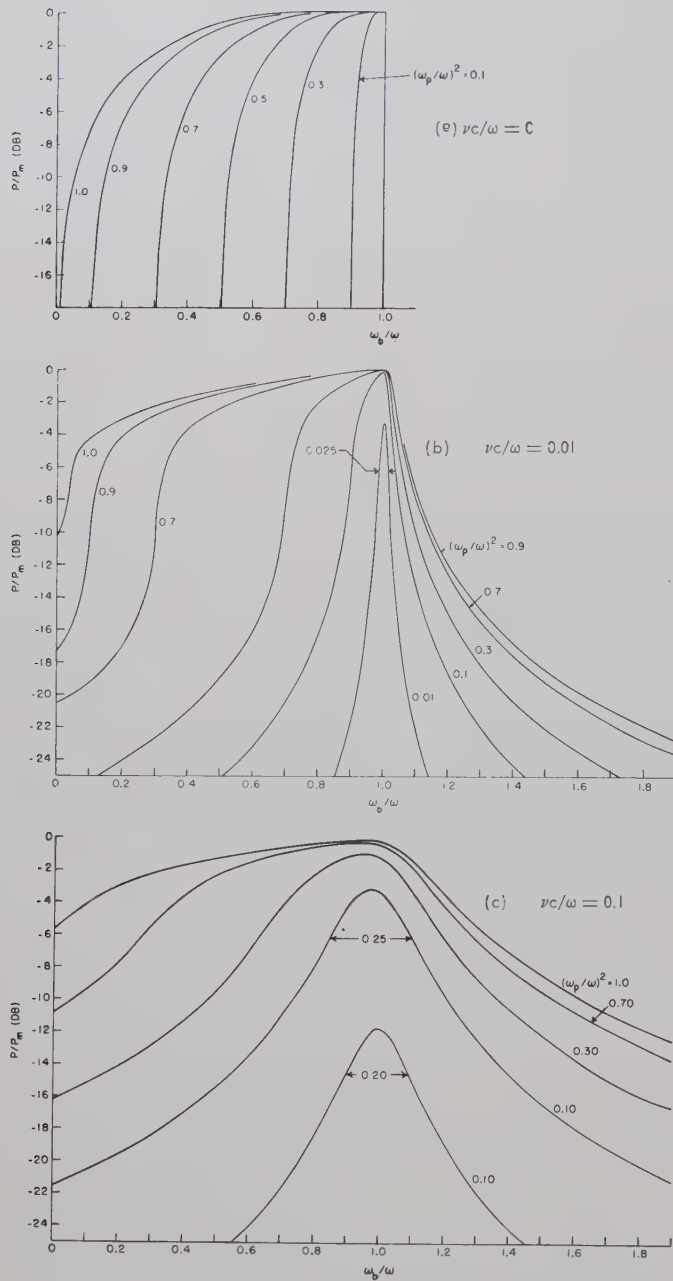


Fig. 6—Attenuation of a right-hand polarized wave transmitted through a plasma slab.

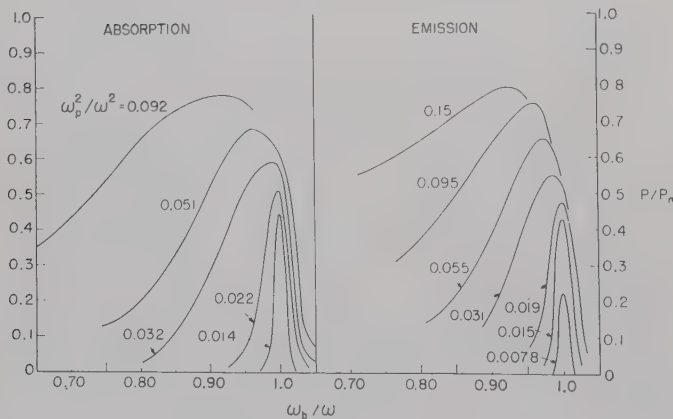


Fig. 7—Observed absorption and emission of microwaves from a plasma.

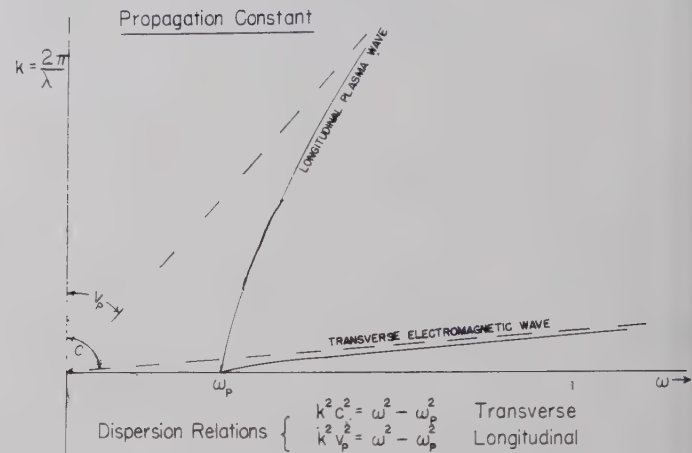


Fig. 8.

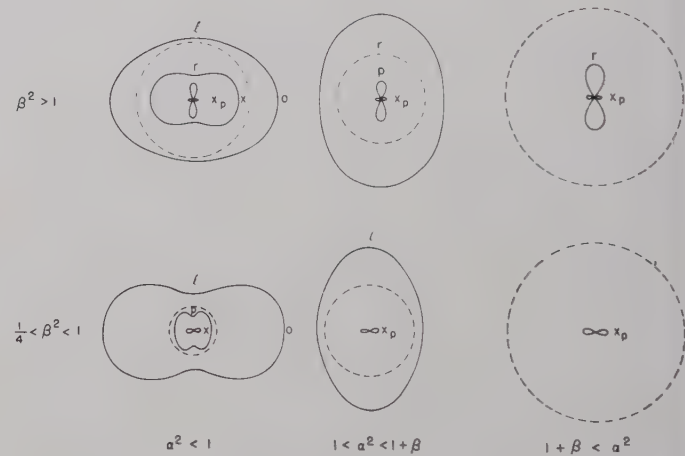


Fig. 9—Normal wave surfaces including electron temperatures.

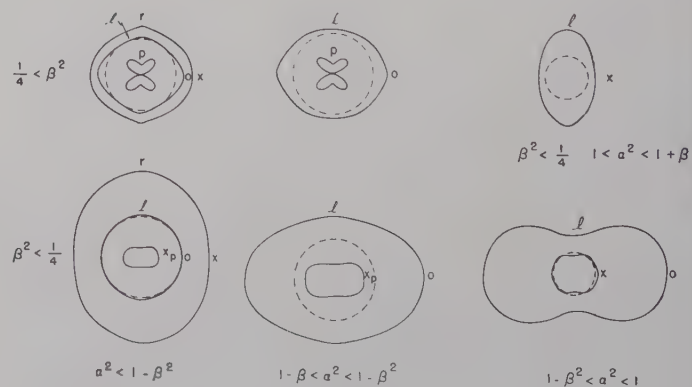


Fig. 10—Normal wave surfaces including electron temperatures.



# Magnetoplasma Effects in Solids\*

BENJAMIN LAX†

**Summary**—Plasmas in solids show a more complex behavior than in gases since they reflect the symmetry properties of crystals. Since the carrier concentration has a wide range in semiconductors and metals, the plasma phenomena can be studied from microwaves to the ultraviolet. The effect of magnetic fields on the electromagnetic properties of plasmas has been experimentally investigated at microwave and infrared frequencies and has been utilized to measure dielectric constant and band structure of such solids in the limit of low magnetic fields. The magneto-plasma exhibits effects analogous to the galvanomagnetic phenomena. However, near resonance in the classical limit, they show up as depolarizing effects in semiconductors and also give rise to a new type of cyclotron resonance under anomalous skin conditions in metals.

## INTRODUCTION

THE electromagnetic properties of plasmas in ionized gases have been considered from the phenomenological classical magneto-ionic theory<sup>1</sup> in the linear limit for two sets of particles, *i.e.*, electrons and ions. Many of the phenomena, studied theoretically and observed experimentally in the various limits designated by Allis,<sup>2</sup> can also be found in solids. In addition, due to the nature of crystalline solids, these effects are further enriched by added complexities associated with the symmetry and band structure of the crystals. Still other differences arise from the dielectric properties and the greater electron densities which are possible. The latter may vary, for practical purposes, in a semiconductor from  $10^6/\text{cc}$  to  $10^{22}/\text{cc}$  for metals. Thus, in actuality, plasma effects in solids have been observed from microwave frequencies well into the vacuum ultraviolet.

## MAGNETOREFLECTION

One of the first experiments performed was the ionospheric reflection from the *E* and *F* layers of the ionosphere.<sup>3</sup> If we neglect the collision of electrons and assume, therefore, that the medium is essentially dispersive, we can write the following expression for the complex index of refraction  $(n + jk)$ :

$$(n + jk)^2 = 1 - \frac{\omega_p^2}{\omega^2}; \quad \omega_p^2 = \frac{Ne^2}{m\epsilon_0}, \quad (1)$$

where  $\omega$  is the angular frequency of the electromagnetic wave;  $\omega_p$  the plasma frequency;  $N$ ,  $e$ , and  $m$  the den-

sity, charge, and mass, respectively, of the electron; and  $\epsilon_0$  the permittivity of free space. An electromagnetic wave incident normally on an idealized ionosphere will be reflected if its frequency is below a critical value, *i.e.*,  $\omega < \omega_p$  since  $n$  is imaginary. Above this frequency, the medium can transmit the wave. The reflection coefficient  $R = [(n-1)^2 + k^2] / [(n+1)^2 + k^2]$  plotted as a function of frequency has the form shown in Fig. 1 for both the ionosphere and a solid.

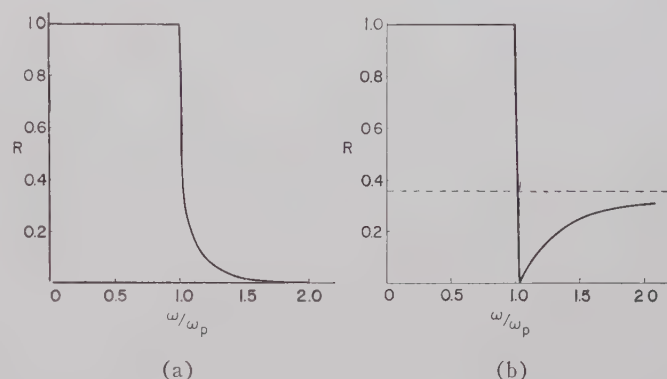


Fig. 1—Variation of the reflection coefficient  $R$  with frequency for (a) an idealized ionosphere, and (b) a solid.

Above the critical frequency  $\omega_p$  the ionosphere is transparent and the reflection goes to zero. In case of a solid the situation is different, even for an isotropic plasma, since the material has a dielectric constant  $\epsilon$  which differs from that of free space, so that

$$n^2 = \epsilon \left( 1 - \frac{\omega_p^2}{\omega^2} \right), \quad \omega_p^2 = \frac{Ne^2}{m^*\epsilon}. \quad (2)$$

Thus, for frequencies just above the plasma frequency, the index of refraction can become unity, and the reflection is zero. Above this value the reflection increases to a higher value which at very high frequencies corresponds to the reflection of a pure dielectric with a dielectric constant  $\epsilon$ . Another distinction between the solid and a gaseous plasma is that the mass of the carrier differs from that of the free electron and is designated by  $m^*$ , the effective mass.  $m^*$  is usually smaller than  $m$ , the free electron mass, although in a few cases it can also exceed this value. The position of the edge or the minimum ( $n=1$ ) has been utilized to determine  $m^*$  in semiconductors by measuring the carrier concentration  $N$  by the Hall effect and  $\epsilon$  by reflection at short wavelengths in the infrared.

The situation becomes quite interesting when a magnetic field is applied. For the two cases of interest, the

\* Received by the PGMTT, July 12, 1960. The work reported in this paper was performed with the joint support of the U. S. Army, Navy and Air Force under contract AF 19(604)-5200.

† Lincoln Lab., M.I.T., Lexington, Mass.

<sup>1</sup> E. V. Appleton, *Proc. Phys. Soc. (London)*, vol. 37, pp. 16D; 1925.

D. R. Hartree, *Proc. Cambridge Phil. Soc.*, vol. 25, pp. 47; 1929.

<sup>2</sup> W. P. Allis, "Propagation of waves in a plasma in a magnetic field," this issue pp. 79-82.

<sup>3</sup> E. V. Appleton and M. A. F. Barnett, *Nature*, vol. 115, pp. 333; 1925.

G. Breit and M. Tuve, *Phys. Rev.*, vol. 28, pp. 554; 1926.

index of refraction becomes

$$n_{\pm}^2 = \epsilon \left[ 1 - \frac{\omega_p^2}{\omega(\omega \mp \omega_c)} \right]; \quad \omega_c = \frac{eH}{m^*c},$$

$$n_{\perp}^2 = \epsilon \left[ 1 - \frac{\omega_p^2(\omega^2 - \omega_p^2)}{\omega^2(\omega^2 - \omega_p^2 - \omega_c^2)} \right], \quad (3)$$

where  $\omega_c$  is the cyclotron frequency,  $n_{\pm}$  corresponds to the indexes of the right- and left-hand circularly polarized waves for propagation along the magnetic field, and  $n_{\perp}$  is the index for a linearly polarized wave with the electric vector  $\mathbf{E}$  perpendicular to the magnetic field  $\mathbf{H}$  and propagating transverse to it. There is also an  $n_{\parallel}$  for transverse propagation, which is given by (2) and corresponds to a linear polarization with  $\mathbf{E} \parallel \mathbf{H}$ . The plasma edge as shown in Fig. 1(b) is now split into two parts by the magnetic field. The condition is given by setting the indexes equal to zero. The results for the critical frequencies are identical for both the longitudinal and the transverse waves, since the propagation constant is zero. Hence, both physically and mathematically, there is no distinction. The critical or cutoff frequencies due to the plasma are then given by

$$\omega_{\pm} = \frac{\sqrt{\omega_c^2 + 4\omega_p^2} \pm \omega_c}{2}. \quad (4)$$

Eq. (4) intrinsically contains the essence of a variety of magnetoplasma phenomena which have been discussed in the literature. Perhaps the first, considered by Appleton and Hartree, is the splitting of the ionospheric reflection by the earth's magnetic field; such experiments were used in measuring its intensity. The conditions for the ionospheric case as well as that for many solids is that  $\omega_c \ll \omega_p$ . Hence, if (4) is expanded in terms of the magnetic field, we obtain

$$\omega_{\pm} = \omega_p \pm \frac{\omega_c}{2} + \frac{\omega_c^2}{8\omega_p}. \quad (5)$$

It is apparent that the plasma edge is split by the cyclotron frequency  $\omega_c$  as depicted by the reflection spectrum shown in Fig. 2. The shape of the pattern for longitudinal and transverse propagation differs as shown. The latter is depicted for linear polarization, *i.e.*,  $\mathbf{E} \perp \mathbf{H}$ . In the case of solids, these effects can be used to measure the effective mass of electrons since the magnetic field and the frequency splitting of the edges can be determined. Indeed, such an experiment has been performed by Wright<sup>4</sup> in semiconductors with infrared radi-

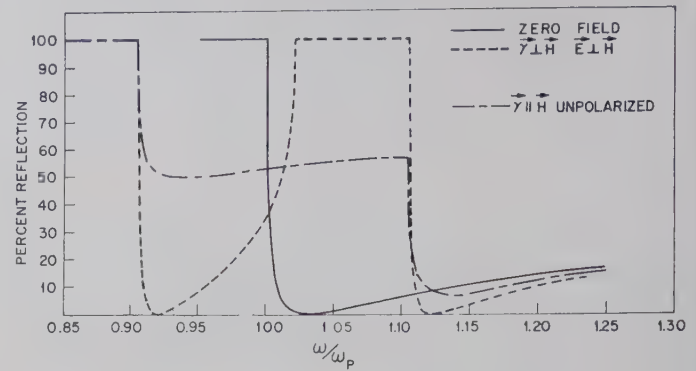


Fig. 2—Theoretical curves of magnetoplasma reflection for isotropic carrier and  $\omega\tau \gg 1$ .  $\omega_c = 0.2 \omega_p$ . (Taken from Lax and Wright.<sup>4</sup>)

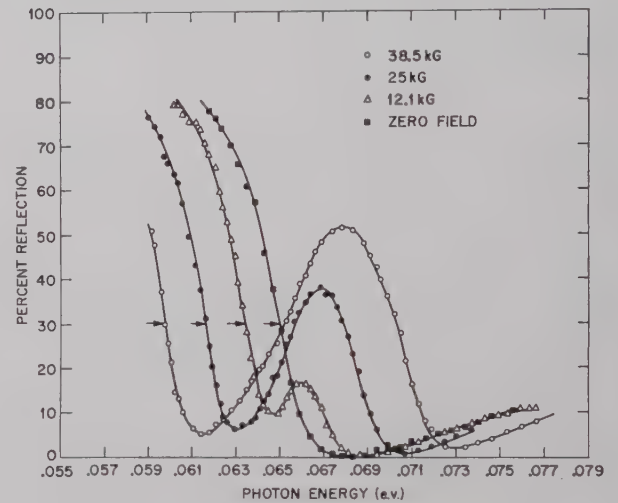


Fig. 3—Magnetoplasma reflection in *n*-type InSb,  $N = 1.8 \times 10^{18} \text{ cm}^{-3}$ . (Taken from Lax and Wright.<sup>4</sup>)

ation as shown in Fig. 3. From such experiments he has determined the effective masses of electrons in InSb and HgSe.

The phenomenon in this limit of magnetic field is of more basic interest for solids than is the determination of a simple effective mass. Actually, for somewhat higher fields, where the quadratic term of the magnetic field becomes important and the quadratic shift of the plasma edge can be observed, the magnetoplasma effect can be shown to be the dispersive analog of the classical galvanomagnetic phenomena. The latter can be discussed in terms of the component of current along an electric field, wherein the current density vector  $\mathbf{J}$  is expanded in terms of the magnetic field as follows:

$$\mathbf{J}_i = \sigma_i E_i + \sigma_{ij} E_i E_j + \sigma_{ijk} E_i H_j H_k + \dots \quad (6)$$

In this case, the first coefficient  $\sigma_i$  is the usual conductivity along the component of the electric field  $E_i$ . The second coefficient, which is linear in  $H$ , is associated with the Hall effect, and is used to determine the Hall mobility and the carrier concentration. The third co-

<sup>4</sup> B. Lax and G. B. Wright, "Magnetoplasma reflection in solids," *Phys. Rev. Lett.*, vol. 4, pp. 16-18; January 1, 1960.



efficient which is quadratic in  $H$  is exhibited by the magnetoresistance of the solid. Thus, the galvanomagnetic effects can reflect the anisotropic properties of the crystal or that of the energy bands of the carriers which contribute to the conductivity. In an analogous manner, (6) can represent the current density of a plasma in a solid in the presence of an electromagnetic wave and a dc magnetic field. In this instance, however, the current vector, which is substituted into Maxwell's equations for evaluating the propagation constant, is assumed to be dispersive, *i.e.*,  $\omega\tau \gg 1$ , where  $\tau$ , the scattering or collision time, is assumed large. Then the first term in (6) gives rise to the plasma frequency, the second term is associated with the linear splitting of the plasma edge and also with the Faraday rotation due to carriers in such materials, and the third term represents the quadratic shift of the plasma edges with magnetic field. Thus, the study of the magnetoplasma effects can reflect the anisotropy properties of the solids. One of the advantages of the magnetoplasma effects over the galvanomagnetic effects is that the latter measures conductivities or mobilities which are expressed as the ratio of the scattering time and the effective mass, *i.e.*,  $\tau/m^*$ , whereas the magnetoplasma effects determine the effective masses directly. Thus, if there is any anisotropy in  $\tau$ , this is not distinguished by the classical Hall effect or magnetoresistance.

To show how the magnetoplasma effects reflect the properties of the energy bands, we have worked out explicit results for electrons in germanium and silicon<sup>4,5</sup> whose motion is associated with spheroidal energy-momentum surfaces. The plasma frequency is given by

$$\omega_p^2 = \frac{Ne^2}{m^*\epsilon}; \quad m^* = \frac{3K}{2K+1} m_i; \quad K = m_l/m_t, \quad (7)$$

where  $m_t$  is the transverse effective mass of the elongated spheroid and  $m_l$  is the longitudinal mass,  $m_l \gg m_t$ . The frequency splitting of the plasma edge is isotropic in a cubic crystal such as germanium and silicon and is given by

$$\Delta\omega = \omega_i(K+2)/(2K+1), \quad (8)$$

where  $\omega_i = eH/m_t c$  is the cyclotron frequency of the transverse mass. Thus, from the determination of the plasma edge and the splitting, one can determine  $m_t$  and  $K$  if the electron density  $N$  and the dielectric constant  $\epsilon$  are known from independent measurements. The quadratic shift in a cubic crystal is not isotropic, and for a system of ellipsoidal surfaces in germanium and silicon for  $\mathbf{E} \parallel \mathbf{H}$ , it has the form

$$\Delta\omega = \frac{\omega_i^2}{\omega} \frac{(K-1)^2}{rK(2K+1)}, \quad (9)$$

where  $r=3, 9$ , and  $6$  for  $H$  parallel to the  $[001]$ ,  $[111]$ , and  $[110]$  crystal axes, respectively, in germanium; and  $r=3$  or  $8$  for  $H$  along the  $[111]$  or  $[110]$  axes in silicon.  $\Delta\omega=0$  for  $H \parallel [001]$  in silicon. Analogous results can be obtained for the quadratic shift for  $\mathbf{E} \perp \mathbf{H}$ . The importance of these results is that if the quadratic effect is studied together with the linear effect,  $\omega_i$  and  $K$  can be directly measured, and also the disposition of the family of ellipsoidal energy surfaces can be deduced from the anisotropy of the quadratic shift. The method can also be employed to study more complicated energy bands such as those associated with the holes in germanium and silicon.<sup>6</sup> The coefficients of (6) can be evaluated in terms of the band parameters in this case also. For noncubic crystals, information can be obtained from the plasma effects at zero magnetic field which can show anisotropy with crystal orientation and polarization of the electromagnetic waves. In bismuth such effects have been observed in the infrared on reflection<sup>7</sup> and are shown in Fig. 4. Additional information can be obtained if the magnetoplasma effect of these edges is studied in detail.

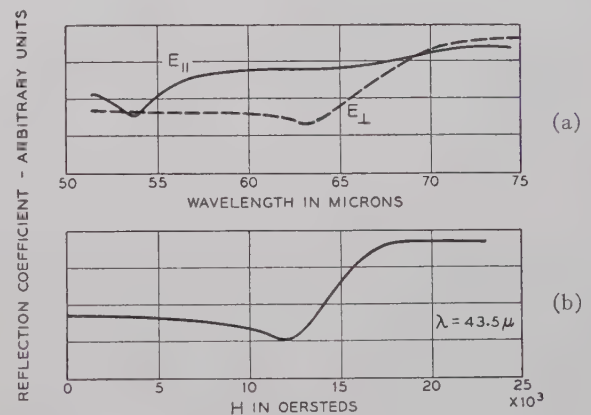


Fig. 4—(a) The reflection coefficient for a single crystal of pure bismuth with the surface normal to a twofold axis.  $E_{\perp}$  and  $E_{\parallel}$  refer to plane-polarized radiation perpendicular or parallel to a threefold axis. (b) The reflection coefficient, for the same sample as (a), shown as a function of magnetic field at a wavelength of 43.5 microns. The magnetic field is normal to the plane of the sample. (Taken from Boyle, Brailsford, and Galt.<sup>7</sup>)

### CYCLOTRON RESONANCE

Another limit of (6) which has been considered in connection with cyclotron resonance is the case where

<sup>6</sup> B. Lax and J. G. Mavroides, "Statistics and galvanomagnetic effect in germanium and silicon with warped energy surfaces," *Phys. Rev.*, vol. 100, pp. 1650-1657; December 15, 1955.

J. G. Mavroides and B. Lax, "Magnetoresistance of holes in germanium and silicon with warped energy surfaces," *Phys. Rev.*, vol. 107, pp. 1530-1534; September 15, 1957.

<sup>7</sup> W. S. Boyle, A. D. Brailsford, and J. K. Galt, "Dielectric anomalies and cyclotron absorption in the infrared: Observations on bismuth," *Phys. Rev.*, vol. 109, pp. 1396-1989; February 15, 1958.

<sup>5</sup> B. Lax and L. M. Roth, "Propagation and plasma oscillation in semiconductors with magnetic fields," *Phys. Rev.*, vol. 98, pp. 548-549; April 15, 1955.

$\omega_c \gg \omega_p$ . Usually, however, in such experiments, particularly at microwaves, the frequency is fixed and the magnetic field is varied. In this instance, only the positive index of refraction of (3) applies, since this is the one with the singularity corresponding to cyclotron resonance, *i.e.*,  $\omega = \omega_c$ . If, then, (3) is solved for the cyclotron frequency  $\omega_c$  for  $n_+ = 0$ , we find

$$\omega_c = \omega - \frac{\omega_p^2}{\omega} \quad (10)$$

For frequencies near the plasma frequency but above it, this corresponds to cyclotron resonance; however, there is a plasma correction  $\omega_p^2/\omega$  which must be made to evaluate the effective mass. The above situation also holds for resonance in the infrared where the magnetic field is varied. Such experiments were carried out by Lipson<sup>8</sup> on InSb with fixed frequencies obtained by the use of reststrahlen plates which gave selected wavelengths in the far infrared centered at 63  $\mu$ , 83  $\mu$  and 94  $\mu$ . The plasma frequency, which at room temperature for the intrinsic carrier concentration of about  $\sim 1 \times 10^{16}/\text{cc}$  corresponds to a wavelength of  $\sim 180$  microns, produces a shift of the resonance frequency as the wavelength becomes larger, as shown in Fig. 5. Thus, at 94  $\mu$  there is a correction of about 25 per cent to the resonance condition as shown by the intersection of the dotted line with the reflection curve.

In the infrared with a prism or a grating instrument, it is usual to vary the frequency; then, in the limit of  $\omega_c \gg \omega_p$ , (6) gives

$$\omega_1 = \omega_c + \frac{\omega_p^2}{\omega_c}, \quad \omega_2 = \frac{\omega_p^2}{\omega_c} \quad (11)$$

The first of these equations is the equivalent of the previous result and gives the plasma correction for the cyclotron resonance condition. The second result represents a resonance which has been obtained in a somewhat different form by Dresselhaus, Kip and Kittel<sup>9</sup> which they designated as "magnetoplasma resonance." Their analysis involved resonance absorption in a sample of finite dimension, small compared to a wavelength or the penetration depth in the medium as limited by the plasma. This occurs when the plasma frequency is larger than that of the electromagnetic wave. The equation of motion of the carriers taking into account the depolarizing effect due to the plasma, which builds up charges on the surface of the specimen, can be written

$$m^*(\nu + j\omega)\mathbf{v} = q\mathbf{E}_i + q\mathbf{v} \times \mathbf{H}/c, \quad (12)$$

<sup>8</sup> H. Lipson, S. Zwerdling, and B. Lax, "Far infrared cyclotron resonance and magneto-plasma effects in InSb," *Bull. Am. Phys. Soc.*, Ser. 2, vol. 3, p. 218; May 1, 1958.

<sup>9</sup> G. Dresselhaus, A. F. Kip, and C. Kittel, "Plasma resonance in crystals: Observations and theories," *Phys. Rev.*, vol. 100, pp. 618-625; October 15, 1955.

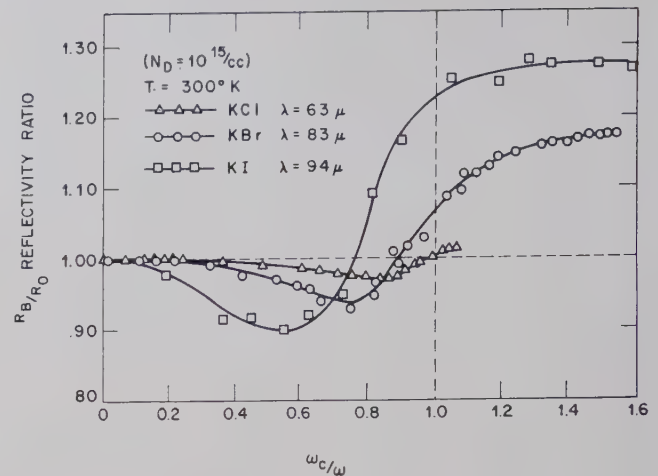


Fig. 5—Far infrared cyclotron resonance in InSb showing the magnetoplasma effect which shifts reflection minimum and crossover to lower fields. (Taken from Lipson, Zwerdling, and Lax.<sup>8</sup>)

where  $\nu$  is the collision frequency and  $q$  the charge of the carrier, and the internal field  $E_i$  is given in terms of the external field  $E$  by

$$(1 + L\chi_0) \cdot E_i = E + jL \cdot \nu \frac{Nq}{\omega\epsilon_0}, \quad (13)$$

where  $\chi_0$  is the dielectric susceptibility,  $N$  the number of carriers, and  $L$  the depolarizing tensor. If (12) and (13) are solved for the velocity components, an effective conductivity tensor for a finite sample can then be obtained. From the tensor components it is possible to obtain expressions for the absorption of energy in specimens of different geometries. These results have been given for flat disks with magnetic field perpendicular, thin flat slabs with the field parallel, and long cylinders with an axial field. For the first configuration, the magnetoplasma effect is eliminated. For the other two, the depolarizing factors produce interesting effects which can be most simply illustrated for the cylindrical geometry. If this is excited by circularly polarized waves, then the effective conductivities become

$$\sigma_{\pm}/\sigma_0 = \left[ 1 + j \left\{ \omega - \frac{\omega_p'^2}{\omega} \mp \omega_c \right\} \gamma \right]^{-1}, \quad (14)$$

where

$$\sigma_0 = \frac{Ne^2\tau}{m^*} = \omega_{p0}^2\epsilon_0\tau$$

$$\omega_{p0}^2 = Ne^2/m^*\epsilon_0; \quad \omega_p' = \omega_{p0}/\sqrt{2 + \chi_0}.$$

The absorption can then be calculated by taking the real part of the conductivities. The surprising result which evolves is that the negative circularly polarized wave interchanges roles with the positive one as the carrier density goes above a critical value  $\omega_p' = \omega$ . This is the condition for obtaining magnetoplasma reso-



nance, and in the limit of high density where  $\omega_p' > \omega$ , the negative polarized wave has a resonance corresponding to

$$\omega\omega_c \approx \omega_p'^2, \quad (15)$$

analogous to the low-frequency result of (11). The results are shown graphically for the real parts of  $\sigma_+$  and  $\sigma_-$  for the cylinder in Fig. 6. For low densities  $\omega_p' < \omega$ , there is a resonance peak for the positive polarization at the usual cyclotron frequency. At the critical frequency  $\omega_p' = \omega$ , no resonance absorption occurs for either sense of polarization. However, at large densities  $\omega_p' > \omega$ , resonance occurs only for the negative circularly polarized wave. In this case, it can be shown that resonance occurs even when  $\omega\tau < 1$ . The condition for a resolvable peak requires that  $(\omega_p'^2/\omega)\tau = \omega_c\tau > 1$ .

The magnetoplasma effects have been observed at microwave frequencies<sup>9</sup> in *n*-type InSb with the magnetic field both parallel and perpendicular to a finite disk, so that both  $L_{||}$  and  $L_{\perp}$  had finite values. The "magneto-plasma resonance" absorption for *H* perpendicular to the sample is then given by

$$(\omega\omega_c)_{\perp} \approx \omega_{p0}^2 \frac{L_{\perp}}{1 + L_{\perp}\chi_0}. \quad (16)$$

When the magnetic field is parallel to the disk, the resonance condition becomes

$$(\omega\omega_c)_{||} \approx \omega_{p0}^2 \sqrt{\frac{L_{\perp}L_{||}}{(1 + L_{\perp}\chi_0)(1 + L_{||}\chi_0)}}. \quad (17)$$

The ratio of the resonance fields for these two configurations is then obtained from the above and gives

$$\frac{\omega_{c\perp}}{\omega_{c||}} = \sqrt{\frac{L_{\perp}(1 + L_{||}\chi_0)}{L_{||}(1 + L_{\perp}\chi_0)}}. \quad (18)$$

This ratio should be independent of the frequency, and for the results shown in Fig. 7 it has a value  $\sim 0.8$  with  $L_{\perp} \approx 0.15$ ,  $L_{||} \approx 0.7$ , and  $\chi_0 = 15$ ; this is in reasonable agreement with the experimental results.

#### ANOMALOUS SKIN EFFECT

A phenomenon which can also be attributed to the existence of a high-density electron plasma is found in metals at low temperatures. The scattering time is rather long for pure metals, and therefore the medium at microwave frequencies can be considered to be dispersive; *i.e.*,  $\omega\tau > 1$ . Nevertheless, at these wavelengths the plasma behaves as a medium below cutoff or as a perfect reflector in which the penetration depth of the electromagnetic wave is given by  $\delta \approx c/\omega_p$ . For a metal such as copper, this penetration depth is of the order of  $10^{-5}$  cm. In a metal such as bismuth,  $\delta$  is of the order of  $10^{-4}$  cm. The mean free path in these materials, how-

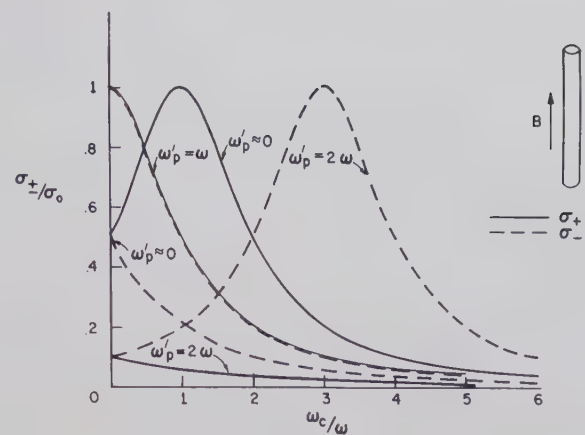


Fig. 6—Magnetoplasma effect for a circular cylinder with the magnetic field along the axis. Here  $\omega\tau = 1$ ,  $\omega' = \omega - (\omega_p')^2/\omega$  has the values shown. The absorption for linear polarization is proportional to  $\sigma_+ + \sigma_-$ . (Taken from an unpublished figure by B. Lax and L. M. Roth.)

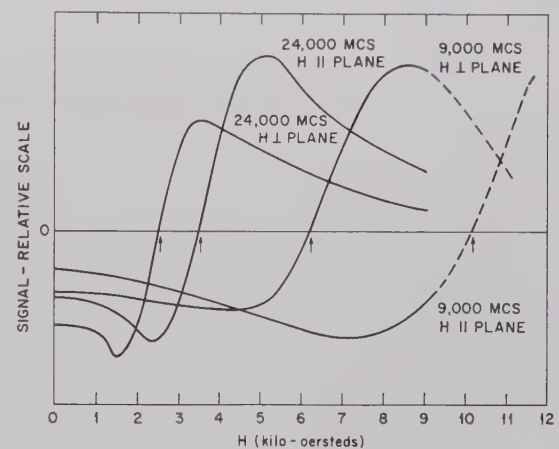


Fig. 7—Experimental plasma resonance absorption signals obtained with carrier modulation in a thin disk of *n*-type indium antimonide at 77°K, at 9000 Mc and 24,000 Mc as indicated. The static magnetic field is directed normal to, or parallel to, the plane of the disk in separate runs. The broken lines connect the curves below 9000 oersteds with single terminal points determined at higher fields. The resonance condition is determined approximately by the crossover points. (Taken from G. Dresselhaus, A. F. Kip, C. Kittel, and G. Wagoner, *Phys. Rev.*, vol. 98, pp. 556–557; 1955.)

ever, is considerably longer at liquid helium temperatures, being of the order of  $10^{-2}$  cm. Consequently, it is certain that electrons which participate in the interaction with the electromagnetic waves do so under a condition known as the anomalous skin effect. In the presence of a magnetic field, this results in a new and useful phenomenon which was first discovered by two Russian theoretical physicists, Azbel and Kaner.<sup>10</sup> According to their theory, if the magnetic field is parallel to the surface of the metal, some of the electrons move in a helical path cycle in and out of the skin depth con-

<sup>10</sup> M. I. Azbel and E. A. Kaner, "The theory of cyclotron resonance in metals," *Soviet Phys. JETP*, vol. 3, pp. 772–774, December, 1956; "Theory of cyclotron resonance in metals," vol. 5, pp. 730–774; November, 1957.

taining the RF electric field, as shown in Fig. 8. If the magnetic field is tuned to resonance, then the electron and the electric field are in phase much similar to that in the cyclotron, where the skin depth now acts as do the dees in a cyclotron. This occurs when the magnetic field is tuned to the condition that  $\omega_c = \omega$ . However, the electrons can also show resonant absorption when the cyclotron rotation occurs in phase over several cycles of the RF field so that  $n\omega_c = \omega$ . Thus, this phenomenon gives rise to multiple or to subharmonic resonance absorption. The theory for the impedance of such absorption was worked out under the anomalous skin effect by using the Boltzmann transport theory.<sup>10,11</sup> The real part of this impedance which is proportional to the absorption is shown in Fig. 9. This phenomenon has now been observed on a number of metals at microwave frequencies<sup>12</sup> and the results, as observed in zinc, are shown in Fig. 10. Indeed, the behavior well confirms the theoretical predictions.

### FARADAY EFFECT

The last phenomenon which we shall consider is well known to those who have worked in the field of microwave ferrites, *viz.*, the Faraday effect. Plasmas in a longitudinal magnetic field are capable of producing a measurable rotation in the spectral region from microwave frequencies into the infrared.<sup>13</sup> It has been found to be particularly useful for the study of semiconductors in the spectral range from a few microns to about 20 microns where polarizers and analyzers using optical techniques can be built. The theory is analogous to that of the ferrite case, and in the limit where the cyclo-

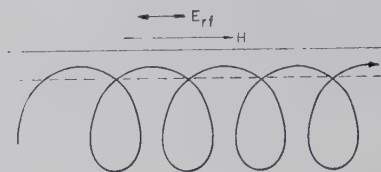


Fig. 8—Possible electron trajectory in a metal under the conditions of the Azbel-Kaner effect.

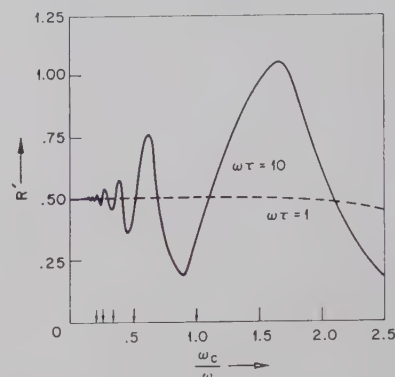


Fig. 9—Theoretical plot of  $R' = R(16\pi\omega/3^{3/2}c^2)^{-1}(3\pi^2\sigma_0\omega/c^2v_F\tau)^{1/2}$ , where  $R$  is the resistive component of the surface impedance, vs  $\omega_c/\omega$  for  $\omega\tau = 1$  and 10. The first five harmonics are indicated by arrows. The fundamental and first harmonic are appreciably shifted toward lower magnetic fields. This shift remains even for longer relaxation times. (Taken from Mattis and Dresselhaus.<sup>11</sup>)

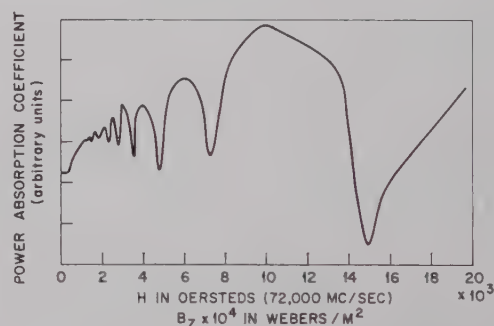


Fig. 10—Cyclotron resonance at 1.3°K in zinc with the magnetic field in the sample plane and along a sixfold axis. (Taken from Galt, Merritt, Yager, and Dail.<sup>12</sup>)

<sup>11</sup> D. C. Mattis and G. Dresselhaus, "Anomalous skin effect in a magnetic field," *Phys. Rev.*, vol. 111, pp. 403-411; July 15, 1958.

S. Rodriguez, "Theory of cyclotron resonance in metals," *Phys. Rev.*, vol. 112, pp. 1616-1620; December 1, 1958.

<sup>12</sup> E. Fawcett, "Cyclotron resonance in tin and copper," *Phys. Rev.*, vol. 103, pp. 1582-1583; September 1, 1956.

J. E. Aubrey and R. G. Chambers, "Cyclotron resonance in bismuth," *J. Phys. Chem. Solids*, vol. 3, pp. 128-132; 1957.

A. F. Kip, D. N. Langenberg, B. Rosenblum, and G. Wagoner, "Cyclotron resonance in tin," *Phys. Rev.*, vol. 108, pp. 494-495; October 15, 1957.

W. R. Datars and R. N. Dexter, "Cyclotron absorption in antimony," *Bull. Am. Phys. Soc.*, ser. 2, vol. 2, pp. 345-346; November, 1957.

P. A. Bezuglyi and A. A. Galkin, "Cyclotron resonance in tin at 9300 Mcs," *Soviet Phys. JETP*, vol. 6, pp. 831-833; April, 1958.

J. K. Galt, F. R. Merritt, W. A. Yager, and H. W. Dail Jr., "Cyclotron resonance effects in zinc," *Phys. Rev. Lett.*, vol. 2, pp. 292-294; April 1, 1959.

D. N. Langenberg and T. W. Moore, "Cyclotron resonance in aluminum," *Phys. Rev. Lett.*, vol. 3, pp. 137-138; August 1, 1959; "Cyclotron resonance in copper," vol. 3, pp. 328-330; October 1, 1959.

E. Fawcett, "Cyclotron resonance in aluminum," *Phys. Rev. Lett.*, vol. 3, pp. 139-141; August 1, 1959.

<sup>13</sup> R. Rau and M. E. Caspari, "Faraday effect in germanium at room temperature," *Phys. Rev.*, vol. 100, pp. 632-639; October 15, 1955.

T. S. Moss, S. D. Smith, and K. W. Taylor, "The infrared faraday effect due to free carriers in indium antimonide," *J. Phys. Chem. Solids*, vol. 8, pp. 323-326; January, 1959.

R. N. Brown and B. Lax, "Infrared faraday rotation in InSb," *Bull. Am. Phys. Soc.*, vol. 4, p. 133; March 30, 1959.

tron frequency  $\omega_c \gg \omega$  and the medium is dispersive,  $\omega\tau \gg 1$ , which holds even at room temperature in the infrared; the result from classical theory is

$$\Theta = \frac{Ne^3H}{2\omega^2 m^* c^2 \sqrt{\epsilon}}, \quad (19)$$

where  $\Theta$  is the angle of rotation of a linearly polarized field propagating along a magnetic field, and the other parameters are those already defined in the text. The importance of this result is that it can be utilized in measuring  $m^*$  by determining  $N$  and  $\epsilon$  by the Hall effect and reflection measurements, respectively, where other techniques are not feasible. Furthermore, the effective mass as a function of energy in the band can be



studied by varying the concentration  $N$ . Such studies have been carried out by Smith, *et al.*<sup>14</sup>

### CONCLUSION

A variety of phenomena involving the behavior of a plasma in a solid in the presence of a magnetic field has been described. With almost no exception, each of these in one form or another reflects the band properties of the semiconductor or metal which is being investigated. Although the phenomena are complex and of primary interest to physicists who wish to measure the fundamental parameters associated with holes and electrons in these materials, the results are, neverthe-

<sup>14</sup> S. D. Smith, T. S. Moss, and K. W. Taylor, "The energy-dependence of electron mass in indium antimonide determined from measurements of the infrared faraday effect," *J. Phys. Chem. Solids*, vol. 11, pp. 131-139; September, 1959.

less, already of some practical significance to engineers who wish to utilize these effects for developing new kinds of devices. Obviously, these magnetoplasma effects can be utilized as polarizers and for nonreciprocal components in the regions of the far infrared spectrum where such devices do not exist. However, this type of investigation is attractive because it may be instrumental in the development of an infrared cyclotron resonance maser. The magnetoplasma effects permit not only the investigation of the anisotropy of the effective masses, but also their variations with energy, an important requirement for the development of such a cyclotron resonance maser.<sup>15</sup>

<sup>15</sup> B. Lax, "Cyclotron resonance and impurity levels in semiconductors," *Quantum Electronics Conference 1959*, Columbia University Press, New York, N. Y., p. 429; 1960.

B. Lax and J. G. Mavroides, "Cyclotron Resonance, Solid State Physics," Academic Press, New York, N. Y., vol. 11, pp. 261-400; 1960.

## Coherent Excitation of Plasma Oscillations in Solids\*

DAVID PINES†

**Summary**—Considerations are put forth concerning the feasibility of observing the coherent excitation of plasma oscillations in a two-component plasma of electrons and holes in semiconductors or semimetals. By coherent excitation is meant the onset of a high-frequency ("two-stream") instability arising from an appreciable drift of electrons vs holes under the action of an applied electric field. Conditions favorable to coherent excitation include a sizeable difference in electron and hole masses, and long relaxation times for both kinds of particles. The extent to which such conditions are present in InSb is discussed.

THE PLASMA formed by the electrons and holes in a semiconductor or semimetal offers, in many respects, a promising "laboratory" for carrying out experiments of interest on collective properties of plasmas. By gaseous standards, the plasma is well behaved. One can measure and vary in simple fashion the concentrations, mass ratios, and temperature ratios of the two plasmas. The principal drawback to carrying out plasma experiments is that the electrons and holes in this fully ionized plasma are not completely free; they are scattered by phonons, impurity atoms, and, in some cases, one another, to an extent which may be important for the study of collective phenomena. Indeed, if  $\omega$  is the frequency of interest for the phenomenon under investigation, and  $\tau_{\pm}$  represents the

electron (or hole) relaxation time associated with the scattering mechanisms, then it is necessary that

$$\omega \tau_{\pm} \gtrsim 1,$$

in order that the collective behavior be observable.

In the present paper some theoretical investigations of collective behavior in solid-state plasmas, which have been carried out in collaboration with J. R. Schrieffer,<sup>1</sup> will be summarized. The problem of particular concern was the feasibility of observing in such plasmas a high frequency instability associated with the coherent excitation of plasma oscillations. The instability, which resembles the "two-stream" instability encountered in electron beam studies, arises if a sufficiently large drift of electrons vs holes is produced under the action of an applied electric field.

Most previous studies<sup>2</sup> of instabilities in the two component plasmas were carried out under the assumption that the electron and ion (or hole) temperatures were equal. In these circumstances the required drift velocity is of the order of  $1.3v_{-}$ , where  $v_{-}$  is the electron thermal

\* Received by the PGM-TT, July 18, 1960. This work was carried out under a joint General Atomic-Texas Atomic Energy Research Foundation program on controlled thermonuclear reactions.

† John Jay Hopkins Lab. for Pure and Appl. Science, General Atomic Div., General Dynamics Corp., San Diego, Calif. and Depts. of Phys. and Elec. Engrg., University of Illinois, Urbana, Ill.

<sup>1</sup> D. Pines and J. R. Schrieffer, "Collective Behavior in Solid State Plasma," General Atomic Div., General Dynamics Corp., San Diego, Calif., Rept. No. GAMD-987, November, 1959; to be published in *Phys. Rev.*

<sup>2</sup> M. Rosenbluth, private communication.  
O. Buneman, "Dissipation of currents in ionized media," *Phys. Rev.*, vol. 115, pp. 503-517; August, 1959.

J. D. Jackson, "Longitudinal plasma oscillations," *J. Nuclear Energy*, pt. C: *Plasma Physics*, pp. 171-189; July, 1960.

velocity, defined by  $mv_-^2 = \kappa T_-$ . However, when the electron-ion temperature ratio,  $T_-/T_+$ , is sufficiently large, the critical drift velocity may be reduced below  $v_-$ , to a value of the order of  $(m_-/m_+)^{1/2} v_-$ ,<sup>3</sup> where  $m_{\pm}$  are the electron and hole effective masses. It does not appear out of the question to produce drift velocities of this latter order of magnitude in a semiconductor, so that one is led to investigate closely the question of instabilities for a plasma in which  $T_- \gg T_+$ .

There are two aspects to the problem. First, it is desirable to calculate the conditions for the existence of instabilities, and their associated growth rates, for a considerable range of electron and hole effective mass and temperature ratios, and their net drift velocity  $v_d$ . Such a calculation is carried out by solving the dispersion relation for the plasma oscillations in the solid. The dispersion relation tells us the allowed frequencies  $\omega$ , for an oscillating longitudinal mode of wave-vector  $k$ ; that is, the conditions for a potential wave, of the form

$$\phi_k \exp i(\mathbf{k} \cdot \mathbf{x} - \omega t)$$

to exist in the solid. The frequency  $\omega$  is in general complex,

$$\omega = \omega_1 + i\omega_2.$$

Where  $\omega_2 < 0$ , the oscillation is damped, and where  $\omega_2 > 0$ , the oscillation will grow, and an instability exists;  $\omega_2 = 0$  defines the boundary between growing waves and damped waves.

The second aspect concerns the possibility of achieving, in practice, the desired range of effective masses, concentrations,  $n_{\pm}$ , temperature ratios, and drift velocities, such that a certain growth rate  $\omega_2$  for the instability might be expected. Here, one attempts to solve the "hot electron" problem to determine the extent to which a given electric field will act to produce heating of the electrons and holes, plus a net drift velocity of electrons vs holes, in the presence of a variety of external scattering mechanisms.

The principal assumption which is made in obtaining the dispersion relation for the plasma oscillations is that there exist two reasonably distinct time scales which characterize the change in the velocity distribution function  $f_{\pm}(\mathbf{r}, \mathbf{v}, t)$ , for the electrons and holes. The first time scale is associated with the macroscopic drift and heating of the particles induced by the external electric field. The second time scale, which is assumed short compared to the first, is that which characterizes the coherent behavior of the system, as manifested by the collective oscillations and their growth rate (where it exists). In these circumstances, the plasma dispersion relation may be obtained from the collisionless Boltzmann equation in which particle

interaction is taken into account by means of a self-consistent field,<sup>4</sup> a procedure which is equivalent to the random phase approximation.<sup>5</sup> The dispersion relation may be written as

$$1 = \frac{4\pi e^2}{\epsilon_0 m_+ k^2} \int d\mathbf{v} \frac{\mathbf{k} \cdot \nabla_{\mathbf{v}} f_+}{\omega - \mathbf{k} \cdot \mathbf{v} + i\delta} + \frac{4\pi e^2}{\epsilon_0 m_- k^2} \int d\mathbf{v} \frac{\mathbf{k} \cdot \nabla_{\mathbf{v}} f_-}{\omega - \mathbf{k} \cdot \mathbf{v} + i\delta} \quad (1)$$

where, for simplicity, we assume that the  $f_{\pm}$  take the form of displaced Maxwellian velocity distributions

$$f_{\pm}(\mathbf{E}_0) = a_{\pm} \exp - \frac{m_{\pm}(\mathbf{v} - \mathbf{v}_{d\pm})^2}{2kT_{\pm}},$$

which will be the case if the collisions between the particles are more effective in relaxing their momentum and energy distributions than their interactions with phonons, impurities, etc. Here  $v_{d\pm}$  and  $T_{\pm}$  are the drift velocities and temperatures brought about by the external field  $E_0$ ; it is these quantities which are assumed to change adiabatically with regard to the times characteristic of plasma effects.  $\epsilon_0$  is the static dielectric constant of the semiconductor, and the small imaginary part  $i\delta$  is introduced to furnish the appropriate prescription for integrating around the poles at  $\mathbf{k} \cdot \mathbf{v} = \omega$ .

The results of the calculations for the boundary between growing waves and damped waves, and the growth rates associated with the low-frequency plasma wave instability are presented in Figs. 1 and 2. The calculations have been carried out for  $m_+ = 14m_-$ , a ratio which is appropriate for InSb, one of the most promising semiconductors in which to study such instabilities. The dispersion relation (1) has been solved for a coordinate system in which the holes have zero drift velocity, and the electron drift velocity is  $v_d = v_{d-} - v_{d+}$ . Furthermore both  $\tau_+$  and  $\tau_-$  have been taken as infinite. The low-frequency plasma modes under consideration are the so-called acoustic modes, in which the electrons and holes oscillate in phase. In Fig. 1 is plotted the boundary between growing waves and damped waves for several values of the ratio  $T_-/T_+$ . Below (or to the right of, in the case  $T_+ = 0$ ), a particular curve, one has growth, while above (or to the left), one has damping. In Fig. 2 there appear the growth rate curves for three cases of interest. The growth rate  $\omega_2$  is measured in units of the hole-plasma frequency,  $\omega_+ = (4\pi n_+ e^2 / m_+ \epsilon_0)^{1/2}$ , while the wave-vector  $k$  is measured in units of the electron Debye wave-

<sup>4</sup> A. Vlasov, "On the kinetic theory of an assembly of particles with collective interaction," *J. Phys. USSR*, vol. 9, pp. 25-40; January, 1945.

<sup>5</sup> L. D. Landau, "On the vibrations of the electronic plasma," *J. Phys. USSR*, vol. 10, pp. 25-34; January, 1946.

<sup>6</sup> D. Pines and D. Bohm, "A collective description of electron interactions: II. Collective vs individual particle aspects of the interactions," *Phys. Rev.*, vol. 85, pp. 338-354; January, 1952.

<sup>3</sup> I. B. Bernstein, E. A. Friedman, R. M. Kulsrud, and M. Rosenbluth, "Ion wave instabilities," *Phys. Fluids*, vol. 3, pp. 136-137; January, 1960.



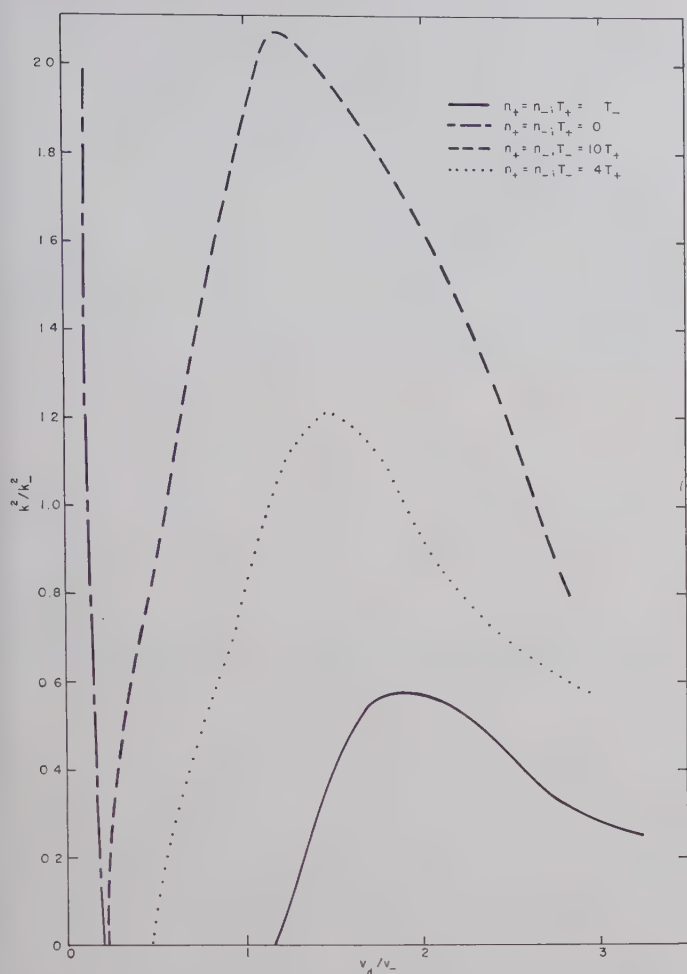


Fig. 1—The boundary between growing waves and damped waves for an electron-hole plasma with  $n_+ = n_-$ ,  $m_+ = 14 m_-$ , and varying values of  $T_-/T_+$ .

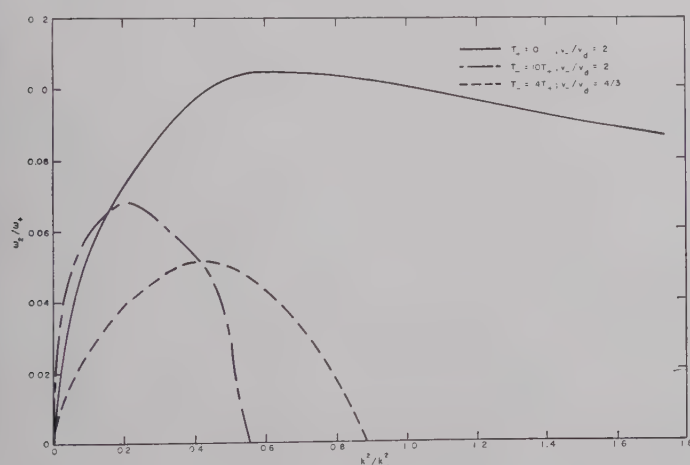


Fig. 2—Growth rate curves for several cases of interest.

vector  $k_- = (4\pi n_- e^2 / \epsilon_0 T_-)^{1/2}$ .

We remark that as the ratio,  $T_-/T_+$ , increases, the drift velocity required to produce an instability is reduced toward  $\sqrt{m_-/m_+} v_-$ . We note further that the growth rates associated with reasonable temperature ratios and values of  $v_d/v_-$  tend to be of the order of 5 per cent to 10 per cent of the hole-plasma frequency.

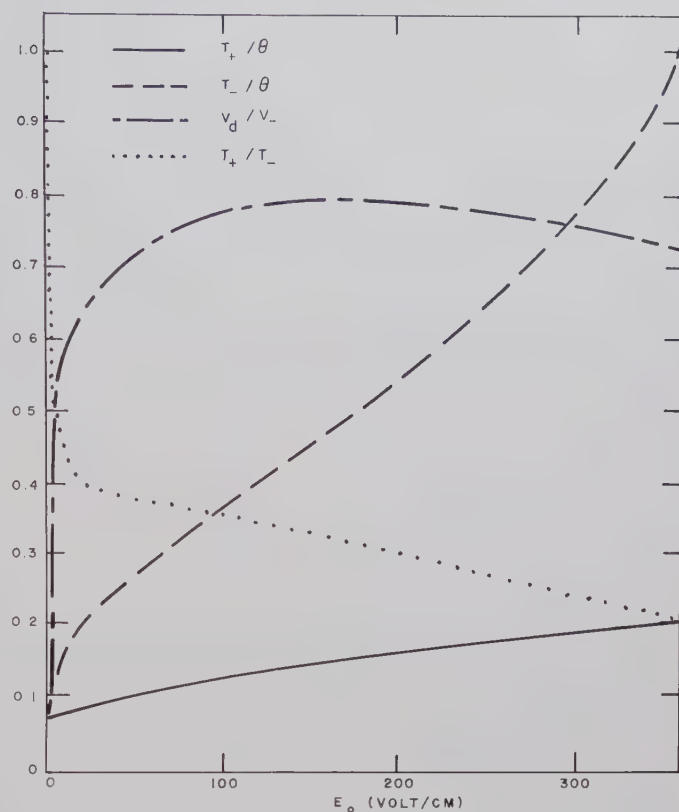


Fig. 3—Hole and electron temperatures and electron drift velocity as a function of field strength in InSb, assuming the following initial conditions:  $T_{\text{lattice}} = 20^\circ\text{K}$ ;  $m_- = 0.03m$ ;  $m_+ = 0.18m$ ;  $N_i = 10^{15}/\text{cc}$ .

In Fig. 3 are shown the results of some studies of the hole and electron temperatures, and the electron drift velocity, as a function of field strength in InSb.<sup>6</sup> These show that substantial temperature ratios  $T_-/T_+$  and drift velocities  $v_d/v_-$  may be achieved with moderate electric fields. By comparing Fig. 3 with Fig. 2 we see that growth rates of the order of  $\omega_+/15$  appear achievable, provided the hole and electron scattering by the lattice is negligible. In the present case, the electron scattering turns out to have little effect on the dispersion relation or growth rate. Hole scattering is, however, quite important, and acts to oppose directly the growth of a low-frequency plasma mode. The net growth rate is, thus,

$$\omega_g' = \omega_g - 1/\tau_+$$

where  $\omega_g$  is the growth rate calculated with neglect of particle-lattice scattering. Hence, a growing wave will be observed only where  $\tau_+$  is sufficiently long that

$$\omega_+ \tau_+ \geq 15 \quad (2)$$

for the cases under consideration. A survey of the experimental relaxation times for the holes in InSb shows

<sup>6</sup> For a discussion of the way in which these results are obtained, see Pines and Schrieffer.<sup>1</sup>

that if one can produce  $\sim 10^{15}$  electrons and holes per cc, while keeping the ionized impurity concentration below  $\sim 10^{15}/\text{cc}$  and the initial lattice temperature below  $20^\circ\text{K}$ , then the condition (2) may be met.

Assuming that the threshold for producing an instability is achieved, what happens next would seem an open question, and a most interesting one. Indeed, our lack of knowledge concerning the subsequent development of an instability is one of the prime reasons for attempting experiments in this area. In this region the behavior of the system is determined by nonlinear

effects, such as the coupling between plasma modes of different wavelength. It is possible to give arguments which tend to show that the relative drift velocity will saturate near the threshold for the coherent excitation of the plasma modes, and it is clear that in time the amplitude of these modes will increase substantially over their thermal level of excitation. However, the detailed dynamic behavior of the system is not at all understood and it is, in my opinion, highly desirable that further theoretical and experimental investigations be carried out in this direction.

## Pulsed Millimeter-Wave Generation Using Ferrites\*

B. J. ELLIOTT†, T. SCHAUG-PETTERSEN‡, AND H. J. SHAW†, MEMBER, IRE

**Summary**—A method is described for generating pulsed RF energy in the millimeter-wave spectrum. Low-loss garnets are used in the uniform precessional mode to store energy at S band and radiate at a higher frequency, which is controlled by the total magnetic field. Details are given of a K-band generator which operates at frequencies up to 32 kMc.

### INTRODUCTION

THERE has been interest for some time in the possibility of using ferrites in simple solid-state RF generators because ferrites have a high density of electron spins, which at room temperature can store magnetic energy and transform this energy into coherent electromagnetic energy in the microwave and millimeter-wave spectrum. A number of studies<sup>1-5</sup> have been reported of schemes in which the energy would be

supplied from a pulsed magnetic field and radiated by the ferrite in the form of short RF pulses. These investigations have disclosed both basic and technological difficulties which are inherent in the problem. These are summarized in an earlier paper on this subject by the present authors.<sup>6</sup>

Some recent experiments with a specific form of pulsed ferrite generator which has proved workable up to 32 kMc are described below. The basic theory and general performance characteristics to be expected from such devices are given in the earlier paper.<sup>6</sup> Briefly, an RF input signal is applied to an yttrium iron garnet (YIG) sphere which is adjusted for gyro-magnetic resonance by means of a steady magnetic field, thus establishing a uniform precession. A pulsed magnetic field is applied along the same direction as the above dc field, thereby increasing the resonant frequency of the spins and adding energy to the spin system. During the flat top of this field pulse, the energy stored in the spin system is radiated into a coupled microwave circuit at the new higher frequency. In this type of solid-state generator then, the output frequency is higher than the input frequency; it is not harmonically related to the input frequency, and it may be varied continuously by adjusting the magnitude of the pulsed magnetic field.

The first reports of successful pulsed generation using ferrites are contained in the preceding article<sup>6</sup> and in

\* Received by the PGMTT, July 18, 1960; revised manuscript received, October 14, 1960. The research reported in this paper was supported by the USASRD, Fort Monmouth, N. J., under Contract DA-36-039 SC-85263.

† W. W. Hansen Microwave Lab., Stanford University, Stanford, Calif.

‡ Norwegian Defense Res. Establishment, Bergen, Norway; formerly at W. W. Hansen Microwave Lab., Stanford University, Stanford, Calif.

<sup>1</sup> R. V. Pound, U. S. Patent No. 2,873,370; 1959.

<sup>2</sup> S. Silver and E. C. Levinthal, "Study of magnetic resonance power source," Levinthal Electronics Inc., Palo Alto, Calif., Rept. No. 106; 1956.

<sup>3</sup> H. C. Heard, "Production of impulse magnetic fields in the millimicrosecond domain," Levinthal Electronics Inc., Palo Alto, Calif., Rept. No. 104; 1955.

<sup>4</sup> F. R. Morgenthaler, "Microwave radiation from ferrimagnetically coupled electrons in transient magnetic fields," IRE TRANS. ON MICROWAVE THEORY AND TECHNIQUES, vol. MTT-7, pp. 6-11; January, 1959.

<sup>5</sup> T. Schaug-Pettersen, "Growing spinwaves in ferrites in unstable equilibrium," *J. Appl. Phys.*, vol. 31, p. 382S; May, 1960.

<sup>6</sup> B. J. Elliott, T. Schaug-Pettersen, and H. J. Shaw, "Pulsed ferrimagnetic microwave generator," *J. Appl. Phys.*, vol. 31, p. 400S; May, 1960.



another paper<sup>7</sup> describing work at the Air Force Cambridge Research Center. These projects employed approximately the scheme just described. In this early work, relatively small pulsed fields and small frequency shifts in the S-band region were employed with the objective of testing the basic theory. Recent efforts have been directed towards obtaining higher output frequencies and higher ratios of output frequency to input frequency. The results of this work to date have been the development of higher pulsed magnetic fields and the generation of higher frequencies, as described in the following two sections.

### PULSED MAGNETIC FIELDS

In the type of device being considered, there are simultaneous requirements on both the magnitude and the rise time of the pulsed magnetic field. The required magnitude is approximately proportional to the output frequency when that frequency is much larger than the input frequency. The required intensity of the pulsed magnetic field is approximately 10 kilogauss for RF output wavelength of 10 mm and 100 kilogauss for output wavelength of 1 mm ( $F=300$  kMc). The rise time of the pulsed field should be short compared to the loaded relaxation time of the ferrite sphere, for efficient conversion of pulsed-field energy to RF output energy.<sup>6</sup> Ferrite material having the longest available internal relaxation time should be used, and as a rough criterion it is desirable to have a pulsed-field rise time of 30  $\mu\text{sec}$  or less.

The basic method of generating the pulsed magnetic fields is to discharge a charged transmission line through a small coil. Fig. 1 shows measured values of magnetic fields vs time on the leading edge of a field pulse reaching 10 kilogauss which is used to generate an output frequency of approximately 32 kMc when the input frequency is 4 kMc. In this instance, the transmission line consists of six RG-55/u coaxial cables connected in parallel, charged to 6.5 kv. The coil has three turns of No. 34 wire with 50-mil inside diameter.

Experiments using a 1.4  $\Omega$  parallel plate line and a very small pulsing coil with a diameter of 50 mils have produced pulsed-field magnitudes up to approximately 100 kilogauss with a rise time less than 25  $\mu\text{sec}$ . This will be used in attempts to reach higher frequencies with the pulsed generator.

### MILLIMETER-WAVE GENERATOR

Fig. 2 is a schematic diagram of apparatus which was used in the initial attempt at millimeter-wave generation. The heart of the system is an open parallel-wire transmission line (Fig. 3) with the garnet sphere

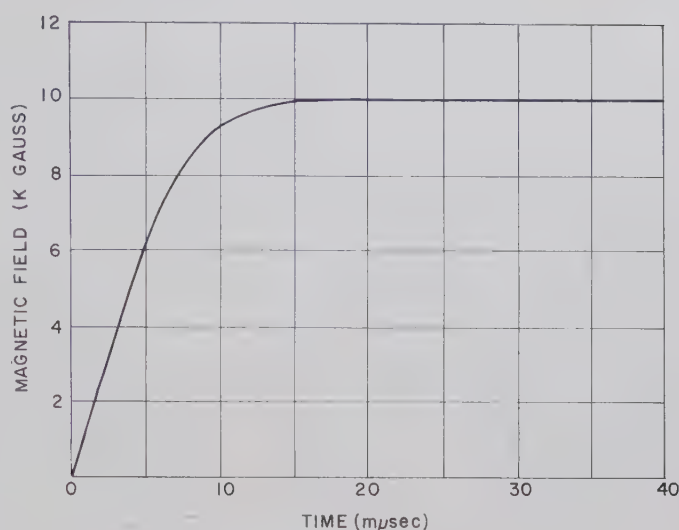


Fig. 1—Pulsed magnetic field.

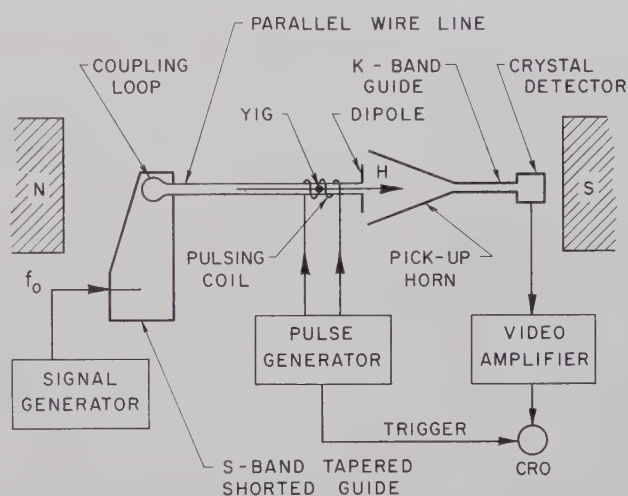


Fig. 2—Schematic diagram of pulsed generator.

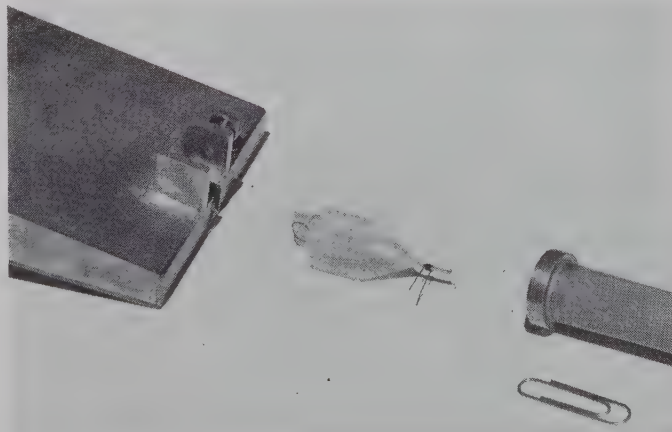


Fig. 3—Pulsed generator components.

<sup>7</sup> M. R. Stiglitz and F. R. Morgenthaler, "Resonance experiments with single crystal yttrium iron garnet in pulsed magnetic fields," *J. Appl. Phys.*, vol. 31, p. 375; May, 1960.

mounted between the wires and the small pulsed field coil surrounding both the line and the garnet. The parallel line is resonant in the  $5\lambda/4$  mode at the input frequency (4 kMc) and is coupled at one end to an *S*-band waveguide which carries the input signal. The garnet is located near a current antinode of the *S*-band mode and is excited by the transverse RF magnetic field due to the input signal.

The parallel line operates in principle as a nonresonant line at the output frequency. It has very small dimensions, being constructed of 8-mil diameter wires spaced 20 mils inside, embedded in a polystyrene assembly (Fig. 3). The generated output signal travels toward the output end of the line where it is radiated by an antenna into a receiving horn. A length of waveguide leading to the detector acts as a high pass filter rejecting all signals having frequencies below its cutoff frequency, including the input signal.

This device has been operating using a single crystal garnet sphere of diameter 10 mils with a relaxation time of 100  $\mu\text{sec}$ . An output pulse was observed having frequency components above 32 kMc ( $\lambda \approx 9$  mm) using a detector waveguide with cutoff frequency of 32 kMc. The output pulse at the detector had a duration of 25  $\mu\text{sec}$  and a peak power of approximately 0.1 mw. When the system is adjusted for 15 kMc operation, the power output is 1 mw.

The qualitative dependence of the output power on variations of  $H_0$ ,  $H_z$ , and input signal amplitude, indicates that the mode of operation of the device is as theoretically predicted. Power output is zero for zero input signal, and increases monotonically with input-signal amplitude. As  $H_0$  is varied, the output reaches a maximum at the value of  $H_0$  corresponding to ferrimagnetic resonance at the input-signal frequency and drops to zero on either side of resonance. For a given detector waveguide with known cutoff frequency  $f_c$ , there is experimental agreement between  $f_c$  and the predicted value of output frequency  $f$ , given by  $f = 2.8 H$  kMc, where  $H$  is the minimum field (in kilogauss) required to generate a detectable output signal at  $f_c$ .

During the course of these experiments a second test was conducted. The dc magnetic field was reversed, allowing the pulsed magnetic field to "invert" the total magnetic field with respect to the spins. This is a situation which has been studied with some interest<sup>4</sup> as a possible means of putting the ferrite in a radiative state without the necessity of an RF input signal. Theoretical studies<sup>5</sup> indicate that this arrangement will be unworkable because of rapid spinwave build-up. The present experiment confirms this prediction to within the sensitivity limitations of the detection system (approximately 20  $\mu\text{w}$ ) as no output signal was detected.

## CONCLUSIONS

The above results demonstrate that RF generation at frequencies up to *K* band is possible with large frequency translation between input and output signals.

The open-wire line was used for two reasons. It allows the pulse coil to be placed outside the RF circuit, thereby avoiding RF shielding of the garnet by the coil. It also allows RF propagation over a wide frequency range so that testing can begin at low output frequencies and proceed in steps toward higher frequencies.

In these initial explorations efficient operation of the ferrite generator as a device was not of prime importance. Indeed, the present output is about two orders of magnitude below that theoretically available from the garnet. This may be the result of nonideal impedance behavior of the parallel-wire circuit.

Ideally, the impedance presented to the ferrite by the circuit must be carefully controlled at all frequencies between the input and output frequencies. A too-low impedance anywhere in this range can damp the ferrite prematurely and result in low power in the desired output frequency range. Such a behavior could result from spurious circuit resonances, such as are likely to exist in the present parallel-wire circuit.

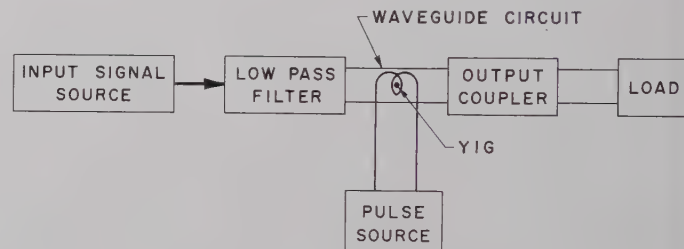


Fig. 4—Idealized generator.

Fig. 4 is a diagrammatic representation of the components of an idealized generator. The purpose of the low-pass filter is to pass the input-signal frequency while isolating the ferrite from the input circuit at all other frequencies. It should be essentially free of higher pass bands in the complete frequency range extending beyond the output frequency. The purpose of the output circuit is to provide the proper low circuit impedance in the output-frequency range so as to damp the ferrite quickly when this frequency range is reached.

For an efficient RF circuit, where careful impedance matching is possible and where inherent circuit and radiation losses are small, fully enclosed waveguides should be employed at millimeter wavelengths. It should be pointed out that this requires placing the pulsing coil inside the circuit. The effects of the coil in distorting the millimeter wave fields at the ferrite should then be investigated.



# Correspondence

## Tuning Range of the Backward Traveling-Wave Parametric Amplifier\*

Experimental results obtained with backward traveling-wave parametric amplifiers<sup>1,2</sup> indicate that their tuning range is greater than that predicted when TEM propagation is assumed.<sup>1</sup> An analytical and graphical examination of the possible tuning range when non-TEM transmission lines are considered is given below. This examination shows how the tuning range may be optimized, and indicates what the maximum range would be using realizable transmission lines.

Consider first a small perturbation which transforms the linear transmission line characteristics to the form

$$\omega_\alpha = v_\alpha \beta_\alpha - c_\alpha \beta_\alpha^2$$

$$(\alpha = p, i, \text{ or } s \text{ for pump, idle or signal.}) \quad (1)$$

The conditions for parametric amplification are<sup>3</sup>

$$\omega_p = \omega_i + \omega_s \quad (2)$$

$$\beta_p = \beta_i - \beta_s. \quad (3)$$

If one takes  $4c_\alpha \omega_\alpha / v_\alpha^2 \ll 1$ , one finds upon combining (1)–(3) that

$$\omega_s = \frac{\omega_p}{2} (1 - r + r\omega_p \epsilon) \quad (4)$$

$$\omega_i = \frac{\omega_p}{2} (1 + r - r\omega_p \epsilon), \quad (5)$$

where  $r = v_s / v_p$ ,  $\epsilon = c_s / v_s^2 - c_p / v_p^2$ , and signal and idle propagate in the same transmission line. It is seen that both  $\omega_s$  and  $\omega_i$  change as  $\omega_p$  is varied. Limitations on the tuning range are imposed by the condition that signal, idle, and pump frequency bands must be separated. For TEM lines, or in the more general case  $\epsilon = 0$ , one must have  $r = r_0 = 0.236$ , in order to achieve the maximum tuning range  $(\omega_{sH} / \omega_{sL})_0 = 1.618$  ( $\omega_{sH}$  and  $\omega_{sL}$  are the highest and lowest signal frequencies).<sup>1</sup> For the perturbation, we let

$$r = r_0 + r_1. \quad (6)$$

Then, to first order, one finds

$$\begin{aligned} \frac{\omega_{sH}}{\omega_{sL}} &= \left( \frac{\omega_{sH}}{\omega_{sL}} \right)_0 \\ &+ \left[ \frac{r_0}{1 + r_0} + \frac{2r_0^2}{(2 + r_0)(1 + r_0)^2} \right] \omega_{pH_0} \epsilon \\ &= 1.618 + 0.224 \omega_{pH_0} \epsilon \end{aligned} \quad (7)$$

for

$$r = r_0 + \frac{2r_0}{2 + r_0} \omega_{pH_0} \epsilon = 0.236 + 0.211 \omega_{pH_0} \epsilon. \quad (8)$$

Thus, the tuning range is increased for  $\epsilon > 0$ .

If instead of (1), one considers the case of a TEM signal-idle line and a high-pass waveguide pump circuit, a perturbation calculation shows that the maximum tuning range must be reduced. It is also reduced when the transmission line characteristics are approximated by

$$\omega_\alpha - \omega_{c\alpha} = v_\alpha \beta_\alpha, \quad (9)$$

where  $\omega_c$  is the cutoff frequency of the transmission line.

Although the above analytical approach is valuable in predicting how the tuning range will be affected, it cannot yield quantitative results since it utilizes only an approximation to  $\omega$ - $\beta$  characteristics actually encountered in experiment. In order to ascertain what the maximum tuning range could be and what value of  $r$  to choose in the amplifier design, one must resort to a graphical technique which is, however, quite simple. Fig. 1 illustrates this procedure, which is as follows:

- 1) Draw the signal-idle circuit  $\omega$ - $\beta$  characteristic (assume it is  $\omega_s = v_s \sin \beta_s / 2$ ).
- 2) Draw an arbitrary pump-circuit  $\omega$ - $\beta$  characteristic (assume  $\omega_p = v_p \beta_p$  and try  $r = 0.4$ ).
- 3) Choose the cutoff of the low-pass signal line as  $\omega_{iH}$ . This will maximize the tuning range, since we know from the analysis that the  $\omega$ - $\beta$  non-linearity is favorable here.
- 4) Find  $\omega_{sH}$  such that  $(\omega_{pH}, \beta_{pH})$  is a point falling on the pump characteristic. This step is a rapid trial-and-error procedure.
- 5) The  $\omega_{sH}$  point is also taken to be  $\omega_{iL}$  and 4) is repeated for the low end of the tuning range.
- 6) Find  $\omega_{sH} / \omega_{sL} = 1.89$ ; note that  $\omega_{pL} > \omega_{iH}$ , indicating that  $r = 0.4$  is not optimum.
- 7) Redraw the pump characteristic with increased  $r$  (try  $r = 0.5$ ).
- 8) Repeat 3)–5) and find  $\omega_{sH} / \omega_{sL} = 2.48$ ; note that  $\omega_{pL} < \omega_{iH}$ , which may not be permitted.
- 9) Redraw the pump characteristic with decreased  $r$  (try  $r = 0.475$ ).
- 10) Find  $\omega_{sH} / \omega_{sL} = 2.31$  and  $\omega_{pL} = \omega_{iH}$  indicating that this last choice of  $r$  is optimum.

If the signal circuit had had a low-frequency cutoff, as shown by the dashed line in Fig. 1, the optimum  $r$  would have been 0.5, but the tuning range would have been only 2.07.

Finally, it is of interest to apply the graphical technique to the actual experimental configuration used by Breitner and Sard.<sup>1</sup> This is illustrated in Fig. 2. The question asked is: what are the expected signal and idle ranges when  $r = \frac{1}{2}$  and the pump frequency is swept from 4.5 to 7.0 Mc? Table I illustrates the excellent agreement between the graphical predictions and the experimental results as computed by Breitner and Sard.<sup>4</sup>

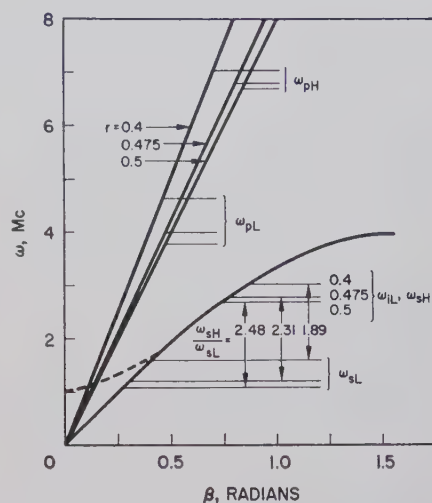


Fig. 1—Illustration of graphical procedure.

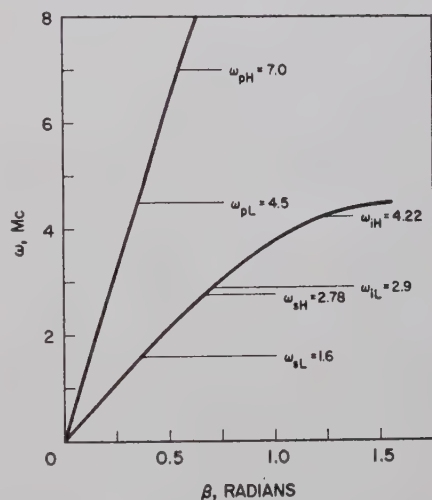


Fig. 2—Graphical construction corresponding to Breitner and Sard's BWPA.<sup>1</sup>

TABLE I

	Graphical Predictions	Experimental Results	Lineary Theory
$\omega_{sH} / \omega_{sL}$	1.73	1.70	1.55
$\omega_{iH} / \omega_{iL}$	1.46	1.48	1.55

In conclusion, it has been shown that tuning ranges considerably larger than 2:1 should be obtained when a proper choice of transmission-line characteristics is made. The predicted tuning range can then be expected to correspond closely with the experimental results.

The author would like to acknowledge useful discussions with Drs. A. D. Berk and P. Gottlieb.

T. M. STRAUS  
Components Div.  
Hughes Aircraft Co.  
Culver City, Calif.

<sup>4</sup> Breitner and Sard, *op. cit.*, Fig. 3.

\* Received by the PGMTT, September 12, 1960.  
<sup>1</sup> D. I. Breitner and E. W. Sard, "Low frequency prototype backward-wave reactance amplifier," *Microwave J.*, vol. 2, pp. 34–37; August, 1959.

<sup>2</sup> H. Hsu, "Backward Traveling-Wave Parametric Amplifiers," presented at Solid State Circuits Conf., Philadelphia, Pa., February 10–12, 1960.

<sup>3</sup> P. K. Tien, "Parametric amplification and frequency mixing in propagating circuits," *J. Appl. Phys.*, vol. 29, pp. 1347–1357; September, 1958.





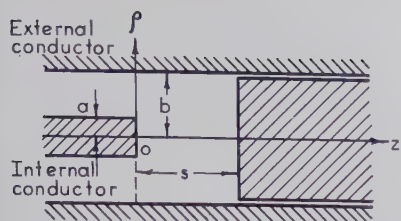


Fig. 1—Cutoff variable reactor.

where both  $A$  and  $B$  are integrating constants and both  $I_1$  and  $K_1$  are modified Bessel functions,

$$\sigma \equiv \sqrt{\left(\frac{\pi}{4s}\right)^2 - \left(\frac{2\pi}{\lambda}\right)^2} \quad (4)$$

and

$$B = \frac{bI_1(\sigma b) - aI_1(\sigma a)}{aK_1(\sigma a) - bK_1(\sigma b)} \quad (5)$$

The input voltage is given by

$$V = \int_a^b \left[ -\frac{1}{j\omega\epsilon} \frac{\partial H_\phi}{\partial z} \right] d\rho. \quad (6)$$

The input reactance is given by dividing (6) by (2) providing (3),

$$X_s = \frac{\sqrt{\frac{\mu}{\epsilon}}}{\frac{16\pi}{\lambda} ab\sigma s} \cdot \frac{\{I_0(\sigma b) - I_0(\sigma a)\} \{aK_1(\sigma a) - bK_1(\sigma b)\} - \{K_0(\sigma b) - K_0(\sigma a)\} \{bI_1(\sigma b) - aI_1(\sigma a)\}}{I_1(\sigma b)K_1(\sigma a) - I_1(\sigma a)K_1(\sigma b)} \quad (7)$$

For example with  $b=2.25$  mm and  $\lambda=3.07$  cm, the reactance  $X_s$  changed as shown in Fig. 3 for various center conductor radii  $a$  and shorting plunger distances  $s$ . This reactor shows high reactance for small values of shorting plunger distances. When the inner conductor radius is 0.4 mm, in order to have 350 ohms, the conventional coaxial plunger requires a shorting plunger distance of 6.72 mm. On the other hand, the same reactance can be obtained by the cutoff reactor with a shorting plunger distance of 1 mm. This space economization is more effective for higher reactances. For 835 ohms, the shorting plunger distance of the conventional coaxial shorting plunger is 7.25 mm. For the same reactance, the shorting plunger distance of the cutoff reactor is 0.045 mm. The latter case was tested by experiment in a reflex klystron amplifier<sup>1,2</sup> circuit. The results of the experiment agreed with the calculations.

<sup>1</sup> K. Ishii, "X-band receiving amplifier," *Electronics*, vol. 28, p. 202; April, 1955.

<sup>2</sup> K. Ishii, "Amplification circuit for the internal cavity-type reflex klystron," *J. Res. Inst. Tech., Nihon University* (Tokyo, Japan), vol. 14, pp. 1-10; December, 1957.

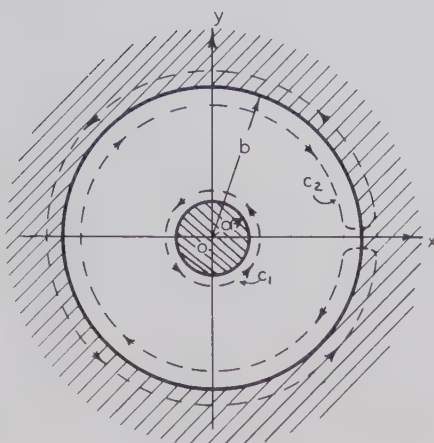


Fig. 2—Integral contour to obtain the input currents.

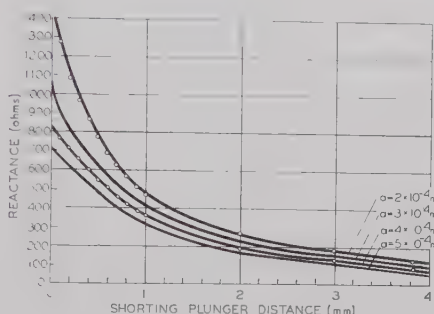


Fig. 3—Reactance of cutoff variable reactor.

The author extends his thanks to R. Robinson, for numerical computation by IBM 650, and S. Krupnik and J. Stefancin for preparation of the manuscript.

KORYU ISHII  
Dept. of Elec. Engrg.  
Marquette University  
Milwaukee, Wis.

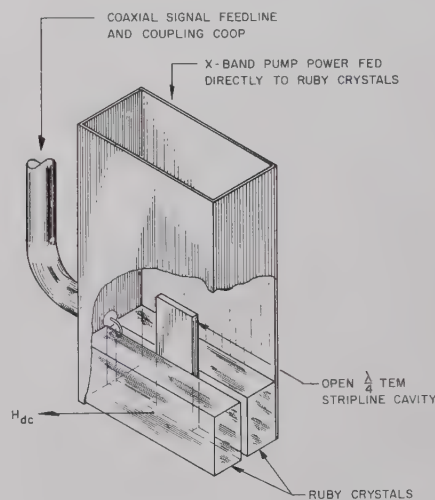
### Single-Mode Cavity Maser at 2200 Mc\*

Cavity masers which have been reported in the literature have utilized a dual-mode cavity resonant at the pump and signal frequencies, but Strandberg, *et al.*,<sup>1</sup> has reported an X-band cavity maser which can be operated with the cavity resonant only at

the signal frequency. Siegmann<sup>2</sup> has also reported a multiplicity of resonances in his cavity maser for the pump signal which might possibly be caused by some sort of dielectric loading effect.

Both these facts suggested to us that an S-band cavity maser using only a single resonant mode at the signal frequency could be developed by using the ruby itself as the pump circuit. If this scheme were practical, design of tunable cavity masers at S-band would be much simpler than it is. With this thought in mind, a maser cavity circuit suitable for operation from 2100–2500 Mc was designed.

The maser's active material was pink ruby,  $\text{Al}_2\text{O}_3\text{Cr}^{+++}$  oriented at an angle  $\theta \cong 90^\circ$ . The cavity is a re-entrant  $\lambda/4$ -TEM stripline type in X-band waveguide with loop coupling as depicted in Fig. 1. The resonant frequency of the cavity is determined primarily by the length of center strip and by the loop volume. The degree of coupling by the loop remained essentially constant over a 400-Mc frequency range. For the cavity filled on both sides as shown in Fig. 1, we estimated the filling factor to be approximately 75 per cent or greater. X-band pump energy is fed directly down the waveguide to the ruby crystals.

Fig. 1— $\lambda/4$  stripline cavity in standard X-band waveguide.

This cavity maser has been operated from 2120 to 2500 Mc by adjusting the length of the center strip and varying the pump frequency and dc magnetic field. Complete inversion of energy levels was obtained for all frequencies without the use of a pump cavity mode, and no pump resonances of any type were observed.

For the master amplifier characteristics considered here, the resonant frequency was 2200 Mc and the pump frequency was 12,470 Mc. Fig. 2 relates the gain-bandwidth products to the level of input power. This

\* Received by the PGMTT, September 20, 1960.

<sup>1</sup> R. J. Morris, R. L. Kuhl, and M. W. P. Strandberg, "A tunable maser amplifier with large bandwidth," *Proc. IRE*, vol. 47, pp. 80-81; January, 1959.

<sup>2</sup> W. S. C. Chang, J. Cromack, and A. E. Siegmán, "Experiments on a High-Performance Cavity Maser Using Ruby at S Band," *Electron Devices Lab., Stanford Electronics Lab., Stanford University, Stanford, Calif.*, Rept. No. T.F. 156-4; July 21, 1959.

gain-bandwidth product curve is less than the calculated values, but there was no way to adjust and optimize the coupling once the loop was formed. In any tunable maser, some method of adjusting the coupling could be easily incorporated to offset this trouble. Fig. 3 shows pump power necessary for saturation vs signal input power. The amount of pump power necessary for saturation is larger than that usually required for the resonant cavity case, but not significantly so. We also noted that the gain of the maser is not dependent upon the frequency stability of the pump source. It was also noted that oscillations could be started over nearly the entire linewidth of the ruby, *i.e.*, 50-Mc tuning range of the pump frequency with little variation in the pump power.

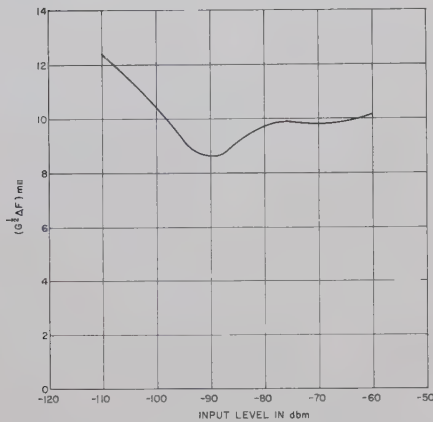


Fig. 2—Gain bandwidth product vs input level in dbm.

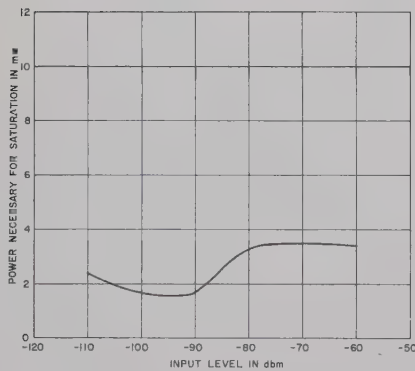


Fig. 3—Saturation pump power vs signal input level in dbm.

In conclusion, it appears feasible that a tunable cavity maser at *S* band could be developed without recourse to a dual-mode cavity system. This would greatly enhance the practicability of this type of amplifier for the 2000 Mc region where masers can be used efficiently for telemetry purposes.

The authors wish to thank Drs. P. S. Carter, Jr., and J. R. Singer for their help and criticisms.

D. W. HANSON  
J. J. ROWLEY  
Missile Systems Div.  
Lockheed Aircraft Corp.  
Sunnyvale, Calif.

## Higher-Order Evaluation of Dipole Moments of a Small Circular Disk for Arbitrary Incident Fields\*

In a recent note<sup>1</sup> the induced electric and magnetic dipole moments  $P$  and  $M$  due to the diffraction of a plane wave on a small circular disk were given. The expression for the electric dipole moment holds, however, only if the electric field vector is parallel to the plane of incidence. In a more general approach the case for an arbitrary primary field has been examined, and the following expressions have been obtained:

$$P_x = \frac{16}{3} a^3 \epsilon_0 \left[ E_x^i + \frac{(ka)^2}{30} \left( 13E_x^i - \frac{3}{k^2} \frac{\partial^2 E_x^i}{\partial z^2} + \frac{2j}{\omega \epsilon_0} \frac{\partial H_z^i}{\partial y} \right) - j \frac{8}{9\pi} (ka)^3 E_x^i + 0((ka)^4) \right],$$

$$P_y = \frac{16}{3} a^3 \epsilon_0 \left[ E_y^i + \frac{(ka)^2}{30} \left( 13E_y^i - \frac{3}{k^2} \frac{\partial^2 E_y^i}{\partial z^2} - \frac{2j}{\omega \epsilon_0} \frac{\partial H_z^i}{\partial x} \right) - j \frac{8}{9\pi} (ka)^3 E_y^i + 0((ka)^4) \right],$$

$$M_z = -\frac{8}{3} a^3 \left[ H_z^i - \frac{(ka)^2}{10} \left( 3H_z^i + \frac{1}{k^2} \frac{\partial^2 H_z^i}{\partial z^2} \right) + j \frac{4}{9\pi} (ka)^3 H_z^i + 0((ka)^4) \right].$$

The axis of the disk is along the  $z$  direction. The incident fields are evaluated at the center of the disk.

We now consider a plane wave ( $E^i, H^i$ ) incident in the  $xz$  plane and with an angle of incidence  $\theta$ . Using the expressions above we obtain

$$P_x = \frac{16}{3} a^3 \left[ 1 + \left( \frac{8}{15} - \frac{1}{10} \sin^2 \theta \right) (ka)^2 - j \frac{8}{9\pi} (ka)^3 + \dots \right] E_x^i,$$

$$P_y = \frac{16}{3} a^3 \left[ 1 + \left( \frac{8}{15} - \frac{1}{6} \sin^2 \theta \right) (ka)^2 - j \frac{8}{9\pi} (ka)^3 + \dots \right] E_y^i,$$

$$M_z = -\frac{8}{3} a^3 \left[ 1 - \frac{1}{10} (2 + \sin^2 \theta) (ka)^2 + j \frac{4}{9\pi} (ka)^3 + \dots \right] H_z^i.$$

$P_x$  and  $M_z$  agree with the values given in reference [1].

W. H. EGGIMANN  
Dept. Elec. Engrg.  
Case Inst. Tech.  
Cleveland, Ohio

\* Received by the PGMTT, September 22, 1960. This work has been sponsored by the Electronics Res. Directorate of the AF Cambridge Res. Center under contract number AF 19(604)3887.

<sup>1</sup> W. H. Eggimann, "Higher order evaluation of dipole moments of a small circular disk," IRE TRANS. ON MICROWAVE THEORY AND TECHNIQUES, vol. 8, p. 573; September, 1960.

## Capacitance Definitions for Parametric Operation\*

The purpose of this note is to reconcile the various definitions of nonlinear or equivalent time-varying capacitance which appear in the literature concerned with parametric devices. The problem considered is one of a nonlinear reactive element, let us say a capacitance, which is pumped by strong pump source at frequency  $f_p$  and which couples two circuit modes at frequencies  $f_s$  and  $f_i$ , usually called the signal and idling frequencies. For parametric operation we demand either  $f_p = f_i + f_s$  or  $f_p = f_i - f_s$ . The nonlinear element (*i.e.*, a capacitance) has a charge-voltage characteristic given by

$$q = f(V). \quad (1)$$

Let us imagine that now we have applied a strong pump voltage  $V_p$  together with a dc bias voltage  $V_0$  and subsequently we shall be concerned with the behavior upon application of small signal voltage  $\delta v$  at signal and idling frequencies. We can now define several capacitances:

1) The total capacitance  $C_T$  is defined as the ratio of total charge to total voltage, or

$$q = C_T V. \quad (2)$$

Obviously from (1)

$$C_T = \frac{f(V)}{V}; \quad (3)$$

this is the definition of capacitance used by Heffner and Wade.<sup>1</sup>

2) The incremental capacitance  $C_i$  is defined by

$$\delta q = C_i \delta V. \quad (4)$$

This is the definition used by Rowe.<sup>2</sup>

Two questions arise: first, in definition 1, what is the relationship between the time-varying capacitance produced by the pump alone to that which is effective in producing parametric action; second, what is the relationship between the two definitions of capacitance?

The first question already has been answered,<sup>1</sup> but it is perhaps worthwhile to add a few more details. If the biased capacitance is acted on by the pump voltage alone, then we would measure a charge,

$$q = (C_{T0} + C_{TP})(V_0 + V_p), \quad (5)$$

where we consider the capacitance to have a dc part  $C_{T0}$  and a time varying part  $C_{TP}$  varying sinusoidally at the pump frequency (for simplicity we will neglect harmonic terms). The time varying part could be measured or could be inferred from a static plot of the nonlinear characteristic. We necessarily demand that the amplitude of the time-varying part be less than or at most equal to the dc part in order to have the

\* Received by the PGMTT, October 4, 1960.

<sup>1</sup> H. Heffner and G. Wade, *J. Appl. Phys.*, vol. 29, pp. 1321-1331; September, 1958.

<sup>2</sup> H. E. Rowe, "Some general properties of nonlinear elements—II. Small signal theory," *Proc. IRE*, vol. 46, pp. 850-860; May, 1958.



total capacitance positive. With the neglect of higher harmonic terms, this implies

$$\left| \frac{C_{TP}}{C_{T0}} \right| \leq 1. \quad (6)$$

Suppose now in addition to the bias and pump voltage ( $V_0 + V_P$ ), we apply a small signal voltage  $\delta v$  with components at signal and idling frequencies. What is the increment in charge which flows? From (1) we have

$$\delta q = C_T \delta v + \delta C_T V,$$

and

$$\delta C_T = \left. \frac{dC_T}{dV} \right|_{(V_0+V_P)} \delta v. \quad (7)$$

The first term in the equation for charge represents the ac charge produced by the pumped capacitance. It includes the action of the time-varying capacitance produced by the pump voltage mixing with the small voltages at signal and idling frequencies, giving rise to charge components at idling and signal frequencies. The second term represents the effect of the small signal voltages in varying the nonlinear capacitance and the resulting mixing with the large bias and pump voltages also to produce charge components at signal and idling frequencies. It is not difficult to show that this second nonlinear effect is equal in magnitude to the first.

For simplicity, let us assume a linear relationship between capacity and voltage, that is, a second order nonlinearity in the charge-voltage characteristic.

$$C_T = c_0 + cV. \quad (8)$$

Then in terms of the notation of (4) when only the bias and pump voltages are applied, the dc portion of the total capacity is

$$C_{T0} = c_0 + cV_0, \quad (9)$$

and the time-varying portion is

$$C_{TP} = cV_P.$$

In this notation, the substitution of the capacitance characteristic of (8) into (7) gives

$$\delta C_T = c\delta v, \quad (10)$$

and

$$\begin{aligned} \delta q &= (C_{T0} + C_{TP})\delta v + c\delta v(V_0 + V_P) \\ &= (C_{T0} + cV_0)\delta v + 2C_{TP}\delta v. \end{aligned} \quad (11)$$

Thus, in so far as the small signals are concerned, the nonlinear capacitor appears to have a static capacitance of  $(C_{T0} + cV_0)$  and a time-varying portion of  $2C_{TP}$ , that is, twice the value produced by the pump alone. This is the value of the equivalent time-varying capacitance  $C_3$  used by Heffner and Wade.<sup>1</sup>

$$C_3 = 2|C_{TP}|. \quad (12)$$

From (6) we see

$$\frac{C_3}{C_{T0}} \leq 2, \quad (13)$$

where we have compared the ac capacitance seen by the signal and idling frequencies to the static capacitance observed when only the bias and pump are applied. There is no

such limit to the ratio of pumped ac to static capacitance if both are measured at signal or idling frequencies.

The second question raised concerns the relationship between the definition of total capacitance  $C_T$  and incremental capacitance  $C_i$ . In the case of the incremental capacitance, we imagine that we have applied the bias voltage  $V_0$  and the pump voltage  $V_P$  and then observe the increment in charge produced by applying a small-signal voltage  $\delta v$  with components at signal and idling frequencies.

$$q = \left. \frac{df(V)}{dV} \right|_{V_0+V_P} \delta v = C_i \delta v. \quad (14)$$

Here the incremental capacitance

$$C_i = \left. \frac{df(V)}{dV} \right|_{(V_0+V_P)} \quad (15)$$

has dc and time-varying components. In Rowe's notation<sup>2</sup>

$$C_i = \sum_{n=-\infty}^{\infty} C_n e^{in\omega_P t}, \quad (16)$$

One might wonder whether this definition included not only the effect of capacitance change at the pump frequency mixing with signal and idle voltage but also the terms due to variation in capacitance produced by the small signal and idling voltages mixing with the pump voltage, an effect which we have seen is of the same magnitude as the first. It is easy to show that the incremental capacitance approach does indeed include both effects and is identical to the total capacitance approach by returning to (7) which can be written,

$$\delta q = C_T |_{(V_0+V_P)} \delta v + \left[ \left. \frac{dC_T}{dV} \right|_{(V_0+V_P)} \delta v \right] V, \quad (17)$$

and (3), which relates  $C_T$  to the nonlinear characteristic

$$C_T = \frac{f(V)}{V}. \quad (3)$$

With this substitution for  $C_T$  (7) becomes

$$\begin{aligned} \delta q &= \left. \frac{f(V)}{V} \right|_{(V_0+V_P)} \delta v \\ &+ \left[ \left. \frac{df(V)}{dV} \right|_{(V_0+V_P)} - \frac{f(V)}{V} \right]_{(V_0+V_P)} \delta v \\ &= \left. \frac{df(V)}{dV} \right|_{(V_0+V_P)} \delta v = C_i \delta v. \end{aligned} \quad (18)$$

Thus, the two definitions are consistent. If one includes only that portion of the incremental capacitance which varies at the pump frequency  $C_i$ , one sees from (16) in Rowe's notation,<sup>2</sup>

$$|C_i| = 2|C_1|; \quad (19)$$

and from (11), (12), and (13)

$$C_3 = |C_i| = 2|C_1| = 2|C_{TP}| \leq 2C_{T0} \quad (20)$$

where, as before,  $C_{T0}$  represents the static capacitance observed when only the bias and pump voltages are applied.

H. HEFFNER

Dept. of the Navy

Office of Naval Res., Branch Office

London, England

## A Tunnel-Diode Amplifying Converter\*

Sufficient literature has already been presented to establish the fact that tunnel diodes appear to have a bright future as relatively low noise, low power consumption, amplifying devices.<sup>1-4</sup>

In this note it is desired to report the results of using the tunnel diode as a mixing element rather than a single-frequency amplifying device.

In the usual microwave or VHF receiver, superheterodyne principles are most often utilized. In this system the signal is received by some form of antenna, amplified, and then transmitted to a mixer or transmitted directly to the mixer without amplification. In the mixer, the received signal and the local oscillator signal operate usually on a nonlinear variable-resistance device from which the intermediate frequency signal is then derived.

This mixer is usually quite noisy and quite lossy, the diode-noise figures being on the order of 7.0 db and the diode losses being on the order of 6.0 db.

It is very possible to place a negative-resistance amplifier before the mixer to minimize the effects of the mixer noise figure and loss; but the peculiar current-voltage (I-V) characteristic of the tunnel diode presents a much more desirable solution.<sup>5</sup> The RF amplifier and variable resistance mixer can be entirely eliminated and the tunnel diode used to obtain the necessary high-gain and low-noise figure and to convert from the signal frequency down to the IF frequency.

Fig. 1 is representative of the I-V characteristic of the diode used in the experi-

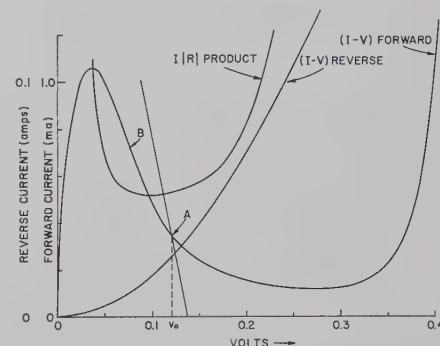


Fig. 1—Current-voltage characteristic of the germanium diode used in the calculations.

\* Received by the PGMTT, October 4, 1960. This research was supported by the United States Air Force through WWRNGW of the Wright Air Dev. Div. of the Air Res. and Dev. Command.

<sup>1</sup> H. S. Sommers, Jr., "Tunnel diode as high-frequency devices," *Proc. IRE*, vol. 47, pp. 1201-1206; July, 1959.

<sup>2</sup> K. K. N. Chang, "Low-noise tunnel diode amplifier," *Proc. IRE*, vol. 47, p. 1268; July, 1959.

<sup>3</sup> I. A. Lesk, N. Halonyak, U. S. Davidsohn, and M. W. Aarons, "Germanium and silicon tunnel diodes—design, operation and application," 1959 WESCON CONVENTION RECORD, pt. 3, pp. 9-31.

<sup>4</sup> M. E. Hines, "High-frequency negative resistance circuit principles for Esaki diode applications," *Bell Sys. Tech. J.*, vol. 34, pp. 477-513; May, 1960.

<sup>5</sup> K. K. N. Chang, G. H. Heilmeier, and H. J. Prager, "Low-noise tunnel diode down converter having conversion gain," *Proc. IRE*, vol. 48, pp. 854-858; May, 1960.

ments. Fig. 2 is an oscilloscope presentation of the conductance of the same diode vs voltage.

The tunnel diode is used as the mixing diode, the bias adjusted for stable operation at point A. The total dc-source resistance ( $r_1$ ) must be less than the magnitude of the negative resistance of the diode (point B).

The local oscillator (LO) signal is coupled into the mixer by the usual techniques. Sufficient LO drive must be supplied to modulate the tunnel diode about the  $I_0 - V_0$  point. The LO is decoupled sufficiently such that it loads neither the RF nor IF circuits.

The RF equivalent circuit used to define the device parameters is shown in Fig. 3(a). Fig. 3(b) shows the equivalent circuit of the

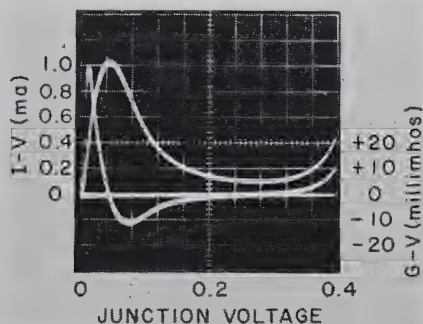
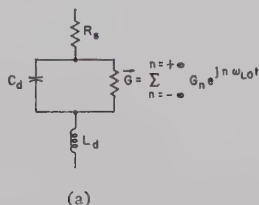
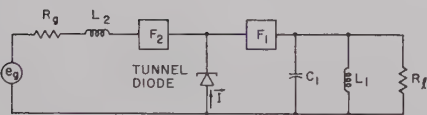


Fig. 2—Oscilloscope presentation of the conductance vs voltage characteristics of the diode used in the experiments.



(a)



(b)

Fig. 3—(a) RF equivalent circuit of tunnel diode. (b) Circuit of the tunnel diode mixer.

complete mixer as used in the experiments.  $G$  is the exponential Fourier series representation of the conductance waveform under local oscillator modulation.  $I$  is the exponential Fourier series representation of the diode current under LO modulation.  $F_2$  is a band pass filter arranged in such a manner as to pass the input signals from the generator, and to act as an open circuit for the image signals.  $F_1$  is a low-pass filter which passes the IF signals but blocks the RF-input signals.

With the circuit configuration as shown in Fig. 3, let the following quantities be defined:

$$Q_2 = \frac{\omega_2(L_2 + L_d)}{R_g + R_s} \quad Q_1 = \frac{\omega_1 C_1}{(G_l + G_0)}$$

$$\bar{Q}_2 = \frac{\omega_2 C_d}{(G_0 + G_s + G_0)} \quad (1)$$

$$G_g + G_s = \frac{1}{(R_g + R_s)(1 + Q_2^2)} \quad (2)$$

$$\frac{G_s}{G_g} = \frac{R_s}{R_g} \quad (3)$$

$$\begin{aligned} G_0 &= -0.007 \text{ mho} & I_0 &= 0.408 \text{ ma} & G_{eq0} &= 0.00816 \\ G_1 &= -0.0031 \text{ mho} & I_1 &= 0.14 \text{ ma} & G_{eq1} &= 0.0056. \end{aligned}$$

where

- 1)  $R_g$  is the series-source resistance and  $G_g$  is the equivalent-source conductance.
- 2)  $R_s$  is the series-loss resistance and  $G_s$  is the equivalent shunt-loss conductance.
- 3)  $R_s \ll R_g$ ;  $L_d \ll L_1$ .

Using the above definitions for the equivalent conductances, the conversion power gain ( $W_p$ ) may be shown to be

$$W_p = \frac{G_l G_g}{G_1^2} \frac{4\alpha^2}{(1 - \alpha)^2} \quad (4)$$

where

$$\alpha = \frac{G_1^2}{(G_l + G_0)(G_g + G_s + G_0)} \quad (5)$$

and the bandwidth ( $B$ ) may be found from the following relation,

$$B = \frac{\omega_1(1 - \alpha)}{\bar{Q}_1 + \bar{Q}_2 \left( \frac{\omega_1}{\omega_2} \right)} \quad (6)$$

The noise figure is given by

$$\begin{aligned} F &= 1 + \frac{T}{T_0} \left[ \frac{G_s}{G_g} + \frac{G_{eq0}}{G_g} \right. \\ &\quad \left. - \frac{G_{eq1}}{G_1} \left( \frac{G_g + G_s + G_0}{G_g} \right) \right. \\ &\quad \left. + \frac{(G_{eq0} + \frac{T_1}{T} G_l)(G_g + G_s + G_0)^2}{G_g G_1^2} \right], \quad (7) \end{aligned}$$

where

$$\begin{aligned} T_0 &= \text{reference (source) temperature in degrees Kelvin,} \\ T &= \text{temperature of the diode,} \\ T_1 &= \text{temperature of the load,} \\ G_{eq0} &= \text{equivalent-noise conductance of the diode} = eI_0/2KT, \\ G_{eq1} &= e(2I_1)/2KT. \end{aligned}$$

A converter using germanium tunnel diodes has been operated at 1200 Mc. The IF frequency was 30 Mc with the local oscillator set at 1170 Mc. The diode had a peak current of 1 ma.

Several noise figure calculations were made for various points of operation about the point of maximum positive slope of the conductance curve in the negative resistance region. Best noise figures were obtained upon biasing such that  $V_0$  is between 0.1 and 0.2 volt; this corresponds closely to the position

of minimum IR product<sup>6</sup> or I/G ratio.<sup>7</sup> With 50 mv of peak LO drive, moderate values of  $G_1$  may be obtained with relatively large negative values of  $G_0$ . The best calculated value for the noise figure was about 4.7 db, and can be obtained from the following data.

For a bias voltage of 125 mv, and a peak local oscillator voltage of 50 mv, the following parameters are obtained:

It has been assumed that the LO voltage waveform at the junction remains sinusoidal.

The series resistance,  $R_s$ , and the junction capacity are known ( $R_s = 1 \text{ ohm}$ ;  $C_d = 5 \text{ } \mu\text{f}$ ); therefore, the equivalent-loss conductance  $G_s = 0.0015 \text{ mho}$ . Assuming an  $\alpha$  in (5) to be  $\alpha = 0.7$ , and generator conductance  $G_g = 0.006$ ,  $G_1$  is found to be 0.0338 mho. By (4), the gain is found to be about 26 db; assuming in (7)  $T/T_0 = T_1/T = 1$ , the noise figure is found to be 4.7 db. By (6) the band-pass is calculated to be about 4.0 Mc.

A block diagram of the converting system as tested is shown in Fig. 4. A ferrite

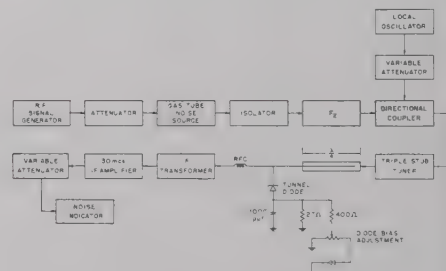


Fig. 4—Block diagram of the experimental system.

isolator was used at the input to insure good termination for the gas-tube noise source and also to isolate the converter from changes in the generator impedance (the differences in the fired and unfired condition of the noise source).  $F_2$  is a cavity band-pass filter which, in conjunction with the triple stub tuner, acted to pass the signal but reflect the image in such a manner as to present a short circuit to the image. The directional coupler serves only the cause of LO injection with good decoupling ( $\approx 25 \text{ db}$ ). The quarter-wave section shown serves not only to pass the signal, but also to block the IF. The IF transformer changes the IF impedance (50 ohms) to the desired value of about 30 ohms.

With the system adjusted as described, it was a relatively easy task to bring the measured noise figure within the range of 6–8 db. By fine adjustments of the tuning on the RF side, the bias point, the local oscillator drive, the noise figure was brought within the range of the calculated value. With the noise figure brought down to about 4.5 db the measured bandwidth was about 4.0 Mc. The

<sup>6</sup> K. K. N. Chang, "The optimum noise performance of tunnel diode amplifiers," PROC. IRE, vol. 48, pp. 107–108; January, 1960.

<sup>7</sup> J. J. Tieman, "Shot noise in tunnel diode amplifiers," PROC. IRE, vol. 48, pp. 1418–1423; August, 1960.



signal generator was used to measure the bandwidth and also to insure the absence of image response and other spurious responses that might cause erroneous noise figure indications.

An unexpected result of this fine tuning of the system was the realization of noise figures better than that calculated. Additional fine tuning of the input impedance, diode bias, and local oscillator drive gave rise to a measured noise figure of approximately 3 db and a bandwidth of 1–2 megacycles. This condition realized very high conversion gain and was not extremely stable.

There remains now a question of relative merit of the tunnel diode converter vs the tunnel-diode amplifier followed by a standard converter. There is no generalization that can apply. The question must be resolved for each separate application, since each application will have a different set of rules governing stability, gain bandwidth, over-all noise figure and so forth. As has been pointed out,<sup>8</sup> the noise figure of the converter is in general higher than that of the amplifier. As can be seen from (4)–(7), as the gain is made very large the term  $(G_o + G_s + G_n)$  becomes very small and the noise-figure equation reduces to that which applies to the one-port negative conductance amplifier. If the high-gain converter is used the system noise figure may approach or surpass that of the system using the negative conductance amplifier, for in the process of converting from signal to IF there is no loss diode mixer involved.

L. E. DICKENS  
C. R. GNEITING  
Radiation Lab.  
The Johns Hopkins University  
Baltimore, Md.  
Formerly with Bendix Radio Div.  
Bendix Corp.  
Towson, Md.

<sup>8</sup> D. I. Breitner, "Noise figure of tunnel diode mixer," *Proc. IRE*, vol. 48, pp. 935–936; May, 1960.

## Impedance Matching by Charts\*

In a previous correspondence, Somlo<sup>1</sup> sought to rectify a misstatement in an article by Hudson,<sup>2</sup> by showing a Smith Chart method of matching impedances. The method entailed finding the correct line length of the right characteristic impedance that would match two arbitrary impedances. The method Somlo shows is substantially that given in various texts,<sup>3,4</sup> although in the

texts it is done with rectangular transmission line charts rather than with Smith Charts. Indeed, for this application, the rectangular transmission line chart offers advantage over the Smith Chart. With the rectangular transmission line chart one can find the needed line length directly without having to replot the impedances and draw a second circle, as with the Smith Chart in this application as put forth by Somlo.

The statement of Somlo, "If this circle lies fully within the Smith Chart, the question has a solution, otherwise not,"<sup>1</sup> can be modified. What one can say is that if the circle does not lie fully within the Smith Chart (or fully in the right half plane of a rectangular impedance chart) then the impedances cannot be matched with a single length of line. In this case the thing to do is to place a third impedance on the chart so that circles between it and the first two impedances will lie fully in the domain of positive resistances (right half plane of the rectangular impedance chart or within the Smith Chart). Then the first two impedances can each be matched to the third. This will involve a matching transformer of two sections which for the correct choice of the intermediate impedance will have a wider band than a transformer of one section.<sup>5</sup> Even broader band transformers could be made by increasing the number of intermediate impedances and, hence, the number of matching sections. It is possible that for certain values of mismatched impedance more than one additional intermediate impedance will have to be inserted.

MICHAEL R. LEIBOWITZ  
Radio Receptor Co. Inc.  
Advanced Dev. Lab.  
Westbury, L. I., N. Y.

<sup>5</sup> LePage and Seeley, *op cit.*, pp. 347–348.

## Theoretical Evaluation of Resonance Frequencies in a Cylindrical Cavity with Radial Vanes\*

When the walls of a cavity resonator are altered from a simple geometrical configuration by a small amount, the effect on the resonance frequencies can be determined by applying perturbation methods involving the use of plausible trial fields.

The case of radial vanes inserted into a cylindrical cavity poses a relatively difficult problem, especially when the vane penetration is large. The calculation of the perturbation usually involves a volume integral over the volume enclosed between the perturbed surface and the unperturbed surface<sup>1</sup> (or a surface integral that reduces to a similar volume integral<sup>2</sup>). The volume thus enclosed,

in the case of vanes assumed to be infinitesimally thin, is also infinitesimally small. Since the fields being integrated over the volume are finite, the integral would be infinitesimally small and thus would not represent the effect of the perturbation correctly.

An alternative approach has been worked out and has been tried out in detail for the case of lower-order modes in a shallow cylindrical cavity, perturbed by a pair of radial vanes. Good agreement between calculated and experimental values has been obtained up to changes of 28 per cent between perturbed and unperturbed frequencies.

Basically, the analysis proceeds by first dividing the cavity into different regions by an assumed cylindrical surface, passing through the inner edges of the vanes (Fig. 1). A plausible field distribution at this surface, for the  $E$  field, e.g., and a plausible value for the resonance frequency are assumed. The electromagnetic field in two regions on opposite sides of the surface (regions 1 and 2) is built up by appropriately summing up the field distribution associated with the orthogonal modes in a simple cylindrical cavity. (It is to be noted that in these expressions the frequency is also involved.)

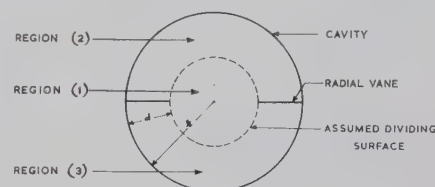


Fig. 1—Diagram showing cross section of the cavity and illustrating the method of analysis.

The Fourier components of the assumed distribution at the dividing surface are used in arriving at the above summation. For region 1 the Fourier components are so chosen that the assumed distribution is obtained for the entire range of azimuthal variation from 0 to  $2\pi$ . For region 2, a different set of components is chosen so that the assumed distribution is obtained only across region 2, but the  $E$  field is zero at the location of the vanes for all the modes. It is to be noted that unlike some of the other perturbation methods, the boundary conditions are satisfied by the trial fields at the perturbed surface also. This makes the method applicable to cases of large vane penetration.

Since the assumed distribution and frequency are only first approximations, the  $H$  fields obtained in regions 1 and 2 will not be continuous across the dividing surface. An iterative procedure has been developed by which better approximations to the frequency and the assumed field distribution are obtained in successive alternate steps, while working towards continuity of  $H$  field. The matching of fields across the dividing surface need be done in detail only for regions 1 and 2. The matching across region 1 and region 3 follows from symmetry considerations.

In the first step in the iteration, a better approximation to the frequency is obtained

\* Received by the PGMTT, October 10, 1960.

<sup>1</sup> P. I. Somlo, "A logarithmic transmission line chart" (Correspondence), *IRE TRANS. ON MICROWAVE THEORY AND TECHNIQUES*, vol. MTT-7, pp. 277–281; April, 1959.

<sup>2</sup> A. C. Hudson, "A logarithmic transmission line chart," *IRE TRANS. ON MICROWAVE THEORY AND TECHNIQUES*, vol. MTT-7, pp. 277–281; April, 1959.

<sup>3</sup> J. C. Slater, "Microwave Transmission," McGraw-Hill Book Co., Inc., New York, N. Y., p. 51; 1942.

<sup>4</sup> W. R. LePage and S. Seeley, "General Network Analysis," McGraw-Hill Book Co., Inc., New York, N. Y., p. 347; 1952.

\* Received by the PGMTT, October 10, 1960.

<sup>1</sup> J. C. Slater, "Microwave Electronics," D. Van Nostrand Co., Inc., New York, N. Y., p. 81; 1950.

<sup>2</sup> A. D. Berk, "Variational principles for electromagnetic resonators and waveguides," *IRE TRANS. ON ANTENNAS AND PROPAGATION*, vol. AP-4, pp. 104–111; April, 1956.

TABLE I

TM <sub>010</sub> Mode		Radius of Cavity = 1.500 inches		
Ratio of vane penetration $d$ to radius of cavity $r$	Resonance frequency in Mc			Percentage change between perturbed and unperturbed frequency
	Calculated	Observed	Percentage Difference	
0.0	3013	3015	0.07 per cent	0.0 per cent
0.2	3102	3095	0.23 per cent	2.9 per cent
0.4	3338	3337	0.03 per cent	10.8 per cent
0.5	3559	3565	0.17 per cent	18.2 per cent
0.6	3783	3810	0.73 per cent	25.7 per cent

TABLE II

TM <sub>110</sub> Mode		Radius of Cavity = 1.500 inches		
Ratio of vane penetration $d$ to radius of cavity $r$	Resonance frequency in Mc			Percentage change between perturbed and unperturbed frequency
	Calculated	Observed	Percentage Difference	
0.0	4800	4790	0.2 per cent	0.0 per cent
0.2	5025	5000	0.5 per cent	4.7 per cent
0.4	5530	5550	0.4 per cent	15.1 per cent
0.5	5765	5870	1.8 per cent	20.0 per cent
0.6	6155	6170	0.2 per cent	28.1 per cent

from an equation arising out of matching the surface integral of the Poynting vector across the dividing surface between regions 1 and 2. Next, a better approximation to the field distribution is obtained by means of a variational principle derived from the requirement of point by point continuity of the  $H$  field across the dividing surface. By successive steps, more accurate values of fre-

quency and distribution are thus obtained.

The same process can be carried out by starting with an  $H$  field distribution. In this case the correct value of frequency is approached from the other direction (under conditions to be presented in a full paper). Thus, the limits within which the correct frequency lies are ascertained.

Tables I and II give computed and ex-

perimental values for frequencies of the TM<sub>010</sub> and TM<sub>110</sub> modes, respectively, as perturbed by two radial vanes located diametrically opposite to each other for varying degrees of vane penetration. In the case of TM<sub>110</sub> mode, the vanes are assumed to be located at the azimuthal angle where the  $E$  field is maximum in the undisturbed case. The assumed distribution used two terms of a Fourier series. It is seen that, in practically all cases, the two sets of values agree to within 1 per cent, up to a change of 28 per cent.

The method has also been extended to the case of an interdigital resonator with vanes. It was in relation to the mode control of such a resonator that the problem first arose.<sup>3</sup>

Many helpful discussions with Dr. W. S. Lucke, in the early stages of this work, and the help of G. S. Sidhu and H. S. Dewan in the experimental observations quoted above, are thankfully acknowledged.

A. SINGH

R. A. RAO

Central Electronics Engg.

Res. Inst., Pilani

Rajasthan, India

<sup>3</sup> A. Singh, "Modes and operating voltages of interdigital magnetrons," *Proc. IRE*, vol. 43, pp. 470-476; April, 1955.



# 1960 National Microwave Symposium



Award of Microwave Prize to Bert A. Auld (left) by A. A. Oliner (right).

Members of the PGMTT San Diego Chapter appeared before the PGMTT Administrative Committee at Palo Alto, Calif., in January, 1959, to present a plan for holding the 1960 National Meeting in San Diego. The plan, which was accepted, emphasized the Symposium in a noncommercial, semi-isolated location where a technical atmosphere with a minimum of outside distractions could be obtained.

Immediately afterwards a Steering Committee, later to become the Symposium Committee, was organized. The Committee broke precedent with previous Symposia by making the Technical Program Committee an integral part of the Symposium Committee, rather than treating it as a separate unit.

The Symposium Committee members were as follows:

**Chairman:** D. Proctor, Convair-Astronautics

**Vice-Chairman:** W. E. Moore, Convair-Astronautics

**Finance:** B. I. Small, U. S. Navy Electronics Laboratory

**Technical Program:** Dr. D. B. Medved, Convair-Astronautics

**Local Arrangements:** H. D. Dickstein, Cubic Corporation

**Publicity:** H. A. Babbitz, Convair-Astronautics

**San Diego Section Representative:** R. E. Honer, Convair-Astronautics

**Administrative Committee Representative:** Dr. R. C. Hansen, Space Technology Laboratories

**Student Activities Representative:** Dr. C. R. Moe, San Diego State College

**Women's Activities:** Mrs. Kirk Abbey

**1959 Symposium Representative:** W. L. Pritchard, Raytheon and Company

The symposium was held at the Del Coronado Hotel in Coronado, Calif., across the bay from San Diego. Registrations totaled 512, of which 170 were from the East Coast and 4 from foreign countries.

There were seven technical sessions, including a panel session on Parametric Amplifiers on Monday evening, May 7. A total of thirty-nine papers, including ten invited

papers, was presented. An additional panel session on Microwave Propagation in Plasmas and Solids was held on Wednesday, May 9. Eighty-two papers were submitted; however, due to the crowded program, many fine papers could not be accepted. It appears that future meetings might advantageously include an extra day, or that two meetings a year may be in order.

A banquet was held in the Crown Room at the Del Coronado Hotel on Tuesday night, May 8, featuring an address by Dr. W. A. Edson on "Future Microwave Power Sources." The Microwave Prize was announced by Dr. A. A. Oliner and presented to Dr. B. A. Auld of Stanford University, for his paper, "The Synthesis of Symmetrical Waveguide Circulators," which appeared on pages 238-246 of the April, 1959, issue of these TRANSACTIONS.

The 1960 Symposium was a departure from previous Symposia in that it was not held in an area of great microwave activity; it was an experiment in having a meeting in semi-isolated resort areas offering a greater opportunity for exchanging ideas and getting the most out of the technical sessions.

(See additional Symposium photos on next page.)





Symposium banquet. Head table (left to right); H. D. Dickstein, *Chairman, San Diego Chapter*; Mrs. Dickstein; Mrs. Tomiyasu; Kiyo Tomiyasu, *Vice-Chairman, Administrative Committee*; Dr. B. A. Auld, *Microwave Prize winner*; A. A. Oliner, *Chairman, Administrative Committee*; Mrs. Proctor; D. Proctor, *Chairman, Symposium Committee*; W. E. Edson, *Speaker*; Mrs. Edson; R. E. Honer, *Chairman, San Diego Section*; Mrs. Honer; D. B. Medred, *Chairman, Technical Program*; Mrs. Medred; W. E. Moore, *Vice Chairman, Symposium Committee*.



First session.



First session speakers.



# Contributors

William P. Allis was born in Menton, France, on November 15, 1901. He was educated at the Massachusetts Institute of Technology, Cambridge, Mass., receiving the B.S. degree in 1923, the M.S. degree in 1924, from this institution, and the D.Sc. degree in 1925 from the University of Nancy, France. He was a Lieutenant Colonel in the U. S. Army from 1942 to 1945 and received the Legion of



W. P. ALLIS

Merit Award in 1945.

He was, successively, a research associate in physics, instructor, assistant professor, associate professor, and professor at M.I.T. He has been chairman of the Gaseous Electronics Conference since 1949 and a consultant to the Los Alamos Scientific Laboratory since 1952. His special field of work is in plasma physics.

Dr. Allis is a Fellow of the American Physical Society, the Association of Physics Teachers, the American Academy of Sciences and The Physical Society, London, and a member of Sigma Xi.



William W. Anderson (S'53-M'59) was born in Tacoma, Wash., on February 26, 1933. He received the B.S. and M.S. degrees in electrical engineering from the Massachusetts Institute of Technology, Cambridge, in 1956, under the electrical engineering cooperative program, and the Ph.D. from Stanford University, Stanford, Calif., in 1959.



W. W. ANDERSON

While at M.I.T. he worked alternate semesters in the cooperative program at the Naval Ordnance Laboratory, Silver Spring, Md. Since 1959, he has been associated with the Bell Telephone Laboratories, Murray Hill, N. J., where he has worked on various problems in the Solid-State Electronics Research Department. He is now with the department of electrical engineering, Stanford University, Stanford, Calif.

Dr. Anderson is a member of Sigma Xi.



Frank R. Arams (S'44-A'49-SM'55) was born on October 18, 1925 in the Free City of Danzig. He received the B.S.E. degree in electrical engineering and mathematics from the University of Michigan, Ann Arbor, in 1947, the M.S. degree in applied physics from Harvard University, Cambridge, Mass.,

in 1948, and the M.S. degree in business management from Stevens Institute of Technology, Hoboken, N. J., in 1953.



F. R. ARAMS

He is presently completing the requirements for the doctorate degree in electrical engineering at the Polytechnic Institute of Brooklyn, Brooklyn, N. Y. During World War II, he served in the Army Signal Corps as communications chief of Radio Receiver Station WXH, Ketchikan, Alaska. He joined the Radio Corporation of America, Lancaster, Pa., in 1948, where he was project engineer on various development programs in microwave magnetrons, traveling-wave tubes, and plasma-filled cavities. From 1953 to 1956, he was employed at the Tube Division of the Radio Corporation of America, Harrison, N. J., where he was in charge of the microwave-tube application engineering group. In 1956, he joined the staff of Airborne Instruments Laboratory, Melville, N. Y., where he is presently associated with the Department of Applied Electronics as Consultant, and is concerned with theoretical and experimental work on microwave solid-state devices, such as new types of solid-state maser amplifiers, microwave ferrite devices, and parametric amplifiers. He is presently directing programs in the microwave ferrite, and microwave and optical maser fields.

Mr. Arams is a member of Tau Beta Pi, Eta Kappa Nu, the American Physical Society, and the Editorial Boards of the IRE TRANSACTIONS ON MICROWAVE THEORY AND TECHNIQUES and the *Microwave Journal*.



Isidore Bady (A'42-M'54-SM'56) was born on July 21, 1913, in Brooklyn, N. Y. He received the B.S. degree from the College of the City of New York in 1933 and the M.E.E. degree from the Polytechnic Institute of Brooklyn, New York, in 1949. He is currently working towards a doctoral degree at Rutgers University, Princeton, N. J.



I. BADY

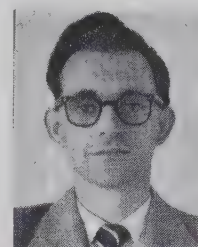
He has been employed by the United States Army Signal Research and Development Laboratory, Fort Monmouth, N. J., since 1941. Initially, he worked on instrumentation for the evaluation of components and materials. The frequency range covered was from dc through microwaves. Instrumentation under pulse conditions was also included. For the past four years he has

worked in the field of magnetic materials, particularly ferrites.

Mr. Bady is a member of Phi Beta Kappa.



Brian J. Elliott was born on August 29, 1929, in Auckland, New Zealand. He received the B.Sc. and M.Sc. degrees in 1953 and 1956, respectively, from the University of New Zealand. From February, 1956, to February, 1957, he was on the teaching staff of the Auckland University College. Since April, 1957, he has been employed as a research associate at the Microwave Laboratory, W. W. Hansen Laboratories of Physics, Stanford University, Stanford, Calif.



B. J. ELLIOTT

Research for the M.Sc. degree involved precision current and voltage regulation problems. His work at the Hansen Laboratories has been concerned with high powered modulator design, millimicrosecond pulse technology, and most recently, ferrites at microwave frequencies.



Sverre T. Eng (M'58), was born in Harstad, Norway, on July 30, 1928. He received the Master's degree in electrical engineering from Chalmers University of Technology, Gothenburg, Sweden, in 1953.



S. T. ENG

From 1953 to 1956, he was a research associate at the Laboratory of Electronics of Chalmers University, where he worked in the field of microwave systems and radio astronomy. From 1956 to 1957 he worked with the Semiconductor Division of Hughes Aircraft Co., Los Angeles, Calif., on high-frequency transistor characterization and circuits. During the years 1957 to 1958 he did some special studies in electronics at Stanford University, Palo Alto, Calif., and worked as a research assistant on advanced transistor circuitry.

He rejoined Hughes Semiconductor Division, this time at Newport Beach, Calif., in 1958. Since then he has been working on research and development of parametric amplifier diodes, mixer diodes, and microwave characterization and application of semiconductor devices. In 1958 Mr. Eng. became a section head; he is presently in charge of microwave semiconductor electronics.

Mr. Eng is a member of the Scientific Research Society of America.



M. E. Hines (S'46-A'47-M'50) was born on November 30, 1918, in Bellingham, Wash. He attended the California Institute of



M. E. HINES

Technology, Pasadena, where he received the B.S. degree in applied physics in 1940 and, as a member of the Air Force Weather Service, the B.S. degree in meteorology in 1941. After World War II, he returned to the California Institute of Technology, where he received the M.S. degree in electrical engineering in 1946.

He has been employed since 1946 at the Bell Telephone Laboratories at Murray Hill, N. J., where he has been engaged in the development of traveling-wave tubes, microwave triodes and storage tubes. He has also been concerned with the development of pulse-code modulation transmission systems. Most recently, he has been in charge of a group interested in solid-state microwave devices. Mr. Hines is now associated with Microwave Associates, Inc., Burlington, Mass.



Tom M. Hytlin (S'51-A'54-M'60) was born in Temple, Tex., on October 22, 1930. He received the B.S. degree in electrical engineering from the University of Texas, Austin, in 1957.



T. M. HYTLIN

From 1953 to 1956, he was employed by Kiva Exploration Corporation in Austin where he was engaged in the design and development of electronic geophysical prospecting equipment. In 1956, he joined the staff of the Electrical Engineering Research Laboratory at the University of Texas, where he worked on instrumentation for millimeter wave propagation studies.

He was with Temco Aircraft Corporation for one year, working on various projects in missile guidance. In 1958, he joined Texas Instruments, Apparatus Division, where he is now engaged in solid-state microwave device development in the Research and Development Department.



Frank Keywell was born on March 16, 1923, in Detroit, Mich. He received the B.A. degree in physics-meteorology from the University of California at Los Angeles in 1944. During World War II, he served with the United States Air Force in the fields of weather forecasting and aircraft operations. He received the M.S. degree in 1951 and the Ph.D. degree in 1954 in physics from the University of Southern California. His thesis work, done under an ONR contract, was related to high-vacuum's sputtering of metals due to ion bombardment and a statement of the phenomenon in terms of radiation damage in metals.

tion damage in metals.

After graduation, he joined the Bell Telephone Laboratories, Murray Hill, N.J. where he did work in the field of silicon junction transistor development by means of gaseous diffusion techniques. He worked on development of diffused silicon mesa parametric diodes for two years in the employ of Hughes Aircraft Company. Since 1960, he has been Director



F. KEYWELL

of Research and Development for Semiconductor Devices Incorporated, Newport Beach, Calif., his main interest being in the field of parametric diodes and applications of semiconductor materials to the microwave region.

Dr. Keywell is a member of the American Physical Society and Sigma Xi.



Kenneth L. Kotzebue was born in San Antonio, Tex., on December 4, 1933. He received the B.S. degree in mechanical engineering from the University of Texas, Austin, in 1954, the M.S. degree in engineering from the University of California at Los Angeles in 1956, and the Ph.D. degree in electrical engineering in 1959 from Stanford University, Stanford, Calif.



K. L. KOTZEBUE

During 1954-1956 he was a member of the technical staff of Hughes Aircraft Company, Los Angeles, Calif., while a participant in the Master's Cooperative Program. He was research assistant at Stanford University for two years, working in the field of solid-state parametric amplifiers. In 1958 he became a senior engineer with the Apparatus Division of Texas Instruments, Inc., Dallas, where he worked in the field of semiconductor diode parametric amplifiers and harmonic generators. Since 1959 he has been a member of the technical staff of Watkins-Johnson Company, Palo Alto, Calif., engaged in research and development of solid-state microwave devices.

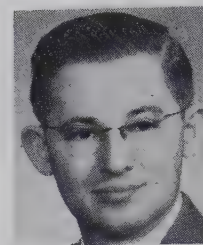
Dr. Kotzebue is a member of Tau Beta Pi and Sigma Xi.



Dr. Benjamin Lax was born in Hungary on December 29, 1915. He received the B.M.E. degree from Cooper Union, New York, N. Y., in 1941 and the Ph.D. degree in physics from the Massachusetts Institute of Technology, Cambridge, in 1949.

While serving in the army from 1942 to

1946, he attended radar school at Harvard University, Cambridge, Mass., and M.I.T. He was a radar officer assigned to M.I.T.



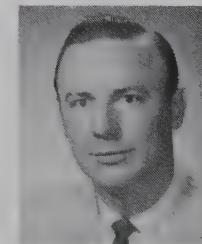
B. LAX

Radiation Laboratory from 1944 to 1946. In 1946 he became a consultant for Sylvania Electric Company. From 1949 to 1951 he carried on research in microwave gas discharge for the Geophysical Directorate of Cambridge Research Center. In November, 1951 he joined the Solid-State Group at Lincoln Laboratory, M.I.T., and in 1953 he became head of the ferrites group. In 1955 he became head of the Solid State Group. In 1957 he became associate head of the Communications Division at Lincoln Laboratory, in charge of solid-state physics in several laboratory groups, and was appointed head of the Solid-State Division when it was established in 1958. He was also appointed director of the new M.I.T. Magnet Laboratory in July, 1960.

Dr. Lax was recipient of the 1960 Oliver E. Buckley prize of the American Physical Society for his fundamental contributions to microwave and infrared spectroscopy of semiconductors. He is a Fellow of the American Physical Society and a member of the Executive Committee of the Solid-State Division, the Solid-State Advisory Panel of the Office of Naval Research. He was associate editor of the *Journal of Applied Physics* from 1957-1959, and is now associate editor of the *Physical Review* and the *Microwave Journal*. He is a member of Sigma Xi.



James A. Luksch (M'58) was born in Buffalo, N. Y. on July 12, 1930. He received the B.S. degree in electrical engineering from the University of Buffalo, Buffalo, N. Y., in 1957 and the M.S. degree in electrical engineering from the University of Pennsylvania in 1960.



J. A. LUKSCH

In 1957 he joined RCA as a microwave engineer with the Missile and Surface Radar Department, where he has worked on the design of microwave components and low-noise devices. He is presently concerned with the development of solid-state microwave components.

Mr. Luksch is a member of Tau Kappa Chi.



George L. Matthaei (S'49-A'52-M'57), for a photograph and biography, please see page 675 of the November, 1960, issue of these TRANSACTIONS.



Edgar W. Matthews, Jr. (S'46-A'47-M'54-SM'60), was born in Johnstown, Pa., on May 19, 1925. He received the B.E.E. and M.E.E. degrees from Rensselaer Polytechnic Institute in 1946 and 1950, respectively, and the Ph.D. degree from Harvard University in 1954.



E. W. MATTHEWS

From 1946 to 1947 he worked as a junior engineer at the Westinghouse Research Laboratories, and from 1947 to 1949 he was an instructor at R.P.I. While at Harvard (1949-1953) he held first a Teaching Fellow appointment and later an AEC Predoctoral Fellowship. From 1953 to 1955 he was employed in the microwave research section of Sperry Gyroscope Company. He returned to R.P.I. in 1955 for combined teaching and research, as an assistant professor and later as an associate professor of electrical engineering. He joined the RCA Missile and Surface Radar Division, Moorestown, N. J., in 1958, where he has been engaged in the development and application of low-noise parametric and tunnel diode amplifiers for use in monopulse radars. In 1960 he was appointed a group leader in the Microwave Antenna Unit. He has also been associated with the RCA-Villanova Graduate Program.

Dr. Matthews is a member of Tau Beta Pi, Eta Kappa Nu, Sigma Xi, and the American Society for Engineering Education.



David Pines was born in Kansas City, Mo., on June 8, 1924. He received the B.A. degree from the University of California, Berkeley, in 1944, and the M.A. and Ph.D. degrees from Princeton University, Princeton, N. J., in 1948 and 1950, respectively.

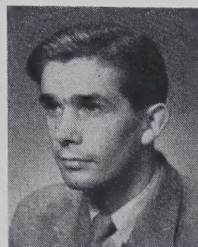
He was a member of the faculty of the University of Pennsylvania, Philadelphia, from 1950 to 1952, of the University of Illinois, Urbana, from 1952 to 1955, and of Princeton from 1955 to 1958. He was a National Science Foundation Senior Post-Doctoral Fellow and an exchange professor at the University of Paris during 1957-1958, and a visiting member of the Institute for Advanced Study during 1958-1959. Dr. Pines is presently professor of physics and electrical engineering at the University of Illinois, and is also affiliated with the John Jay Hopkins Laboratory for Pure and Applied Science, General Atomic Division of General Dynamics Corporation, San Diego, Calif.



Tor Schaug-Pettersen was born in Narvik, Norway on June 4, 1928. He received the E.E. degree from Chalmers Institute of

Technology, Gothenburg, Sweden, in 1952.

Since 1951 he has been employed at the Norwegian Defense Research Establishment, Bergen, Norway, doing research on microwave communication and microwave network theory. From 1958 to 1960 he spent 18 months at the Microwave Laboratory of Stanford University, working mainly on microwave properties and applications of ferrites.



T. S. PETTERSEN

Mr. Schaug-Pettersen is a member of Sigma Xi and the Tensor Club of Great Britain.



W. M. Sharpless (A'28-M'38-SM'43-F'58) was born in Minneapolis, Minn., on September 4, 1904. He received the B.S. degree in electrical engineering in 1928 and the E.E. degree, both from the University of Minnesota, Minneapolis.



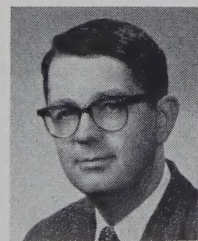
W. M. SHARPLESS

He is a member of the Radio Research Department of the Bell Telephone Labs., Holmdel, N. J., where for the past years he has been associated with many important research projects. His most recent work has been on studies having to do with the investigation of the resistive and reactive properties of high frequency point contact diodes.

Mr. Sharpless is a member of the Scientific Research Society of America and the American Physical Society.



Herbert J. Shaw (M'55) was born in Seattle, Wash., on June 2, 1918. He received the B.S. degree from the University of Washington, Seattle, in 1941, and the M.A. and Ph.D. degrees in 1942 and 1948, respectively, from Stanford University, Stanford, Calif.



H. J. SHAW

In 1941 he was a test engineer at General Electric Co. in Schenectady, N. Y. Since then he has been at Stanford University, where he is presently a senior research associate in the Microwave Laboratory and a research associate in the physics department. He was acting director of the Microwave Laboratory during the summer of 1960. He is engaged in research in microwave tubes and microwave physics.

Dr. Shaw is a member of Tau Beta Pi and Sigma Xi.

Isamu Tatsuguchi was born in Hauula, Oahu, Hawaii on November 22, 1926. He received the B.S. degree in electrical engineering in 1951 from Milwaukee School of Engineering, Milwaukee, Wis. He served as a teaching assistant and later as a research assistant while at the University of Wisconsin, Madison, where he received the M.S. and Ph.D. degrees in electrical engineering in 1953 and 1955, respectively.



I. TATSUGUCHI

He joined the Bell Telephone Laboratories in Whippany, N. J., in 1955. As a member of the technical staff there, he has been engaged in research, development and measurement work involving low noise microwave components and circuits.

Mr. Tatsuguchi is a member of Sigma Xi.



George A. VerWys (M'57) was born in Kalamazoo, Mich., on March 28, 1933. He received the B.S. degree in electrical engineering from the University of Michigan, Ann Arbor, in 1956.



G. A. VERWYS

In 1956 he joined RCA as a design engineer in the Missile and Surface Radar Division at Moorestown, N. J., where he has worked with radar components and, in particular, with low-noise receivers.



Rolf D. Weglein (A'52-SM'58) was born in Ichenhausen, Germany, on August 13, 1920. He received the B.S.E.E. and M.S.E.E. degrees from the California Institute of Technology, Pasadena, in 1953 and 1954, respectively.



R. D. WEGLEIN

In the years since his graduation, he has been a member of the technical staff of the Research Laboratory of the Hughes Aircraft Company, now at Malibu, Calif. Early work in research and development of backward-wave oscillators has recently resulted in his interests in solid-state devices. He now heads a group concerned with solid-state parametric amplifiers.

Mr. Weglein is a member of Tau Beta Pi, RESA, Sigma Xi, and the American Physical Society.







## INSTITUTIONAL LISTINGS

MICROWAVE DEVELOPMENT LABS, INC.  
92 Broad St., Babson Park 57, Mass.

Designers, Developers and Producers of Microwave  
Components and Assemblies, 400 Mc to 70 kMc

SCIENTIFIC-ATLANTA, INC.  
2162 Piedmont Rd., N.E., Atlanta 19, Ga.

Complete Antenna Pattern Range Instrumentation,  
Special RF and Antenna Systems Development

PRD ELECTRONICS, INC.  
202 Tillary St., Brooklyn 1, N.Y.

Complete Line of Microwave and Electronic Test Equipment  
Waveguide and Coaxial Components

SYLVANIA MICROWAVE DEVICE OPERATIONS  
Sylvania Electric Products Inc.  
500 Evelyn Ave., Mountain View, Calif.

Magnetrons, Klystron, TWT's, BWO's, Ferrite Devices,  
Waveguide Windows, Microwave Diodes

SAGE LABORATORIES, INC.  
3 Huron Dr., Natick, Mass.

Microwave Attenuators, Couplers, Crystal Holders,  
Filters, Hybrids, Mixers, Rotary Joints

WATKINS-JOHNSON COMPANY  
3333 Hillview Ave., Palo Alto, Calif.

Res., Dev., Microwave Electron Devices, TWT's,  
BWO's, Parametric Amplifiers, Microwave Systems

WHEELER LABORATORIES, INC.  
Great Neck, N.Y.  
Antenna Lab., Smithtown, N.Y.

Consulting Services, Research & Development,  
Microwave Antennas & Waveguide Components

(See outside back cover for additional listings.)



## INSTITUTIONAL LISTINGS

The IRE Professional Group on Microwave Theory and Techniques is grateful for the assistance given by the firms listed below, and invites application for Institutional Listing from other firms interested in the Microwave field.

AIRTRON, INC.  
A Division of Litton Industries  
200 East Hanover Ave., Morris Plains, N.J.  
Designers and Producers of Complete Line of  
Microwave Electronic and Aircraft Components

FXR, INC.  
25-26 50th Street, Woodside 77, N.Y.  
Precision Microwave Test Equipment, High Power Microwave  
Electronics, Microwave Components & Instrumentation

ALFORD MANUFACTURING COMPANY  
299 Atlantic Ave., Boston 10, Mass.  
RF Instruments, Coaxial Components,  
Antennas and Air Navigation Aids

HUGHES AIRCRAFT CO.  
Florence and Teale Sts., Culver City, Calif.  
Res., Dev., Mfg.: Radar Systems and Components, Microwave  
Devices and Components, Antennas, Tubes

CASCADE RESEARCH  
Div. of Lewis & Kaufman Electronics Corp.  
5245 San Fernando Rd., Los Angeles, Calif.  
Research, Development, Production: Microwave Ferrite Devices,  
Microwave Components & Subsystems

ITT FEDERAL LABORATORIES  
500 Washington Ave., Nutley 10, N.J.  
Line-of-Sight and Over-the-Horizon Microwave  
Systems; Test Equipment and Components

EIMAC TUBES, EITEL-McCULLOUGH, INC.  
301 Industrial Way, San Carlos, Calif.  
Microwave Tubes, TWT-VTM-Reflex Klystrons,  
Power Grid Tubes, Amplifier Klystrons

LITTON INDUSTRIES  
Electron Tube Division  
960 Industrial Rd., San Carlos, Calif.  
Magnetron, Klystrons, Carcinotrons, TWT's, Backward Wave  
Oscillators, Gas Discharge Tubes, Noise Sources

(See inside back cover for additional listings.)

The charge for an Institutional Listing is \$50.00 per issue or \$210.00 for six consecutive issues. Applications for Institutional Listings and checks (made out to The Institute of Radio Engineers, Inc.) should be sent to Robert A. Rivers, PGMTT Advertising Editor, Aircom Inc., 354 Main St., Winthrop 52, Mass.